Politecnico di Torino

ScuDo
Scuola di Dottorato ~ Doctoral School
WHAT YOU ARE, TAKES YOU FAR

Doctoral Dissertation
Doctoral Program in Mechanical Engineering (34^{th}cycle)

Agri.Q

Sustainable Rover for Precision Agriculture

By

Andrea Botta

******

Supervisor(s):
Prof. Giuseppe Quaglia, Supervisor

Doctoral Examination Committee:
Prof. Giuseppe Carbone , Referee, Università della Calabria
Prof. Giulio Reina, Referee, Politecnico di Bari

Politecnico di Torino
2022

Declaration

I hereby declare that, the contents and organization of this dissertation constitute my own original work and does not compromise in any way the rights of third parties, including those relating to the security of personal data.

Andrea Botta
2022

* This dissertation is presented in partial fulfillment of the requirements for **Ph.D. degree** in the Graduate School of Politecnico di Torino (ScuDo).

Abstract

The thesis reports on the design, development, and integration of the articulated mobile robot for precision agriculture and its control architecture. Starting from bibliographic research on precision agriculture with a particular focus on terrestrial robotic platforms (UGVs), the Agri.Q project was then developed with the aim of creating an articulated robot for agriculture in vineyards, or on fields with large slopes, with particular attention to the issue of sustainability and the integration of the robotic platform with monitoring drones and a redundant robotic arm dedicated to collect field samples or to interact with the environment. The thesis therefore reports the mechanical and electronic design process of the robot, focusing on the peculiarities and salient features. The thesis also gives wide space to the study and analysis of the kinematic and dynamic behavior of the robot navigation through models, simulations, and experimentation on the prototype itself. These results become functional for the implementation of appropriate control strategies to overcome some problems related to the robot architecture and to make it a robust and functional platform. The thesis is accompanied by further phases of experimentation on more specific topics, such as the evaluation of power flows and the effectiveness of solar charging, an initial integration of a redundant robotic arm, and the beginning of preparatory activities for the implementation of an autonomous driving.

Contents

List of Figures

List of Tables

Chapter 1

Introduction

1.1 Precision agriculture and sustainability

The world population is constantly growing and it keeps requiring increasing food production. For example, according to Sylvestere [2] agricultural production, in particular field agriculture [3], has to expand by 70% by 2050, when the global population is expected to reach 9 billion people. At the same time, the intensification of agriculture activities results in the waste and exploitation of irrigation water, fertilizer, and other phytosanitary products, which have a negative impact on environmental sustainability and farmers' profit [4]. Since agriculture dominates the world land usage, the urgent need to substantially increase the intensive food production over the next years using less land and water would inevitably require considerable social, economic, and environmental costs. Identifying methods and technologies to reduce such costs by enhancing productivity and profits while protecting the environment is, thus, essential [5].

In conventional agriculture, standard management procedures comprise the uniform use of water and agrochemicals, ignoring the variability within the field of crop conditions and needs [6]. On the global scale, this system is no more sustainable to achieve a high level of production while minimizing the environmental impact, therefore it is imperative to propose and introduce new sustainable solutions, such as Precision Agriculture (PA) [7]. Precision agriculture is a farming trend that has received considerable attention in the last few years [8], as it entails the application of current information and communication technology with the goal of increasing

agricultural yields and profitability. At the same time, precision agriculture reduces the amount of investment in resources such as arable land, water, fertilisers, and other agrochemicals required to cultivate fields [9]. Pierce and Nowak [10] gave the most common definition of PA: *"Precision Agriculture is the application of farming strategies and methodologies to do the right thing, in the right place and at the right time"*, while data and technologies detect and decide what is right [11]. Hence, PA is a data-driven method for gathering, analyzing, and better managing farm data with the goal of enhancing knowledge and management of soil and resources to predict and manage crops. As a result, it has the potential to increase agricultural production (yield) and profit, resulting in improved environmental quality. Furthermore, it supports farmers in making sound judgments while also automating certain essential farming operations [12, 13]. In other terms, PA can be seen as a holistic and sustainable strategy in which farmers can vary and modulate their actions and cultivation methods (such as planting, tillage, harvesting, application of fertilisers, pesticides, and water) to match the varying soil and crop conditions and needs within the field [6].

Srinivasan [5] stated that PA differs from conventional farming, as it is based on determining crop variation more precisely and linking spatial and temporal relationships to actions on the field, thereby allowing farmers to manage their farms, crops and practises from an entirely new perspective, thereby leading to

- reduction in costs,
- optimisation of yields and quality in relation to the productive capacity of each site,
- better management of the resources, and
- protection of the environment.

PA has the potential to transform agriculture by providing a wide range of benefits in terms of profitability, productivity, sustainability, crop quality, environmental protection, on-farm quality of life, food safety, and rural economic development [14, 15]. On a regional level, spatial and temporal categorization of farms can aid in identifying developing patterns in elements that affect sustainability, whether in geographically adjacent areas or specific agro-ecological zones, and directing viable solutions. Building geo-referenced datasets for each field in an area will help identify

the reasons and elements that underlie each cropping system productive aspect, and provide a synthesis of the proportion and severity of factors that hinder or improve sustainability within and between fields [5].

Many elements of PA have been investigated, including relevant technologies, environmental implications, profitability, adoption rates, and the reasons for adoption and non-adoption. Many researchers [16–18] have proven the environmental and economic benefits of PA. Nonetheless, both academic surveys and professional reports continue to reflect a low incidence of PA adoption [19–21].

1.2 Sustainable Development Goals in agriculture

The Sustainable Development Goals (SDGs) are "a universal call to action to end poverty, protect the planet, and improve the lives and prospects of everyone, everywhere. The 17 Goals were adopted by all UN Member States in 2015, as part of the 2030 Agenda for Sustainable Development, which set out a 15-year plan to achieve the Goals" [22]. The application of new technologies and methods in agricultural processes has piqued the interest of the engineering research community among the many scientific and technical difficulties arising from the pursuit of the SDGs agenda [23]. In reality, such technologies are ideal for the precision agriculture paradigm, which attempts to improve the long-term viability of agricultural production by using specialised equipment. Profitability and efficiency are also increased as a result of this [24]. In the PA scenario, the SDG 2, SDG 6, SDG 12, SDG 13, and SDG 15 are addressed (Figure 1.1):

- Adopting sustainable agricultural practises that increase productivity and production, help sustain ecosystems and strengthen the capacity to adapt to climate change, extreme weather conditions, drought, floods, and other disasters, as well as gradually improving the quality of land and soil. All of that is the key for achieving the aims of SDG 2 - *Zero Hunger* by 2030 [25]. By adopting PA, farmers and agricultural organisations have access to technologies that allow them to maximise yields, check product quality, improve crop management, and reduce resource use costs with the goal of ensuring food security around the world and overcoming the hunger problem.

Fig. 1.1 Sustainable Development Goals and agriculture

- Global water demand will increase by more than 50% by 2030, and agriculture alone will require more than can be supplied. As a result, in agreement with SDG 6 - *Clean Water and Sanitation* [26] to promote access to and sustainable management of water and sanitation, PA solutions enable farmers to manage agrochemicals and avoid misuse or needless application of fertilisers and pesticides, preserving water and soil quality.

- The UN is working towards sustainable management and effective use of natural resources as the goals targeted by SDG 12 - *Responsible Consumption and Production* [27]. As a result of the implementation of active innovation in the development of its products, the PA approach assists farmers to achieve safe management of phytosanitary products and other wastes and avoid the use of harmful substances where possible, reducing their adverse effects on soil, water, and air, and thus on human health.

- SDG 13 - *Climate Action* requires urgent efforts and actions to face climate change and its consequences [28]. The PA strategies provide users with tools and technologies that not only ensure sustainability and boost production and

profit, but also provide instruments to monitor the climate and allow them to take adequate preventive measures to protect both fields and the environment.

- Unsustainable land use and management practises, as well as extreme climatic occurrences caused by diverse social, economic, and governance issues, constitute a serious and rising danger to soil degradation. PA moves toward the goals given by SDG 15 - *Life on Land* [29] that promotes action in favour of restoration, prevention, and sustainable use of land and soil thanks to planned and appropriate interventions on crops and fields.

1.3 Enabling technologies in precision agriculture

The precision agriculture process is composed of three key phases that repeat cyclically (Fig.1.2). In particular, such phases can be identified as

1. the data analysis and treatment plan phase,
2. the precision treatments application phase, and
3. the monitoring and data collection phase.

In the first step, the available data is post-processed and integrated with soil and crop models, to divide the field into management zones (MZs) characterised by homogeneous treatment requirements. MZs become the areas of intervention where precise and defined treatments are applied [30, 31]. Consequently, the soil is treated by MZs by supplying the correct quantities of fertiliser, water, or agrochemicals, and then sowing begins. During crop growth, the soil and the crop are continuously monitored and mapped with the aim of planning and performing any crop management activity (like watering, applying herbicides or pesticides, removing weeds) locally and only if it is needed. When the crop is ready, it is harvested and the yield is measured and mapped. This phase does not require autonomous treatment application, but only that the treatments are done according to the plan made in the previous phase. In the last phase, all data collected in the previous phases and during any other monitoring activity are processed to create maps describing field conditions, such as topography, soil composition, soil nutrients, crop condition, and yield maps. All of these raw data are then sent to the first phase of a new cycle to be processed, analysed, and interpreted to define new and appropriate MZs and their treatments.

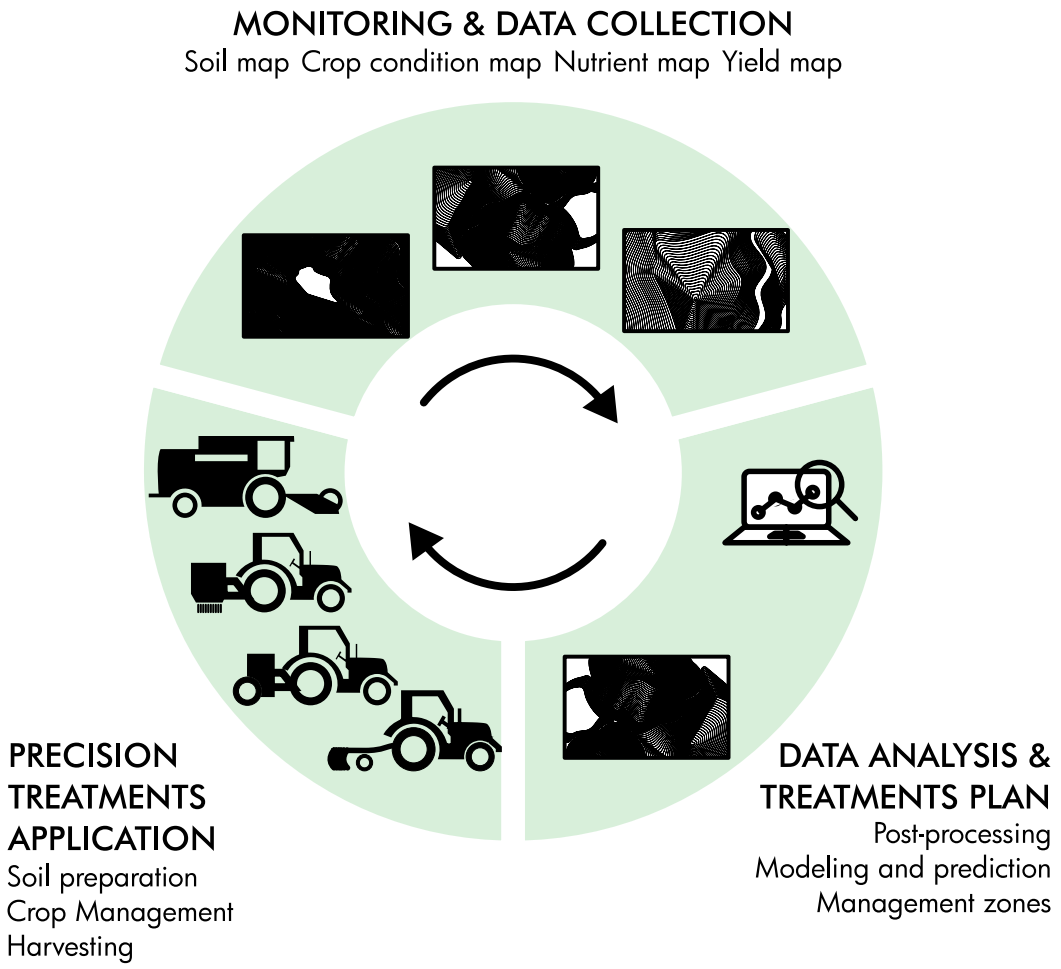

Fig. 1.2 The precision agriculture cycle and its main phases

From this very generic and brief description of a PA cycle, it is clear that PA is data-intensive and requires several technologies, but the application of its concepts and principles does not require heavy equipment or large fields [5]. Instead, the PA approach can be adapted and applied to various settings. It also appears that the key functionalities required by automated agricultural vehicles and systems acting on the field can be grouped into four categories [32]:

- **Navigation**: the vehicle has to autonomously navigate in the field following a predefined path, reaching some relevant way-points, and avoiding any obstacle or collision.
- **Sensing**: the PA vehicle must be able to detect, measure and sample anything that could be useful to plan the crop and soil management actions.

- **Mapping**: the sensing activity results in a large set of data that is usually post-processed in Geographic Information System (GIS) that basically are maps collecting all the relevant field features.
- **Action**: the mapping defines several MZs and then in each MZ the needed treatment is performed. Therefore, PA vehicles must be designed to perform such tasks autonomously.

As for all autonomous vehicles, the navigation is based on all the technologies that allow an agent to localise in an environment and eventually to map it, doing what is known as Simultaneous Localisation and Mapping (SLAM) . Therefore, the correct implementation of a localisation system, like the GNSS , with a set of exteroceptive sensors (e.g., image-based systems, sonars, radars, LIDARs, etc.) to locate and map at the same time, is key to autonomous navigation.

Post-processing and mapping of the data may provide farmers with knowledge of essential resources, as well as information on how much and when they should be applied by analysing the information provided by these solutions before they can provide agronomic suggestions or instructions [9]. This is the core of PA and requires expert knowledge on the collected sensing data to properly process them to define the required actions. Due to the complexity of this task and the increasing adoption of PA, newer sensors are now developed with user-friendliness in mind [33]. The action category of PA agriculture is generally the evolution in terms of automation and local application of the conventional applications of mechanised agriculture, therefore autonomous systems are in general specialized for a limited set of tasks.To conclude, the sensing part of PA is the crucial element, together with mapping, that really defines the precision agriculture approach. Whatever technology used, the objective of the PA sensing is to measure soil and crop statuses (i.e., soil pH, humidity, nutrients composition, and crop conditions and yield), and generally, this is done through remote or proximal sensing.

1.3.1 Remote sensing

Remote sensing methods and image analytics to assess soil status and vegetation health from distance by employing images collected in different spectra are a fascinating and continuously developed trend in PA. Aerial monitoring, which uses photos

acquired by satellites, manned aircraft, and unmanned aerial vehicles (UAVs), is one of the most widely used remote sensing approaches [34]. Sometimes unmanned ground vehicles are also equipped with remote sensors. Several prior studies [35–40] presented review papers on different elements of robotics and remote sensing in PA. Remote sensing is a broad category that encompasses all noninvasive and nondestructive methodologies for assessing crop and plant states by analyzing and parametrising their morphology and physical description. According to Yadun Navarez et al. [39], optical visible and near-visible spectrum sensors and technologies for estimating phenotyping variables from intensity, spectral, and volumetric data may be divided into three categories based on their target use:

- **Structural characterization:** Estimating factors including canopy volume, plant height, leaf area coverage, and biomass, among others, leads to choices that improve the agricultural process. Using canopy volume data, a number of studies [41, 42] were able to enhance the spraying of pesticides and fertilizers on fruit trees in terms of input savings and environmental costs. Furthermore, Mora et al. [43] employed leaf area coverage for crop growth monitoring and yield prediction since it represents several elements of vegetation's physiological processes. Additionally, biomass mapping and monitoring allow for the detection of changes in plantation condition caused by storms, drought, or diseases [44, 45]. Further, since bio-energy derived from certain crops has become one of the most widely utilized energy sources, Kankare et al. [46] were able to assess crop biomass as a productivity evaluation criterion.

- **Plant/Fruit detection:** The accuracy of the detection of items of interest within the environment is required for successful outcomes in automated tasks like pruning, harvesting, and seeding. Several plant and fruit traits and attributes, including colour, shape, and temperature, have been exploited to attain this goal. In robotic fruit picking or crop harvesting, colour is a feature which can be utilized to identify the fruit inside the canopy [47, 48], or in the agricultural field [49]. Furthermore, for automated robotic pruning, the morphology of the stems is the trait that offers the cutting directions in the majority of situations, as reported by Karkee et al. [50].

- **Physiology assessment:** The physical reaction of the canopy to sunlight results in distinct spectral patterns that provide information about the plant

physiological health. As a result, numerous indices [51, 52] based on crop spectral responses have been established to analyse factors such as nitrogen deficits, chlorophyll content, water stress, and pest infestation. Furthermore, various sensing instruments (for example, infrared gas analysers) allow for the direct measurement of a variety of physiological parameters in plants. Many of them need direct contact with the crop, resulting in more precise readings; nonetheless, the measurement procedure follows a personalised route, making this technique time-consuming in most circumstances [53].

Remote sensing technologies mainly fall within two main groups: vision-based and range sensors.

Vision-based sensors

The most basic vision-based sensors are RGB or colour cameras. Parameters like texture and geometrical aspects can be derived from colour data, which have been shown to be useful in agricultural applications. The biggest disadvantage of employing these types of sensors, particularly in outdoor locations, is the impact of changing ambient illumination conditions. A frequent example of how this technology can be used is to identify fruits or vegetables inside the canopy using colour cameras for use in automated harvesting operations. Zhao et al. [54], for example, reported on the application of a variety of segmentation approaches based on colour characteristics and shape to accurately distinguish immature green citrus. Furthermore, the colour and shape collected from the RGB imagery were employed for robotic apple picking operations and berry yield estimates, respectively, in [47] and [55]. Barbedo et al. [56] described a way to recognise plant disease, whereas Nandi et al. [57] demonstrated how to assess mango ripeness using a colour camera.

While it is feasible to estimate depth data with a single camera, stereo vision systems are mostly used for three-dimensional reconstruction of the world. This measuring technique produces a 3D point cloud that displays the scene, comparable to systems that combine a colour camera with a depth sensor. Applications in agricultural research include identifying plants or fruits and estimating structural parameters that represent plant morphology, such as the estimation of tree height, diameter, and volume, or the estimation of plant height and leaf area. For example,

Wang et al. [58] investigated fruit identification applications employing stereoscopic vision in apple orchards.

Temperature has shown to be a significant metric outside of the visible spectrum for several agricultural tasks such as crop diagnosis and fruit identification. A thermal camera can be used not only to segment a tree from the rest of the picture, but also to assess the canopy state. Furthermore, Baluja et al. [59] identified plant temperature as an indication of plant water availability, allowing the creation of localised irrigation based on plant temperature. Similarly, Jones et al. [51] described a link between the temperature of the leaves and water stress using thermal cameras, as described. However, they also claimed that accurate crop water stress detection necessitates the use of a multi-sensor technique. Fruit identification is another use for thermal cameras, since fruits absorb and irradiate sun radiation differently than plants, allowing for the development of reliable detection techniques. For example, Wachs et al.[60] employed a thermal camera in conjunction with RGB images to identify green apples using image processing techniques, obtaining an accuracy of up to 74%. Reina et al. [61] also suggested that thermal imaging is also an appealing approach to improve the ambient awareness of agricultural robots, for example, by identifying human operators or animals particularly obscured by dense foliage.

Structured Light Cameras detect distances accurately by projecting an infrared (IR) pattern across the scene and examining the distortion of the pattern returned back. They are mainly used in laboratories or greenhouses [62] because their performances are highly affected by lighting conditions. A structured light sensor is mainly employed to detect structural factors such as size, height, and volume of plants and trees. Chéné et al. [63], for example, implemented a leaf segmentation method using data from a commercial structured light camera. The same sensor has previously been used in [64] and [65] for the characterisation of sweet onions and cauliflowers, respectively, proving that the sensor is adequate for identifying fruits and vegetables.

Radiation absorption and reflection in certain bands of the electromagnetic spectrum are strongly correlated with a variety of physiological factors such as chlorophyll levels, nitrogen concentration, and water stress. For example, the chlorophyll pigment reflects green light while absorbing red and blue light. Similarly, the crop water content affects the reflectance in the central infrared band. Reflectance data from crops, plants, and trees are measured through spectrometers or cameras,

generally categorised as multispectral or hyperspectral. Multispectral imaging can estimate the reflectance of a scene in a few wide spectral bands that are not necessarily contiguous. On the contrary, hyperspectral cameras provide their reflectance measurements in a narrow but continuous band of the spectrum. Mulla [66] has a comprehensive collection of several indices to estimate physiological features that can be derived from spectral imagery. Water fluctuation, vigour, chlorophyll detection, crop yield, nitrogen stress, plant stress, weed and pest infestations, and soil composition and nutrients are just a few of the things that have been studied using multispectral or hyperspectral images by a number of researchers [67, 68, 59, 69–71].

Range sensors

Ultrasound range sensing is one of the earliest technologies. It consists of a high-frequency, short-duration acoustic pulse that travels through the air, hits the target, and returns as an echo. The distance is calculated by the electronics within the sensor depending on the duration between sound production and reception of the echo signal. Several articles described its use to estimate crop metrics such as volume, density, and height. In particular, Palleja and Landers [72] proposed a real-time method to evaluate canopy density on apple trees and grapevines by means of ultrasonic sensors on a tractor. Previous studies by Escolà et al. [73] employed a similar system to estimate tree volume to control the appropriate dosage of agrochemicals to be sprayed.

Time-of-Flight (ToF) cameras, which use an array of detectors and a source of light to provide 3D measurements of distance and intensity, have lately piqued interest. Specifically, these cameras have been used in agricultural studies to identify structural characteristics of plants or fruits. For example, a number of studies [74, 75] suggested the employment of a time-of-flight camera for obtaining geometrical characteristics of the plant allows for individual leaf modelling and monitoring. Both studies were conducted inside, under laboratory circumstances, as sunlight can cause detectors to become saturated, resulting in poor performance, as documented by Kazmi et al. [76]. If colour information is included (the device is often referred to as an RGB-D camera), plant characterisation and detection significantly improve. As an example, Vitzrabin and Edan [77] described the use of RGB-D data to identify red sweet peppers in greenhouses, resulting in up to 90.9% true positive rates. The use of RGB-D cameras placed on a movable platform to collect data in an over-the-row

route inside apple orchards is documented in full by Gongal et al. [48]. The use of a RGB-D camera for 3D reconstruction and modelling of apple trees is described in [78].

LIDAR sensors are also used to calculate structural metrics of crops, including, among other things, volume, leaf area coverage, and height [44, 79]. Within LIDAR sensors, there are two kinds of laser scanner: 3D and 2D LIDARs; however, the latter are more often used, as they are less expensive and can be used to get 3D data with an appropriate setup. Several studies have reported on the use of point clouds derived from 2D or 3D LIDARs to extract structural information from the canopy such as volume, area, leaf density, and branch dimensions. The use of terrestrial and aerial applications to categorize vegetation in vast landscapes or acquire a geometric description of the crop has been described by numerous publications [80, 81]. Fieber et al. [82] described how a laser scanner was used to categorize trees, grass, and ground exploiting the landscape back-scattering. The data from a LIDAR is utilized to create allometric models for measuring the biomass and volume of individual trees in [83] or, similarly, in [84]. The hyperspectral LIDAR, in particular, is the most unique and is currently being researched. This device aims to combine the advantages of traditional laser scanners with the capability to recognise different wavelengths [85]. Livny et al. [86] described the use of a hyperspectral LIDAR to analyse the state of vegetation in controlled situations, confirming the potentiality of this sort of LIDAR in vegetation spectrum analysis. Furthermore, as demonstrated by Du et al. [52] for rice leaves, hyperspectral LIDAR may be used to estimate parameters such as nitrogen concentration (which is generally done using spectral cameras or spectrometers).

Figure 1.3 collects and summarises the previously introduced technologies grouping them by phenotype features that can be estimated [39].

1.3.2 Proximal sensing

Although remote sensing may give large coverage, measurements are generally indirect and, considering the assessment of soil properties, they are often limited to the surface. Furthermore, the resolution is too coarse to assess the soil variability of a field. On the other hand, using traditional point-sampling approaches alone, the process of characterising fields is considerably time-consuming, costly, and

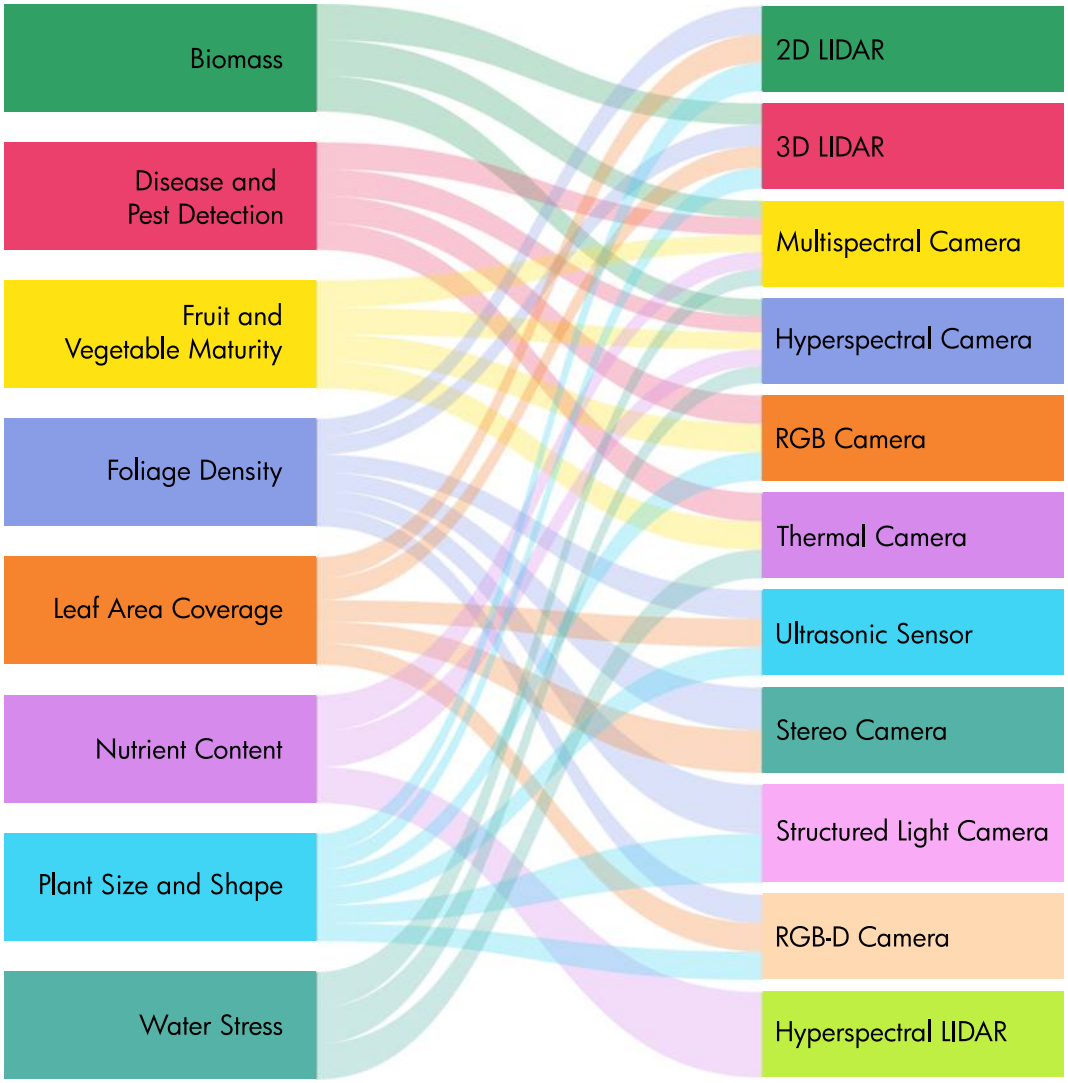

Fig. 1.3 Remote sensing phenotype features and the corresponding technologies

impracticable. As a consequence, proximal soil sensing is gaining popularity as a means of filling the data gap between high-resolution point data and lower resolution remote sensing data.

When a sensor to assess soil properties, directly or indirectly, is in close proximity or even in contact with the ground, it can be categorised as a proximal sensor [87].

According to Allred et al. [88], electromagnetic induction, electrical resistivity, and Ground-penetrating radar are the most regularly utilized technologies for soils proximal sensing. Ground-penetrating radar has been primary employed to assess soil depth and structure by transmitting short pulses to the ground and then analysing

the reflected signals [89]. Moreover, such sensors have been successfully used to map soil water content, as Klotzsche et al. reported [90]. Electromagnetic induction methods generates eddy currents to flow through the soil and measures the corresponding electromagnetic field to evaluate the electrical conductivity of the soil, a soil property that can provide several information about it. In the first applications, they were employed to measure soil salinity, but nowadays they can be used to assess soil texture, compaction, pH, and organic matter content but also water content [91]. Similarly to electromagnetic induction, electrical resistivity methods evaluate soil resistivity by injecting a current by inserting electrodes in the ground or by exploiting capacitative coupling [88]. The measured resistivity has been used to estimate soil structure, composition, and water content [92].

According to Adamchuk et al. [93], less popular soil sensing technologies include mechanical interactions, magnetic-based, time domain reflectometry, optical reflectance, X-ray fluorescence, γ-ray spectroscopy, ion-selective potentiometry, and seismic. To assess soil mechanical resistance, mechanical, acoustic, and pneumatic sensors may be utilised. From the measure, it is also possible to evaluate soil compaction and type, and also water content (with auxiliary moisture sensors). Magnetic-based sensors instead measure magnetic susceptibility to evaluate soil composition (in particular magnetic minerals) and water content. Soil moisture has also been measured employing time domain reflectometry. Proximal optical sensors use the same technologies of vision-based remote sensors but applied at the soil surface or even below ground. Such sensors can measure a variety of soil characteristics such as soil composition and water content. X-ray fluorescence and γ-ray spectroscopy sensors measure the reflected wave at the corresponding frequency to evaluate soil composition and water content. Instead, ion-selective potentiometry consists of evaluating the presence of specific ions to define soil composition and water content. Finally, seismic sensors generate vibrations to assess soil compaction, porosity, and water content.

Figure 1.4 resumes the previously introduced technologies for proximal sensing and shows what properties they can assess.

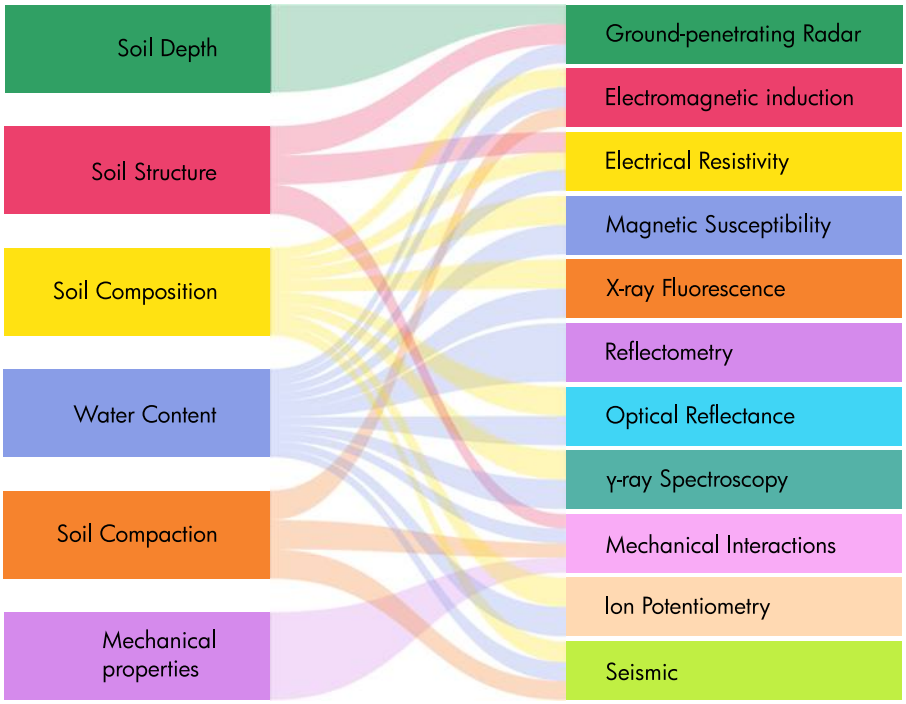

Fig. 1.4 Main proximal sensors for precision agriculture

1.4 Robotics and agriculture

As a consequence of intensification, mechanisation, and automation, agricultural production has improved dramatically throughout the years [94, 95]. Agricultural equipment productivity has improved significantly as a result of automation, which has boosted efficiency, dependability, and accuracy while lowering the need for human involvement [96]. Nevertheless, agriculture continues to face a significant shortage of personnel with minimal training, particularly in the horticultural industry. The challenges caused by the lack of workers are exacerbated by trends such as growing farm size, declining farmer numbers, and increasing environmental consequences of food production that demand even more efficient agricultural techniques [97], and the productivity of traditional farming, in which crop cultivation and management are done manually by farmers, can be considerably improved by using intelligent machines [98]. Moreover, it is necessary to exceed the highly productive levels of conventional crop cultivation and produce a new agricultural system that minimizes human intervention through advanced automated techniques.

In the context of precision agriculture, the use of robots in agriculture arises as a promising solution [99, 100] since it allows for repeated labour to be completed without compromising precision throughout the working day. This type of application is becoming increasingly popular in robotic research, and various robots are currently available for purchase [101]. In fact, agricultural robotics aims to achieve more than the application of robotic technology to farming. Most agricultural vehicles that are utilized for weed identification, pesticide dissemination, terrain levelling, irrigation, and other tasks are currently manually operated. Because information about the environment may be autonomously gathered and the robot can then perform its mission accordingly, the autonomous performance of such robots would allow for continuous field management and improved productivity and efficiency [32]. For robots to operate adequately in agricultural settings and perform agricultural tasks, research must concentrate on the integration of numerous complementing sensors to obtain acceptable localisation and monitoring abilities, the design of simple manipulators to achieve the required agricultural activity, the development of path planning, navigation, and guidance algorithms adapted to situations other than open fields, and the integration with workers and operators in this complex and highly dynamic scenario. It is a key objective for the deployment of numerous technologies aimed at increasing crop output and quality while lowering agricultural expenses. In fact, the main long-term goal of food security during climate change calls for a change in the current agricultural paradigm focused on reducing the use of natural resources to increase crop production. As an example, precision seeding and planting, combined with precise treatment application, which implies only adding water and plant nutrients required by the crop at the optimal place and time, have been proved by Tremblay et al. [102, 103] to not only an increase in the average plant size and uniformity of plant maturity, but also a reduction in the ratio of phytosanitary products and water to crop production and, therefore, environmental impact. Moreover, according to recent research, using robots or autonomous tractors to perform different agricultural jobs reduces fuel consumption and pollutants [104, 105].

In the early 1960s, agricultural research on autonomous vehicles began, with an emphasis on the development of automated steering systems [106]. The vast majority of mechanical activities in field crop farming in the 1990s comprised massive, powerful, and high-capacity machinery with significant energy needs and high handling and running expenses. However, research at many universities and

research institutes across the globe has experienced a paradigm change in the last decade: the automation of agricultural robots is now deemed vital for boosting overall productivity and should include the potential for improving fresh produce quality, cutting production costs, and eliminating the repetitive tasks of manual labor [107]. Yet, cultivation and production methods are complex in nature, varied, labor-intensive, and often unique to each crop. Many variables influence the kind of procedure and its components, such as crop qualities and needs, the geographical environment, and climatic and meteorological contexts. This implies that the technology, equipment, and techniques needed to complete an agricultural operation involving a certain crop and environment may not be appropriate for a different crop or environment.

Nonetheless, in recent years, a considerable body of research on this subject has proved the technological feasibility of agricultural robots for a range of crops, agricultural activities, and robotic characteristics [108]. However, automation solutions for field operations have not yet been commercially deployed effectively and broadly, and just a few recent advances have been validated, adopted, and put into service [109, 110]. The majority of the methods were modified from an industrial standpoint [111]. Many agricultural robotics and intelligent automation research projects have never made it to the implementation stage in the last three decades. The main reasons for these failures were the high cost of the designed system, the inability to perform the essential agricultural work, the poor durability of the system, and the inability to effectively repeat the same operation in slightly different settings or fulfill mechanical, economic, and/or industrial requirements.

Bechar and Vigneault [112, 113] stated some requirements whose fulfilment can guarantee,in most circumstances, that robots technology can be used in agriculture:

- The cost of using robots is less than the cost of using any other approach.
- Using robots increases agricultural production capabilities, yield, profit, and survival while also improving the quality and consistency of the output.
- In growth and production processes, the employment of robots reduces uncertainty and variance.
- In comparison to the traditional system, the introduction of robots allows the farmer to make higher-resolution judgments and/or improve the quality of the output, allowing for optimisation in the growth and production phases.

- The robot is capable of doing particular activities that are deemed unsafe or impossible to complete manually.

In the literature, it is possible to identify two major trends in robotics for agriculture, namely, flying drones for remote sensing and some minor crop management tasks and ground rovers for all-around local monitoring and multi-tasks specialisation.

1.4.1 UAV in precision agriculture

As introduced before, remote sensing from aerial images is a widely adopted solution to monitor a whole field. For the average farmer, satellite photos are too expensive and their resolution and quality are sometimes inadequate and impractical due to weather conditions. As a result, aerial images obtained by human-piloted aircraft have a higher quality than satellite images, but they are still expensive for most farmers [34]. Unmanned Aerial Vehicles (UAVs) recently entered the market and have found several applications in many fields, and most studies confirm the large potential of UAVs in PA [34, 33, 40](Figure 1.5). UAVs can provide centimetre-level resolution, combine 3D canopy height and orthophoto data, provide multiangular data, provide high-quality hyperspectral data, and have a wide range of auxiliary sensors. UAVs have the potential to become the standard platform for remote sensing applications needing very high-resolution, thermal, or hyperspectral data, such as early drought stress assessment, weed identification, and early crop disease detection [33].

Several authors [34, 33, 40] have tried to categorise the most common UAV application in PA. Soil and crop monitoring by remote sensing is the most common application, followed by patch spraying [34]. remote sensing is based on collecting several aerial images in different spectra. For example, drought stress detection relies mainly on thermal imagery, while pathogen detection through the fusion of thermal and hyperspectral data shows great results. Weed detection, instead, is based on machine learning object-based image analysis done with RGB cameras. Nutrient status assessment and yield prediction with UAVs are promising, but integration with models can improve its applicability [33]. According to recent research, combining electrical conductivity data with elevation and slope maps, as well as crop indices that describe crop vigour, can help enhance the definition and quality of MZs in

Fig. 1.5 A UAV monitoring a field

vineyards or fields with considerable slope [114]. It appears clear that there is a complete lack of standardisation since different techniques are employed for the same application [40, 33, 115], except for irrigation management, where thermal and/or multispectral sensors monitor the needs of water of the crops [40].

Although UAVs may offer individual plant monitoring, the average spatial resolution of the MZ is about 10 m (e.g., sprayers with independent nozzles). As a result, UAVs can encourage technology advancement to improve management zones resolution [33].

1.4.2 UGV in precision agriculture

Unmanned ground vehicles (UGV) can perfectly fit the UAVs monitoring resolution gap since they can be deployed locally and act on the required spot. Moreover, UGVs are not limited to remote sensing, but they can perform proximal sensing and are often designed to do one or more specific agricultural tasks such as seeding, planting, weeding, treating, pruning, picking, handling, and harvesting. The robot must also be able to do many supporting activities in order to complete its main function that

are instead simpler or even neglected in UAVs, such as localisation and navigation with obstacle avoidance, detection of the item to treat, the treatment or action to conduct, and so on. For example, in developing a disease monitoring robot [116], the main activity is disease monitoring, but the robot also needs to be able to perform the secondary tasks of self-localisation, trajectory planning, steering, and navigating in the field, collaborating with workers and operators, or interacting with other robots or unexpected objects. Similarly, Ceres et al. [117] designed and implemented a framework for a human integrated citrus harvesting robot, whereas Nguyen et al. [118] created and implemented a framework for motion and hierarchical task planning for an apple harvesting robot. Hellstrom and Ringdahl [119] created a framework for agricultural and forestry robots.

Many available examples in the market and academic literature are re-adaptation of agricultural machines where different degrees of automation are implemented. Although actual tractors and agricultural machinery in general (autonomous or not) are massive and powerful, they tend to increase soil degradation and traversability [120]. For this reason, more recently, dedicated robotic UGVs have been developed tailored to some specific tasks to reduce bulkiness, weight, and soil degradation due to undesired compaction while still being able to fit into the requirements of the PA approach. Compared to UAVs, where the mobile robotic platform makes little difference while the focus is mainly on the employed remote sensing, the design of agriculture UGVs is producing more unique proposals that are highly centred on and related to the work environment and the capabilities required by the activities [121, 122].

In the following, a very brief state of the art about commercial and academic agricultural UGVs is given. In addition, different kinds of agricultural robots classification are proposed based on the most notable trends.

Agricultural robot main functions taxonomy

The vast majority of agricultural robots are exclusively dedicated to remote or proximal monitoring of the soil or the crop (also known as phenotyping, i.e., measuring plant traits to identify their status and potential beneficial treatments), partially because related technologies can be easily employed in UAVs. Since the focus in this class of robots is mostly on the sensors, their designs are usually quite straightforward. Underwood et al. [126] proposed a mobile robot mounting a scanning system

(a) [123]

(b) [124]

(c) [125]

Fig. 1.6 Examples of robots employed in monitoring activities

for almond orchards that can efficiently map flower and fruit distributions, as well as estimate and forecast production for individual trees. Mueller-Sim et al. [127] presented a robot capable of autonomously navigating below the canopy of row crops such as sorghum or corn and deploying a manipulator to gather plant phenotypic data with a modular array of non-contact sensors. Virlet et al [128] developed instead a quite different and massive robot based on an overhead gantry architecture employing sensors such as RGB, chlorophyll fluorescence, hyper-spectral, and thermal cameras to produce high throughput and detailed monitoring data. Cubero et al. [123] and Rey et al. [129] proposed instead two different robotic platforms with the particular task of detecting pests and disease on carrot fields and olive trees respectively. Barbosa et al. [130] successfully tested an autonomous robot for monitoring cotton and soy crops; the robot proposed by Menendez-Aponte et al.[131] specialise in strawberry field scouting; ByeLab is instead a robot developed to monitor plants volume and health in orchards [132–135]. Some robotic platforms have recently become commercially available [124, 125].

The second most popular function for mobile robots in agriculture is mechanical and chemical weed removal. Researchers are mostly focusing on systems employing a vision system for weed detection and classification to then proceed to its removal

by a precise mechanical actuator or a localised application of chemicals. A decade ago, Bakker et al. [136] proposed a versatile research vehicle with a diesel engine, hydraulic transmission, four-wheel drive, and four-wheel steering to test one of the first autonomous weeding robots. More recently, Bawden et al. [137] tested a robot that removes weeds chemically or mechanically based on the species with an accuracy of correct weed detection of 92.3% by employing a vision-based online algorithm. Utstumo et al. [138] proposed instead a three wheeled robotic platform for chemical weeding in indoor carrot fields that achieved a substantial reduction in herbicide use, avoiding overdosing herbicides that would otherwise affect and harm the vegetables. In addition, the industrial sector seems particularly interested in autonomous weeding robots. Naïo Technologies developed three weeding robot models of different size: Oz [139], DINO [140],and TED [141]. Carré instead designed Anatis [142] to mechanically remove weeds without a detection system, an autonomous solution closer to conventional agricultural machinery with the typical three-point hitch to mount weeding equipment. On the contrary, AVO by Ecobotix [143] is an autonomous robot with a large photovoltaic panel accurately spraying herbicide to remove weeds thanks to a vision-based detection.

(a) [137]

(b) [138]

(c) [140]

(d) [142]

Fig. 1.7 Weeding agricultural robots

Another significant fields of application of agricultural robots are seeding, planting, and transplanting. For example, Haibo et al. [144] carried out a study and an experimental campaign on a robot for wheat precision seeding with an accuracy of about 90%. Also Ruangurai et al. [145] achieved a similar seeding accuracy for a peculiar three-wheel rice seeding robot. Hassan et al. [146] proposed a low-cost modular robot with a custom designed seeding mechanism, Srinivasan et al. [147] instead designed a modular tracked robot. Several authors designed and tested their precision seeding system employing very simple and low-cost autonomous robotic platforms [148–153]. Mohammed and Jassim [154] manufactured and tested a robot for combined seeding, i.e., a robot for seeding, fertilisation, and watering. Li et al. [155] developed instead a unique robotic seeder for desert areas inspired by tumbleweed powered by solar and wind energy. Also, Iqbal et al. [156] designed a robotic pepper transplanter moving on rails for indoor farming, while Liu et al. [157] made a crawler-type sweet potato transplanting robot.Few commercial solutions are available, Rowbot [158], an autonomous seeding robot for row crops, is one of them.

(a) [155]

(b) [157]

(c) [158]

Fig. 1.8 Seeding and planting agricultural robots

Robotic harvesters are also a quite popular trend heavily focusing on integrating vision-based crop detection systems, dedicated manipulators, and suitable mobile

platforms. In 2006, Foglia and Reina [49] developed and tested a pneumatic robotic arm for the harvesting of red radicchio guided by one of the first vision-based systems to precisely locate the plants. More recently, some authors proposed their variation of tomato harvesting robots [159, 160], but there are also a lot of harvester for strawberries [161–163], sweet peppers [164–166], carrots and cantaloupes [167], lettuce [168], asparagus [169], apples [170] or fruits in general [171].

(a) [161]

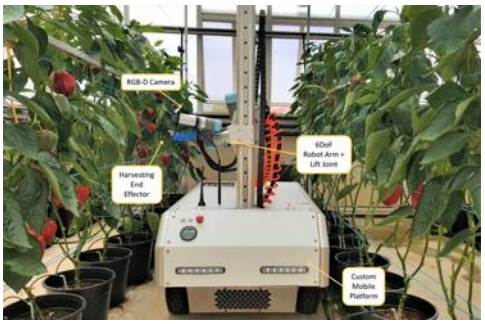

(b) [166]

Fig. 1.9 Harvesting agricultural robots

Spraying agrochemicals is another activity heavily relying on vision-based systems to precisely apply just the required amount of chemical products to avoid their hazardous dissemination. Chemical weeding robots fall within this category, but there are also other treatments that are achieved through spraying, specially in orchards. Cantelli et al. [172] provided several insights in developing a reconfigurable robot for the distribution of plant protection products in greenhouses and the relative spraying management system. Danton et al. [173] traced the development of a robot for vineyards and orchards that is able to autonomously perform spraying tasks to treat vegetation while minimising the dissemination of dangerous products by employing an array of independent sprayers. Following a quite different approach, Terra et al. [174] developed an autonomous sprayer to apply only the required amount of pesticides that is towed by a conventional tractor.

There are also some agricultural robots that do not specialise in a single task, but they are able to perform several, usually thanks to modular implements. For instance, Amrita et al. [175] developed a robot for automatic ploughing, seeding, crop picking and pesticide spraying. Grimstad and From [176] presented Thorvald II, a modular robot that can be configured based on the environment and on the type of crop. Industrial manufacturers, especially agricultural machinery ones, also developed

(a) [172]

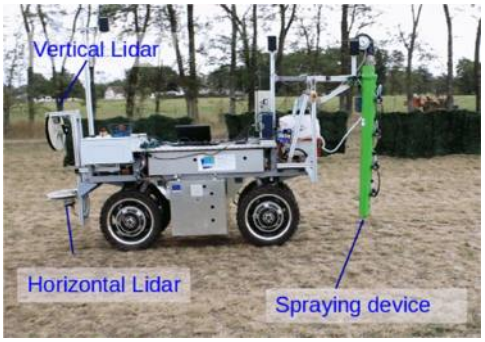

(b) [173]

Fig. 1.10 Agrochemicals spraying agricultural robots

some robotic solutions based on conventional tractors that can be equipped with common agricultural implements [177–179].

(a) [176]

(b) [177]

(c) [178]

(d) [179]

Fig. 1.11 Multi-purposes agricultural robots

The very high flexibility of robotic platforms has also led to more unique solutions for peculiar tasks. Agrobot commercialised Bug Vacuum [180], a pest control robot that removes bugs by aspiring them. Williams et al. [181] tested a novel kiwifruit pollinating robot designed, while Galati et al. [182] developed a tracked robot to compress flax fibers, and Loukatos et al. [183] designed a robot that works together with farmers during harvesting as a fruits or vegetables autonomous carrier.

Agricultural robots and vineyards

Among all possible crops, whose with higher market value seems to be the one where robotics is applied more often. Particularly, vineyards seem to attract a lot of agricultural robot proposals. One good example of an advanced agricultural robot is a selective pesticide sprayer designed by Oberti et al. [184], or the semi-autonomous sprayer by Adamides et al. [185], or even the European project Rovitis4.0 [186]. There is clearly some prototypes dedicated to phenotyping [187], and some designed for mechanical weeding operations [188], but there are also robots developed for pruning [189] and shoot thinning [190], or even multi-purposes robots [191].

(a) [186]

(b) [191]

Fig. 1.12 Agricultural robots for vineyards

Agricultural robots classified by size

When agricultural robots are categorised according to their size, several tendencies in capabilities, design, and features emerge. A significant majority of precision agriculture UGVs are tiny electrically powered robots that solely conduct crop and/or soil monitoring activities. Because of their small size and low power, they are seldom used for activities other than remote and proximal sensing. Despite this, they need less financial investment, are more agile, do not have special energy supply difficulties, and can be adapted to a broad variety of crops.

On the other end of the range of robot size, there are robots with the size and power of traditional agricultural machinery and tractors. In this case, the more widely accepted design tendency, particularly among major agricultural equipment manufacturers, is to implement autonomous characteristics into existing agricultural vehicle architectures (e.g., tractors, combine harvesters) without introducing entirely new designs [96, 192]. Aside from farmers' experience with comparable machinery

and the adaptability of tractor implements (i.e., an autonomous tractor with the typical three-point hitch, or a similar interface, can easily employ conventional agricultural machinery usually pulled and powered by traditional tractors), these systems tend to be expensive and successful only in wide open fields.

Medium-sized robots stand as the best of both worlds, as well as the most varied and distinctive designs. Robots in this category can typically monitor the field by remote and proximal sensing, but they can also carry out operations on the field. As illustrated before, many robots are highly specialised for a relatively narrow range of duties; as a result, their design is entirely determined by the job requirements. Other robots, on the other hand, are multipurpose platforms that can execute a variety of tasks, resulting in more adaptable and modular designs.

Small-medium size systems that can do various processes (i.e., multipurpose systems) are regarded a promising alternative among all of them. Indeed, they have the potential to reduce the needed economic investment [193] and to promote a new production paradigm (particularly in developing countries), an approach that uses profitable technology with considerable environmental and social benefits [194].

Agricultural robot by mobility layout configurations

The reviews on agricultural robots by Fue et al. and Oliveira et al. [195, 196] gave a measure of the most employed mobility layout configurations. According to Oliveira et al. [196], 63% of agricultural robots are four-wheel drive robots or four-steering-wheel robots, where the latter are generally preferred when great manoeuvrability in tight spaces is required. All other layouts (e.g., tracked, legged, on-rail, ...) are significantly less adopted. Fue et al. [195] also highlighted the considerable employment of robots moving on rails within greenhouses, or more in general where the environment is highly structured. The authors of both reviews also gave some attention to legged robots suggesting similar ideas: Despite they are relatively light and excel in very impervious terrain, their feet must be designed appropriately to avoid soil damaging by penetration and potential sinkage of the robot due to the high pressure present in the small contact points.

Vidoni et al. [197] carried out an interesting comparison on mobile robotic platform configurations, employing an ad hoc simulator, to evaluate which mobility architecture configuration is the most suitable for agricultural operations on steep

slopes, embankments or hills. According to the authors, a tracked vehicle can face the steepest inclines while guaranteeing good manoeuvrability, improving traction, and reducing soil compaction. Nevertheless, track slippage is inevitable and it causes serious damage to the soil that can favor erosion, landslips, and exposure to rain and water [198–204]. Wheeled configurations have many advantages such as high efficiency and top speed. Yet, when wheeled platform faces a particularly loose or rough soil, the efficiency drops dramatically and the vehicle could even get stuck. Among all wheeled solutions compared by Vidoni et al. [197], a three-wheel layout proved to be agile and simple but easily toppled when employed on steep inclines. On the contrary, a four-wheel platforms maintain wheeled locomotion benefits with significantly better stability over large inclines. Moreover, according to the authors, articulated wheeled vehicles proved to be the best suited for uneven and side-slope terrains because of their superior steering capacity, agility, and stability.

1.4.3 Collaboration of multiple robots in precision agriculture

UAVs can be employed to monitor vast fields, but on the other hand, their equipped sensors are often constrained in terms of airspeed and altitude, as well as attitude uncertainty, limiting their potential to correctly perform remote sensing . On the contrary, UGVs are machines that can operate in the field and over a range of terrain monitoring the environment and interacting with the soil and the crop. UGVs can be used to precisely interact with targets, but they lack the quick mobility of UAVs and their navigation is heavily constrained by obstacles, barriers, and features of the fields in general. The natural evolution of these concepts is establishing a heterogeneous collaboration of multiple flying and ground robots in order to achieve more effective results [205–207]. A system composed of a team several heterogeneous, aerial and ground, mobile robots enables a farm operator to oversee the whole process and manage the activities required to complete a complex task composed of many steps or even an entire mission autonomously. [208, 209]. As an example, Figure 1.13 illustrates how the PA activities can be done by a team of robotic agents throughout a growing season.

Due to the obvious benefits of robots collaboration in PA, recent academic literature is largely focused on integrating a fleet of collaborating robots in agricultural activities. As an example, the European Flourish project [210] optimised existing aerial and ground robots in order to enhance PA processes, such as monitoring

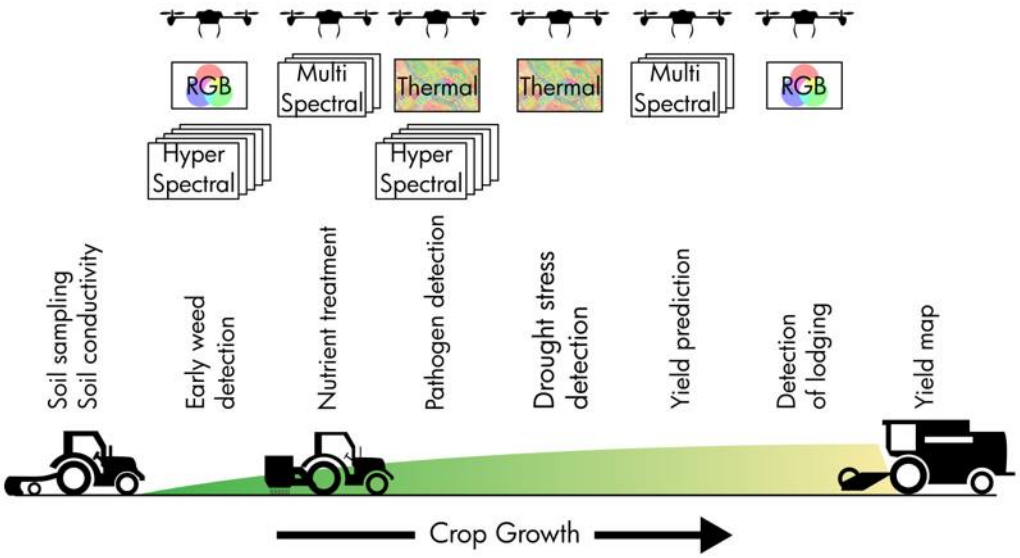

Fig. 1.13 Schematic overview of the different ways to extract spatial information and the useful robotic platforms throughout a growing season.

multiple crops. Similarly, Tokekar et al. [13] and Bhandari et al. [211] examined the use of teams made of commercial and low-cost UAVs and UGVs for data collection in agricultural fields. In Gonzales de Santos et al. [212], the objective was to design, implement, and test a fleet of heterogeneous UGVs and UAVs to address diverse agricultural scenarios, such as effective weed and pest control, enhancing crop quality, and improving farm operators health and safety. Ribeiro et al. [208] developed and tested within the European RHEA project a team comprising aerial and ground unmanned robots that effectively collaborate to apply precise treatments to crops. Davoodi et al. [12] instead presented a unique team composed only of optimally deployed UGVs such that coverage of the whole field and monitoring of the MZs were maximised. There is also some work done by a fleet of robots within greenhouses, instead of open fields and orchards [213].

1.5 Contribution

Almost all available robotic solutions for agriculture, except for a few small-scale prototypes used only for monitoring purposes, target flat fields or fields with no significant steep and impervious terrain. In the case of Italy, substantial regions of agricultural production are in hilly or mountainous areas, particularly when orchards,

olive groves, and vineyards are taken into account [214]. This occurrence may rise in the future as a result of the climate change impact, which may force people to move to higher zones in order to meet temperature needs and maintain product quality [215]. As a result, robotic platforms must overcome and deal with a variety of challenges, for example, to address traction concerns, wheel slippage, tight spaces between rows, instabilities associated with terrain irregularities and changing slopes, poor GPS signal reception, and dedicated awareness (location, terrain, environment) systems and architectures must be built. Furthermore, activities in steep regions are carried out either manually or with small and compact vehicles, exposing the driver to dangerous conditions. For the latter, overturning incidents are virtually exclusively found in hilly/mountainous locations in Italy, with a mean incidence of more than 4 accidents per 100k working hours [216]. Field activities account for 68% of these. These dangers could be reduced or eliminated if autonomous and teleoperated systems were used. Furthermore, it is worth noting how orchards and vineyards activities on steep slopes, terraces, and embankments often need repeated tasks and the physical, non-ergonomic transport of even considerable loads. This, together with the ageing of the population and the resulting shortage of competent workers, provides a potential issue that will need to be addressed in the near future.

In this thesis is featured Agri.Q, an innovative UGV (Figure 1.14). The rover is especially developed for precision agriculture applications in vineyards and can function in an unstructured environment on uneven terrain, collaborating with drones if necessary. It is outfitted with various instruments and sensors to do specific activities, such as field mapping, crop monitoring. Thanks to a redundant 7 degrees of freedom (DOF) collaborative robot arm, it is also possible to interact with the environment, for example performing soil, leaf, and grape samples collection. Furthermore, it boasts a 2 DOF photo-voltaic (PV) panel that can self-orient to assure a secure and always flat drone landing platform or even maximise the gathering of sun rays during the auto-charging phase. The robotic arm is fixed on such a platform, hence the robot manipulation workspace can be dynamically adapted to different tasks and scenarios.

1.6 Thesis outline

In the next chapter, the robotic prototype named Agri.Q is described, providing details about its design and how it has been integrated. Chapter 3 is instead dedicated

Fig. 1.14 Agri.Q in a vineyard in Castagnito, part of the Roero historical region in the south of the Italian region Piedmont

to modelling Agri.Q, in particular how it behaves while driving around. After that, in Chapter 4 are reported the most significant experimental results about some aspects of the robot. In the end, Chapter 5 concludes this work by briefly summarizing the project Agri.Q

Chapter 2

Agri.Q

In this chapter Agri.Q, the mobile robot for precision agriculture, and its design are presented. At first, a very brief overview of the robot is provided, then, after the definition of the main design requirements, the adopted functional design of the PA rover is shown focusing on key parts. At last, the required electronic and control systems are introduced.

2.1 The mobile robot Agri.Q, an overview

As shown before, the rising employment rate of robotics in PA is driving the development of new mobile robotic platforms to monitor, act, and manipulate fields and crops. In addition, to perform local tasks based on PA methods, it is of great interest the collaboration of a UGV with drones, since they are the most employed solution to achieve fields and crops remote monitoring.

The mobile robot Agri.Q enters this scenario. The concept of this robot is shown in Figure 2.1. The robot is composed of two modules connected by a series of joints, resulting in an articulated vehicle. Each module is provided with two driving units with two wheels each. At last, two PV panels, that can be oriented by means of two joints, are mounted on the robot with the idea of being both a landing platform for drones and a solution to increase the robot autonomy in a sustainable way.

In the following sections, the robot design solutions are introduced and explained in detail, providing an update on what was already presented in [217–223].

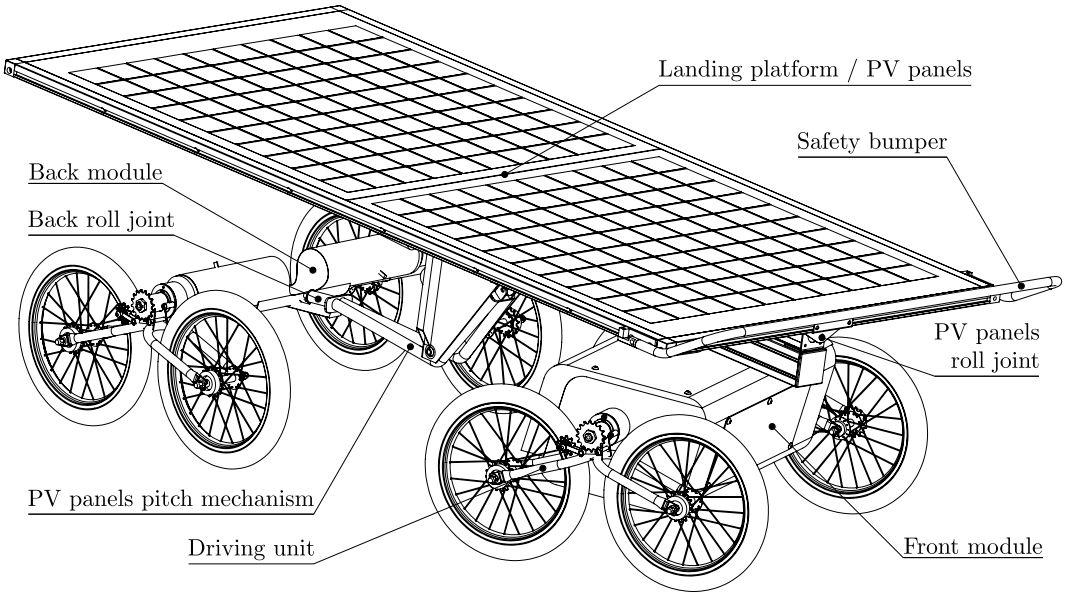

Fig. 2.1 Agri.Q schematic representation

2.2 Design requirements

Agri.Q is planned to be employed for PA tasks in orchards, olive groves, and vineyards. The latter, in particular, is not an arbitrary choice, but instead is due to two main reasons: first, Piemonte, a northwestern region of Italy where Politecnico di Torino is located, has a long and great tradition of wines and vineyards; second, vineyards are profitable and follow very strict production quality standards, therefore it could be a valuable field where propose PA robots. The Piemonte region, but also some other neighbouring Northern Italian regions, namely, Valle d'Aosta and Liguria, share significant geographical and historical similarities since they are classic wine-growing locations that produce many well-known wines, frequently in tough terrain. Vineyard sites can be found at elevations larger than 500 m, grapes grown on slopes greater than 30% on steep hills, terraces or embankments [224]. This characteristic limits the use of conventional mechanized agricultural machinery only where the slopes do not exceed 30% and the vine rows are wide enough [224].

This scenario sets some design requirements for Agri.Q:

- It has to be able to climb very steep terrains with an incline up to, at least, 25%.

- Its size has to be compatible with the vine rows clearance, hence its width has to be less than 1.5 m.
- Its weight has to be below 100 kg and well distributed to minimize soil compaction.
- It has to be able to traverse uneven and soft terrain with good off-road manoeuvrability.
- Its top speed on flat terrain can be limited to about $5\,\mathrm{km\,h^{-1}}$.
- Agri.Q has to be autonomous or remotely controlled.
- Appropriate safety devices have to be mounted to stop the vehicle in emergency conditions.

Other secondary requirements can also be defined, in particular regarding the PV panels, the power flow, and the collaboration with drones:

- Its power consumption has to be minimised to increase the robot autonomy.
- The PV panels have to be able to recharge the robot battery during its tasks, or at least they have to reduce its power consumption.
- The PV panels have to be orientable to maximise the solar exposition.
- The same mechanisms employed to orient the PV panels have to be able to control their attitude to provide an always flat landing surface for drones.
- The PV panels surface has to be as large as possible both to maximise energy collection and to provide a reasonable landing area. Thus, they should be light and robust at the same time.

Agri.Q should also be able to mount and integrate a high dexterity robot arm to be employed in its PA activities.

2.3 Mechanical functional design

As anticipated before, Agri.Q is an articulated mobile robot composed of two modules, namely the front module F and the back module[1] B (Figure 2.2). Each module mounts two driving units composed of two wheels ($W_{\sim\sim B}$ is the rearmost, $W_{\sim\sim F}$ is the one in the front) by means of a passive revolute joint in $C_{\sim\sim}$. As a result, each module is an independent skid-steered part. The back module is connected to the front one through the yaw revolute joint J_δ, the articulation mechanism with a revolute joint in A_0, and the roll revolute joint J_{α_B}. Above the central chassis P, two PV panels (not shown in figure) are mounted in such a way that they can rotate about the roll revolute joint $J_{\alpha_{Panel}}$.

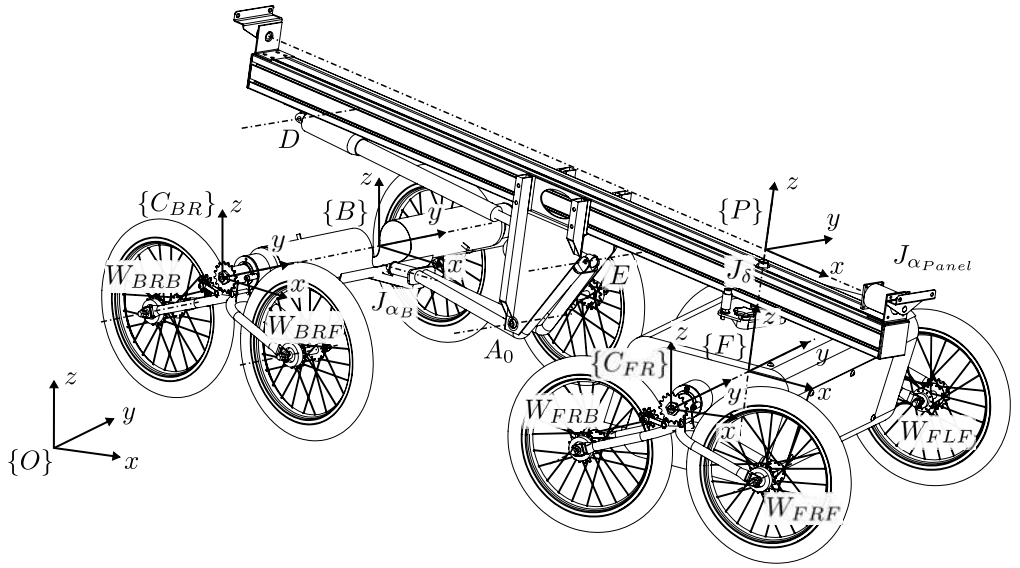

Fig. 2.2 3D representation of Agri.Q and its main reference systems. The PV panels are not shown

Figure 2.3a depicts a schematic view of Agri.Q in a generic configuration. The driving units are free to rotate about the revolute joint in $C_{\sim\sim}$ that links them to their module defining the rotation angle $\Theta_{\sim\sim}$. This feature improves the transversely of rough terrain. The revolute joint J_{α_B} guarantees better wheel-ground contact too: it enables a relative roll rotation α_B between the rear module and the central chassis in order to accommodate ground irregularities. By combining these passive motions, it is possible to guarantee the contact of the wheels with the ground even on very

[1] Back and rear are used interchangeably, but B is always used to refer to the rear module to avoid ambiguity with the symbol R that means right

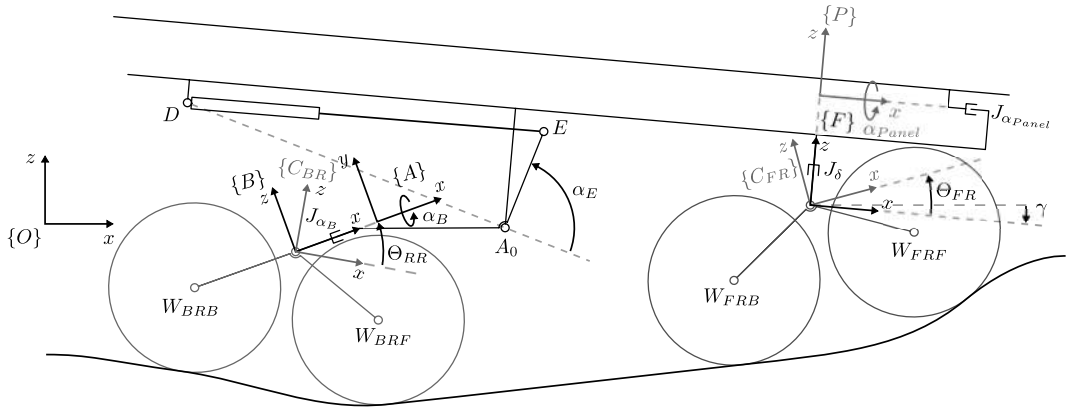

(a) Agri.Q side view

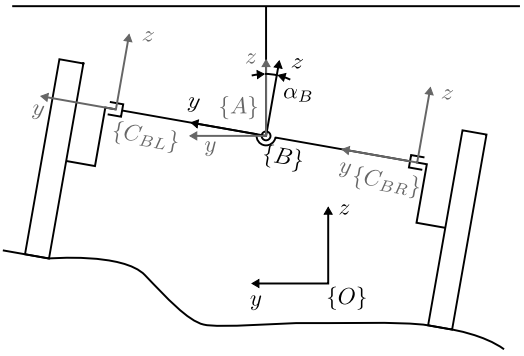

(b) Agri.Q back view

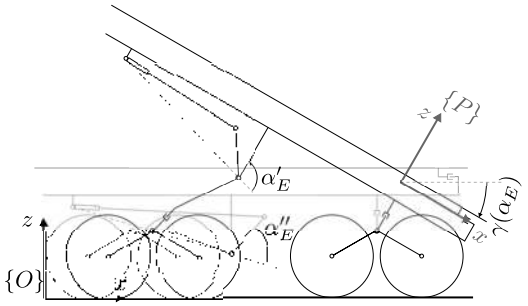

(c) Agri.Q side view with details about the pitch motion

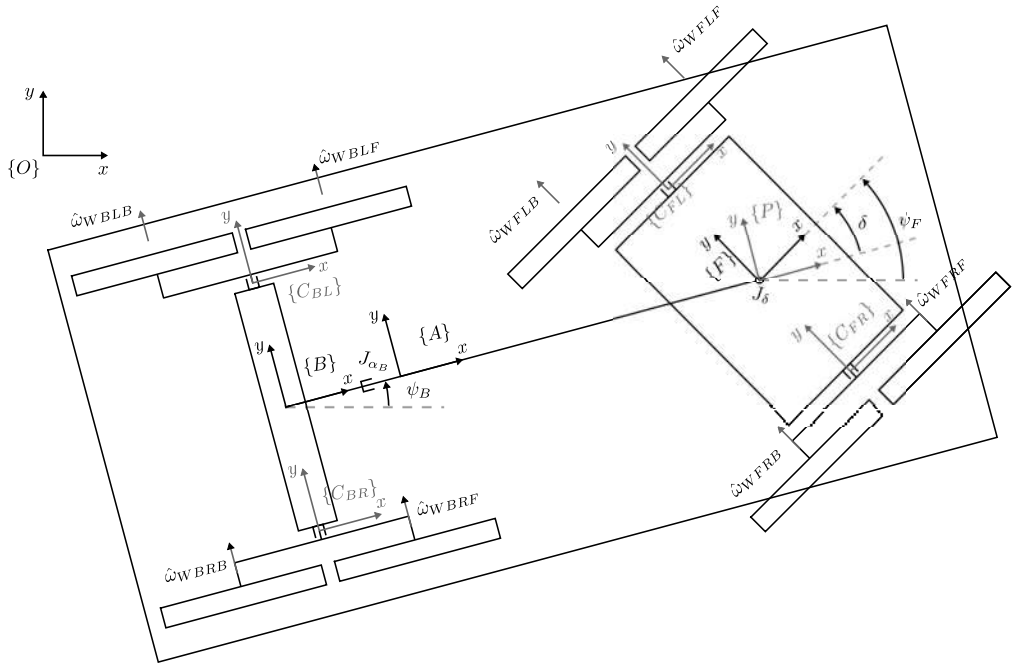

(d) Agri.Q top view

Fig. 2.3 Agri.Q functional schemes

rough terrain, allowing the robot load to be evenly distributed among its multiple contact points to avoid excessive soil compaction. The two motions also let the robot surpass or climb some obstacles.

The front module can be pitched by an angle γ by means of the lever mechanism composed of the lever BA_0E and the linear actuator DE. The same mechanism also imposes the pitch motion to the central chassis and the PV panels, as shown in Figure 2.3c. By employing the joint $J_{\alpha_{Panel}}$ to roll the PV panels of an angle α_{Panel} about $\hat{\mathbf{x}}_P$ together with the pitch motion γ, it is possible to control the panels surface attitude. Hence, it is possible to achieve the two desired panels functions: they can be oriented to face the Sun to maximise the energy collection, but they can also be oriented to provide an always level landing surface for UGVs.

Figure 2.3d illustrates the robot motions in the xy plane. Each module is rotated about the $\hat{\mathbf{z}}_O$ axis of the heading angle $\psi_{\sim}$. The joint J_δ, enables the relative yaw motion between the two modules, acting as a steering joint of the whole robot. Hence, it is possible to define the relative yaw angle (or steering angle) as $\delta = \psi_F - \psi_B$. It is important to recall that the front

To summarise, Agri.Q has two active joints and six passive joints. Namely, the active joints (excluding the locomotion units) are:

- the mechanism with a pivot point in A_0 that defines the pitch angle γ;
- the panels roll joint $J_{\alpha_{Panel}}$;

whereas the passive joints are:

- the relative yaw joint J_δ;
- the rear module roll joint J_{α_B};
- the four revolute joints in $C_{\sim\sim}$ that enables the rotation $\Theta_{\sim\sim}$ of the driving unit rocker;

whose angles are defined as listed in Table 2.1.

Table 2.1 Agri.Q DOFs

Name	Description	Definition
γ	PV panels pitch angle. The front module rotate about the same angle	Rotation angle along $\hat{\mathbf{z}}_P$ between a plane parallel to the ground and the xy plane defined by $\{P\}$
α_{Panel}	PV panels roll angle	Rotation angle along $\hat{\mathbf{x}}_P$ between the xy plane defined by $\{P\}$ and a plane parallel to the PV panels surface
δ	Relative yaw angle. Hitch angle in conventional articulated vehicles	Rotation angle along $\hat{\mathbf{z}}_F$ between $\{F\}$ and $\{P\}$
α_B	Rear module roll angle	Rotation angle along $\hat{\mathbf{z}}_B$ between $\{B\}$ and $\{A\}$
$\Theta_{\sim\sim}$	Rocker rotation angle	Rotation angle along $\hat{\mathbf{y}}_{\sim}$ between $\{C_{\sim\sim}\}$ and $\{\sim\}$, where $\sim$ stands for F or B

2.3.1 Locomotion unit

Agri.Q design has been influenced by its agricultural use, and as a result, an eight-wheel architecture with each pair supported by a rocker has been developed. As with a track system, this method allows the normal forces acting on the ground to be distributed over a larger contact surface. As a consequence, the vehicle is prevented from sinking or becoming stuck in soft ground, and soil compaction is reduced too. Nonetheless, the overall traction efficiency is comparable to that of a four-wheeled rover. Furthermore, the consequences of track slippage whereas turning, which can accentuate soil erosion and landslips on sloping soils exposed to wind and rain, are greatly reduced [198–204].

As another advantage, since the rocker can passively rotate about the module, it can act as a filter in response to the vibrations and oscillations imposed by the ground obstacles and irregularities. Figure 2.4a depicts how the locomotion unit can negotiate an obstacle of height $\Delta z_{W_{\sim\sim F}}$ and how such motion is reduced when transmitted to the module, i.e. the vertical displacement $\Delta z_{C_{\sim\sim}}$ of the rocker passive joint, and hence of the entire vehicle, is reduced. Such behaviour is completely driven by the passive rocker geometry. By design, the rocker points $W_{\sim\sim F}$, $C_{\sim\sim}$, and $W_{\sim\sim B}$ form an isosceles triangle where the distance $\overline{W_{\sim\sim F}W_{\sim\sim B}}$ is the locomotion

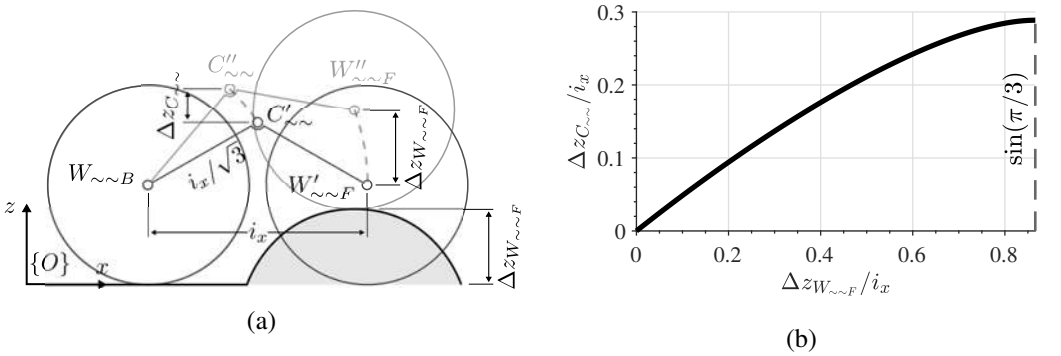

(a) (b)

Fig. 2.4 Rocker mechanism negotiating an obstacle

unit wheelbase i_x, and its opposing angle β_W is chosen to be 120° as a compromise between robot height, wheelbase length, and wheel radius. Therefore, the length l_{rocker} is

$$l_{rocker} = \frac{i_x}{2\cos 30^\circ} = \frac{2i_x}{2\sqrt{3}} = i_x/\sqrt{3} \tag{2.1}$$

while climbing an obstacle of height $\Delta z_{W_{\sim\sim F}}$, the whole locomotion unit rotate of an angle $\Theta_{\sim\sim}$ about the rear wheel centre $W_{\sim\sim B}$. Hence

$$\Delta z_{W_{\sim\sim F}} = i_x \sin\Theta_{\sim\sim} \tag{2.2}$$

and

$$\Delta z_{C_{\sim\sim}} = l_{rocker}\sin(\Theta_{\sim\sim} + \pi/6) - l_{rocker}\sin(\pi/6) \tag{2.3}$$

by combining Eq.(2.1) with Eq.(2.3)

$$\Delta z_{C_{\sim\sim}} = \frac{\sqrt{3}i_x \sin\left(\Theta_{\sim\sim} + \frac{\pi}{6}\right)}{3} - \frac{\sqrt{3}i_x}{6} \tag{2.4}$$

and then by substituting Eq.(2.2) in Eq.(2.4) it is possible to obtain the relation between the two vertical displacements

$$\Delta z_{C_{\sim\sim}} = i_x \left(\frac{\sqrt{3}\sin\left(\arcsin\left(\frac{\Delta z_{W_{\sim\sim F}}}{i_x}\right) + \frac{\pi}{6}\right)}{3} - \frac{\sqrt{3}}{6} \right) \tag{2.5}$$

The relation between the two displacements is also shown in Figure 2.4b, where the two quantities have been normalized about the locomotion unit wheelbase i_x. As said before, the vertical displacement $\Delta z_{C_{\sim\sim}}$ is notably reduced compared to the

wheel motion. When the ratio $\Delta z_{W_{\sim\sim F}}/i_x$ reaches the value of $\sin(\pi/3)$, the rocker has rotated of 60°, therefore the front wheel is exactly above the rear one.

Figure 2.5 goes into more detail about the functional design of the locomotion units. Each unit features two wheels, $W_{\sim\sim F}$ and $W_{\sim\sim B}$, of radius r_W connected to a rocker that can freely rotates about the passive joint $C_{\sim\sim}$ that links the subsystem to the corresponding module. A gear-motor $M_{\sim\sim}$, located within the module and co-axial with the joint $C_{\sim\sim}$, drives a roller chain transmission that links a motor sprocket with radius r_{P1} with two wheel sprockets of radius r_{P2}. A chain tensioner is fixed to the rocker to ensure enough chain tension. Consequently, the locomotion unit is defined by two transmission ratios that can be combined to define the transmission ratio of the whole subsystem. First, the gear-motor has its own transmission ratio $\tau_{M\sim}$ that may be different for the modules but the same for the two sides of each module. Then, the chain drive defines a second transmission ratio $\tau_{C\sim}$. Therefore, the transmission ratio of the whole locomotion unit $\tau_{\sim}$ can be defined as follows

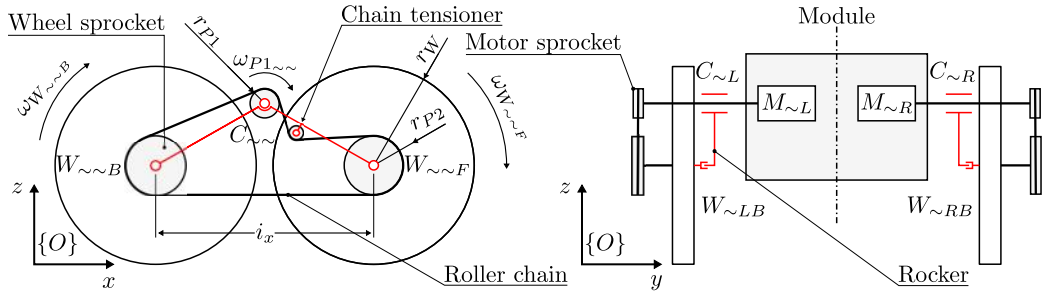

Fig. 2.5 Locomotion unit chain drive functional scheme

$$\tau_{\sim} = \tau_{M\sim}\tau_{C\sim} = \tau_{M\sim}\frac{r_{P2}}{r_{P1}} = \frac{\omega_{M\sim\sim}}{\omega_{P1\sim\sim}}\frac{\omega_{P1\sim\sim}}{\omega_{W\sim\sim\sim}} = \frac{\omega_{M\sim\sim}}{\omega_{W\sim\sim\sim}} \tag{2.6}$$

where $\omega_{M\sim\sim}$ and $\omega_{W\sim\sim\sim}$ are the angular speed of the motor sprocket and the angular speed of the wheels.

By design, the front and rear locomotion units are not equal. The employed motors are the same, but both the gearbox and the chain drive have different transmission ratios (Table 2.2). Moreover, the rear motors are wired in such a way that they can only spin in the same direction and at the same speed. On top of that, each rear wheel comes with a freewheel clutch that disconnects the wheel from the transmission when it rotates faster than the driveshaft or when it spins backwards. As a result, the rear module is not skid-steered, thus its motors could be activated

only if the front module requires additional traction power (e.g., climbing a hard slope, facing an obstacle, or negotiating extremely tight curves) but not produce a yaw moment in the back. In all other cases, the rear wheels disengage from the locomotion unit transmission to avoid unnecessary power losses.

Table 2.2 Locomotion unit parameters

Parameter	**Value**	**Parameter**	**Value**
i_x	440 mm	$\tau_{MF} = \omega_{MF\sim}/\omega_{P1F\sim}$	15.88
β_W	120 °	$\tau_{MB} = \omega_{MB\sim}/\omega_{P1B\sim}$	28.93
r_W	203.2 mm	$\tau_{CF} = \omega_{P1F\sim}/\omega_{WF\sim\sim}$	3
r_{P1}	32.55 mm	$\tau_{CB} = \omega_{P1B\sim}/\omega_{WB\sim\sim}$	1
r_{P2F}	97.65 mm	$\tau_F = \omega_{MF\sim}/\omega_{WF\sim\sim}$	47.64
r_{P2B}	32.55 mm	$\tau_B = \omega_{MB\sim}/\omega_{WB\sim\sim}$	28.93

A very simple dynamic model of Agri.Q may be built to drive the traction motors choice by assuming a set of appropriate simplifications. Figure 2.6 depicts such a simplified approach. To identify a maximum motor torque, the rover is studied in a quasi-static situation while ascending a slope with an incline of $\alpha_{ground} = 15°$ (28% incline, as listed in the requirements). Since the robot nominal speed is restricted to $5\,\mathrm{km\,h^{-1}}$, the inertial effect and rolling frictions between wheels and ground can be neglected. By estimating a robot total mass of $m_{AgriQ} = 100\,\mathrm{kg}$ that is equally distributed among the two modules, and that the slope with inclination $\alpha_{ground} = 15°$ has to be climbed at the speed of $v_F = 3.6\,\mathrm{km\,h^{-1}} = 1\,\mathrm{m\,s^{-1}}$ with a transmission efficiency of $\eta = 0.9$, the power required by a motor of the front module without the contribution of the rear motors is

$$P_{MF\sim} = \frac{v_F m_{AgriQ} g \sin(\alpha_{ground})}{2\eta} = 141\,\mathrm{W} \tag{2.7}$$

A DC motor, NDP 120/522 made by Transtecno, with the following characteristics has been selected

- Continuous duty cycle (defined as S1) nominal power $P_{nom,S1} = 120\,\mathrm{W}$
- Short time duty cycle (defined as S2) nominal power $P_{nom,S2} = 160\,\mathrm{W}$
- Continuous duty cycle (S1) nominal torque $T_{nom,S1} = 0.38\,\mathrm{N\,m}$
- Short time duty cycle (S2) nominal torque $T_{nom,S2} = 0.55\,\mathrm{N\,m}$

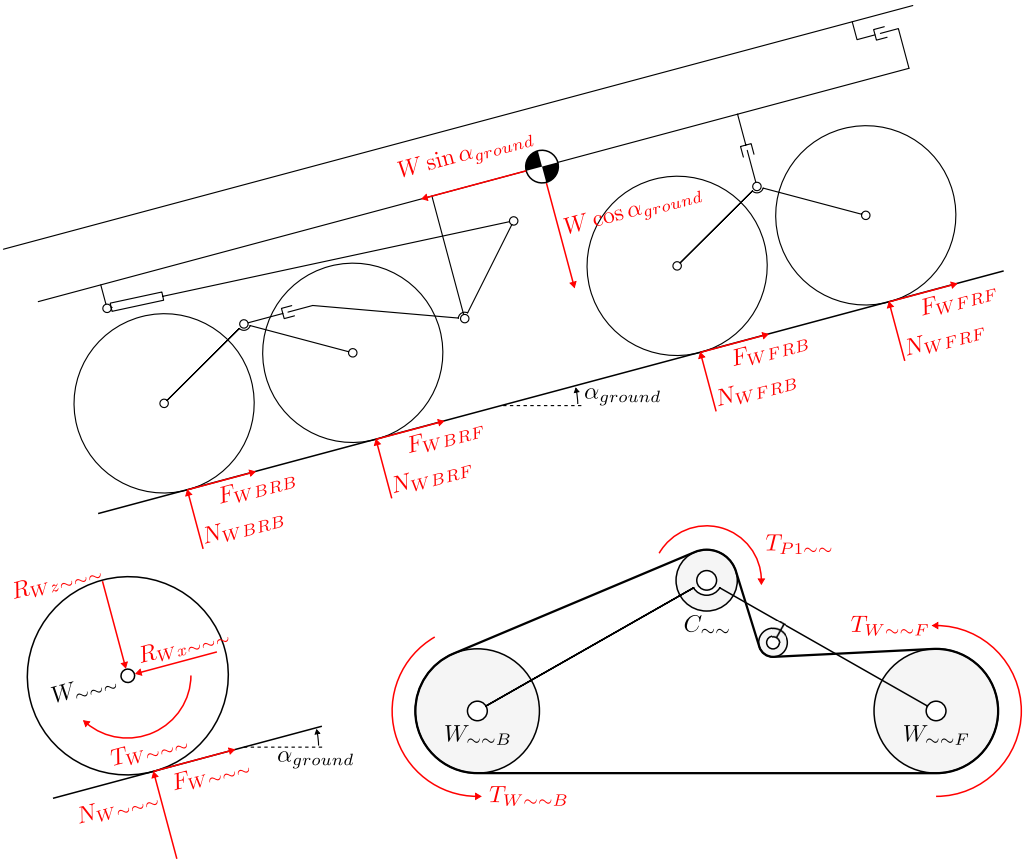

Fig. 2.6 Simplified free body diagrams of Agri.Q on an incline

- Maximum torque $T_{max} = 1.10\,\mathrm{N\,m}$
- Continuous duty cycle (S1) nominal angular speed $\omega_{nom,S1} = 315\,\mathrm{rad\,s^{-1}}$
- Maximum angular speed $\omega_{max} = 350\,\mathrm{rad\,s^{-1}}$

By activating all the motors, the maximum incline that could be faced is about 36° or 73%.

The transmission ratio introduced before has been selected iteratively to reach the desired performance. In particular, the chain drive sprocket radii have been selected starting from their number of teeth. The following relation holds

$$D_{pitch} = \frac{p}{\sin\left(\frac{180^\circ}{Z}\right)} \tag{2.8}$$

where D_{pitch} is the sprocket pitch diameter, $p = 12.7$mm is the pitch of a $1/2'' \times 3/16''$ (or ISO 084) chain, and Z is the number of teeth. The motor sprocket has to be as small as possible, hence, given the technological limits, a number of teeth equal to $Z_{P1} = 16$ was chosen. The front wheel sprockets instead should be as large as possible, but, at the same time, they should be smaller than the wheel to avoid interference with the ground, therefore it was chosen $Z_{P2F} = 48$. By design, it has been chosen that the rear chain drives have a unitary transmission ratio, so $Z_{P2B} = 16$.

2.3.2 PV panels attitude mechanisms

The remaining robot active joints control the attitude of the robot PV panels to achieve the two desired behaviours: an always level landing platform for UAVs working together with Agri.Q and orientable PV panels to maximise the Solar energy collection. The two DOF related to the joints are the pitch γ and roll α_{Panel} rotations.

The α_{Panel} roll angle and the revolute joint $J_{\alpha_{Panel}}$ are driven by a linear actuator mounted between the central chassis and the PV panels (Figure 2.7). The range of motion of α_{Panel} is set to $\pm 20^{\circ}$ to compensate for any transversal inclination within that range. Such a range has been defined as a design compromise between transversal incline compensation, solar tracking, limited PV panels height from the ground, and sufficient clearance between the panels and the wheels.

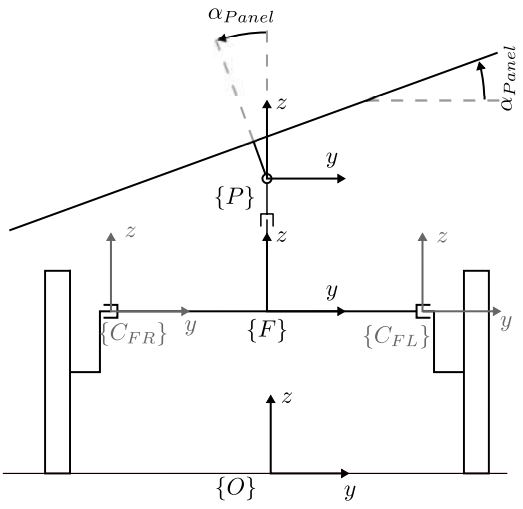

Fig. 2.7 Agri.Q PV panels roll DOF

The pitch motion γ is also controlled to achieve the double behaviour of self-leveling landing surface or solar energy collection optimisation. Consequently, it is possible to define some key PV panels pitch angles γ related to some requirement position (Figure 2.8):

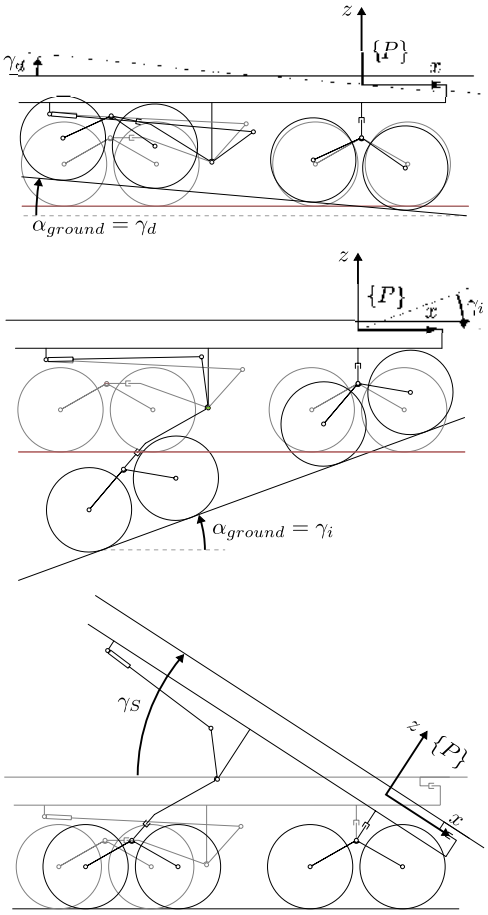

Fig. 2.8 Agri.Q in relevant poses with respect to the nominal one. Top, requirement of a self-levelling PV surface in slight descends. Centre, requirement of a self-levelling landing surface in the maximum slope incline. Bottom, the maximum PV panels tilt angle to maximise Sun rays collection

- $\gamma = \gamma_N = 0°$, nominal (N) condition where the panels surface is parallel to the ground;
- $\gamma = \gamma_d =$ -5°, pitch angle to compensate slight descents (d);
- $\gamma = \gamma_i = 24°$, pitch angle to compensate the maximum slope incline (i);
- $\gamma = \gamma_S = 33°$, max pitch angle to track the Sun (S)

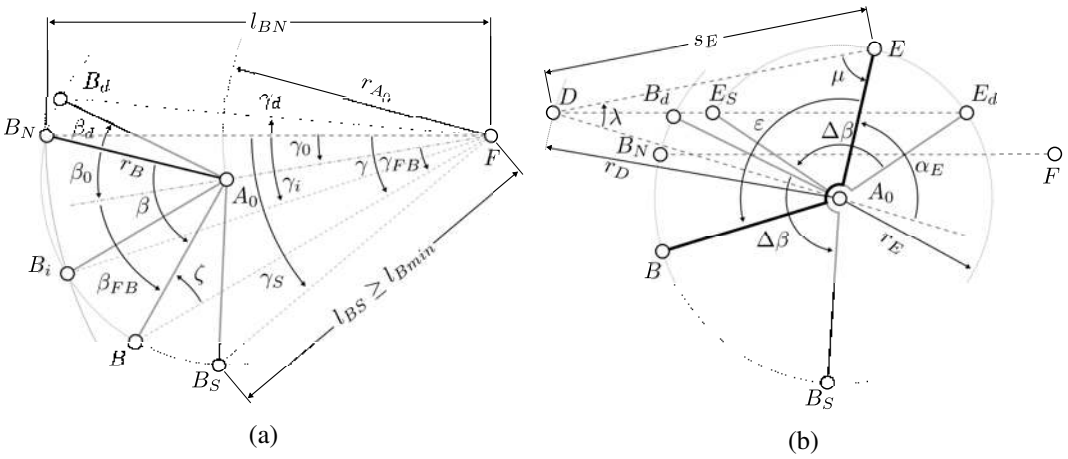

Fig. 2.9 Pitch mechanism kinematic schemes

A specifically designed linkage BA_0E drives the pitch motion. The linkage is pivoted on the chassis at A_0, is connected to the rear module at B, and is actuated by a linear actuator fixed in D and moving the point E. The dimensional synthesis of this mechanism is provided below, and focused on the selection of the location of the kinematic pairs and the determination of the link lengths, utilizing the kinematic inversion approach, thereby maintaining the chassis fixed and moving the positioning device. As illustrated in Figure 2.9a, the pivot joint A_0 is located on the γ_i bisecting line; as a result, the actual trajectory of B, rotation around A_0, corresponds to imposing that the key points B_N and B_i that are the same distance l_{BN} from F. To put it another way, the angle γ_0 is selected to be equal to $\gamma_i/2$. At the maximum pitch angle γ_S, the distance $\overline{A_0B}$, i.e. r_B, is set as the maximum one consistent with the necessity to avoid self-collision of rear and front wheels since the mechanism can shorten the distance l_B up to a minimum value equal to $l_{Bmin} = 2r_W + i_x$. This approach also means that a minimal variation of l_B within the 0-γ_i range is ensured in order to avoid affecting the robot dimensions while driving. The relation between the desired rotation γ of B about $C_{F\sim}$ (platform orientation) and the rotation β of the link BA_0 driven by the positioning mechanism is depicted graphically in Figure 2.9a. Instead of utilizing the variables β and γ, (having $\beta = 0°$ when $\gamma = 0°$), the A_0F direction is used as a baseline for measuring the angles β_{FB} and γ_{FB}, having $\beta = \beta_{FB} + \beta_0$ and $\gamma = \gamma_{FB} + \gamma_0$. The angular shift between the two reference systems is identified by the constant angles β_0 and γ_0.

To obtain the mechanism function $\beta = \beta(\gamma)$ it is convenient to use the auxiliary angle ζ. Hence

$$\zeta = \beta_{FB} - \gamma_{FB} \tag{2.9}$$

$$r_B \sin(\zeta) = r_{A_0} \sin(\gamma_{FB}) \tag{2.10}$$

therefore

$$\beta_{FB} = \gamma_{FB} + \zeta = \gamma_{FB} + \arcsin\left(\frac{r_{A_0}}{r_B}\sin(\gamma_{FB})\right) \tag{2.11}$$

$$\beta_0 = \gamma_0 + \arcsin\left(\frac{r_{A_0}}{r_B}\sin(\gamma_0)\right) \tag{2.12}$$

where $\gamma_0 = \gamma_i/2$ by definition. The angle β and its range of motion $\Delta\beta$ can be defined as functions of γ as follows

$$\beta = \beta(\gamma) = \beta_{FB} + \beta_0 = \beta_0 + (\gamma - \gamma_0) + \arcsin\left(\frac{r_{A_0}}{r_B}\sin(\gamma - \gamma_0)\right) \tag{2.13}$$

$$\Delta\beta = \beta_S - \beta_d \tag{2.14}$$

recalling that $\gamma = \gamma_{FB} + \gamma_0$.

The rotation β is obtained thanks to a linear actuator hinged between the point D, fixed to the chassis, and the point E, which is part of the linkage BA_0E, and their variable distance s_E (Figure 2.9b). The mechanism actuation design parameters are the position of the point D, the shift angle ε, and the lengths r_E and r_D. According to the figure, one has

$$r_D + r_E \cos(\alpha_E) = s_E \cos(\lambda) \tag{2.15}$$

$$r_E \sin(\alpha_E) = s_E \sin(\lambda) \tag{2.16}$$

By means of the non-dimensional parameter $p_1 = r_D/r_E$, it is possible to get the auxiliary angle λ and the non-dimensional input $w_E = s_E/r_E$ as function of the output angle α_E

$$\lambda = \lambda(p_1, \alpha_E) = \arctan\left(\frac{\sin(\alpha_E)}{p_1 + \cos(\alpha_E)}\right) \tag{2.17}$$

$$w_E = w_E(p_1, \alpha_E) = \frac{s_E}{r_E} = \frac{p_1 + \cos(\alpha_E)}{\cos(\lambda(p_1, \alpha_E))} = (p_1 + \cos(\alpha_E))\sqrt{\frac{\sin(\alpha_E)^2}{p_1^2 \cos(\alpha_E)^2} + 1} \tag{2.18}$$

Moreover, the mechanism transmission angle μ can be worked out as

$$\mu = \begin{cases} \alpha_E - \lambda, & \text{if } \alpha_E - \lambda \leq \pi/2 \\ \pi - (\alpha_E - \lambda), & \text{otherwise} \end{cases} \tag{2.19}$$

Figure 2.10 depicts some results of the parametric analysis in terms of the angular position α_E, the linkage instantaneous transmission ratio $\partial\alpha_E/\partial w_E$ and the transmission angle μ as functions of the non-dimensional input $w_E = s_E/r_E$ at different value of the non-dimensional parameter $p_1 = r_D/r_E$. The desired pitch angle range of motion $\Delta\gamma = \gamma_S - \gamma_d = 38^\circ$ defines, thanks to Eq.(2.13) and Eq.(2.14), a corresponding $\Delta\beta = \beta_S - \beta_d = 81.93^\circ - (-12.55^\circ) = 94.48^\circ$. This window is then useful to identify the appropriate range of w_E for where the angle α_E has an almost linear variation and the instantaneous transmission ratio $\partial\alpha_E/\partial w_E$ is as constant as possible in order to optimise the actuator effort. At the same time, a minimum acceptable value of the transmission angle μ has to be guaranteed. The angle ε and the length r_D are chosen to reduce the volume occupied by the whole mechanism during its motion. The final parameters are listed in Table 2.3. To achieve the desired performance, the Mecvel L03 linear actuator has been chosen to be mounted between the anchor points D and E. It is a 24 V DC linear actuator with a stroke of 360 mm and a maximum speed of 20 mm s^{-1}.

Table 2.3 Pitch linkage parameters

Parameter	**Value**	**Parameter**	**Value**
r_{A_0}	723 mm	α_{E_d}	42.44°
r_B	498 mm	w_{E_d}	4.055
r_E	247 mm	s_{E_d}	1002 mm
r_D	807 mm	γ_S	33.00°
p_1	3.264	β_S	81.93°
ε	121°	α_{E_S}	137.31°
$\gamma_0 = \gamma_i/2$	12.00°	w_{E_S}	2.615
β_0	30.00°	s_{E_S}	646 mm
γ_d	-5.00°	$\Delta\beta$	94.48°
β_d	-12.55°	Δs_E	356 mm

Figure 2.11 depicts the PV panels range of motion projected into the local sky following the methodology discussed in [225]. In particular, the red area represents the surface covered by the PV surface centre only due to the previously described PV

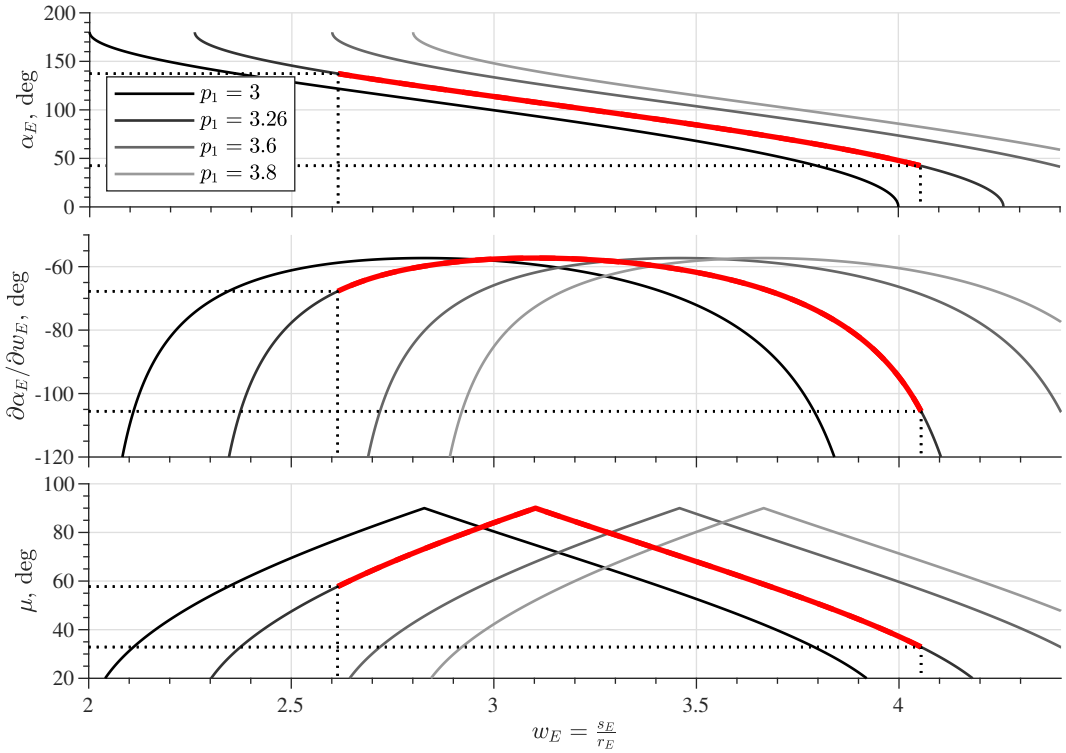

Fig. 2.10 Pitch linkage mechanism parametric analysis. The red colour highlights the final design range

panels attitude mechanisms, i.e. the α_{Panel} and γ DOFs. The grey area, instead, is the sky surface covered by Agri.Q panels if its planar motion, namely, its possibility to assume any heading angle, is considered. As a result, the PV panels can cover a spherical surface defined by an elevation angle between $90° - \gamma_S = 57°$ and $90°$ and a azimuth angle between $\pm 20°$ or $\pm 180°$, when the rover is static or moving respectively. The figure also shows the daily Sun path during the Winter Solstice, the two Equinoxes, and the Summer Solstice. Hence, during the year, the Sun follows a similar path that starts in the east at sunrise, reaches its maximum elevation around noon, and ends in the west with sunset. Such a path is always bound between the Solstice curves. Whenever the daily Sun path intersects the PV panels surface coverage, it means that at that time of the day it is possible to orient the PV surface normal to the Sun as a means to collect the maximum Solar radiation possible. If the path does not intersect the projected surface, the PV panels attitude is always sub-optimal in terms of energy collection. Figure 2.11 illustrates as an example the daily Sun paths in North-West Italy (at 45°04′N 7°42′E). When Agri.Q is on flat terrain, it is able to optimally orient its PV surface only during some days before and

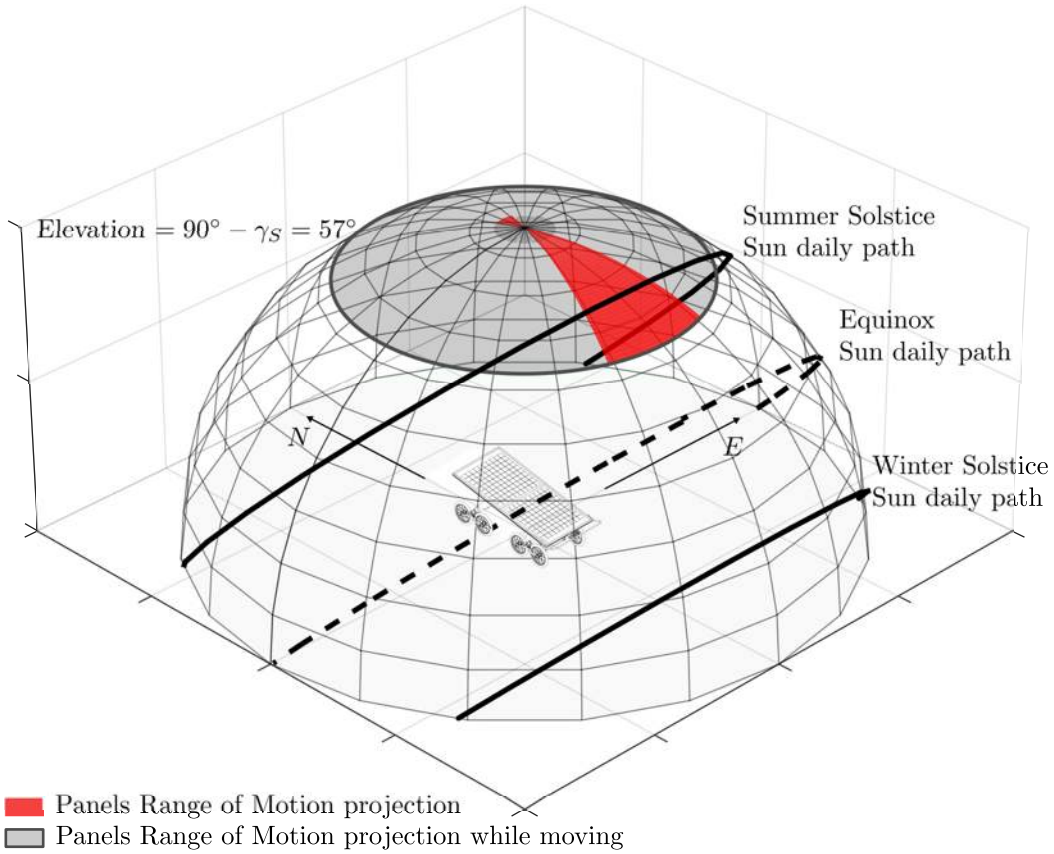

Fig. 2.11 PV panels range of motion compared to the Sun paths at 45°04′N 7°42′E

after the Summer Solstice and during the central hours of the day (the actual time period is between the 22^{nd} of April and the 20^{th} of August). Nevertheless, Agri.Q is designed to operate in hilly terrains and vineyards on hard slopes, therefore, the ground inclination can reduce the elevation angle in order to be able to increase the range of days and hours around noon in which it is possible to optimal orient the PV panels.

2.4 Final mechanical design

This section presents the final mechanical design of the Agri.Q rover and its main parts. First, an overview of the final assembly is provided, and then the two modules and the central chassis are discussed. At last, the locomotion unit final design and the integration of a commercial robotic arm are presented.

Assembly

Figure 2.12 shows a schematic representation of the final design of Agri.Q (Figure 2.13). The whole robot (except for the safety bumper and the accessory robotic arm) is within the size of the PV panels assembly (1050 $\times$ 2122 mm). When the PV surface is flat, the robot height is about 650 mm. The robot is mostly made of aluminium and weighs 112 kg. When the robot is on flat ground, the PV panels are parallel to it and the two modules have the same heading (i.e, $\delta = 0°$), the centre of mass (*CoM*) of the assembly, with respect to $\{F\}$ is located in $(-534, -15, 90)$ mm, which roughly corresponds to the point E. Hence, in the static condition, the front-back mass distribution is about 59%-41%.

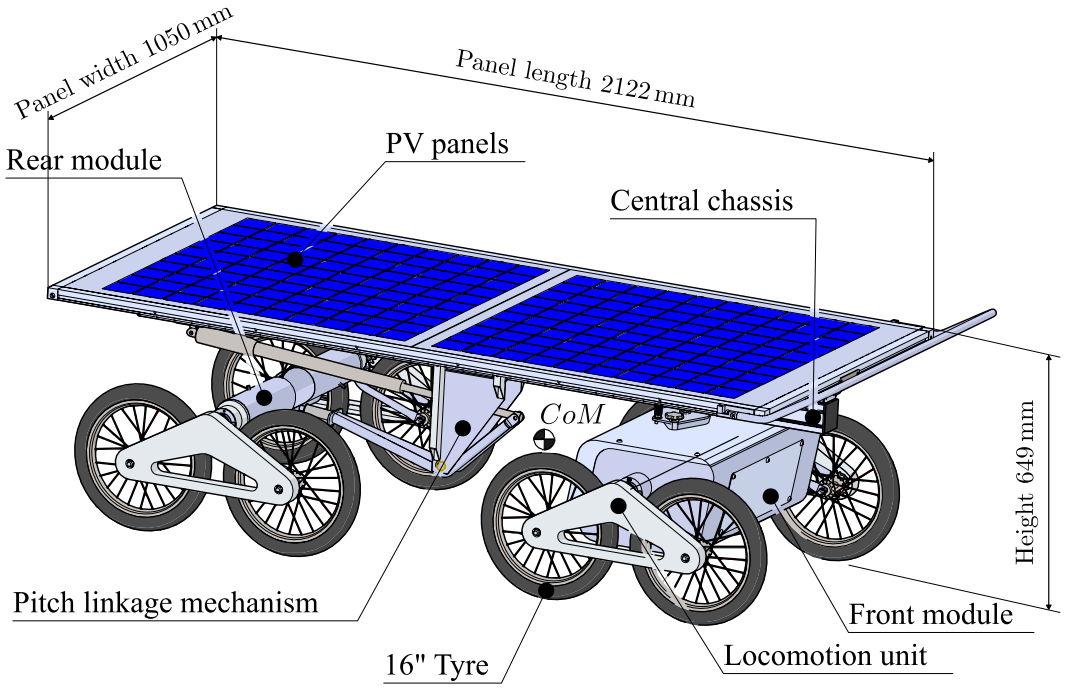

Fig. 2.12 Agri.Q assembly main parts and dimensions

Front module

The front module is an aluminium box that houses most of the robot electronic systems and the traction motors of the two front locomotion units. Figure 2.14 depicts the main dimensions of the front module. On its left and right side, it is linked to the two locomotion unit rockers by means of a passive revolute joint in

Fig. 2.13 Agri.Q final assembly

$\{C_{F\sim}\}$. On the top side, there is instead the passive revolute joint J_δ that enables the relative yaw motion between the robot modules. Its axis is slightly off the box centre, however, it is generally considered passing through the module centre to maintain the definition of the reference frame $\{F\}$ as the reference frame defined by the axis of the front traction motors and the J_δ axis. There is a grill mounted on the box front face to improve ventilation, whereas on the back are housed all the connectors required to receive and send signals from and to the rest of the robot.

Rear module and central chassis sub-assembly

Figure 2.15 highlights the rear module and the central sub-assembly (both shown in detail in Figure 2.16 and Figure 2.17). The central chassis is based around a standard square aluminium extrusion ($2020 \times 80 \times 80$ mm) onto which the anchor points of the pitch linkage mechanism A_0 and D, and the revolute joints J_δ and $J_{\alpha_{Panel}}$ are fixed. Then, the pitch linkage mechanism links the rear module and the central chassis by means of the passive revolute joint J_α that enables the rotation of the rear module about the roll axis.

The rear module (Figure 2.16) is a very simple tubular stainless steel housing for the two rear traction motors similarly to what happens in the front module. However,

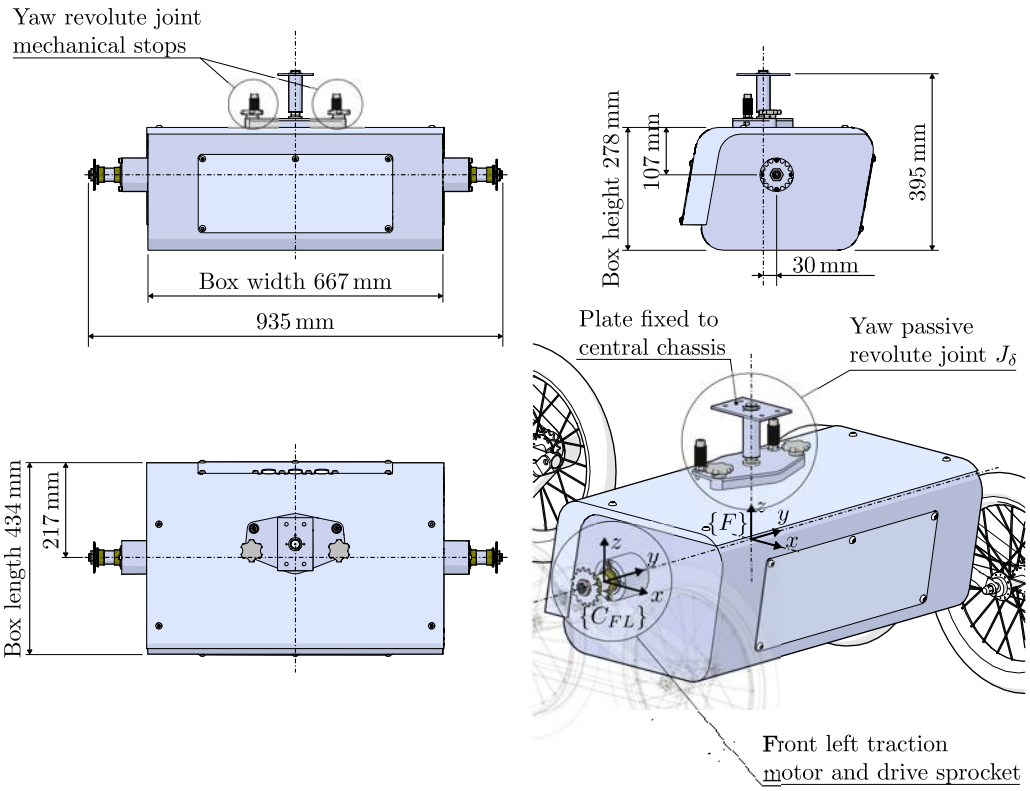

Fig. 2.14 Final design of the front module

the rear module is slightly larger than the front one. The passive revolute joint J_α, made of a simple bushing, has its rotation axis parallel to $\hat{\mathbf{x}}_B$ but it is mounted slightly lower than the main axis of the rear module, namely the $\hat{\mathbf{y}}_B$ axis.

The pitch linkage (Figure 2.17) is made of 304 stainless steel tubings welded together to obtain the sizes and shape defined previously (Table 2.3) and graphically summarised in Figure 2.18.

Also, Figure 2.19 shows how the distance l_B changes due to the action of the pitch linkage mechanism. While the robot is in its nominal condition (i.e., the PV panels are parallel to the ground) or when $\gamma = \gamma_i = 20°$, the two modules are spaced out by $l_{BN} = 1197$ mm. Between $\gamma = 0°$ and γ_i, this distance increase very slightly (about 11 mm) reaching its maximum at $\gamma = \gamma_0 = \gamma_i/2$. While the PV panels are pitched by the maximum angle $\gamma = \gamma_S = 33°$ instead, the robot reach its minimum length of $l_{BS} = 1067$ mm. This limitation is due to the minimum length of the linear actuator DE, but it is above the minimum required margin of $l_{Bmin} = i_x + 2r_W = 846$ mm.

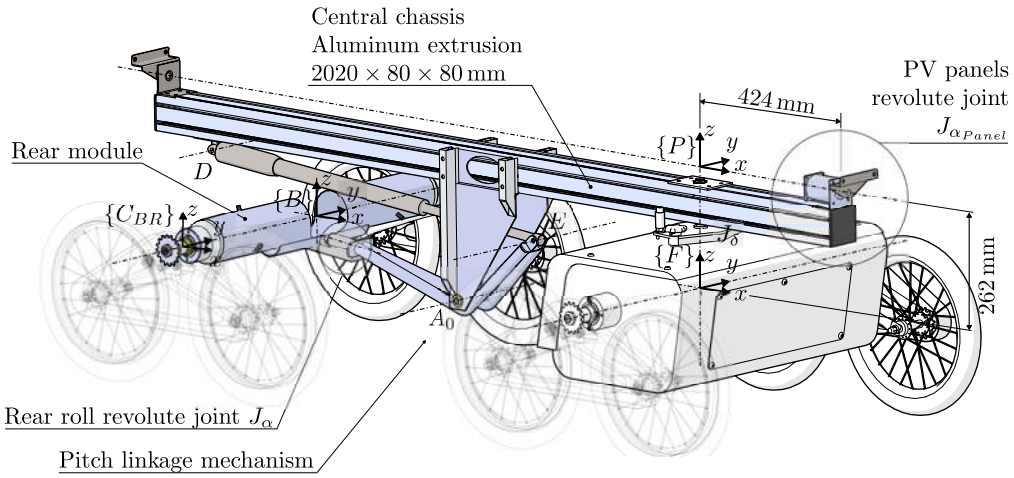

Fig. 2.15 Rear module and central chassis sub-assembly

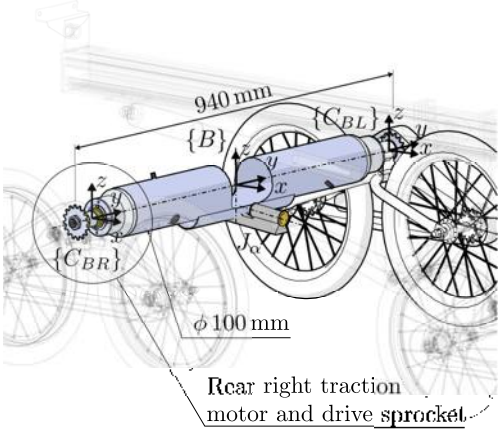

Fig. 2.16 Detail of the rear module

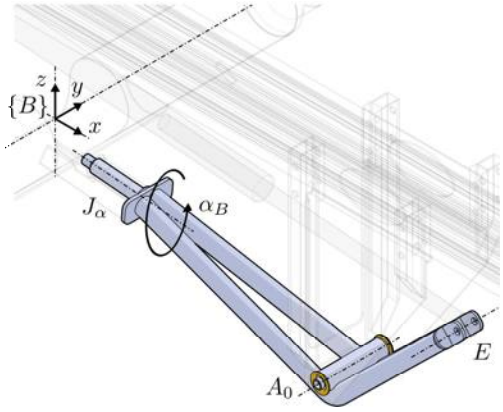

Fig. 2.17 Detail about the pitch linkage

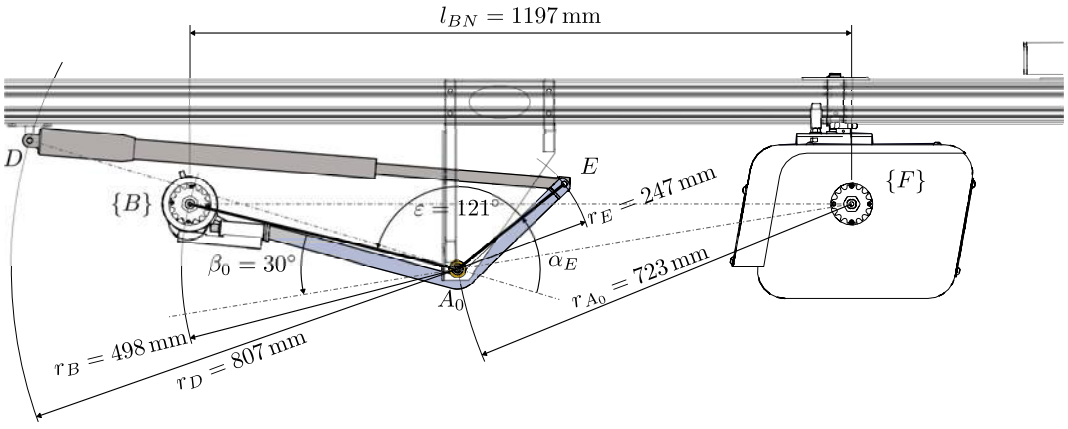

Fig. 2.18 Pitch linkage final design

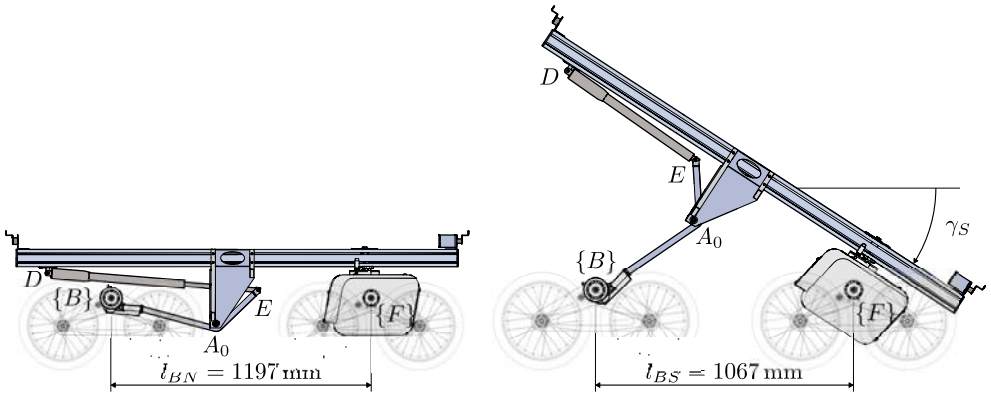

Fig. 2.19 Detail about the two distances between the two modules

(a) (b)

Fig. 2.20 (a) Agri.Q panels compensating the hill incline. (b) Agri.Q at its maximum pitch angle

Locomotion units

Figure 2.21 illustrates how a locomotion unit is made. In particular, it shows the front left unit, however, all units are almost identical, since in the rear units the only differences are the wheel sprockets and the motor planetary gearbox, and the units on the right side are simply mirrored. As anticipated, the locomotion unit is driven by the NDP 120/522 DC traction motor with an integrated negative brake and an incremental encoder to measure its speed. The motor mounts a commercial planetary gearbox with a transmission ratio of $\tau_{MF} = 15.88$ in the front units and of $\tau_{MB} = 28.93$ in the back. The gear motor drives a chain transmission through an Ergal (7075 T6 aluminium alloy) sprocket with 16 teeth. The drive chain is a common $1/2" \times 3/16"$ (or ISO 084) bicycle roller chain. The chain transmission drives the two $16" \times 1.95"$ ($r_W = 203.2\,\text{mm}$) mountain bike tyres that are fixed to

the wheel sprocket. In the front units, the sprocket has 48 teeth whereas in the back it has 16 teeth like the motor sprocket. Hence the chain transmission ratio is $\tau_{CF} = 3$ and $\tau_{CF} = 1$ respectively. By combining the locomotion unit transmissions, the final transmission ratios between the motor and the wheel are $\tau_F = 47.65$ and $\tau_B = 28.93$, respectively for the front and rear units. The whole transmission is protected by an aluminium cover.

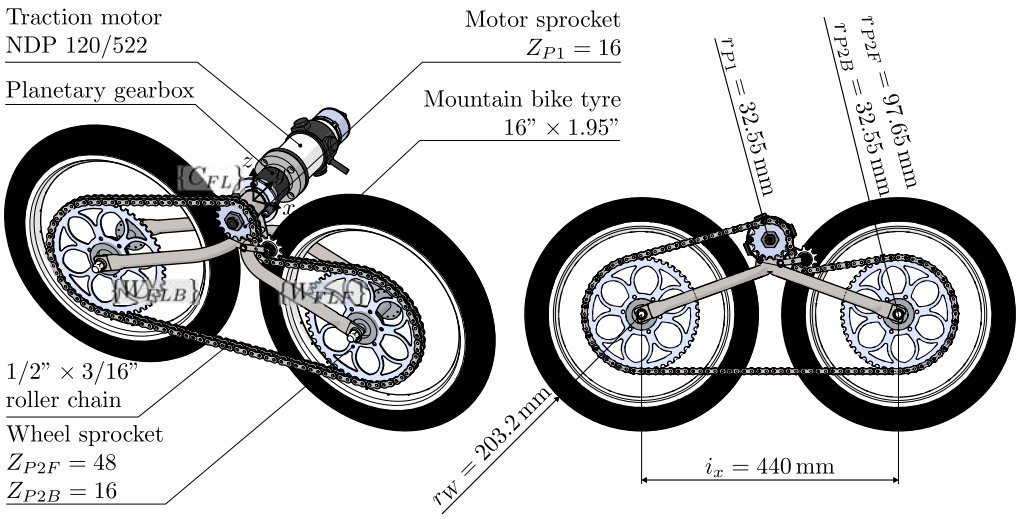

Fig. 2.21 Locomotion unit details. The front left unit is shown, the right one is mirrored, and the minor changes in the rear modules are annotated

The locomotion units were initially designed to be equal except for the different planetary gearbox. However, the torque required to steer the front module was higher than initially expected, hence the front transmission ratio has been increased to produce more torque by increasing the wheel sprocket to the size reported here.

As said before, the rear module is slightly larger than the front one, hence the front and rear module tracks are $i_{yF} = 817\,\text{mm}$ and $i_{yB} = 845\,\text{mm}$ respectively (Figure 2.22). Moreover, the wheels of the rear locomotion units mount a freewheel mechanism hub to transmit the rear motors power only while going forward.

Figure 2.23 illustrates in more detail how the passive revolute joint $C_{\sim\sim}$ connecting the locomotion units to the corresponding module. The motor shaft driving the corresponding sprocket rotates about a flange fixed to the module, whereas the rocker can freely rotate about the same module flange in a similar fashion.

Figure 2.24 shows a sequence of frames where Agri.Q was successfully climbing a step thanks to its locomotion units. The actual step height that the rover can surpass

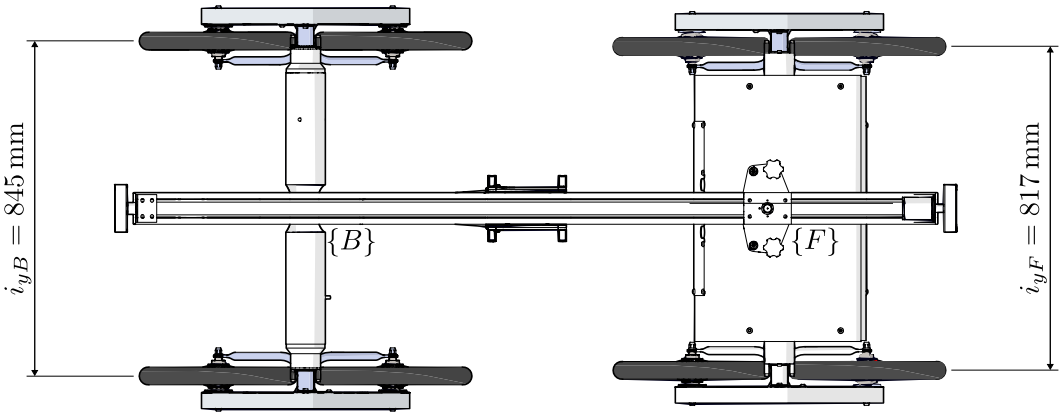

Fig. 2.22 Detail about the front and rear module tracks $i_{y\sim}$

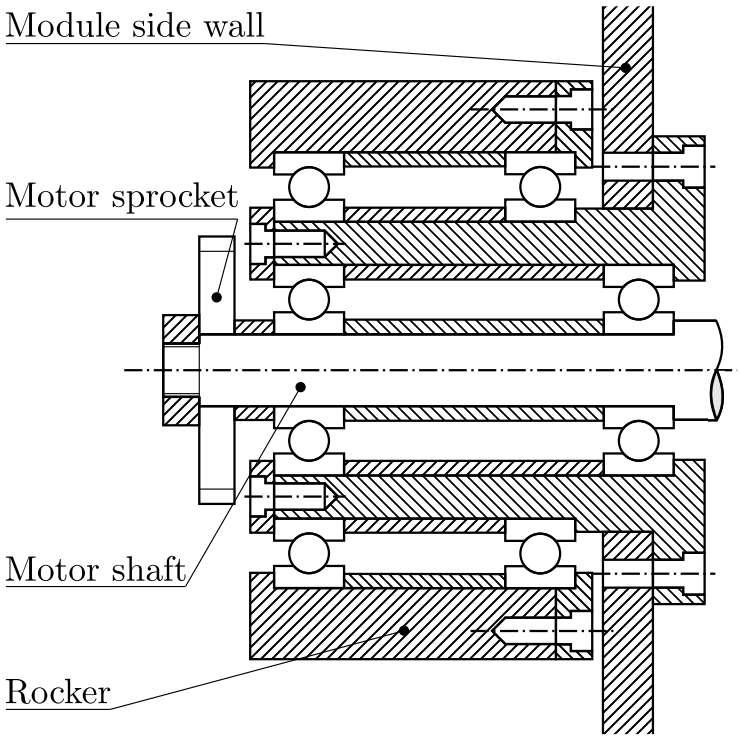

Fig. 2.23 Detail of the $C_{\sim\sim}$ passive revolute joint

highly depends on a proper traction control of all the locomotion units. Steps are not a common obstacle in fields, however, since all the locomotion units are independent, the same ability holds for more natural obstacles, such as rocks, large fallen branches or roots.

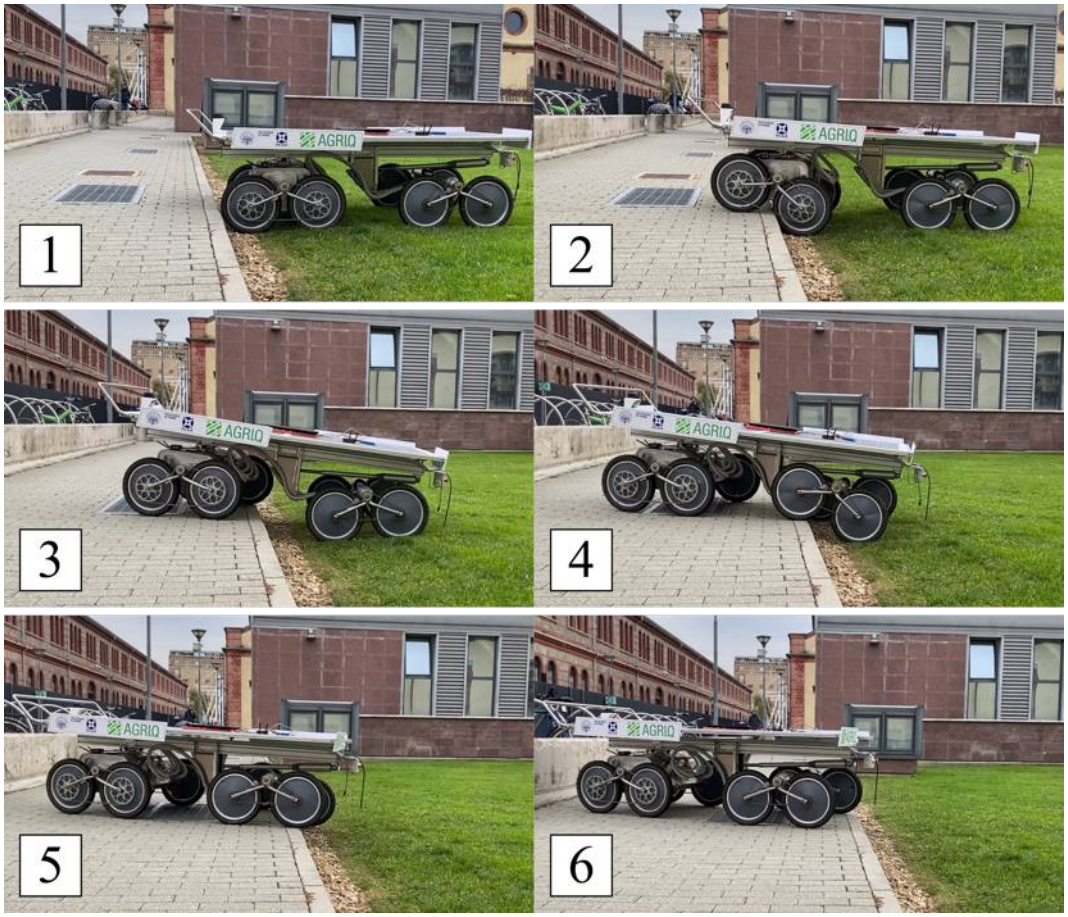

Fig. 2.24 Sequence of Agri.Q surpassing a step exploiting its locomotion units

High dexterity robotic arm

The rover is outfitted with a robotic manipulator to be able to gather crop, soil, or leaf samples for field monitoring. It should also be able to reach a large section of the landing platform to interact with a landed platform (e.g., handing over the collecting samples to the drone to be delivered to a testing laboratory). The robot arm workspace must be such that it can reach both the ground and crops. The workspace should also be fairly symmetrical in order for the robot to work easily in all directions. Therefore, workspace-wise, the robot arm has to collect a sample that could be anywhere from the ground to the top of a typical vineyard (about 2 m).

The robot should be redundant in order to have several configurations for a given end-effector position, allowing for better interaction with a confined environment. This kinematic redundancy enables the main task (e.g., collecting samples) to be

completed while a secondary activity is completed (e.g., collision avoidance with branches of plants or with the rest of the rover). To accomplish this, both target tracking and collision avoidance algorithms must be implemented with the aim of directing the end-effector toward the target while the rest of the arm is avoiding collisions [226–228].

The robot arm capabilities must allow it to transport loads of at least 0.5 kg with minimal power consumption. Finally, the robot must be light in order for the rover to carry it effortlessly.

The Jaco2, a 7 DOF collaborative robot arm from the Canadian manufacturer Kinova [1], was chosen as the robotic manipulator to meet these objectives. Figure 2.25a and Table 2.4 summarise the dimensions of the robot arm. Figure 2.25b depicts instead a kinematic diagram of the robot arm. It is made of 7 revolute joints, hence it is clearly identifiable as a redundant robot. This joint space redundancy allows for limitless arm configuration given a desired position of the end-effector. In particular, Figure 2.25b shows the so-called swivel circumference: the locus of the possible elbow positions for a given end-effector pose.

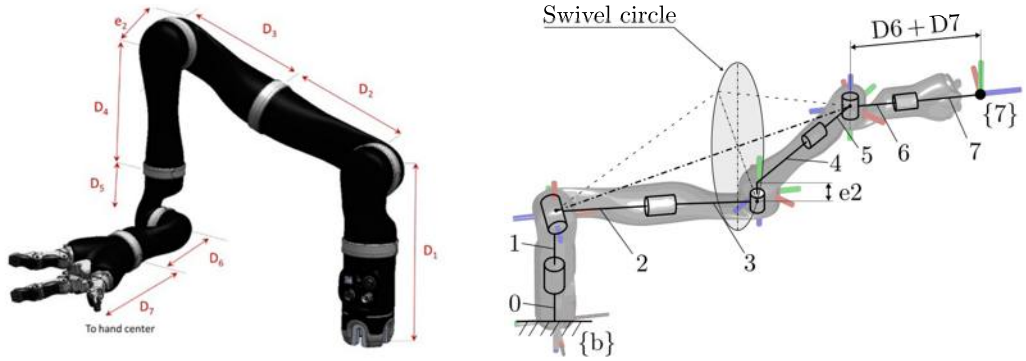

(a) (b)

Fig. 2.25 Kinova Jaco2 robot arm dimensions [1] and kinematic diagram

Kinematic analysis was performed to investigate the workspace of the robot end-effector without the gripper. The workspace as a consequence is shown in Figure 2.26a. From the shoulder centre, the workspace is a quasi-spherical region with a primary radius of 825 mm. It is critical to choose properly how to mount the robot arm on the rover to meet the criteria for robot mobility with the aim of allowing the gripper to reach different places in a large vertical and lateral region. Therefore, the Jaco2 workspace is not fixed in space since the arm is mounted on the

Table 2.4 Kinova Jaco2 robot arm dimensions [1]

Parameter	**Value**	**Length,** mm
D1	Base to shoulder	275.5
D2	First half upper arm length	205.0
D3	Second half upper arm length	205.0
D4	Forearm length (elbow to wrist)	207.3
D5	First wrist length	103.8
D6	Second wrist length	103.8
D7	Wrist to center of the hand	160.0
e2	Joint 3-4 lateral offset	9.8

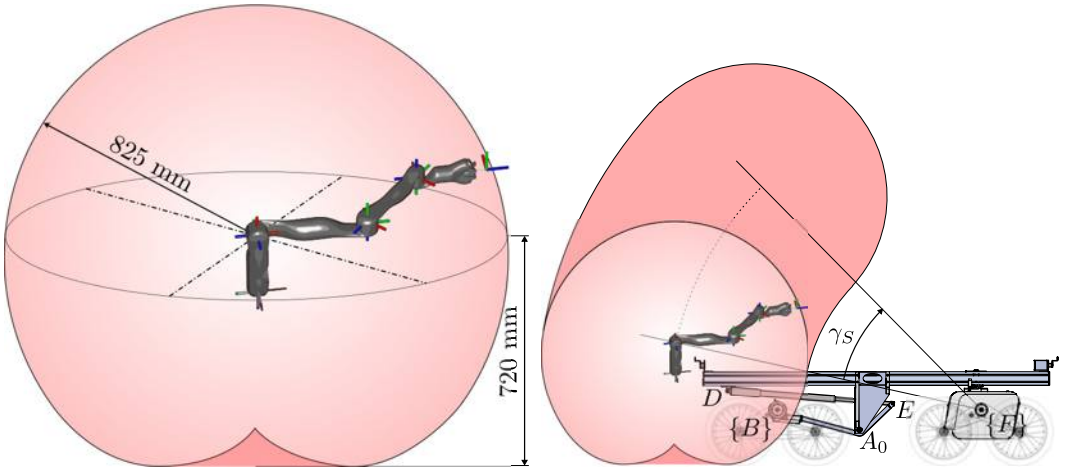

(a) (b)

Fig. 2.26 Jaco2 workspace and the extended workspace when it is mounted on Agri.Q

rear end of the central chassis of Agri.Q, which acts as a mobile platform. Moreover, since the robot arm is fixed to the central chassis, the workspace can be rotated about the front locomotion units axis thanks to the pitch linkage mechanism, as depicted in Figure 2.26b. This allows the robot effective workspace to be expanded to fulfil intended tasks such as collecting samples and interfacing with the top of a vineyard (the highest point of the extended workspace reaches about 2.5 m). Indeed, the robot workspace also allows to perform soil-related tasks, but it also partially covers the PV panels surface, enabling some collaboration with a UAV landed within the workspace.

Figure 2.27 shows Agri.Q interacting with the environment using the extended workspace capability.

(a)

(b)

Fig. 2.27 (a) Agri.Q interacting with an hedge.(b) Agri.Q extending the robot arm workspace to reach the top of a vineyard row

2.5 Electrical and electronic systems design

This section is dedicated to providing an overview of the design of the electrical and electronic systems. Figure 2.28 depicts an overview of the electrical and electronic systems in Agri.Q. In this section particular attention is placed on detailing how the main subsystems work, namely, the whole robot power supply, the drivers of the rover actuators and the embedded control units.

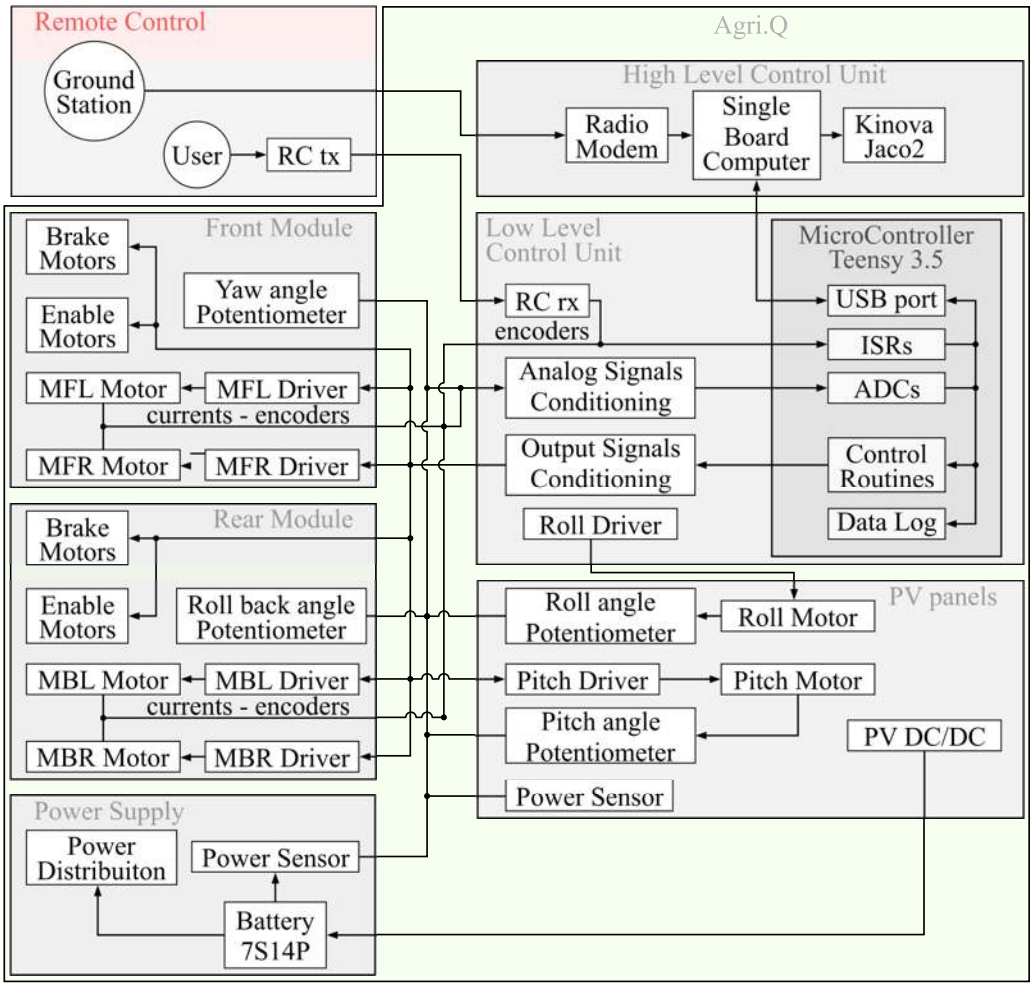

Fig. 2.28 Electrical and electronic systems overview

2.5.1 Power supply

Agri.Q is powered by a lithium ion (Li Ion) battery with cells arranged in 7 series of 16 parallel (7s 16p). The single cell model is Samsung 35E, which main features are a nominal voltage of 3.6 V (with a maximum value of 4.2 V), a maximum continuous discharge current of 8 A, and a nominal capacity of 3.5 A h. Hence, the whole battery features a nominal voltage of 25.2 V (29.4 V when fully charged), a nominal discharge current of 128 A, and a capacity of 56 A h. To complete the battery pack, a BMS (battery management system) is employed to manage the charging and discharging of the battery by balancing the load between the cells and avoiding overcharge or overdischarge of the cells.

The battery can be charged in two different ways that can be selected through a switch on the front module (Figure 2.29). First, a dedicated wall charger can be employed to charge the battery when in close proximity to a power source. Second, by switching the charge mode to solar power, the PV panels DC/DC converters (Genasun GVB-8-Li-28.4 V) are enabled to charge the battery.

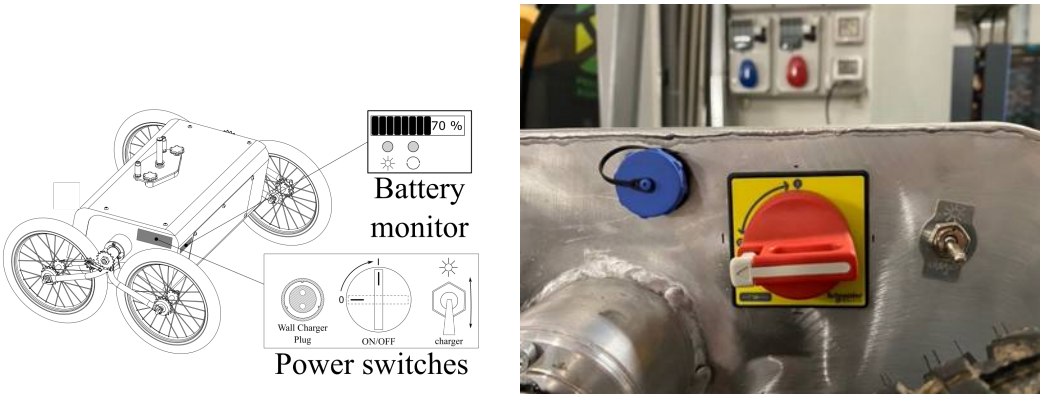

(a) (b)

Fig. 2.29 Detail of Agri.Q battery meter and power switches

In particular, two flexible light-weighted panels (SXp 154Q by Solbian) have been installed to provide an adequate recharging capability without affecting the robot dynamics with an excessive load. Some technical details of a single panel are shown in Figure 2.30. The data refers to a perpendicular solar irradiation of $G_0 = 1000\,\mathrm{W\,m^{-2}}$ at the working temperature of 25° C. Given the panel rated peak power of $W_p = 154\,\mathrm{W}$, the single panel surface $S = 1.0418\,\mathrm{m^2}$, and the reference irradiation G_0, it is possible to estimate the panels efficiency as follows

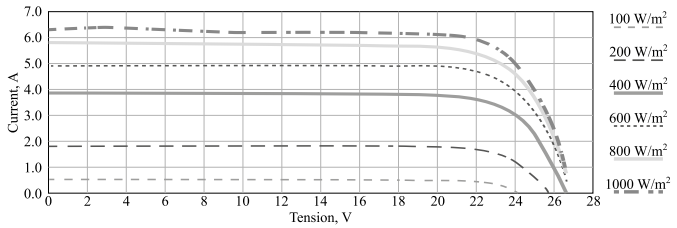

Peak power	$154\,W$	Maximum tension	$18.2\,V$
Dimensions	$1046 \times 996\,mm$	Maximum current	$4.84\,A$
Mass	$2.4\,kg$	Working temperature	$-45/+48°\,C$

Fig. 2.30 Current/voltage characteristic of a single Solbian SXp 154Q PV panel at different levels of Solar incident power and some of its relevant data

$$\eta_p = \frac{2W_p G_0}{2S} = 0.1478 \tag{2.20}$$

then, the panel efficiency enables to evaluate the nominal PV power from the Solar Global Horizontal Irradiance (GHI) data

$$P_{PV,nominal} = S\eta_p \mathrm{GHI} \tag{2.21}$$

Two custom-made power sensors have been placed in series before and after the battery for experimental purposes: by measuring the battery voltage and the charge and discharge currents, and therefore the power required by the rover and the power generated by the PV panels it is possible to evaluate the power balance of the whole robot during its activities (Figure 2.31). In particular, Figure 2.32 shows the designed and assembled partially populated 30×45 mm 2-layer PCB.

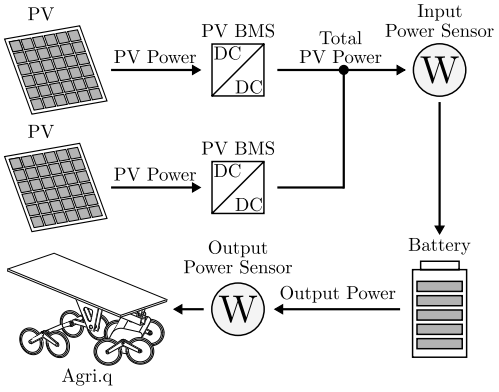

Fig. 2.31 Agri.Q power flows schematic representation

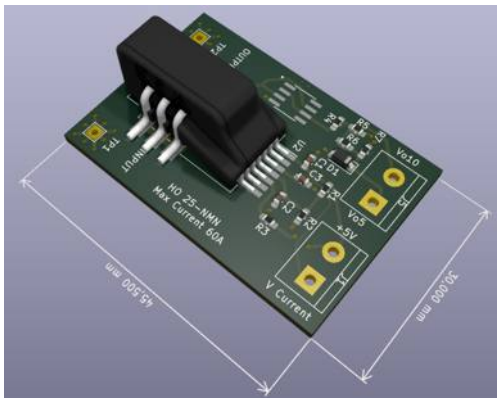

Fig. 2.32 Custom power sensor PCB

Figure 2.33 depicts the electronic layout of the power sensor. It is composed of two subcircuits, one measures the current flowing through the PCB terminals, whereas the other measure the voltage across them. The current sensing circuit was designed around the HO sensor family by LEM. Two different IC models were employed depending on the side of the rover battery where they were mounted. That is, a HO-6P is used to measure the current generated by PV panels (it measures currents between ± 20 A with a resolution of $100\,\mathrm{mV\,A^{-1}}$), whereas a HO-25P (it measures currents between ± 62.5 A with a resolution of $32\,\mathrm{mV\,A^{-1}}$) is employed to measure the current absorbed by the whole robot. In both cases, an analog signal between 0 and 5V and proportional to the measured current is generated and then

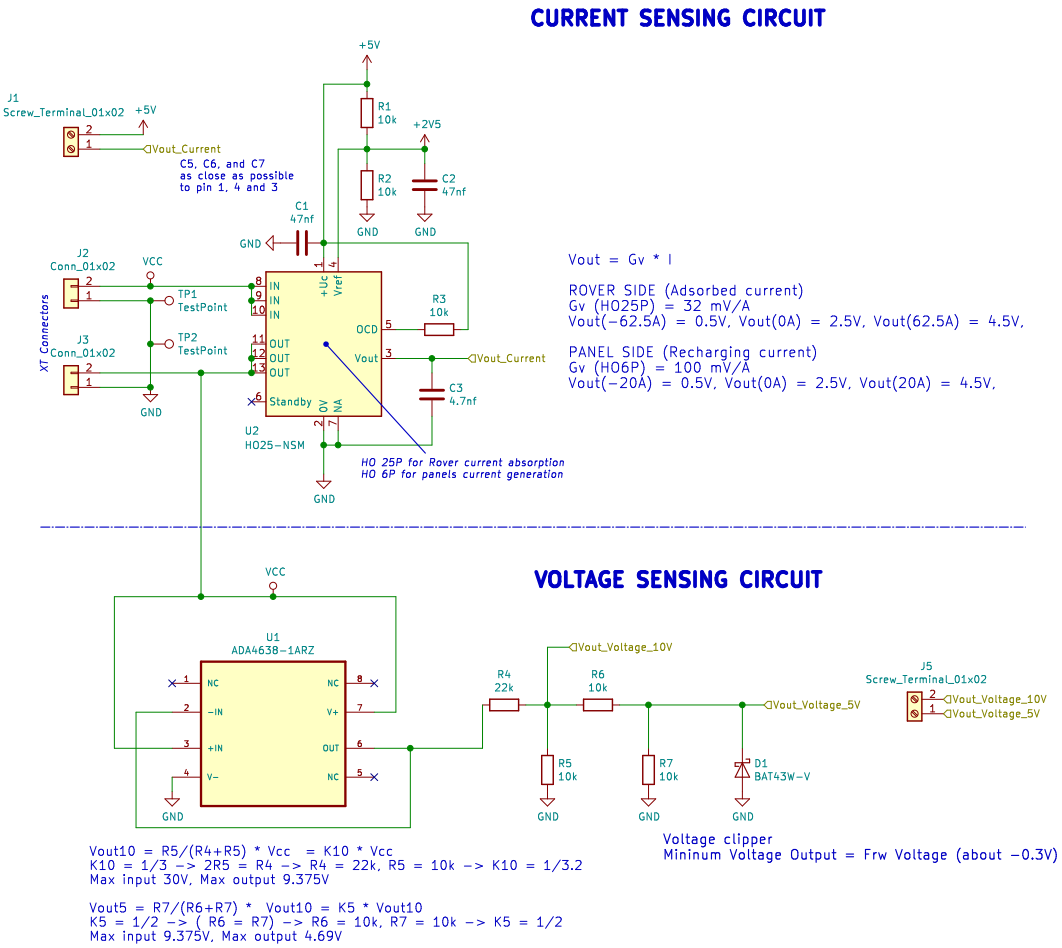

Fig. 2.33 Power sensor electronic layout. The current sensor model change based on the application, i.e., a HO-25P is employed for measuring the current absorbed by the rover, whereas a HO-6P measures the PV panels current

acquired by the control unit ADC. As result, the following relation holds

$$V_{current} = V_{ref} + \frac{G_v}{1000} I_{measured} \tag{2.22}$$

where $V_{current}$ is the analog voltage signal generated by the sensor, $V_{ref} = 2.5\,\text{V}$ is the reference voltage that corresponds to zero current, G_v is the sensor resolution (it depends on the sensor model), and I is the measured current.

Some passive components (i.e., resistors and capacitors) were added following the sensors datasheets to achieve the desired output voltage range and to improve signals quality.

To measure the voltage across the power sensor terminals, first an Op-Amp (a ADA4638) is used as a voltage follower to decouple the input and output signals, then two voltage divider are used to scale down an input voltage in the 0 - 30 V range to the 0 - 10 V and 0 - 5 V ranges. Therefore, the sensor gain is $1/3.2$ and $1/6.4$ respectively. An optional voltage clipper could be added as over-voltage protection. The lower voltage output signal is then acquired by the control unit ADC.

Table 2.5 summarises the main signals related to the power sensors.

Table 2.5 Power sensor raw signals

Name	**Description**	**Measured**	**Voltage signal**
PanelCurrent_RAW	PV panels current	0 - 20 A	2.5 - 5 V
PanelVoltage_RAW	Battery voltage (PV side)	19.6 - 29.4 V	0 - 5 V
PanelVoltage_10V_RAW	Battery voltage (PV side)	19.6 - 29.4 V	0 - 10 V
BatteryCurrent_RAW	Battery current	0 - 60 A	2.5 - 5 V
BatteryVoltage_RAW	Battery voltage	19.6 - 29.4 V	0 - 5 V
BatteryVoltage_10V_RAW	Battery voltage	19.6 - 29.4 V	0 - 10 V

The battery power line goes through the output power sensor, then there are a series of two diodes to slightly lower the maximum voltage[2], a 60 A fuse, a battery monitor, the power switch (Figure 2.29), and a e-stop switch mounted on the back (Figure 2.34). After that, the power is distributed wherever is required. The battery ground is also connected to the robot chassis.

Figure 2.35 represents the complete power supply subsystem. On the left, there are the two power inputs, i.e., the PV panels and the wall charger, and their auxiliary elements. In the centre, there is the robot battery with a power sensor on each side to measure the power flow as described before. To complete the system, the power line (+BATT and GND) is distributed in the robot after a series of diodes, switches, and emergency stop buttons.

[2]When the battery is fully charged generates a voltage of 29.4 V. At this voltage, the traction motor drivers turn off to avoid over-voltage issues. Hence, as a temporary fix, the diodes are used to drop the battery voltage by 1.4 V. This solves the over-voltage issue, but the solution is very inefficient.

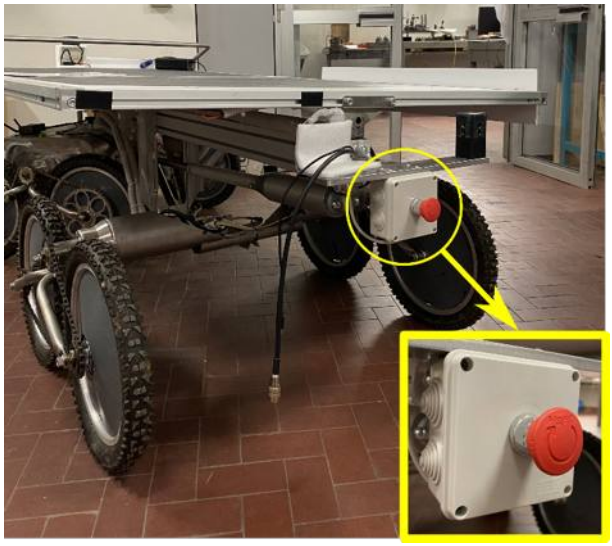

Fig. 2.34 Agri.Q E-Stop button mounted on the back of the central chassis

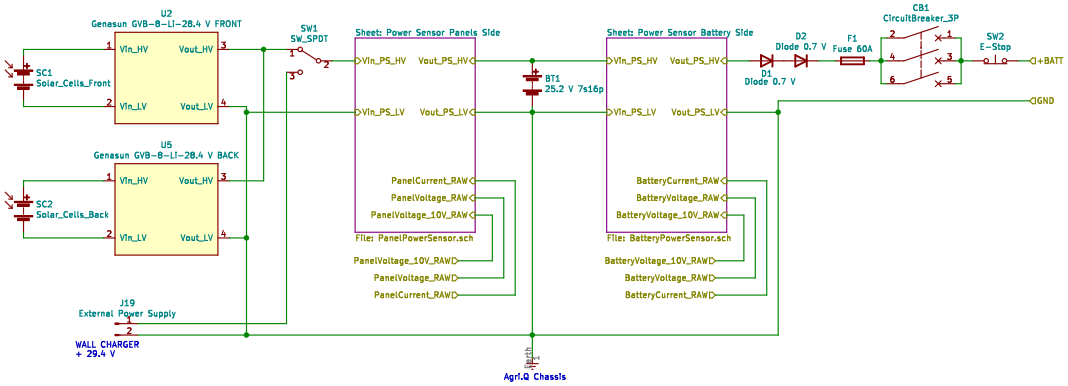

Fig. 2.35 Agri.Q power supply subsystem layout

2.5.2 Wired remote controller and switching relays

Before going into other details about the robot electronic layout, it is important to describe the wired remote controller and the switching relays to better understand some parts of the layout. Initially, it was possible to use a wired remote controller to drive the actuators as an alternative to the wireless controller. Therefore, a series of relays is still present to act as selectors between the two controllers, i.e., when the wired controller was plugged, the control signals generated by the control unit were neglected and, on the contrary, when the wired controller was unplugged, the control unit was able to drive the robot (the control unit is described in a following section).

In the present iteration of Agri.Q, the wired controller is obsolete, but the relays are still present even if they are not needed anymore.

In particular, the wired remote controller was an electrical box with some potentiometers and switches to generate the required analog and digital signals (Figure 2.36). The top diagram in Figure 2.37 depicts how the wired remote controller worked. Three potentiometers were used to generate the reference of the traction motors. More specifically, the potentiometers defined the angular speeds of the front left and front right motors and the torques of the rear ones (the same reference to both motors). A number of switches were employed to engage or disengage the robot brakes and to enable and disable the front and rear traction motors. To conclude the user inputs, two switches were dedicated to drive the PV panels pitch and roll motions. The wired remote also mounted an additional emergency stop button that acted identical to the one mounted on the back of the robot. The wired remote interfaced with the robot through a 25 pin serial port whose signals are shown in the bottom diagram in Figure 2.37. The remote is directly powered by the robot battery, but the dual supply across the potentiometers ($\pm$9.8V) was provided by the respective traction motor drivers. As said before, the remote generated references for motors and brakes and a signal called *CmdRELAY* that was responsible for driving the switching relays to enable the robot wired control.

Fig. 2.36 Wired remote controller

Figure 2.38 illustrates the switching relays layout. As anticipated, the *CmdRELAY* signal, when set to a high voltage, was used to drive the robot by employing the wired remote signals. On the contrary, when *CmdRELAY* is low (i.e., when the wired remote is not plugged), the onboard control unit is used. The switching relays are composed of 3 main relays (HJ4-DC24V) whose function is to select between the

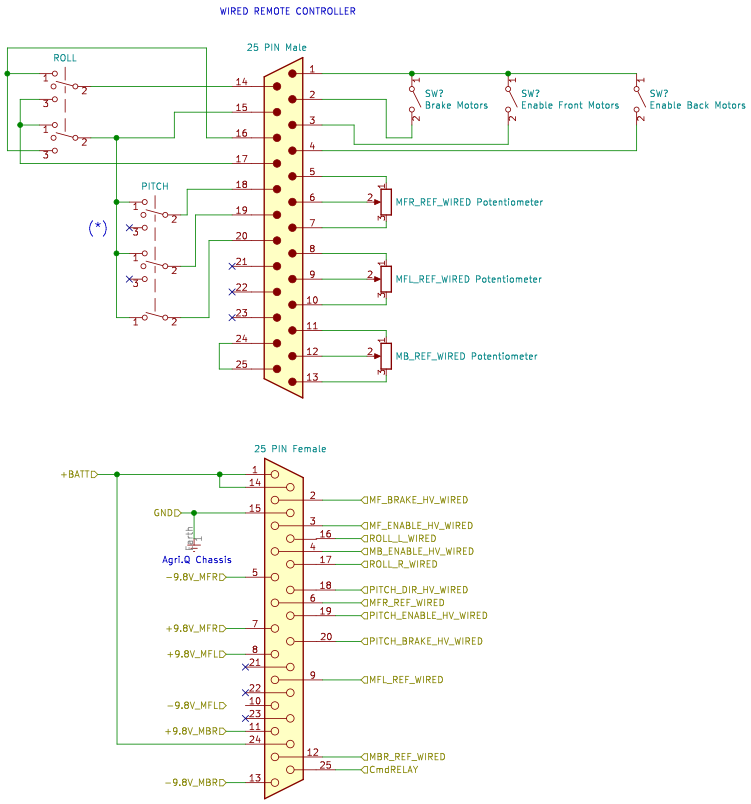

Fig. 2.37 Wired remote controller layout. The top diagram shows the remote elements, and the bottom diagrams depicts the exchanged signals between the robot and the remote

two alternate control modes generating reference signals for pitch, roll, and traction motors. One of the relays also drives a secondary relay to generate a high current signal required to engage or disengage the robot brakes. Thus, a low current signal from one of the controller is employed to switch this relay to directly connect the battery to the brakes when they must be disengaged.

Although the wired remote is now obsolete since the control unit can be controlled by a wireless remote controller and because all traction motors require a torque reference value, the relays layout is still present, but it could be replaced or even removed in future Agri.Q revisions.

2.5.3 Control unit

Inside the front module, there is the robot control unit. It consists of two main controller units that are referred to as high and low level control units. The boundary

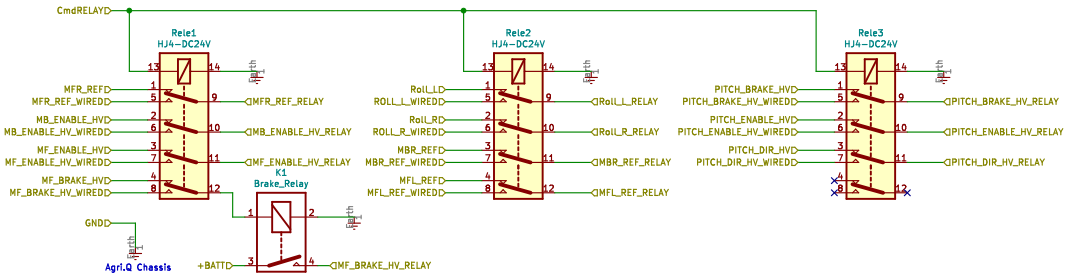

Fig. 2.38 Switching relays layout

between them is not strictly defined, however, in the following the low level control unit is the electronic subsystem mainly dedicated to interfacing with the hardware such as actuators and sensors. On the contrary, the high level controller focuses on managing the low level and complex sensors and actuators, like the robot arm. Up to this time, the system design has heavily focused on the development of the low level control unit in terms of hardware and software. The high level control unit is still in a test and integration phase, but it is planned to be the foundation of the development of the autonomous features.

High level control unit

The core of the high level control unit is the single board computer (SBC). In particular, it is an AmITX-SL-G SBC by Adlink with the Mini-ITX form factor. It features a 6th generation i7 Intel core, three display ports, two gigabit Ethernet ports, USB ports, and SATA 6 Gb/s ports. Expansion is provided by one PCIe x16, one PCIe x1, and two mini-PCIe slots. The onboard feature connector provides GPIO, SMBus, and I2C support. The computer can be accessed and controlled remotely thanks to a radio modem (pMDDL2450 by Microhard) that establish a connection with the ground station. It is also connected to the low level control unit micro-controller ($\mu-$controller in short) through a serial port (a USB port). At the moment this connection is used to program the $\mu-$controller remotely, but also to log and store any data coming from the low level unit. In the future, this communication channel will be exploited to properly integrate features like autonomous navigation. Furthermore, the SBC is also the brain behind the Kinova Jaco2 robot arm and other sensors that are going to be implemented, such as LIDAR and cameras among the others. To manage this complex architecture, it is planned to implement a ROS framework. This last step will be crucial to develop an autonomous robot.

Low level control unit

The low level control unit is responsible for collecting robot sensors data and for generating proper commands to manage the system. This subsystem is highly related to its robotic platform, therefore a custom 2-layer PCB has been developed and implemented to achieve the desired functionalities. The board design was quite straightforward and consisted mostly of integrating a $\mu-$controller, designing input and output signals conditioning circuits, adapting the component suppliers' application notes and properly routing the signals to reduce any issue related to EM noise.

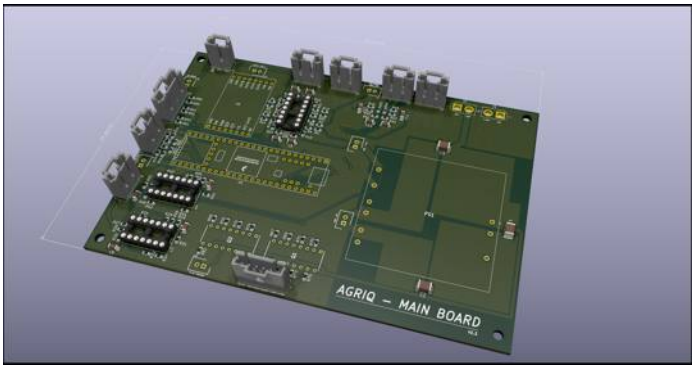

(a)

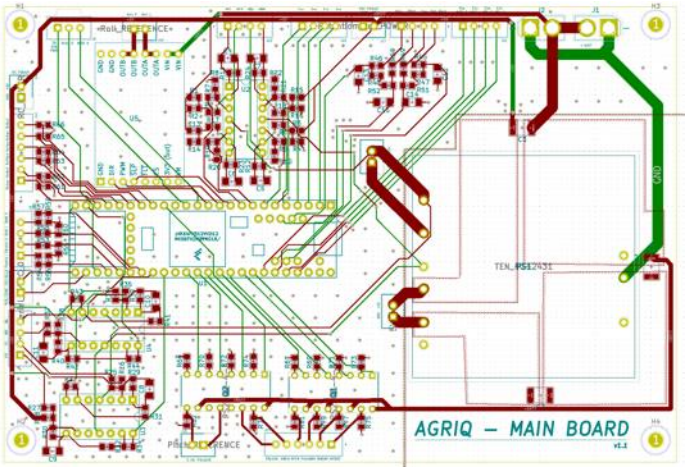

(b)

Fig. 2.39 (a) Partially populated render of the low level control unit PCB. (b) PCB tracing. The red traces are in the top layer, the green traces are in the bottom one

As shown in Figure 2.39a, the PCB use SMD passive components, whereas connectors and the more sensitive elements are through-hole devices. Whenever possible

the design has followed the principle of easy substitution of faulty components, thus DIP sockets are directly assembled on the PCB to quickly replace a part. The final PCB has a size of $154 \times 104 \times 1.6$ mm, it has been manufactured by Aisler as a standard 2-layer PCB. Figure 2.39b shows the PCB tracing. In red there are the top layer traces, while the green ones are on the bottom one. To better clarity, copper pours are not shown, but both copper layers are filled with the ground reference plane (several vias connect them). In the bottom right corner there are specific copper pour dedicated to the power supply based on the DC converter application note to reduce EM noise. The PCB manufacturer also assembled the SMD components, while all other elements were soldered by hand.

In the following sections, the main subcircuits featured in the low level control unit are presented.

Remote controller

A user can directly send some signals to the low level $\mu-$controller by means of an RC transmitter. In particular, the Spektrum DX9 sends 6 of its 9 channels to a receiver placed in the front module of Agri.Q. Figure 2.40a depicts the RC controller and the 6 channels. The left 2-axes joystick (Joystick 1) generates two analog reference for the pitch (up-down axis, signal ξ) and roll (left-right axis, signal χ) motions. Similarly the right 2-axes joystick (Joystick 2) manage the longitudinal (up-down axis, signal λ) and lateral (left-right axis, signal ν) behaviour of the robot. Then, there are two 3-state switches (Sw1 on the right, Sw2 on the left) that can produce two discrete signals with 3 distinct values each. Sw1 is employed to manage the brake state (engaged or disengaged), but also to activate a programmable state. Sw2, instead, can selectively enable the front traction motors, all traction motors, or turn them off. More details on the input management are given in a dedicated section more focused on the control features.

Moving back to the electronic design, the radio receiver generates for each channel a PWM signal whose on-state duration represents the signal value. Consequently, the $\mu-$controller needs 6 dedicated hardware interrupt ports to deploy 6 corresponding interrupt service routines (ISRs) in order to measure the PWM signal duty cycle (Figure 2.40b). This means that when one of the signals passes a threshold value, it triggers a high priority routine that computes the time elapsed between a rising edge and a falling edge.

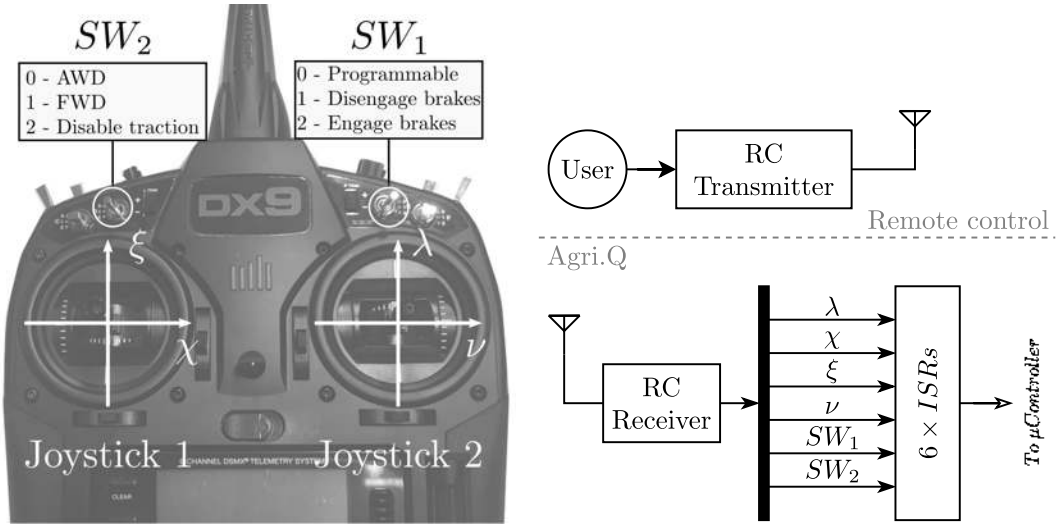

(a) (b)

Fig. 2.40 (a) 6 channels remote controller: ξ, χ, λ, and ν are continuos axes, SW_1 and SW_2 are discrete channels. (b) Remote controller working principle

To reduce the PWM signals sensitivity to noise, a pulldown resistor is added to each line before the $\mu-$controller interrupt ports (FIGURE 2.41). Moreover, since signal timing is critical to properly measure the on-state duration, the proposed layout does not implement any filtering circuits to avoid any potential signal distortion. If some sort of filter is required, it can be implemented digitally.

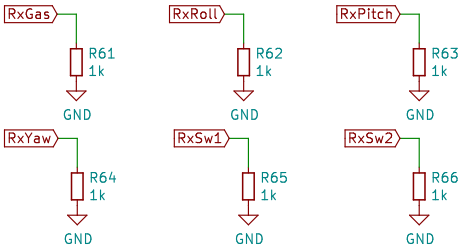

Fig. 2.41 Receiver pulldown layout. *RxGas*, *RxRoll*, *RxPitch*, and *RxYaw* are the PWM signals associated to λ, χ, ξ, and ν, respectively

PCB power supply

The Power Supply group is responsible for accepting power from the battery and delivering all power signals required for the functioning of the devices on the PCB. This is performed using the Ten40-2431 commercial DC-DC converter by Traco

Table 2.6 Traco Power Ten40-2431 main specifications

Descripiton	**Value**
Input voltage	18 - 36 V
Output 1	5 V / 6.0 A
Output 2	+12 V / 0.4 A
Output 3	-12 V / 0.4 A
Power	40 W
Efficiency	87%

Power whose specifications are shown in Table 2.6. Figure 2.42 represents the sub-circuit layout. The three capacitors C1, C2 and C3 were sized for filtering reasons but also to comply with the norm EN 55032 about conducted and radiated emissions, accordingly to a manufacturer application note. Similarly, the subsystem layout in the PCB and the power signals copper pours followed the same directions.

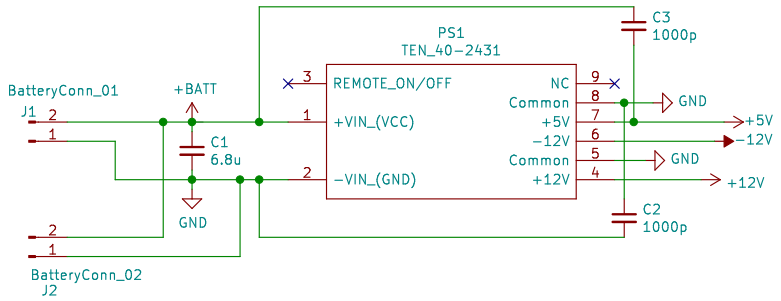

Fig. 2.42 PCB power supply

The DC-DC converter is directly powered by the robot battery, which is also responsible for powering the roll motor driver that is mounted on the PCB. The dual $\pm$12V power line is needed to supply the OP-Amps employed for signals conditioning, whereas the 5 V power line is used to power the angular sensors (potentiometers), the power sensors, and the remote controller receiver. For both lines, some power connectors are available to power up any new external device. Although the $\mu-$controller could be powered by the 5 V line, it is instead powered by the USB connection with the SBC that is required to share data between them. This solution was mainly due to avoiding altering a dedicated $\mu-$controller trace.

PCB connectors

The low level control unit PCB connects to the robot by means of a number of connectors. Such connectors can be divided into 3 main groups, as shown in Figure 2.43: input, output, and power signals. Moreover, both input and output signals can be also categorised as analog and digital signals. During the design of the PCB and the tracing of its connections, care has been taken in physically separating as much as possible the two types of signal.

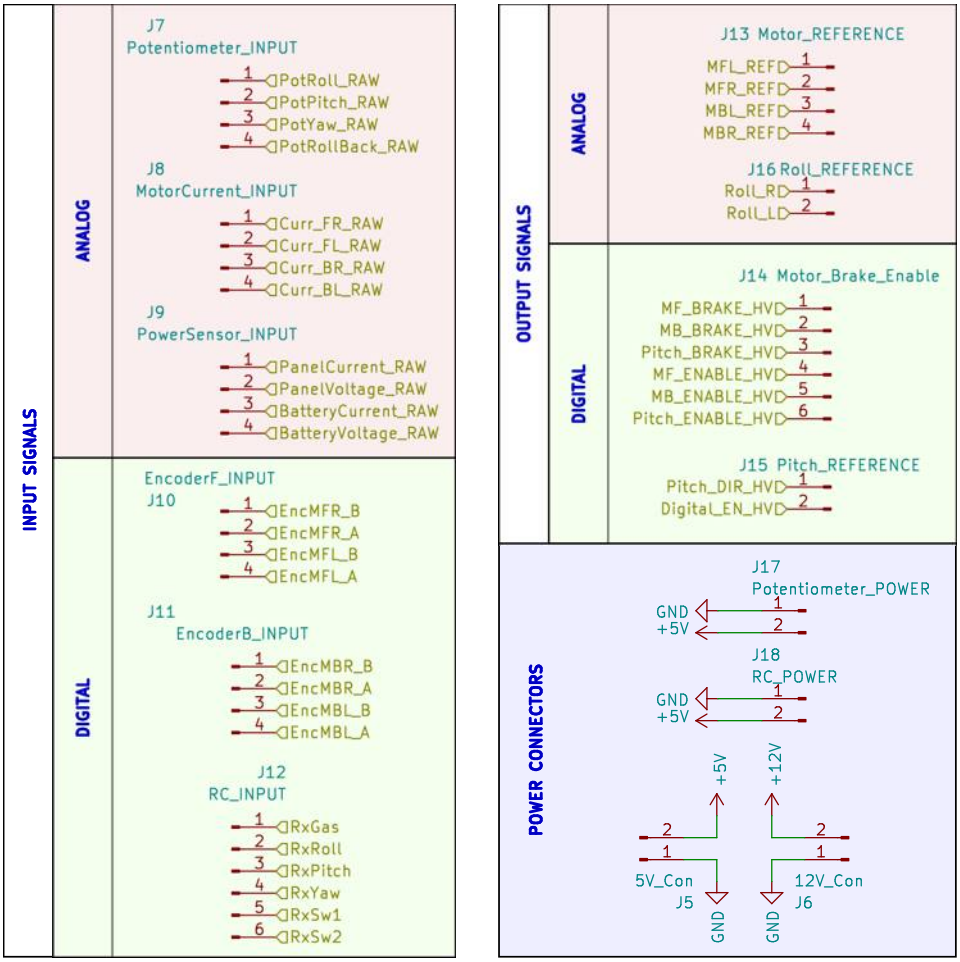

Fig. 2.43 PCB connectors divided by function and type

In the following tables are summarised all signals passing through the PCB connectors. In particular, Table 2.7 collects the analog input signals, Table 2.8 the digital input signals, Table 2.9 the analog output signals, Table 2.10 the digital output signals, and Table 2.11 the power lines.

Table 2.7 Analog Input Signals

Connector	**Signal**	**Description**	**Value**
J7 Potentiometer input	*PotRoll_RAW*	Roll angle α_{Panel} potentiometer	0 - 5 V
	PotPitch_RAW	Pitch angle γ potentiometer	0 - 5 V
	PotYaw_RAW	Relative yaw angle δ potentiometer	0 - 5 V
	PotRollBack_RAW	Rear module roll angle α_B potentiometer	0 - 5 V
J8 Traction motor currents	*Curr_FR_RAW*	Front right traction motor absorbed current I_{MFR} (gain 2.5 A V^{-1})	$\pm$8 V
	Curr_FL_RAW	Front left traction motor absorbed current I_{MFL} (gain 2.5 A V^{-1})	$\pm$8 V
	Curr_BR_RAW	Rear right traction motor absorbed current I_{MBR} (gain 2.5 A V^{-1})	$\pm$8 V
	Curr_BL_RAW	Rear left traction motor absorbed current I_{MBL} (gain 2.5 A V^{-1})	$\pm$8 V
J9 Power sensors	*PanelCurrent_RAW*	PV panels current I_{PV}	0 - 5 V
	PanelVoltage_RAW	Battery Voltage (PV side)	0 - 5 V
	BatteryCurrent_RAW	Robot adsorbed current	0 - 5 V
	BatteryVoltage_RAW	Battery Voltage	0 - 5 V

Table 2.8 Digital Input Signals

Connector	Signal	Description	Value
J10 Front traction motor encoders	*EncMFR_B*	Front right traction motor encoder channel B	0-5 V
	EncMFR_A	Front right traction motor encoder channel A	0-5 V
	EncMFL_B	Front left traction motor encoder channel B	0-5 V
	EncMFL_A	Front left traction motor encoder channel A	0-5 V
J11 rear traction motor encoders	*EncMBR_B*	Rear right traction motor encoder channel B	0-5 V
	EncMBR_A	Rear right traction motor encoder channel A	0-5 V
	EncMBL_B	Rear left traction motor encoder channel B	0-5 V
	EncMBL_A	Rear left traction motor encoder channel A	0-5 V
J12 Remote controller receiver	*RxGas*	Agri.Q longitudinal motion PWM signal λ	0-5 V
	RxRoll	PV panels roll motion PWM signal χ	0-5 V
	RxPitch	PV panels pitch motion PWM signal ξ	0-5 V
	RxYaw	Agri.Q lateral motion PWM signal ν	0-5 V
	*RxSw*1	Agri.Q state switch PWM signal SW_1	0-5 V
	*RxSw*2	Agri.Q state switch PWM signal SW_2	0-5 V

Table 2.9 Analog Output Signals

Connector	Signal	Description	Value
J13 Traction motor references	*MFL_REF*	Front left traction motor torque reference voltage $V^T_{MFL,ref}$	$\pm 10\,\mathrm{V}$
	MFR_REF	Front right traction motor torque reference voltage $V^T_{MFR,ref}$	$\pm 10\,\mathrm{V}$
	MBL_REF	Rear left traction motor torque reference voltage $V^T_{MBL,ref}$	$\pm 10\,\mathrm{V}$
	MBR_REF	Rear right traction motor torque reference voltage $V^T_{MBR,ref}$	$\pm 10\,\mathrm{V}$
J16 Roll motor references	*Roll_R*	PV panels roll motor supply, terminal R	$0\,\mathrm{V}$ - $+BATT$
	Roll_L	PV panels roll motor supply, terminal L	$0\,\mathrm{V}$ - $+BATT$

Table 2.10 Digital Output Signals

Connector	Signal	Description	Value
J14 Motors Brake and Enable	*MF_BRAKE_HV*	Front traction motors parking brake	$0\,\mathrm{V}$ - $+BATT$
	MB_BRAKE_HV	Rear traction motors parking brake	$0\,\mathrm{V}$ - $+BATT$
	Pitch_BRAKE_HV	PV panels pitch motor parking brake	$0\,\mathrm{V}$ - $+BATT$
	MF_ENABLE_HV	Front traction motors enable	$0\,\mathrm{V}$ - $+BATT$
	MB_ENABLE_HV	Rear traction motors enable	$0\,\mathrm{V}$ - $+BATT$
	Pitch_ENABLE_HV	PV panels pitch motor enable	$0\,\mathrm{V}$ - *Open circuit*
J15 Pitch reference	*Pitch_DIR_HV*	PV panels pitch motor direction signal	$0\,\mathrm{V}$ - *Open circuit*
	Digital_EN_HV	High voltage digital signal. Not used	$0\,\mathrm{V}$ - $+BATT$

Table 2.11 Power connectors

Connector	Signal	Description	Value
J17 Potentiometer power	+5 V	Potentiometers supply voltage	5 V
	GND	Potentiometers reference ground	0 V
J18 Remote controller receiver power	+5 V	Receiver supply voltage	5 V
	GND	Receiver reference ground	0 V
J5 General purpose 5 V	+5 V	supply voltage	5 V
	GND	Reference ground	0 V
J6 General purpose 12 V	+12 V	supply voltage	12 V
	GND	Reference ground	0 V

Input signals conditioning

Most of the input signals require some form of conditioning to be properly acquired by the $\mu-$controller ADC or its digital inputs ports. This generally means that analog input signals have to be scaled down to the 0-3.3 V voltage range and eventually filtered, whereas the digital have to be scaled down to a 0-3.3 V or 0-5 V logic voltages and sometimes need some auxiliary circuits to stabilize the logic levels against noise.

For instance, as described in 2.5.3, the 6 PWM signals generated by the remote receiver are simply stabilized with a pulldown resistor each to reduce sensitivity to noise, while the signal voltage ranges remain unaltered as they are already 0-5 V signals. Also, the 8 traction motor encoder signals remain unchanged since they are in a proper voltage range. Moreover, the $\mu-$controller internal pullup resistors proved to be enough to acquire clear logic levels, thus, no auxiliary circuits are required. As for the PWM signals, the encoder signals must be acquired by the $\mu-$controller hardware interrupt ports to achieve the best results. Such interrupts drive dedicated ISRs to decode direction and magnitude of the motors angular speed based on the states of the encoder channels. For all these digital signals that require an ISR to measure a quantity is crucial that the pullup or pulldown circuits work

properly to avoid any noise triggering the ISR and drastically affecting the final measure.

Agri.Q α_{Panel}, γ, δ, and α_B angles must be measured with an absolute angular sensors. As a means to achieve that, a potentiometer for each angle has been mounted in measuring the rotations about the highlighted axes shown in Figure 2.44a. Whereas α_{Panel}, δ, and α_B are directly measured, the angle γ is computed from the measure of the angle β of the linkage mechanism previously described in 2.3.2 with a linearized version of Eq.(2.13). As hinted before, the 4 potentiometers are supplied by the DC-DC 5 V line, therefore, each sensor outputs a raw analog signal between 0 and 5 V proportional to the measured rotation (Figure 2.44b).

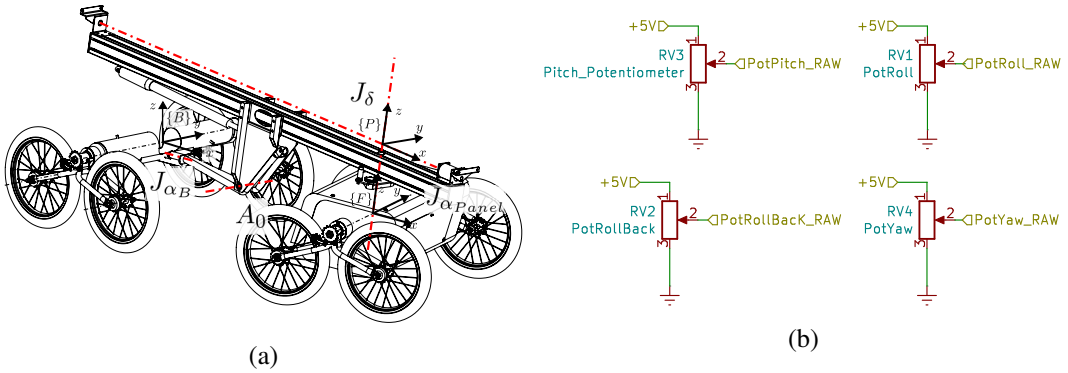

(a) (b)

Fig. 2.44 (a) Agri.Q absolute angular sensors axes. Note that the PV panels pitch angle γ is not directly measured, but the angle β is measured and used to derive γ. (b) Absolute angular sensors circuit

The $\mu-$controller ADC accepts voltages in the 0-3.3 V range. Hence the potentiometers signal is lowered by means of a voltage divider with a gain of $2/3$, as illustrated in Figure 2.45. The figure also shows that the conditioning circuits present a RC circuit that acts as a low pass filter with a cut-off frequency of about 48.2 Hz [3].

Traction motor drivers provide tensions proportional to the adsorbed currents. The motor current $I_{M\sim\sim}$ is therefore related to the sensor voltage $Curr\_\sim\sim\_RAW$ by a proportional gain of $2.5\,\mathrm{A\,V^{-1}}$. This means that, given a motor current that can oscillate between $\pm$20A, $Curr\_\sim\sim\_RAW$ can span within $\pm$8V. Thus, a linear transformation must be applied to shift the voltage range to 0-3.3 V. In practice, as shown in Figure 2.46, a cascade of two inverting OP-amp is used to achieve the

[3] For example, for the roll potentiometers holds $f_0 = \frac{1}{2\pi\tau} = \frac{1}{2\pi R46C13} = 48.2\,\mathrm{Hz}$. Similar relations are valid for the other angles.

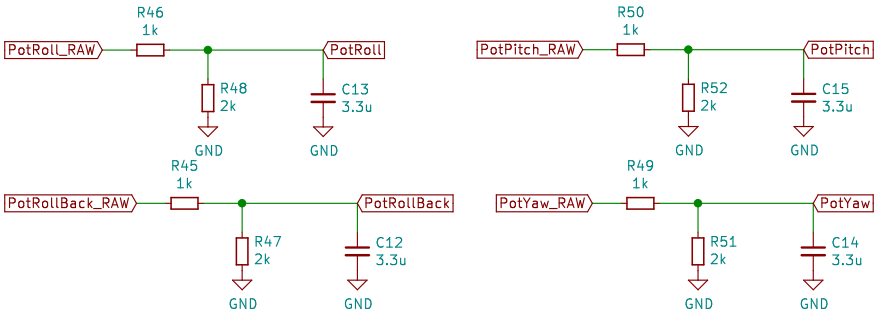

Fig. 2.45 Potentiometers conditioning circuits

results while also filtering the signal. The first OP-amp is needed to scale the voltage, whereas the second is a simple inverting voltage follower to get an always positive output.

To obtain the desired output voltage, the conditioning circuit must produce the following linear relation

$$V_{out} = mV_{in} + b = \frac{V_{out,max} - V_{out,min}}{V_{in,max} - V_{in,min}} V_{in} + (V_{out,min} - mV_{in,min}) \tag{2.23}$$

where $m = -0.206$ and $b = -1.648\,\mathrm{V}$. Considering that the second OP-amp is responsible of changing the signal sign, it is possible to design the first stage aiming for an output voltage of -3.3 - $0\,\mathrm{V}$. By arbitrarily choosing the feedback resistor $R29$ value as $100\,\mathrm{k\Omega}$ and the reference voltage V_{ref} value as $5\,\mathrm{V}$, the remaining resistors are defined as

$$R25 = \frac{R29}{||m||} = 485\,\mathrm{k\Omega} \xrightarrow{\text{Standard value}} 470\,\mathrm{k\Omega} \tag{2.24}$$

and

$$R26 = V_{ref}\frac{R29}{||b||} = 303\,\mathrm{k\Omega} \xrightarrow{\text{Standard value}} 300\,\mathrm{k\Omega} \tag{2.25}$$

The first stage design concludes by adding a $0.033\,\mu\mathrm{F}$ capacitor in parallel to the feedback resistor to obtain an active low pass filter with a cut-off frequency of $f_0 = (2\pi R29C8)^{-1} = 48.2\,\mathrm{Hz}$.

The second stage resistors are chosen arbitrarily with the only constraint of being equal. The same design was repeated for all $Curr\_ \sim\sim \_RAW$ signals.

Two common LM324 by Texas Instrument have been used to implement such an architecture since a single IC contains four OP-amps. Thus each LM324 can handle two motor current signals.

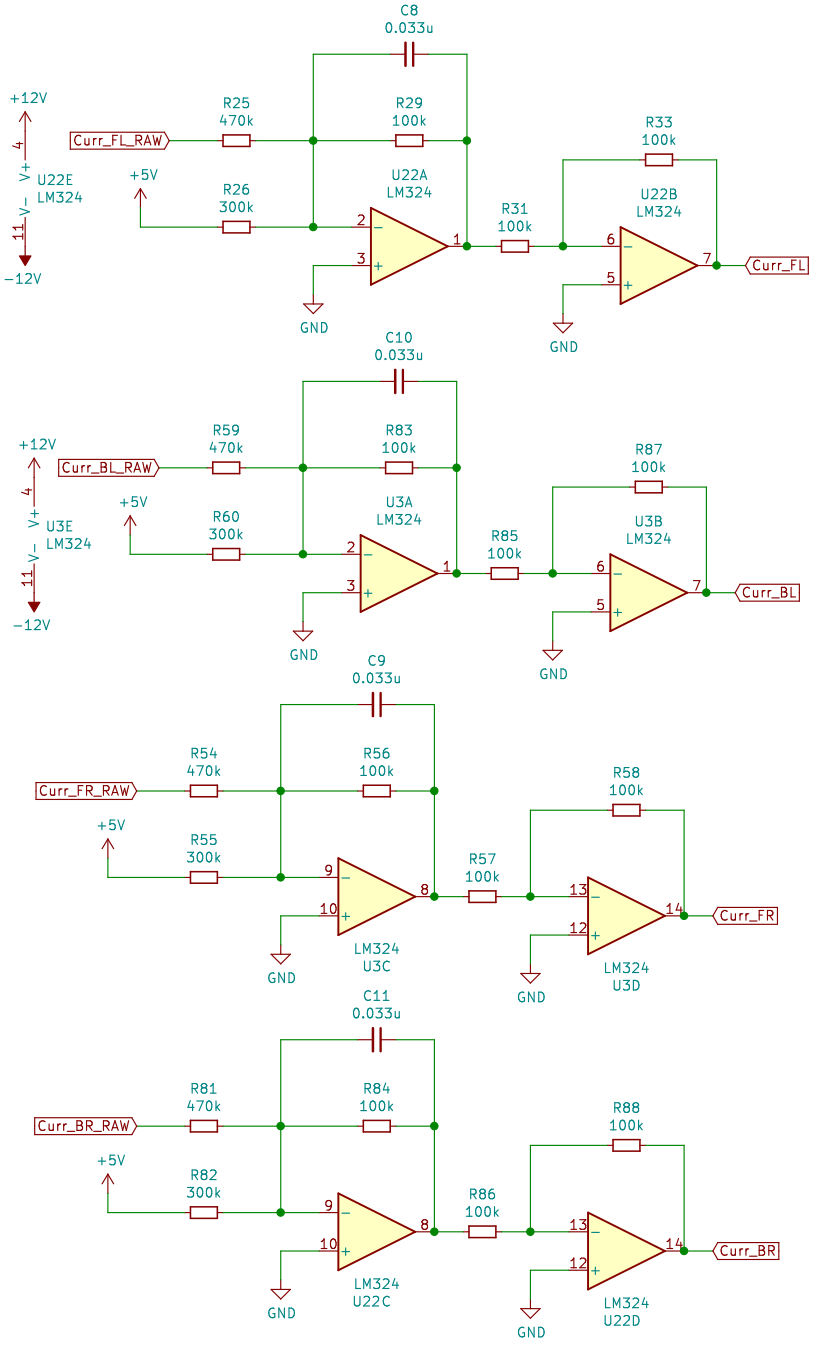

Fig. 2.46 Traction motor current signals conditioning circuit

The last acquired analog signals are the voltage and current signals from the two custom power sensors. They are partially conditioned by the design of the power sensor, but an additional voltage divider for each signal is used to scale down by $2/3$ the signals from the sensors (Figure 2.47). It has been chosen to not implement an analog filter but a digital one within the $\mu-$controller algorithm.

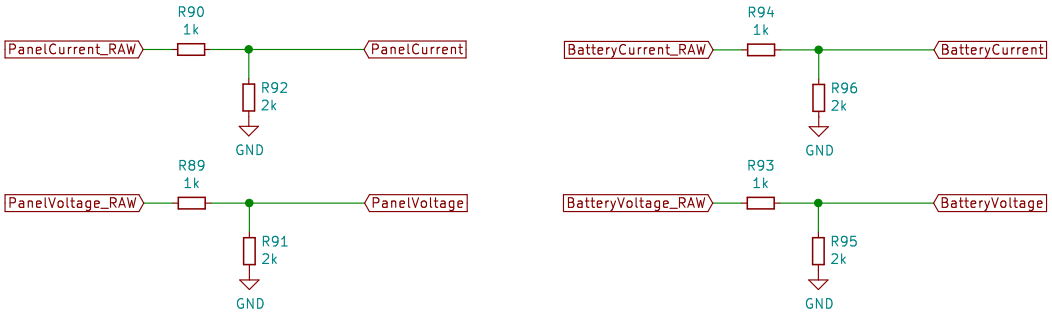

Fig. 2.47 Power sensors signals conditioning circuit

Micro-controller

To control and manage the low level control unit, a Teensy 3.5 powerful and compact development board designed by PJRC was chosen. Teensy 3.5 features the following specifications

- ARM Cortex-M4 at 120 MHz
- Float point math unit, 32 bits only
- 512K Flash, 256K RAM, 4K EEPROM
- 64 digital input/output pins, 20 PWM output pins. All digital pins are 5 V tolerant and have interrupt capability
- 27 analog input pins, 2 analog output pins
- USB port, 12 Mbit/sec
- 6 serial, 3 SPI, 3 I2C ports
- 2 CAN bus
- 1 SDIO (4 bit) native SD Card port

- 16 general purpose DMA channels

Figure 2.48 represents all $\mu-$controller connections. Teensy pins can be programmed to achieve various functions, thus, the signal-to-pin allocation process has been an iterative process to use the proper pins but also to use pins in convenient locations considering the PCB design and the signal tracing.

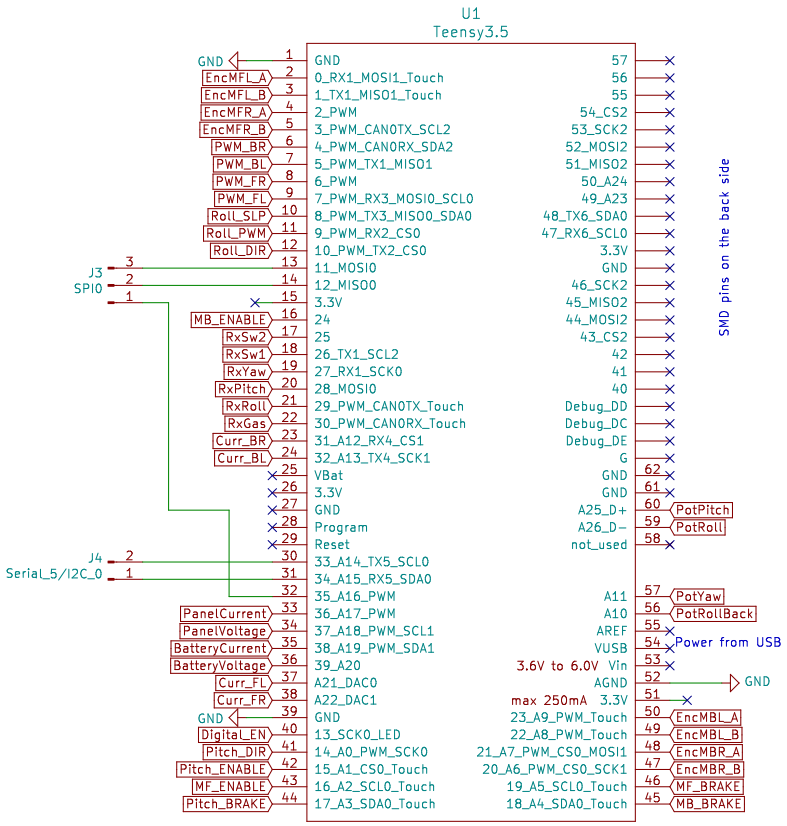

Fig. 2.48 Teensy 3.5 micro-controller layout

The $\mu-$controller also presents two connectors for future functionalities. Connector J3 allows establishing an SPI bus exposing the MISO and MOSI data lines together with a CS signal. If a single SPI peripheral is added, this architecture can work as it is, otherwise, a multiplexer is required because there is a single CS signal. J4 connector, instead, can be programmed to act as an additional serial interface or as an I2C bus. In the latter case, it could be useful to add a pullup resistor to each signal line to improve signal quality, especially if the bus line is particularly long.

As said before, the board is directly powered through its USB connector, which also acts as a serial communication interface, by the SBC. The board could be

powered by its supply pins, but to avoid supply issues with the USB port a trace should be cut.

Output signals conditioning

The $\mu-$controller capability of generating analog signal is limited, therefore it is more convenient to generate PWM signals with an amplitude of 3.3 V at 488.28 Hz and then manipulate them with a dedicated conditioning analog circuit. For example, traction motor drivers require as a reference torque signal an analog voltage $V^T_{M\sim\sim,ref}$ in the range of ∓ 10 V (a negative voltage generates a positive torque and vice-versa). Therefore, the conditioning circuit in Figure 2.49 has been designed to apply a linear transformation from 0 - 3.3 V to ± 10 V. To simplify the circuit, the sign inversion to control torque direction is handled in the $\mu-$controller software, thus, a desired max positive torque generates a 0 V signal that then becomes a -10 V, whereas a desired negative torque at maximum magnitude produces a 3.3 V signal that corresponds to 10 V.

Taking as an example the front left motor reference conditioning circuit, the input-output relation of the proposed architecture is

$$V^T_{MFL,ref} = \left(1 + \frac{R11}{R5 + R1||R2}\right)\frac{R8}{R7+R8} PWM\_FL - \frac{R11}{R5+R1||R2}\frac{R2}{R1+R2}\,5\,\text{V} \tag{2.26}$$

and the desired characteristic is

$$V^T_{MFL,ref} = m PWM\_FL + b \tag{2.27}$$

where

$$m = \frac{V_{out,max} - V_{out,min}}{V_{in,max} - V_{in,min}} = 6.06 \tag{2.28}$$

and

$$b = V_{out,min} - m V_{in,min} = -10\,\text{V} \tag{2.29}$$

The resistor were designed by following an iterative process and by assuming some arbitrary values. The design is the same for all four conditioning circuits. As for the other OP-amp based conditioning a LM324 by Texas Instrument have been used. A single IC is enough for all traction motors.

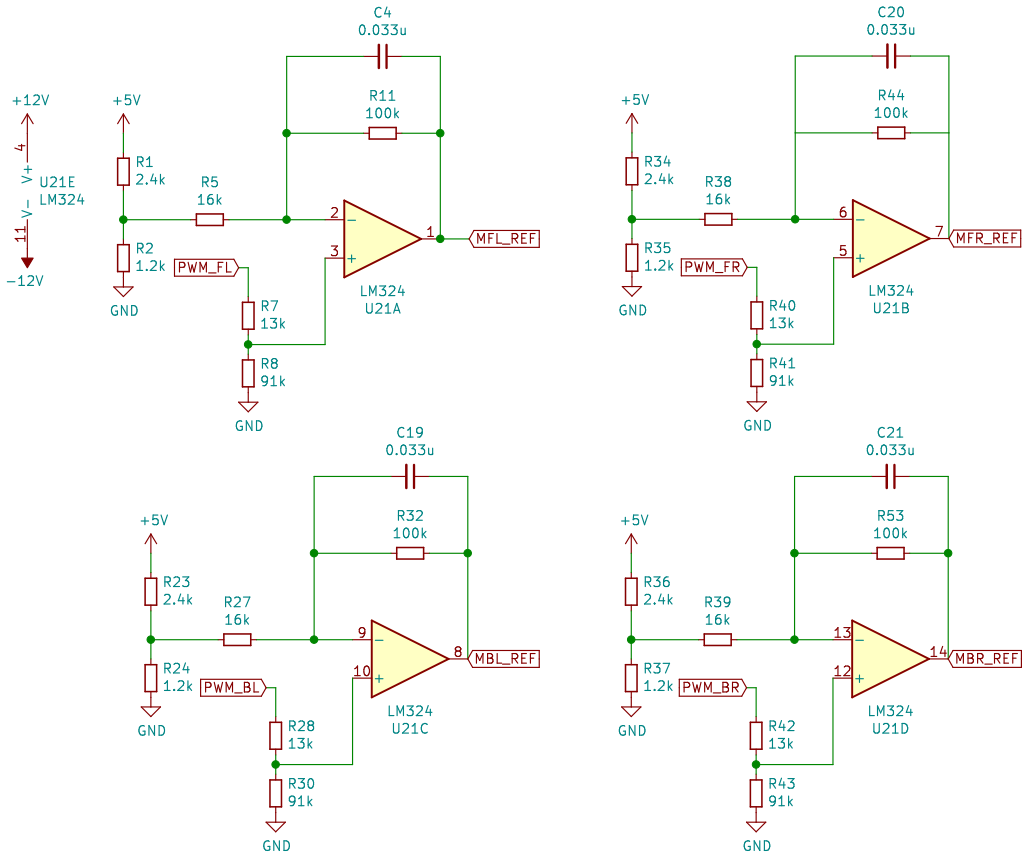

Fig. 2.49 Traction motor reference signals conditioning circuit

Choosing the filter requires a trade-off between reaction speed and eliminating the PWM frequency. The lower the filter corner frequency, the more constant the output becomes, but the slower it reacts to changes. A more advanced filter may give a quicker response and cleaner output, but at the expense of additional components and complexity. In the end, the capacitor C4 was sized to obtain a first-order active low pass filter with a cut-off frequency of 48.2 Hz.

Moving to the roll motor analog output signal, they do not require any conditioning since the corresponding motor driver is mounted on the control unit PCB and can be easily controlled by the $\mu-$controller. More on this topic is described in the further section dedicated to motor drivers.

Motor drivers and brakes logic control signals need to be considerably higher voltage than the voltages that the *mu*−controller can generate. To achieve this, the architecture proposed in Figure 2.50 has been implemented. The PS2502-4 IC is a package containing four NPN silicon Darlington connected phototransistors driven

by a LED each. By doing so, a low voltage digital signal from the $\mu-$controller can generate an high voltage digital signal (with voltage equal to $+BATT$ and current up to 1 A) suitable for driving Motor drivers and brakes logic control signals, i.e., enable and direction signals for motors and activation signals for the stationary brakes.

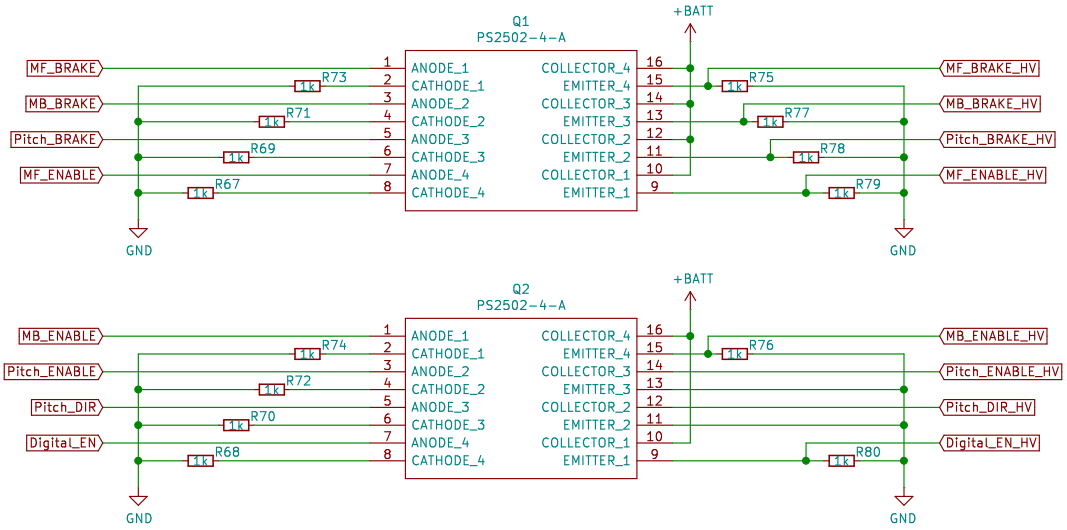

Fig. 2.50 Photocoupler layout for high voltage output digital signals

Since an additional channel was available, there is also an extra signal called *Digital_EN_HW* that can be used for future applications. Also note the different wiring for *Pitch_ENABLE_HV* and *Pitch_DIR_HV*, respectively the signals that enable the pitch motor and that set its direction. Such wiring is required to generate an output signal in the range of 0 V - *Open circuit*.

2.5.4 Actuators drivers

Agri.Q comes with six actuators and each of them is driven by a driver directed by the control unit. In the following, the electric layout of traction, pitch and roll motors are briefly presented.

Traction motors

A similar architecture was implemented for each traction motor since they are the same model, but with different gearboxs between the front and rear modules. A 12-1020 Micro BLDC motor driver by INTECNO drives each motor. Figure 2.51

depicts the electric layout of the traction motor sub-system, whereas Table 2.12 collects and describe the control signals.

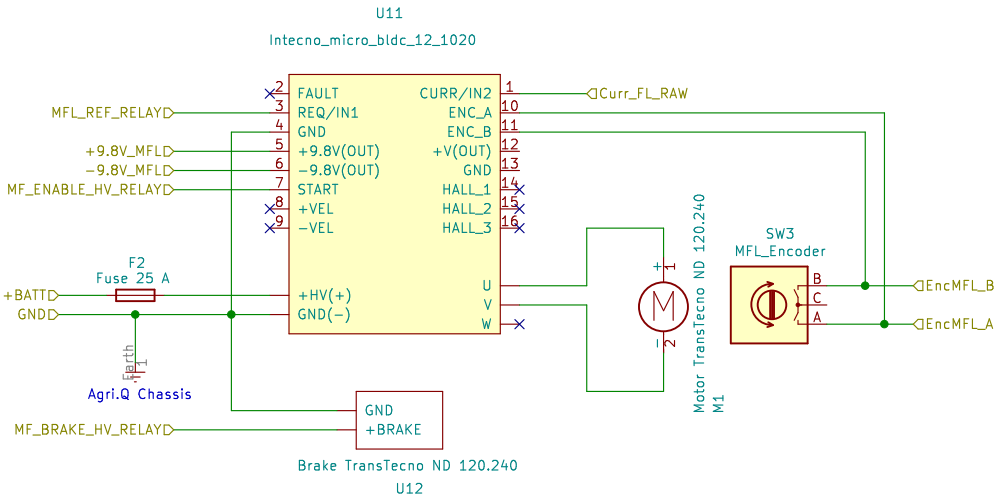

Fig. 2.51 Traction motor subsystem layout. The figure depicts the front left motor, but the layout is similar for the other traction motors

The driver is wired to enable the motor current (that is proportional to the motor torque) closed loop control. Hence the driver receives from the control unit a reference signal $V^{T}_{M\sim\sim,ref}$, an analog voltage proportional to the motor reference torque $T_{M\sim\sim,ref}$. The driver measures the motor current in order to close the loop, but it also generates an analog voltage signal proportional to the current that is acquired by the control unit. Similarly, the driver also mirrors the motor encoder channels to measure the motor angular speed. To conclude the list of signals, the driver and its motor can be enabled or disabled by means of a digital signal. In this case, the motors of the same module are enabled by the same signal. When the wired controller was still in use, the two reference voltages at $\pm 9.8\,\mathrm{V}$ were used to power its potentiometers. Besides the actual driver signals, there is another digital signal employed to engage or disengage a negative brake (ND 120.240 by Transtecno) mounted on each traction motor (i.e., when there is no power the brake is engaged, when it is powered the brake is disabled). A single digital signal commands all negative brakes. Figure 2.52 shows all traction drivers and their signals. Moreover, it clearly depicts that the front motors share the enable signal. The rear motors shares both the enable signal and the reference torque signal, thus, the rear module can not be differentially driven. All driver shares the same brake signal.

Table 2.12 Traction motor driver signals

Name	Description	Value
$M \sim\sim \_REF\_RELAY$	Torque reference analog signal $V^{T}_{M\sim\sim,ref}$. A positive torque requires a negative voltage	$\mp 10\,\mathrm{V}$
$+9.8V\_M \sim\sim$	Auxiliary output voltage. Used to power the wired remote potentiometers	$+9.8\,\mathrm{V}$
$-9.8V\_M \sim\sim$	Auxiliary output voltage. Used to power the wired remote potentiometers	$-9.8\,\mathrm{V}$
$M \sim \_ENABLE\_HV\_RELAY$	Digital voltage. High logic value enables the front/back motors	$0\,\mathrm{V}$ - $+BATT$
$Curr\_ \sim\sim \_RAW$	Voltage proportional to motor current (gain $2.5\,\mathrm{A\,V^{-1}}$)	$\pm 8\,\mathrm{V}$
$EncM \sim\sim \_A$	Motor quadrature encoder channel A signal	0-$5\,\mathrm{V}$
$EncM \sim\sim \_B$	Motor quadrature encoder channel A signal	0-$5\,\mathrm{V}$
$M \sim \_BRAKE\_HV\_RELAY$	Digital voltage. High logic value disengage all motor brakes	$0\,\mathrm{V}$ - $+BATT$

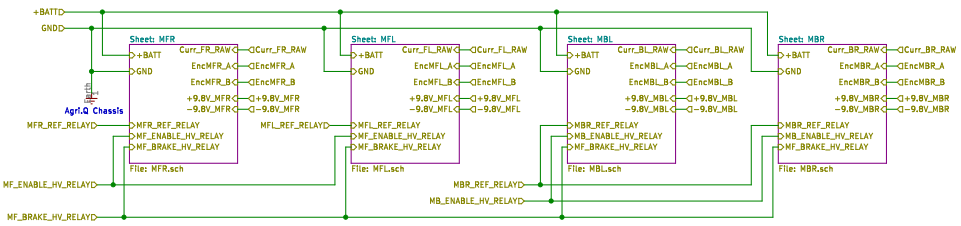

Fig. 2.52 Traction motors subsystem block diagram

PV panels pitch motor

The DC linear actuator employed in the pitch linkage mechanism is driven by a Kelvin K SCD10_10 driver (Figure 2.53). This driver is wired in such a way that the motor reference speed is always half of the maximum speed, i.e., the corresponding reference voltage at pin *SET* is always at 5 V due to the voltage divider. Therefore,

the controller only set the direction of motion together with the possibility to enable or disable the motor. Both pins have an internal pullup resistor, thus, they are driven by a voltage that can be exactly 0 V or any other value. At last, a relay driven by the controller is used to manage a negative brake similarly to what happens in a traction motor. Table 2.13 summarises all relevant signals.

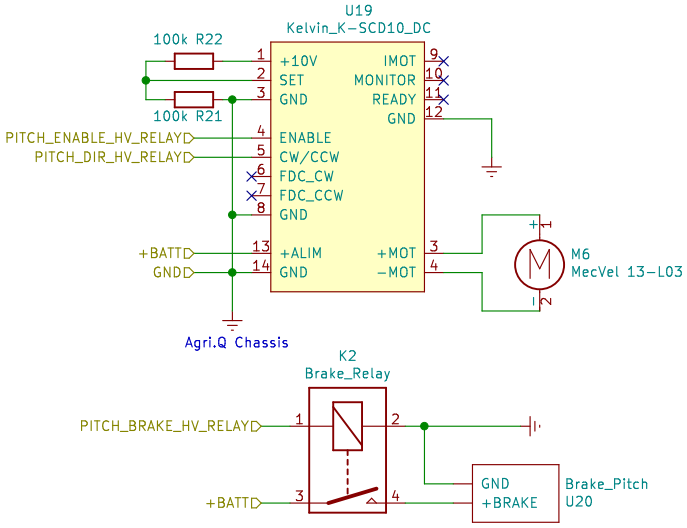

Fig. 2.53 Pitch motor driver

Table 2.13 Pitch motor driver signals

Name	**Description**	**Value**
PITCH_ENABLE_HV_RELAY	Digital voltage. High logic control value set voltage to 0 enabling the motor	0 V - *Open circuit*
PITCH_DIR_HV_RELAY	Digital voltage. High logic control value set voltage to 0 turning the motor clockwise	0 V - *Open circuit*
PITCH_BRAKE_HV_RELAY	Digital voltage. High logic value disengage the motor brake	0 V - $+BATT$

PV panels roll motor

Differently from the other drivers, the roll driver is located on the low level control unit PCB[4]. Figure 2.54 depicts the subsytem diagram. The G2 24v13 driver by Pololu is a simple H-bridge circuit to set the angular speed of the roll motor and its direction. However, the roll linear actuator is quite slow, hence the reference speed is always set to the maximum value or to zero. By doing so, a PWM signal is not required to modulate the motor speed, but a simpler digital signal is enough. As a result, the roll motion is only direction controlled, similarly to the pitch. As with the other motor drivers, a digital signal can turn on or off the motor as required. Since this driver is located in the control unit PCB, it is directly managed by the $\mu-$controller; therefore the digital signals are between 0 and 3.3 V. More generally, Table 2.14 lists all signals of the subsystem.

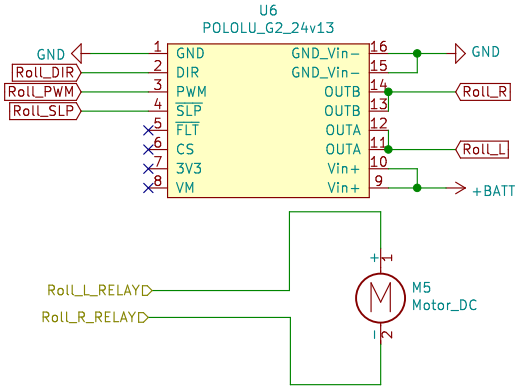

Fig. 2.54 Roll motor driver

Table 2.14 Roll motor driver signals

Name	Description	Value
ROLL_DIR	Digital voltage. High logic set clockwise rotation	0 - 3.3 V
ROLL_PWM	Digital voltage. High logic value set maximum motor speed. Speed reference value can be set continuously if a PWM is used	0 - 3.3 V
ROLL_SLP	Digital voltage. High logic value enable the motor	0 - 3.3 V

[4]Previoulsy, the roll motor was directly driven by the wired remote without any driver.

2.6 Control architecture

In this section, the low level control unit main processes are discussed. Figure 2.55 represents a simplified flowchart of the main control loop implemented into the μ-controller. When turn on, the control unit initialises all required variables and setup all its peripherals. After that the actual control cycle (with a frequency of 100 Hz) begins by acquiring the signals from the remote controller. Then, such signals are conditioned and manipulated to obtain the corresponding signals (*Input Mapping* block). Consequently, the received and elaborated signals are used to drive the following blocks, namely the motors and brakes state, the PV panels roll and pitch controller, and the locomotion units controller. At last, all remaining sensors, i.e. all sensors not required as a controller feedback signal, are collected and then the cycle starts again.

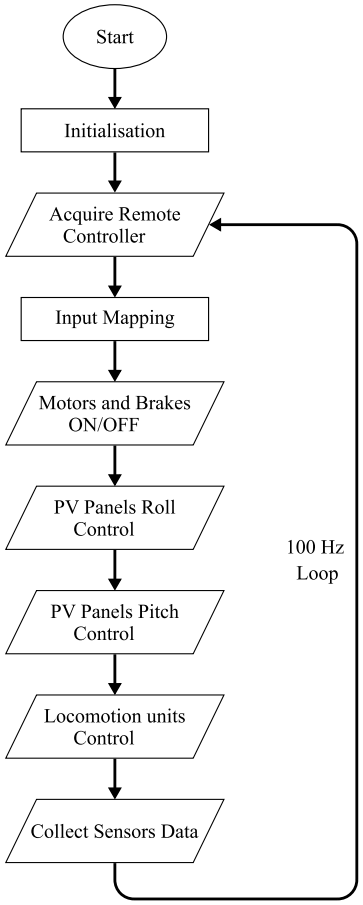

Fig. 2.55 Low level control unit flowchart

In the following sections, the most relevant parts of the low level control unit are described, namely how the remote controller signals are treated to generate reference signals, how the traction motors are controlled, and how the PV panels attitude is managed.

2.6.1 Remote control and signal mapping

As previously introduced, the remote controller can generate 6 different signals. Among them, 4 channels (i.e., $\lambda, \nu, \chi,$ and ξ) are continuous analog signals that the user generates acting on the two axes joysticks. Each signal value is represented by the on-state time of a corresponding PWM signal that can vary between 1000 µs and 2000 µs following the linear characteristic shown in Figure 2.56.

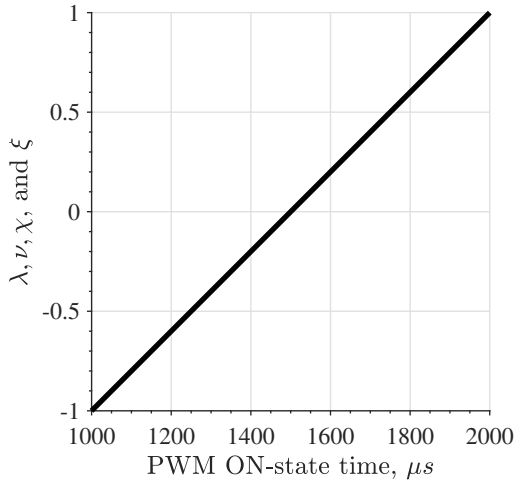

Fig. 2.56 Linear function relating the PWM ON-state time and the value of the corresponding analog channel

Longitudinal and lateral motion references

In particular, signals λ and ν are reference signals related to the longitudinal and lateral motion respectively. Among all possibilities, λ has been chosen as the control variable of the front module reference longitudinal speed $v_{F,ref}$, whereas ν drives the front module reference yaw rate $\dot{\psi}_{F,ref}$. Figure 2.57 shows the chosen relation between the user generated variables and the quantities driven by them. For

both of them, the input-output relation is made by a spline composed of a cubic polynomial, a zero-order polynomial, and then the cubic polynomial again. This arbitrary choice allows establishing a central dead-zone to reduce sensitivity to small joystick movements, but also to provide a smooth transition from zero to the maximum value.

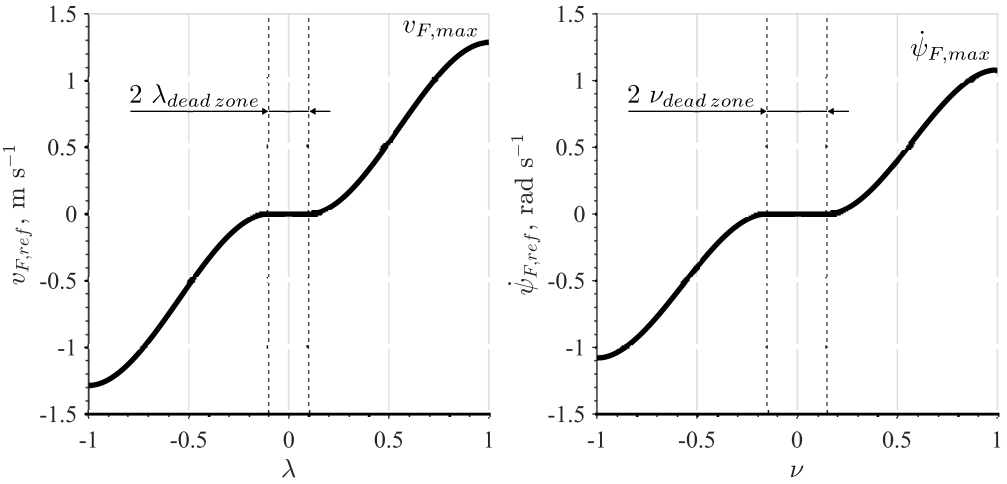

Fig. 2.57 λ and ν channels smooth mapping

Considering λ as an example, the spline relating λ and $v_{F,ref}$ is

$$v_{F,ref} = \begin{cases} 0, & \text{if } |\lambda| \leq \lambda_{dead\text{-}zone} \\ v_{F,max}\text{sign}(\lambda), & \text{if } |\lambda| > \lambda_{saturation} \\ v_{F,max}\left(a_3\lambda^3 + a_2\lambda^2 + a_1\lambda + a_0\right), & \text{if } \lambda_{dead\text{-}zone} < \lambda \leq \lambda_{saturation} \\ v_{F,max}\left(a_3\lambda^3 - a_2\lambda^2 + a_1\lambda - a_0\right), & \text{if } -\lambda_{saturation} \leq \lambda \leq -\lambda_{dead\text{-}zone} \end{cases} \tag{2.30}$$

where

$$a_3 = \frac{2}{(\lambda_{dead\text{-}zone} - \lambda_{saturation})^3}, \tag{2.31}$$

$$a_2 = -3\frac{\lambda_{dead\text{-}zone} + \lambda_{saturation}}{(\lambda_{dead\text{-}zone} - \lambda_{saturation})^3}, \tag{2.32}$$

$$a_1 = \frac{6\lambda_{dead\text{-}zone}\lambda_{saturation}}{(\lambda_{dead\text{-}zone} - \lambda_{saturation})^3}, \tag{2.33}$$

$$a_0 = \frac{\lambda_{dead\text{-}zone}^2(\lambda_{dead\text{-}zone} - 3\lambda_{saturation})}{(\lambda_{dead\text{-}zone} - \lambda_{saturation})^3} \tag{2.34}$$

are the unitary cubic polynomial coefficients, $v_{F,max}$ is the maximum desired longitudinal speed, $\lambda_{dead\text{-}zone}$ is half of the dead-zone amplitude, and $\lambda_{saturation}$ is the value from which starts the output saturation. The last two quantities are chosen empirically since their value is strongly related to how the user interfaces with the joystick. The four polynomial coefficients are defined imposing C^1-continuity (the first derivative is a continuous function) at $\pm\lambda_{dead\text{-}zone}$ and that at $\pm\lambda$ the curve reaches ± 1. The spline relating ν and $\dot{\psi}_{F,ref}$ has the exact same form but different parameters. Table 2.15 collects all value required to define the two splines as function of λ and ν.

Table 2.15 λ and ν channels smooth mapping parameters

Parameter	**Value**
$\lambda_{dead\text{-}zone}$	0.1
$\lambda_{saturation}$	1
$v_{F,max}$	$1.28\,\mathrm{m\,s^{-1}}$
$\nu_{dead\text{-}zone}$	0.15
$\nu_{saturation}$	1
$\dot{\psi}_{F,max}$	$1.08\,\mathrm{rad\,s^{-1}}$

Note that $\dot{\psi}_{F,max}$ is not the maximum yaw rate that the robot can achieve but about 1/3 of it. This choice is made based on several trials to optimize the driving feel.

Due to the differential drive architecture, $v_{F,ref}$ and $\dot{\psi}_{F,ref}$ can not assume any arbitrary value between their minimum and maximum values. In other words, since the front traction motors are responsible for both the longitudinal and angular motion, there are some sets of longitudinal speed and yaw rate that can not be achieved because they can not spin faster than their limit. For instance, considering the robot going straight at top speed, if it has to turn on one side with a desired yaw rate, the inner curve side motor must slow down. Also due to its differential drive nature, the front module can rotate on the spot without moving forward. Input mapping-wise,

all this means that the user signals smoothing is not enough and some more complex mapping has to be implemented.

Since the traction motor speeds are the limiting factors, it is convenient to map the user input in order to achieve feasible motor speeds. To achieve that, a front traction motors reference speeds mapping algorithm has been implemented (Algorithm 1). Such algorithm takes as inputs the user signals λ and ν and the corresponding smoothed reference signals $v_{F,ref}$ and $\dot{\psi}_{F,ref}$, then it checks in which state the reference condition is, i.e., it establishes if the robot is commanded to go forward or backward, to turn left or right, or to rotate the front module on the spot (lines 1, 3, 8, 14, 17, 22, and 28). The previous step allows to compute the reference speed of the motor that needs to spin faster (the outer side turn motor or any motor if turning on the spot) based on the user inputs (lines 5, 10, 19, 24, and 30) and eventually saturate its value to limit its speed (lines 6, 11, 20, 25, and 31). At last, the opposite motor reference speed is computed to achieve the desired yaw rate given the outer motor reference speed (lines 7, 12, 21, 26, and 32). This means that this algorithm gives priority to the yaw rate by automatically reducing the longitudinal reference speed if it is not feasible to obtain the desired yaw rate. In other words, the robot follows the yaw rate reference at any cost, whereas the longitudinal speed is limited to the closest feasible value.

Moreover, the algorithm takes care of keeping the turn direction coherent with the user's intention (line 16). Practically speaking, if the user set the ν axis at a defined value while going forward and then going backwards at the same longitudinal speed value, the two resulting trajectories must be the same one. To achieve that, the yaw rate sign has to be inverted whenever the robot is moving backwards. However, this requirement also means that severe discontinuities occur when λ crosses its zero value. Going back to the previous example, when the robot has to switch direction, the traction motors have to reverse their directions too, and this is done by exerting very high torque, and, thus, currents. Therefore, this behaviour must be handled with care, and this is accomplished by developing a smooth transition between forward and backward motion, while also mapping the front module turning on the spot state. Line 30 of the algorithm use a cubic polynomial to smoothen the transition between $-\lambda_{dead\text{-}zone}$ and $\lambda_{dead\text{-}zone}$, but also to generate a peak value at $\lambda = 0$ to get faster rotation on the spot (Figure 2.58). The polynomial was designed by imposing C^0-continuity at $\pm\lambda_{dead\text{-}zone}$, a peak at $\lambda = 0$ and C^1-continuity at $\lambda_{dead\text{-}zone}$. A fifth-order polynomial could achieve C^1-continuity for any λ within $\pm\lambda_{dead\text{-}zone}$ at

Algorithm 1: Front traction motors reference speeds mapping algorithm

input : λ, ν, $v_{F,ref}$, and $\dot{\psi}_{F,ref}$
output : $\omega_{MFL,ref}$ and $\omega_{MFR,ref}$

if $\lambda > \lambda_{dead\text{-}zone}$ **then** /* Going forward */
  if $\dot{\psi}_{F,ref} \geq 0$ **then** /* Turning left */
    $\omega_{MFR,ref} \leftarrow \tau_F \frac{2v_{F,ref}+\dot{\psi}_{F,ref} i_{yF}}{2r_W}$;
    $\omega_{MFR,ref} \leftarrow \max(-\omega_{MFR,max}, \min(\omega_{MFR,max}, \omega_{MFR,ref}))$;
    $\omega_{MFL,ref} \leftarrow \omega_{MFR,ref} - \frac{\tau_F i_{yF}}{r_W}\dot{\psi}_{F,ref}$;
  else /* Turning right */
    $\omega_{MFL,ref} \leftarrow \tau_F \frac{2v_{F,ref}-\dot{\psi}_{F,ref} i_{yF}}{2r_W}$;
    $\omega_{MFL,ref} \leftarrow \max(-\omega_{MFL,max}, \min(\omega_{MFL,max}, \omega_{MFL,ref}))$;
    $\omega_{MFR,ref} \leftarrow \omega_{MFL,ref} + \frac{\tau_F i_{yF}}{r_W}\dot{\psi}_{F,ref}$;
  end
else if $\lambda < -\lambda_{dead\text{-}zone}$ **then** /* Turning backward */
  $\dot{\psi}_{F,ref} \leftarrow -\dot{\psi}_{F,ref}$;
  if $\dot{\psi}_{F,ref} \leq 0$ **then** /* Turning left */
    $\omega_{MFR,ref} \leftarrow \tau_F \frac{2v_{F,ref}-\dot{\psi}_{F,ref} i_{yF}}{2r_W}$;
    $\omega_{MFR,ref} \leftarrow \max(-\omega_{MFR,max}, \min(\omega_{MFR,max}, \omega_{MFR,ref}))$;
    $\omega_{MFL,ref} \leftarrow \omega_{MFR,ref} + \frac{\tau_F i_{yF}}{r_W}\dot{\psi}_{F,ref}$;
  else /* Turning right */
    $\omega_{MFL,ref} \leftarrow \tau_F \frac{2v_{F,ref}+\dot{\psi}_{F,ref} i_{yF}}{2r_W}$;
    $\omega_{MFL,ref} \leftarrow \max(-\omega_{MFL,max}, \min(\omega_{MFL,max}, \omega_{MFL,ref}))$;
    $\omega_{MFR,ref} \leftarrow \omega_{MFL,ref} - \frac{\tau_F i_{yF}}{r_W}\dot{\psi}_{F,ref}$;
  end
else /* Turning on the spot */
  $\omega_{MFR,ref} \leftarrow \tau_F \frac{2v_{F,ref}-\dot{\psi}_{F,ref} i_{yF}}{2r_W}\left(\left(\frac{\lambda}{\lambda_{dead\text{-}zone}}\right)^3 - \frac{3}{2}\left(\frac{\lambda}{\lambda_{dead\text{-}zone}}\right)^2 + \frac{3}{2}\right)$;
  $\omega_{MFR,ref} \leftarrow \max(-\omega_{MFR,max}, \min(\omega_{MFR,max}, \omega_{MFR,ref}))$;
  $\omega_{MFL,ref} \leftarrow -\omega_{MFR,ref}$;
end

cost of a higher computational cost, but the third-order polynomial proves to be robust enough to avoid dangerous instabilities.

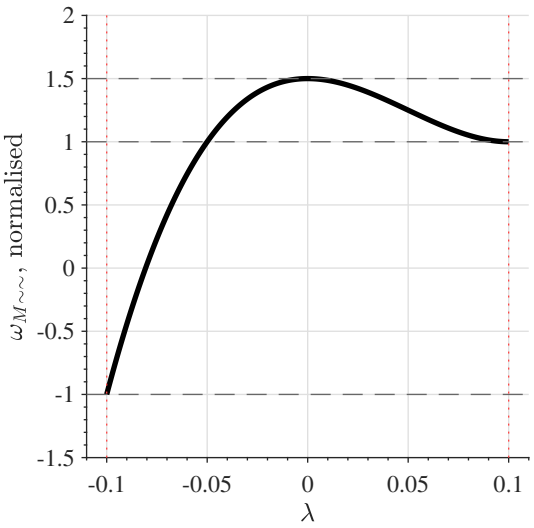

Fig. 2.58 Third-order polynomial to have a smooth transition between backward and forward motion without major discontinuities and to increase yaw rate when turning on the spot. The curve exists between $\pm\lambda_{dead\text{-}zone}$

Figure 2.59 shows the results of the mapping algorithm for the left and right front traction motors. The two maps are mirrored and clearly show the main features of the mapping process. For instance, at high values of λ and v, $\omega_{MFR,ref}$ saturates to its maximum value while $\omega_{MFR,ref}$ drops quite quickly to ensure that the desired yaw rate $\dot{\psi}_{F,ref}$ is achieved. Within the λ dead-band instead, it is visible the effect of the smoothing polynomial that eases the transition between forward and backward motions, but also lets the motor reference speed peak at a higher value when λ is close to 0, and, therefore, the front module is rotating about its centre on the spot.

From these maps it is also possible to compute the actual reference values $v_{F,ref}$ and $\dot{\psi}_{F,ref}$ corresponding to the motor reference speeds, as depicted in Figure 2.60. In both maps is still visible the underlying characteristic previously shown in Figure 2.57, nevertheless, some new features are present. The $v_{F,ref}$ map shows really well that at higher yaw rates the longitudinal speed is reduced to allow the motors to set to the proper angular speeds even if this means that the maximum longitudinal speed can be achieved only while going straight. The $\dot{\psi}_{F,ref}$ mapping, instead, illustrates both the discontinuity between positive and negative values of λ but also how the cubic function allows a smoother transition between the two conditions. Also,

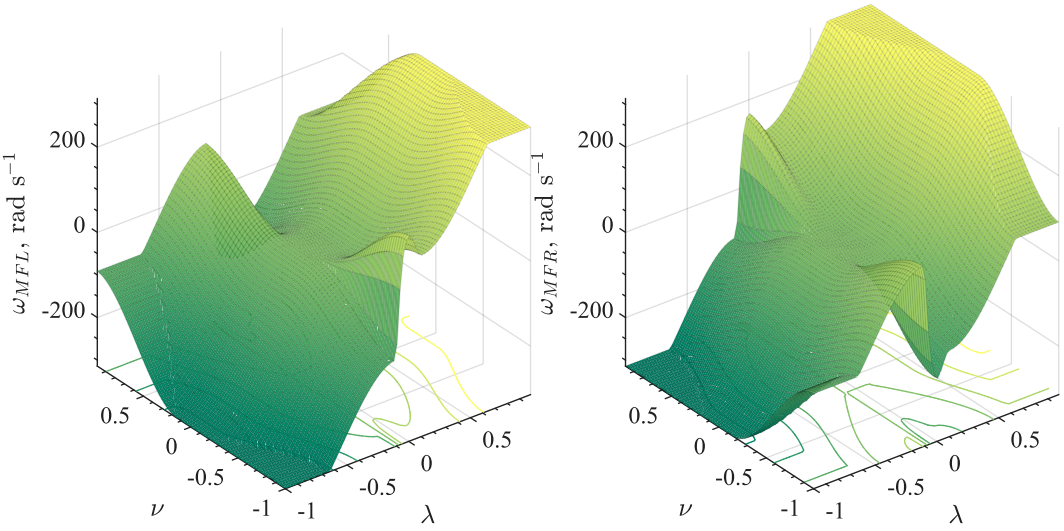

Fig. 2.59 Front left and right traction motor reference speed input mapping

when turning on the spot ($\lambda = 0$), $\dot{\psi}_{F,ref}$ peaks at a value larger than the one allowed while in normal drive mode.

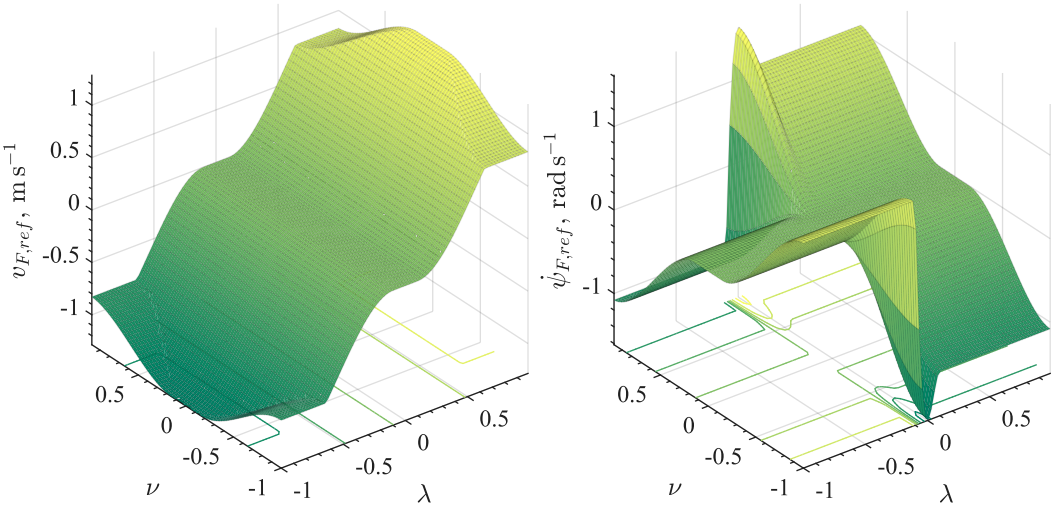

Fig. 2.60 Front module longitudinal speed and yaw rate motor reference speed input mapping

The actual reference values $v_{F,ref}$ and $\dot{\psi}_{F,ref}$ can also be represented through the space of the allowed front module speeds (Figure 2.61). The polygon area and boundary represents all possible combination of the feasible values of $v_{F,ref}$ and $\dot{\psi}_{F,ref}$. This representation shows that the top longitudinal speed can be reached only when the yaw rate is zero, otherwise the robot has to slow down to perform any turn at the re-

quired $\dot{\psi}_{F,ref}$. Below a speed of about $0.85\,\mathrm{m\,s^{-1}}$, the motors can reach the maximum yaw rate of $\dot{\psi}_{F,max} = 1.08\,\mathrm{rad\,s^{-1}}$ without slowing down. The polygon also shows the peak yaw rate at $1.62\,\mathrm{rad\,s^{-1}}$ (1.5 times $\dot{\psi}_{F,max}$). Again, note that $\dot{\psi}_{F,max}$ is not the actual maximum value that the traction motors can reach, but about 1/3 of it. If $\dot{\psi}_{F,max}$ is set to the actual maximum value, the polygon in Figure 2.61 becomes a rhombus with its four vertex at $(v_{F,max}, 0)$, $(0, \dot{\psi}_{F,max})$, $(-v_{F,ref}, 0)$, and $(0, -\dot{\psi}_{F,max})$. This would also mean that if the user set λ and ν to the maximum, the robot barely moves forward to reach the desired yaw rate. Therefore to improve the robot drivability, a lower value of $\dot{\psi}_{F,max}$ where chosen.

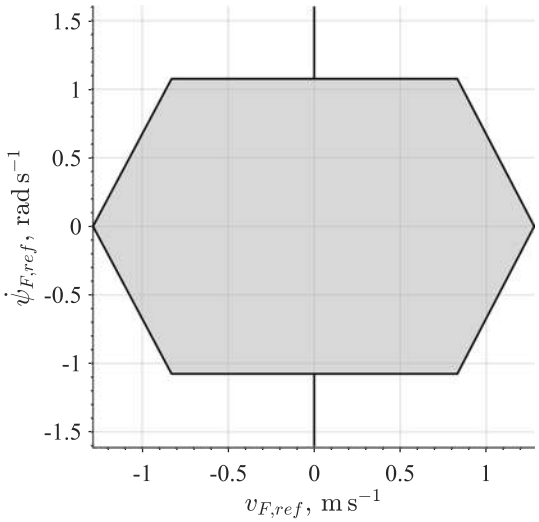

Fig. 2.61 Space of the feasible speeds after the application of the mapping algorithm

PV panels attitude references

Regarding the control of pitch and roll motions of the PV panels, user input mapping is significantly simpler because the two motors dedicated to the rotation are direction controlled. This means that the signs of ξ and χ are sufficient to define the directions (i.e., the signs) of the pitch rate $\dot{\gamma}$ and the roll rate $\dot{\alpha}_{Panels}$. To reduce joystick 1 sensitivity to undesired motions, a central dead zone is applied to both user signals ξ and χ where the corresponding motors are disabled and the brakes are engaged (Figure 2.62).

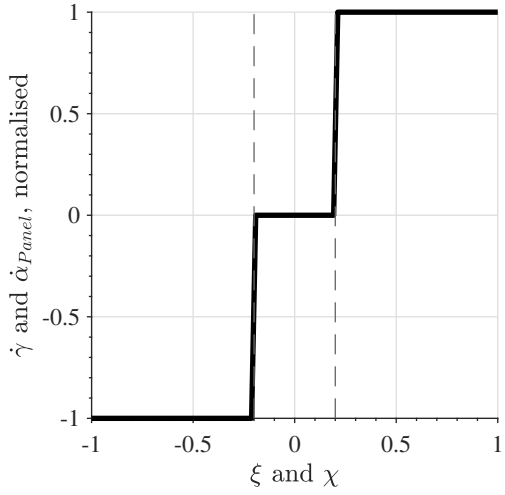

Fig. 2.62 PV panels reference mapping

2.6.2 Traction allocation control

As discussed in the previous section, a user generates the command signals λ and ν related to the longitudinal and lateral behaviour of the robot respectively. In particular, λ defines the reference longitudinal speed $v_{F,ref}$, whereas ν determines the front module yaw rate reference value $\dot{\psi}_{F,ref}$. These four variables are then combined in the mapping algorithm to compute the corresponding front traction motor reference angular velocity. Therefore, in order to let the robot motors follow the reference signals, a closed-loop velocity control architecture is defined. As shown at the top and bottom of Figure 2.63, the front traction motors reference speed $\omega_{M\sim\sim,ref}$ is compared with the actual motor speed $\omega_{M\sim\sim,meas}$ measured by its quadrature encoder. The error, i.e., the difference between the reference value and the measured one, is then feed to a PID controller $C_{M\sim\sim}$. By design, the controller generates a torque reference value $T_{\sim\sim,ref}$ required to compensate for the velocity error. After that, the μ-controller generates a PWM signal whose duty-cycle is a linear function of the torque, then the PWM signal is conditioned (Eq.(2.26)) to obtain an analog reference voltage $V^T_{M\sim\sim,ref}$ proportional to the reference torque (Figure 2.64). At last, this voltage is sent to the motor driver that acts as a closed-loop torque controller based on the reference value and the measured current. In simpler terms, the front traction motors are driven by a controller composed of an external velocity closed-loop and an internal torque closed-loop. The two front motor reference torque $T_{MFL,ref}$ and

$T_{MFR,ref}$ are also sent to a block defined as *Traction Allocation Control Strategy* that is responsible of defining the rear traction motor reference torques $T_{MBL,ref}$ and $T_{MBR,ref}$ based on the front motor torques and the state of $Sw2$. The two torque signals are treated similarly to the front ones being conditioned to become a reference voltage $V^T_{MB\sim,ref}$ to driver the corresponding motor driver torque controller. The figure shows the most general architecture where the two rear motors could receive different references, yet, the actual implementation forces that the two motors receive always the same reference. Moreover, it is important that the rear motors are torque controlled, otherwise, it could be possible that interference between front and rear module controllers may occur if both of them are controlled with a velocity reference. By controlling the rear motors torque, they can adjust their speed to the one dictated by the front ones.

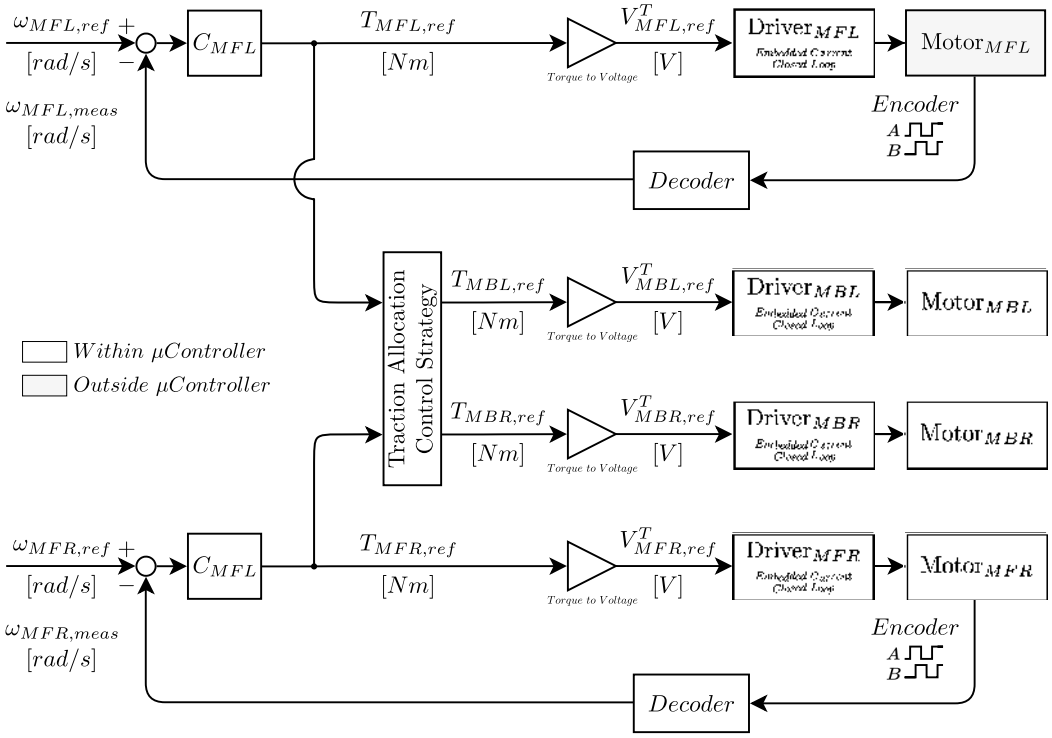

Fig. 2.63 Traction allocation control block diagram

Figure 2.65 illustrates more in detail how the $C_{MF\sim}$ controller is implemented. The controller is based on a parallel PID architecture with some additional features, thus, the proportional, integral, and derivative terms are summed to obtain the control command. This architecture introduces three main features typical of practical applications of PID controllers. First, the control signal is saturated to better represent

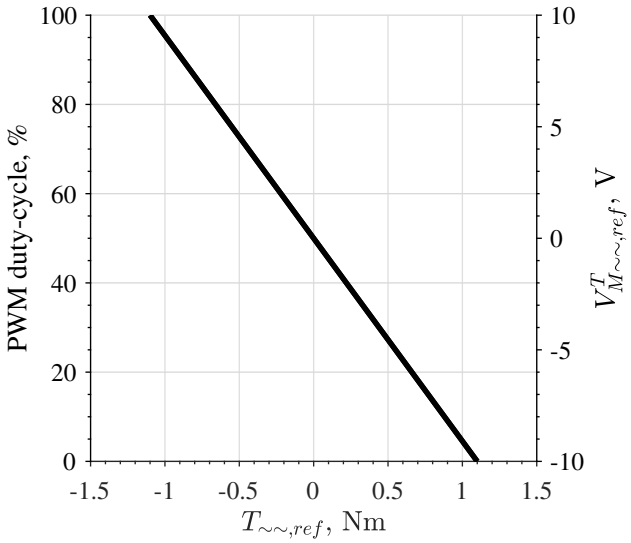

Fig. 2.64 Reference torque, PWM duty cycle, and output voltage relations

the system capabilities. Second, the integral part of the controller implements an anti-windup system that avoids command signal saturation due to the integral term build-up. This feature is obtained by temporary stop the integral term growth when the command has been saturated and the error and the integral term have the same sign (their product is positive). Third, the derivative part only uses the measure and not the error to avoid derivative kicks whenever the reference signal changes. The controller gains $K_{P,MF\sim}$, $K_{I,MF\sim}$, and $K_{D,MF\sim}$ were defined empirically based on experimental step responses and the final value are collected in Table 2.16. The experimental evaluation proved that the derivative term is not required to achieve remarkable results. Also, it is important to recall that these gains are strongly related to the controller time sample of $t_s = 10\,\text{ms}$ (100 Hz), since the actual PID implementation is done on a digital device.

Table 2.16 Traction motor controller $C_{MF\sim}$ PID parameters

Parameter	**Value**
$K_{P,MF\sim}$	$6.0\,\text{Nm}/(\text{rad}/\text{s})$
$K_{I,MF\sim}$	$0.01\,\text{N}\,\text{m}\,\text{rad}^{-1}$
$K_{D,MF\sim}$	$0.0\,\text{Nm}/(\text{rad}/\text{s}^2)$
t_s	10 ms

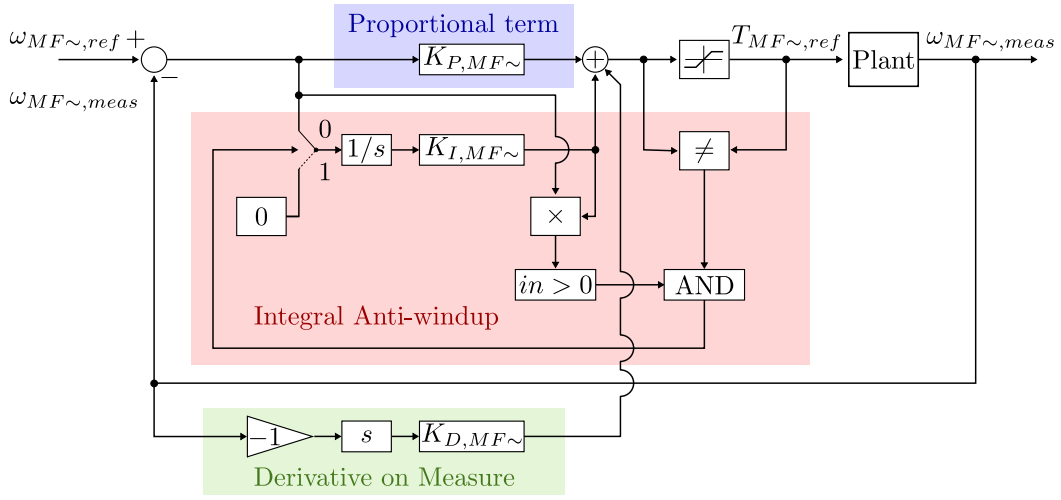

Fig. 2.65 Traction motor controller $C_{MF\sim}$ PID architecture

Heavy and off-road vehicles operate in demanding and frequently harsh work situations. Such vehicles are equipped with enhanced traction solutions to help them deal with severe road conditions. Multiple driven axles, varying degrees of differential locking, and electronic traction control are all part of these systems, which enable the vehicle to handle harsher terrains.

Traction allocation control is a rather novel method that may be applied to most over-actuated systems. In essence, a higher-level controller defines the generalised forces required to achieve the desired behaviour, then a dedicated low level controller, specific to the actual platform, produces such required generalised forces based on the available actuator. This approach allows the high level controller to be independent from the actual vehicle and, thus, to be reusable across other mobile platforms.

The most typical approach to traction allocation in vehicles with all-wheel-drive capabilities is to manage the locking of the vehicle differentials (either inter-wheel differentials or inter-axle differentials). By varying the differentials state between the open and locked configurations, it is possible to manage how the torque is distributed among axles and wheels. Specifically, torque is distributed to achieve a trade-off between steerability and traction by managing wheel slip employing different strategies, e.g., in [229–231] the front/back traction distribution is controlled to improve cornering.

With the introduction of ABS and independently controlled brakes first [232–234], and independent axles or wheels actuation later [235, 236], traction control

allocation strategies defined as torque vectoring further developed to improve vehicles performance, in particular, to enhance vehicle handling and avoid wheels slip. With the spread of electric vehicles, especially vehicles with independent wheel-motors, research about the topic has become even more popular [237–241]. As an example, Sforza et al. [242] reported in their review article several publications regarding various torque allocation strategies for different passenger car architectures.

While Agri.Q front traction motors are required to both define the longitudinal and lateral behaviour of the robot, the rear traction motors can be activated on demand to improve the robot performance. Ideally, Agri.Q could behave similarly to a four independent traction motors electric vehicle, however, the implemented electrical architecture force that the rear motors can only receive the same reference torque signal. This means that the back module can not produce any rear yaw moment, but it can just push the front module. Even if this condition limits the potential of implementing a dedicated yaw motion controller, the simpler architecture allows implementing less complex yet functional traction allocation strategies.

As a first approach, it has been implemented a traction allocation strategy that set a front-back wheel torque distribution based on the value of a distribution ratio k_{TA} defined as

$$k_{TA} = \frac{\overline{T_{WF}}}{\overline{T_{WF}} + \overline{T_{WB}}} \tag{2.35}$$

where $\overline{T_{W\sim}}$ is the average torque of all wheels part of the module $\sim$

$$\overline{T_{W\sim}} = \frac{T_{W\sim LF} + T_{W\sim LB} + T_{W\sim RF} + T_{W\sim RB}}{4} \tag{2.36}$$

When the distribution ratio k_{TA} is 1 then only the front motors are used, when it is 0.5 the torque is equally distributed between front and back wheels, while $k_{TA} = 0$ only the rear module is powered. However, two important notes must be made. First, the distribution ratio does not consider any longitudinal or lateral load transfer, thus the ratio is theoretically correct only in steady state. Nevertheless, its value is still considered valid during transients. Second, when $k_{TA} = 0$, Agri.Q can be seen as a car-like vehicle where the rear motors are responsible for the longitudinal characteristic whereas the front ones are only dedicated to steering (the average front torque is zero). Although this is an interesting behaviour, it is not considered for the first integration of a traction allocation control for many reasons. For instance,

the free-wheel mechanism in the rear locomotion units does not allow them to go in reverse without the intervention of the front motors. Furthermore, the mass distribution and the transmission ratio clearly favour a vehicle that can exert most of its tractive effort at the front.

Considering that the front motors torques are defined by the desired longitudinal velocity $v_{F,ref}$ and the desired yaw rate $\dot{\psi}_{F,ref}$, the rear motors contribution can be compute if a value of k_{TA} is set

$$\overline{T_{WB}} = \frac{1-k_{TA}}{k_{TA}}\overline{T_{WF}} \tag{2.37}$$

then, since all traction motor control procedures are done at motor level, it becomes

$$\overline{T_{MB}} = \frac{\tau_F}{\tau_B}\frac{1-k_{TA}}{k_{TA}}\overline{T_{MF}} \tag{2.38}$$

where $\overline{T_{M\sim}}$ is the mean traction motors torque of the module $\sim$. At last, considering that the rear motors are setup in such a way that they exert the same torque, the average torque corresponds to the torque of one of the two motors, therefore

$$T_{MBL} = T_{MBR} = \overline{T_{MB}} = \frac{\tau_F}{\tau_B}\frac{1-k_{TA}}{k_{TA}}\overline{T_{MF}} \tag{2.39}$$

By substituting to $T_{MB\sim}$ and $\overline{T_{MF}}$ the same value in Eq.2.39, it is possible to compute a significant value of k_{TA} that is $k^*_{TA} = 0.62$. With this particular value of distribution ratio, the traction motor effort is equally distributed among front and back, or, in other terms, the rear motor traction torque is equal to the average of the front motor torques. This particular condition is interesting because with this distribution ratio possible to saturate all traction motors at the same time drastically affecting the robot performance. However, $\overline{T_{MF}}$ saturates only if both front motors have saturated, thus this event generally can occur only while going straight on a slope (it also defines the maximum inclination that can be climbed). It is less frequent that all motors saturate at the same time while turning because when the front motor at the outer side of the turn saturates, the front motor on the other side drops its torque to keep turning at the same yaw rate, thus the front torque average drops too and consequently the rear motors follow. However, on some occasions (e.g., during extreme manoeuvres), the timing of the torque drops may be too slow to avoid sequential saturation of the motors.

The first implementation of the traction allocation control consists of two fixed value of k_{TA} between which the user can choose by setting $SW2$ to front-wheel drive (FWD), when $k_{TA} = 1$, or all-wheel drive (AWD), when $k_{TA} < 1$. A number of tests were made to evaluate the effect of various distribution ratios. Their results are discussed later in Chapter 4.

2.6.3 PV panels attitude control

PV panels pitch and roll motion controls are considerably simpler. Both rotations are driven by setting the direction of motion, i.e., the signs of $\dot{\gamma}$ and $\dot{\alpha}_{Panel}$.

Two modes of operation have been implemented to control the two angles: a user controlled open-loop mode and an automatic angular position close-loop control. The first mode is straightforward, the user set ξ and χ to define $\dot{\gamma}$ and $\dot{\alpha}_{Panel}$ as described in the previous section. Then the sign of $\dot{\gamma}$ and $\dot{\alpha}_{Panel}$ are used to generate the logic direction input. The second mode is instead a bit more interesting, although it is a very simple closed loop architecture. The user defines the desired angles on the SBC and they are sent to the $\mu-$controller through the serial port connection. The $\mu-$controller parses the received message to obtain the two reference angles, then the basic control loops in Figure 2.66 are implemented. The logic operation $e < 0$ is used in both control loops to define the logic signal that defines the direction of rotation. This means that when the error is positive the output of the logic block is 0, whereas when the error is negative the logic value is 1. All this is valid in this particular case because a 0 logic value as direction increases the corresponding angle and a 1 logic value corresponds to a decrease of the angle. When the error is zero, the corresponding motor turns off (i.e., the enable logic value is set to 0).

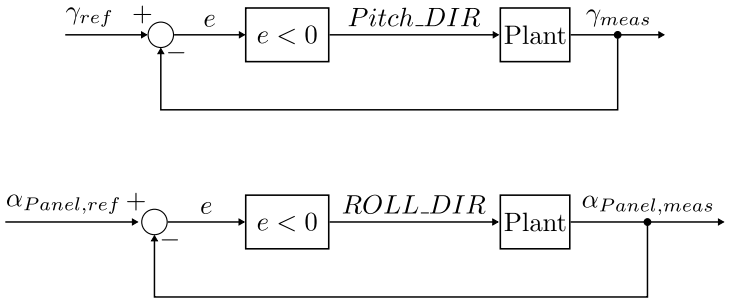

Fig. 2.66 PV panels attitude motors controllers

Chapter 3

Agri.Q Modelling

This chapter is dedicated to modelling various aspects of Agri.Q to better comprehend its behaviour. The chapter mostly focuses on kinematic and dynamic modelling of Agri.Q to assess how the robot act as a vehicle, thus, analysing its longitudinal and lateral behaviours. At first, a kinematic model is defined to get a reference theoretical baseline behaviour, regardless of the strong assumptions made. Then, such hypotheses are relaxed and a dynamic model of the robot is defined in two alternative ways.

This chapter also provides the kinematic modelling of the 7 DOF robotic arm mounted on Agri.Q.

3.1 Agri.Q kinematic modelling

It is critical to define a kinematic model for multi-axle articulated robots in order to assess a robot optimal behaviour and then utilize the findings as a baseline for dynamic models. For example, a kinematic model can contribute to define the theoretical limits of the robot handling behaviour. Also, a kinematic model can give a starting point to understand how Agri.Q behaviour is influenced by its own parameters. Therefore, a simple kinematic model has been developed based on previous works about modelling articulated vehicles with an architecture similar to Agri.Q [243, 244], namely vehicles composed of two skid-steering modules linked together by a joint that enables at least their relative yaw motion where each module has more than one non-steering axle.

In order to simplify the modelling problem, the following hypotheses have been defined:

- The model ignores out-of-plane motions, thus, it only examines planar motions on a flat surface.
- The locomotion units are simplified by using a single equivalent wheel per side whose rotation axis passes through the module geometric centre (Figure 3.1).
- Wheels pure-rolling condition is considered, therefore, longitudinal slip is neglected.

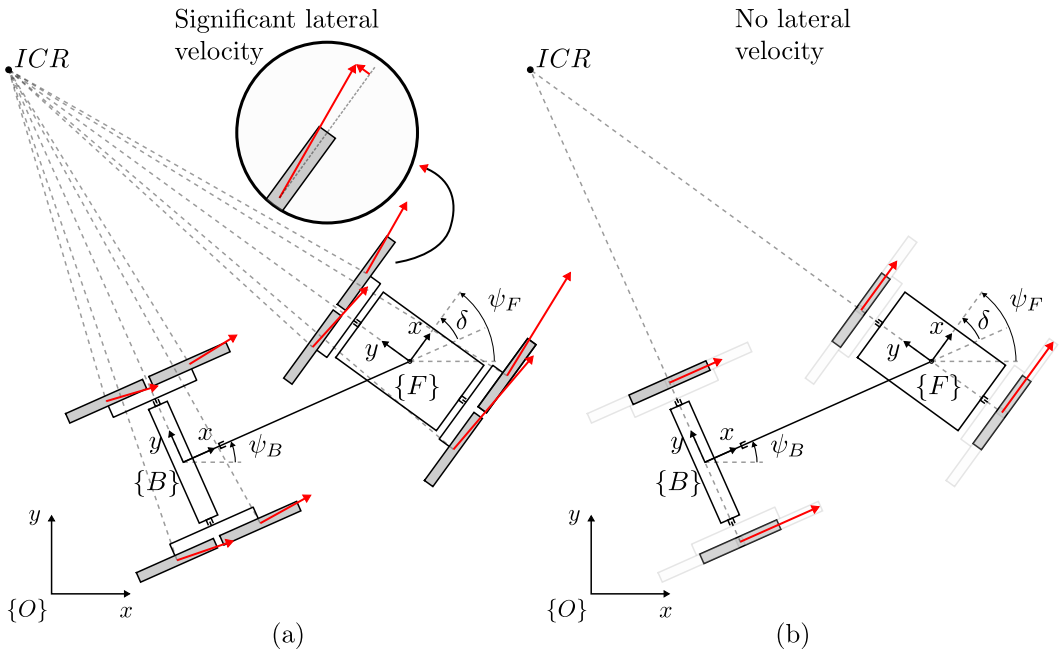

Fig. 3.1 (a) Agri.Q while turning with significant lateral wheels slip. (b) Simplified kinematic model with virtual wheels and no lateral velocity

While the first point is merely due to avoid complicating the model due to secondary motions like pitch and roll rotations of the whole robot of just one of its modules, the second hypothesis is quite strict. As depicted in Figure 3.1, Agri.Q is particularly affected by wheels side slipping while turning, i.e. the lateral velocity component of a wheel is quite significant compared to the wheel linear velocity, because of its architecture composed of multiple non-steerable axles that do not pass through their module centre of mass. Moreover, the aforementioned wheel slip

issue is emphasised by the locomotion unit design that constrains both wheels of the unit to spin at the same velocity. Consequently, the hypothesis of considering only a virtual (or equivalent) wheel per side of each module, instead of the actual architecture, neglects the robot lateral slippage during turns, hence, results from this model can diverge quite significantly from the actual robot behaviour in some limit cases. Also the last hypothesis relates to wheels slip, in particular the longitudinal one: by assuming pure-rolling condition, longitudinal wheels slip is not considered. Considering the low speed of the robot, this hypothesis is not as limiting as the previous one because the longitudinal slip occurs more rarely and for short transient. However, if a loose ground, or more generally driving off-road, is taken into consideration, significant wheels slip may occur, thus, such a model is not well suited for particularly complex terrains.

The diagram of the kinematic model is shown in Figure 3.2 , where $(x_\sim, y_\sim, \psi_\sim)$ represent the pose of the $\sim$ module ($\sim = F$ for the front module, $\sim = B$ for the back), *delta* represents the relative yaw rotation between the modules, $i_y = 0.817\,\text{m}$ is the module wheel track, and $l_{BN} = 1.197\,\text{m}$ represents the distances between the joint J_δ and the rear module. Note that, since only planar motion is considered, the PV panels pitch motion can not affects the distance l_{BN}. The longitudinal and angular speeds of the $\sim$ module in its reference frame are $v_\sim$ and $\dot{\psi}_\sim$, respectively.

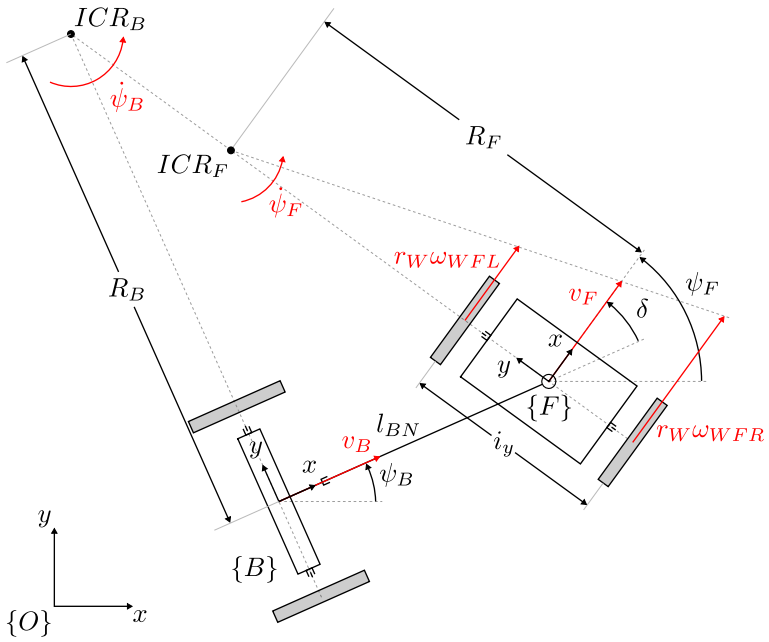

Fig. 3.2 Agri.Q simplified kinematic model diagram

Given the robot architecture, the following constraints can be defined

$$x_B = x_F - l_{BN}\cos\psi_B \tag{3.1}$$

$$y_B = y_F - l_{BN}\sin\psi_B \tag{3.2}$$

$$\delta = \psi_F - \psi_B \tag{3.3}$$

Furthermore, two additional holonomic constraints can be added.

$$\dot{x}_F \sin\psi_F - \dot{y}_F \cos\psi_F = 0 \tag{3.4}$$

$$\dot{x}_B \sin\psi_B - \dot{y}_B \cos\psi_B = 0 \tag{3.5}$$

Where $\dot{x}_\sim$ and $\dot{y}_\sim$ are the time derivatives of $x_\sim$ and $y_\sim$. Such velocities can also be defined as a function of the module longitudinal velocity $v_\sim$:

$$\dot{x}_\sim = v_\sim \cos\psi_\sim \tag{3.6}$$

$$\dot{y}_\sim = v_\sim \sin\psi_\sim \tag{3.7}$$

Hence, the kinematic model of the system can be defined as

$$\dot{\mathbf{q}} = \begin{bmatrix} \dot{x}_F \\ \dot{y}_F \\ \dot{\psi}_F \\ \dot{\delta} \end{bmatrix} = \mathbf{A_{kin}} \begin{bmatrix} v_F \\ \dot{\psi}_F \end{bmatrix} \tag{3.8}$$

where $\mathbf{q}$ is the kinematic model minimum state vector.

While the first three rows of $\mathbf{A_{kin}}$ are straightforward, the function relating $\dot{\delta}$ to v_F and ψ_F can be obtained by differentiating Eq.(3.1), (3.2), and (3.3), and by substituting the results in Eq.(3.5)

$$\dot{\delta} = \dot{\psi}_F - \frac{v_F}{l_{BN}} \sin\delta \tag{3.9}$$

consequently, the kinematic model showed in Eq.(3.8) becomes

$$\dot{\mathbf{q}} = \begin{bmatrix} \dot{x}_F \\ \dot{y}_F \\ \dot{\psi}_F \\ \dot{\delta} \end{bmatrix} = \begin{bmatrix} \cos\psi_F & 0 \\ \sin\psi_F & 0 \\ 0 & 1 \\ -\frac{1}{l_{BN}}\sin\delta & 1 \end{bmatrix} \begin{bmatrix} v_F \\ \dot{\psi}_F \end{bmatrix} \tag{3.10}$$

given that the front module is basically a skid steering robot, it is possible to highlight the following relations that link v_F and $\dot{\psi}_F$ to the angular speed of the virtual front wheels ω_{WFR} and ω_{WFL} (note that the angular speed of the virtual wheel is the same of an actual wheel)

$$v_F = \frac{r_W}{2}\left(\omega_{WFR} + \omega_{WFL}\right) \tag{3.11}$$

$$\dot{\psi}_F = \frac{r_W}{i_y}(\omega_{WFR} - \omega_{WFL}) \tag{3.12}$$

As mentioned before, this kinematic model can be helpful in defining the theoretical limits of this robot architecture, in particular regarding the handling behaviour. In the most generic configuration, each module has its own instantaneous centre of rotation (ICR), and they may not coincide, as depicted in Figure 3.3a. When the articulated robot reaches the steady-state condition during a turn, there is no more relative rotation between the modules ($\dot{\delta} = 0$), thus, the robot can be considered as a whole and a single ICR can be defined (Figure 3.3b).

The steady state configuration represented in Figure 3.3a allows to define a geometric relation between the steady state curvature radius of each module $R_{\sim,ss}$ and the steady state relative yaw angle δ_{ss}, that is

$$R_{F,ss} = \frac{l_{BN}}{\sin\delta_{ss}} \tag{3.13}$$

$$R_{B,ss} = \frac{l_{BN}}{\tan\delta_{ss}} \tag{3.14}$$

or. equivalently, the corresponding curvature $\rho_{\sim,ss}$ is defined as

$$\rho_{F,ss} = \frac{1}{R_{F,ss}} = \frac{\sin\delta_{ss}}{l_{BN}} \tag{3.15}$$

$$\rho_{B,ss} = \frac{1}{R_{B,ss}} = \frac{\tan\delta_{ss}}{l_{BN}} \tag{3.16}$$

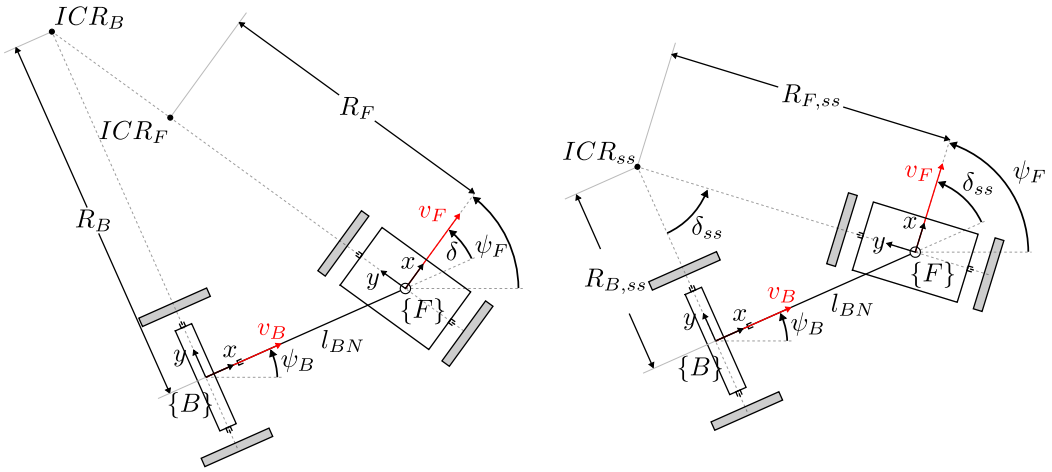

(a) (b)

Fig. 3.3 (a) Agri.Q during a transient turn where the ICRs do not coincide. (b) Steady state turn where the ICRs coincide

Considering that the angle δ can reach up to 40°, the corresponding minimum theoretical turning radii are 1.862 m fore the front module and 1.427 m for the back.

Generally speaking, the curvature radius of the front module is always larger than the rear one, thus the rear module is always at the inner side of the front trajectory (Figure 3.4).

As aforementioned, however, it is important to recall that the significant wheels slip of the actual robot causes Agri.Q to diverge from the kinematic trajectories showing an under-steering behaviour that widen all curved trajectories, as reported later. Nevertheless, it may be possible to compensate for such behaviour acting on the kinematic model and, in particular, on the virtual wheels track i_y. As proven by a previous study on a smaller articulated robot with multi-axle skid-steering modules[243], if the virtual wheels track i_y is not constant but it is a linear function of the front module yaw rate $\dot{\psi}_F$, or alternatively of the ratio v_F/R_F, this kinematic model can partially compensate for un-modelled behaviour of the previously defined model, namely the under-steer effect at lower speeds. Although this path could lead to interesting results, it has never been tested on Agri.Q since it was more valuable to develop a proper dynamic model of the robot.

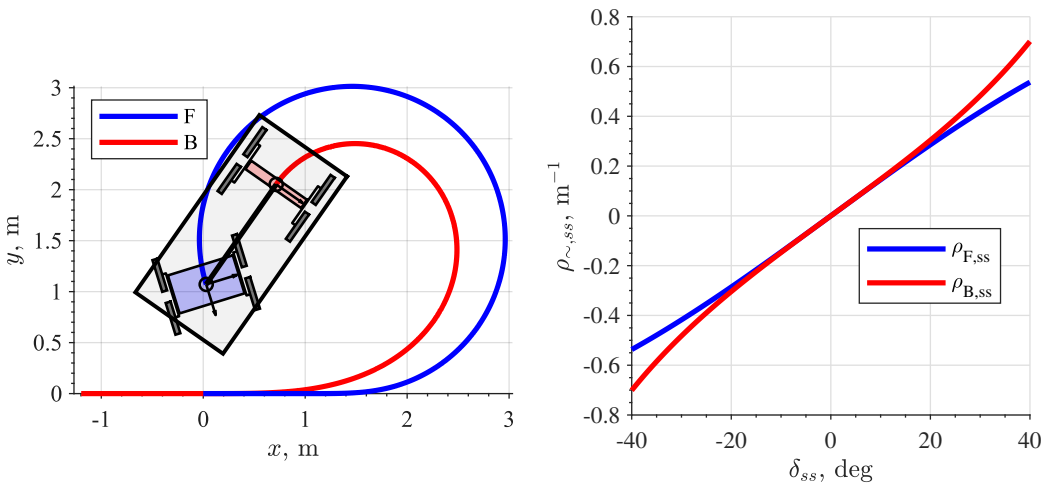

(a) (b)

Fig. 3.4 (a) Agri.Q generic trajectory. (b) Steady state curvature $\rho_{\sim,ss}$ as a function of δ_{ss}

3.1.1 Pure pursuit path tracking

Although the kinematic model presents evident issues, its simplicity makes it very useful for complex tasks such as real-time path tracking. Among all possible path tracking methods, pure pursuit is one of the simplest yet effective and reliable ones. It exploits the simplicity of kinematic models to drive the vehicle toward a moving point along the desired path, hence the name of pure pursuit [245]. A slightly modified version of pure pursuit has been developed in anticipation of the integration of an autonomous navigation system. The proposed algorithm has not been implemented yet, but it was tested with kinematic and dynamic models of Agri.Q.

Figure 3.5 represents the working principle of the pure pursuit methods. The method calculates the circular arc that allows the vehicle to go from its present location to a target point **G** placed at a look-ahead distance L from the vehicle current route projection. The pursuit circular arc can be traced either from the front or the back module with minor differences. Then the front module linear and angular velocity reference values are then calculated using the curvature that has resulted.

As a requirement, the tracking method needs a reference path. The desired path is sampled at a series of points ($\mathbf{P}_0$, $\mathbf{P}_1$, …, $\mathbf{P}_N$) that are linked by segments $\mathbf{S}_n = \overrightarrow{\mathbf{P}_n\mathbf{P}_{n+1}}$. The trajectory pursuit works regardless of the number of points,

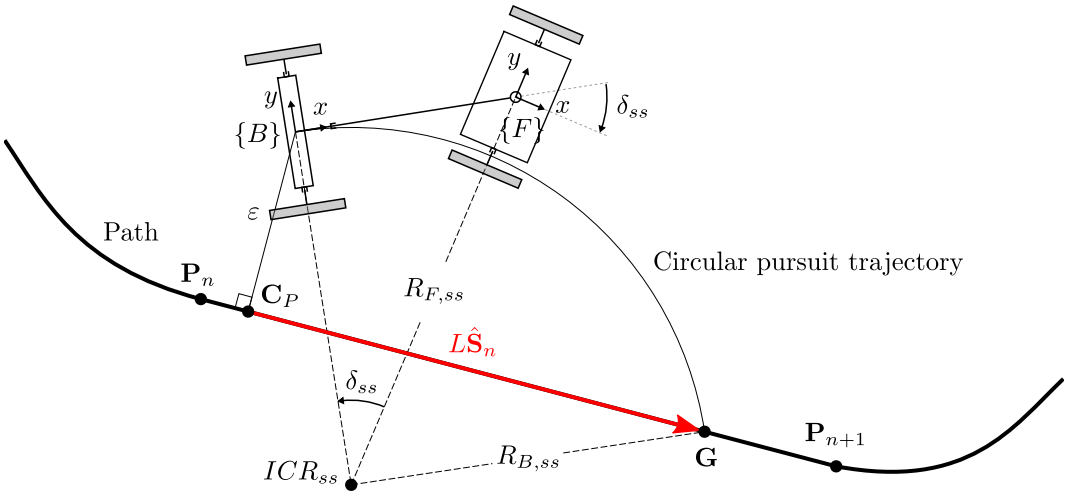

Fig. 3.5 Pure pursuit working principle diagram

however, the more they are, the better the path is tracked. After that, the pure pursuit algorithm performs cyclically the following step until the last point is reached

1. Robot localisation
2. Find robot closest projection on the path
3. Define the target point **G**
4. Compute the curvature ρ_B of the pursuit circular arc
5. Define the corresponding reference value $v_{F,ref}$ and $\dot{\psi}_{F,ref}$

Robot localisation

This step requires the robot to localise itself within the global reference frame where the path has been defined. This phase is heavily affected by the available localisation sensors and by the localisation algorithm employed. Since Agri.Q autonomous navigation integration is still at an early stage, this step has not been properly implemented, instead, the robot pose is assumed to be always known.

Find robot closest projection on the path

Once the robot is localised in the same reference frame of the path, the algorithm has to identify which segment $\mathbf{S}_n$ is the closest to the robot, defined relevant segment. To do so, only a limited subset of segments is chosen starting from the relevant segment of the previous iteration (if it is the first iteration, the subset starts from the first segment). The actual number of segments is a heuristic parameter used to reduce computational time and mostly depends on the total number of segments and the density of the sampled points. Also, this value affects the possibility to skip parts of the path to reach the end as fast as possible or to ensure that the trajectory is followed more strictly. As depicted in Figure 3.6, the origin of the reference frame $\{B\}$ is projected into each segment to evaluate the corresponding distance ε_n, also known as cross-track error. This is done by computing the geometric quantities shown in Figure 3.7, namely the actual segment

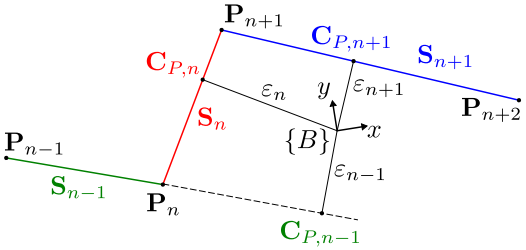

Fig. 3.6 Search for the closest segment diagram

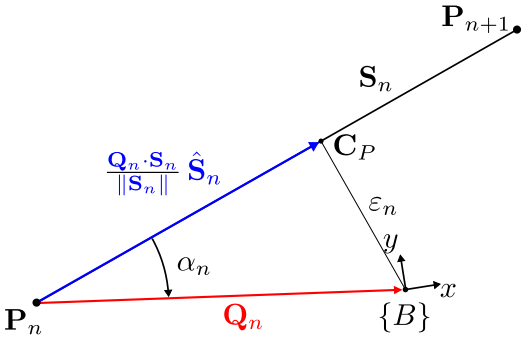

Fig. 3.7 Pure pursuit geometrical parameters

$$\mathbf{S}_n = \overrightarrow{\mathbf{P}_n\mathbf{P}_{n+1}} == [x_S \; y_S]^T \tag{3.17}$$

the location of $\{B\}$ with respect to $\mathbf{P}_n$

$$\mathbf{Q}_n = \overrightarrow{\mathbf{P}_n\mathbf{B}} = [x_Q \; y_Q]^T \tag{3.18}$$

their included angle

$$\alpha_n = \arctan\left(\frac{x_Q y_S - y_Q x_S}{x_Q x_S + y_Q y_S}\right) \tag{3.19}$$

and, thus, the cross tracking error

$$\varepsilon_n = -\|\mathbf{Q}_n\| \sin \alpha_n \tag{3.20}$$

The segment with the shorter cross track error is the closest and, therefore, the relevant segment.

Define the target point G

The classic pure pursuit algorithm finds the target point $\mathbf{G}$ as the intersection between the segment $\mathbf{S}_n$ and a circle centred in $\{B\}$ with radius L. The hereby proposed method instead defines $\mathbf{G}$ as the point at a distance $L\hat{\mathbf{S}}_n$ from the projection of $\{B\}$ onto $\mathbf{S}_n$ (i.e., the point $\mathbf{C}_P$). Therefore, the target point is defined as

$$\mathbf{G} = \mathbf{P}_n + \left(\|\overrightarrow{\mathbf{P}_n\mathbf{C}_P}\| + L \right) \hat{\mathbf{S}}_n = \mathbf{P}_n + \left(\frac{\mathbf{Q}_n \cdot \mathbf{S}_n}{\|\mathbf{S}_n\|} + L \right) \hat{\mathbf{S}}_n \tag{3.21}$$

The previous relation is valid in the most general condition (Figure 3.8a), however there are some limit cases that need particular attention to develop a smoother tracking algorithm. Figure 3.8b depicts the first case, namely when the projection $\mathbf{C}_P$ on the closest segment is behind $\mathbf{P}_n$, or, in other terms, when $\|\overrightarrow{\mathbf{P}_n\mathbf{C}_P}\|\hat{\mathbf{S}}_n < 0$. In such a case, the target point can be defined in two different way depending on the value of L

$$\mathbf{G} = \begin{cases} \mathbf{P}_n + \left(\frac{\mathbf{Q}_n \cdot \mathbf{S}_n}{\|\mathbf{S}_n\|} + L \right) \hat{\mathbf{S}}_n, & \text{if } L > \frac{\mathbf{Q}_n \cdot \mathbf{S}_n}{\|\mathbf{S}_n\|} \\ \mathbf{P}_n, & \text{if } L \leq \frac{\mathbf{Q}_n \cdot \mathbf{S}_n}{\|\mathbf{S}_n\|} \end{cases} \tag{3.22}$$

Figure 3.8c illustrates instead the opposite case, that is when the projection $\mathbf{C}_P$ on the closest segment is beyond $\mathbf{P}_{n+1}$, or, in other way, when $\|\overrightarrow{\mathbf{P}_n\mathbf{C}_P}\|\hat{\mathbf{S}}_n > \|\mathbf{S}_n\|$. When this condition occurs, the following segment $\mathbf{S}_{n+1}$ becomes the relevant one where $\mathbf{G}$ is defined, or, if $\mathbf{P}_{n+1} = \mathbf{P}_N$ (i.e., it is the last point), $\mathbf{P}_N$ becomes the target point.

$$\mathbf{G} = \begin{cases} \mathbf{P}_{n+1} + \left(\frac{\mathbf{Q}_{n+1} \cdot \mathbf{S}_{n+1}}{\|\mathbf{S}_{n+1}\|} + L \right) \hat{\mathbf{S}}_{n+1}, & \text{if } \frac{\mathbf{Q}_n \cdot \mathbf{S}_n}{\|\mathbf{S}_n\|} + L > \|\mathbf{S}_n\| \\ \mathbf{P}_N, & \text{if } \mathbf{P}_{n+1} = \mathbf{P}_N \end{cases} \tag{3.23}$$

Typically the look-ahead distance L is a constant value. A large value of L lets the robot tracks the path very loosely but smoothly, on the contrary, a lower L allows it to

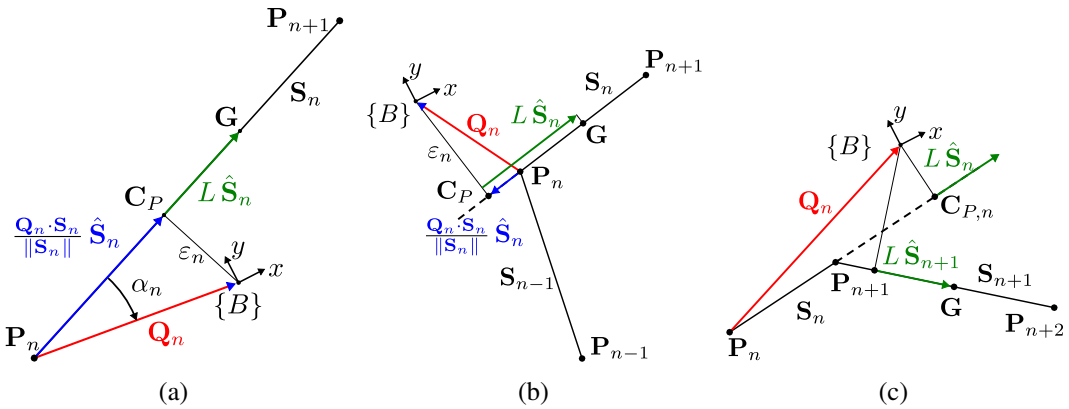

Fig. 3.8 Target point definition cases: (a) General case; (b) case 1; (c) case 2

closely follow the path at the cost of a more nervous behaviour. Since L significantly affects the tracking behaviour, sometimes is more convenient to use an adaptive look-ahead distance. Therefore, this method defines L as a linear function of v_F

Compute the curvature ρ_B of the pursuit circular arc

After that $\mathbf{G}$ has been found, it is possible to represent the same point in $\{B\}$, that is ${}^B\mathbf{G} = \begin{bmatrix} {}^B x_G & {}^B y_G \end{bmatrix}^T$. This change of reference frame allows to easily compute the radius R_B of the pursuit circular arc connecting $\{B\}$ and $\mathbf{G}$ with the hypothesis that its centre ICR_B lies along the rear module virtual axis, which corresponds to $\hat{\mathbf{y}}_B$. In particular, from Figure 3.9 it is possible to define

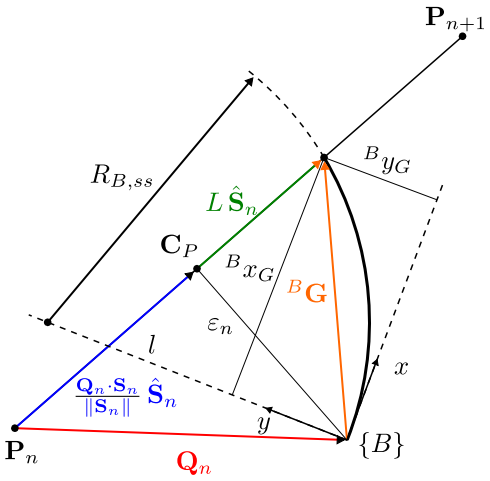

Fig. 3.9 Geometric definition of the circular pursuit arc

$$R_{B,ss}^2 = l^2 + {}^B x_G^2 \tag{3.24}$$

and

$$R_{B,ss} = l + {}^B y_G \tag{3.25}$$

thus

$${}^B x_G^2 + {}^B y_G^2 - 2R_B {}^B y_G = 0 \tag{3.26}$$

therefore, by recalling that ${}^B x_G^2 + {}^B y_G^2 = \|{}^B\mathbf{G}\|^2$, the arc radius is

$$R_{B,ss} = \frac{\|{}^B\mathbf{G}\|^2}{2\,{}^B y_G} \tag{3.27}$$

and the corresponding curvature is

$$\rho_{B,ss} = \frac{2\,{}^B y_G}{\|{}^B\mathbf{G}\|^2} \tag{3.28}$$

Define the corresponding reference value $v_{F,ref}$ and $\dot{\psi}_{F,ref}$

By knowing the radius $R_{B,ss}$ it is possible to find the corresponding radius $R_{F,ss}$ computing first δ_{ss} using Eq.(3.14) and then combining Eq.(3.13) and Eq.(3.14) to obtain

$$R_{F,ss} = \frac{R_{B,ss}}{\cos\delta_{ss}} \tag{3.29}$$

This radius fixes the ratio between the reference longitudinal speed of the front module $v_{F,ref}$ and the reference yaw rate of the front module $\dot{\psi}_{F,ref}$, namely

$$R_{F,ss} = \frac{v_{F,ref}}{\dot{\psi}_{F,ref}} \tag{3.30}$$

but the two reference values can be defined arbitrarily. Although classical pure pursuit algorithm sets $v_{F,ref}$ to a constant value (usually the maximum value), the hereby proposed methods defines $v_{F,ref}$ as a linear function of ${}^B x_G$ that saturates at $v_{F,max}$ when ${}^B x_G \geq L$. This approach allows the robot to slow down when $\mathbf{G}$ is closer and to stop at $\mathbf{P}_N$. On the other hand, $\dot{\psi}_{F,ref}$ is computed based on R_F and $v_{F,ref}$. However, to guarantee that the robot can achieve the desired yaw rate, whenever $\dot{\psi}_{F,ref}$ is larger than $\dot{\psi}_{F,max}$, the reference yaw rate is set to be equal to the maximum value and $v_{F,ref}$ is computed again using $R_{F,ss}$ and $\dot{\psi}_{F,max}$. As a result, the proposed

pursuit algorithm automatically adjusts $v_{F,ref}$ to the path, slowing down before tight curves and speeding up on straight sections.

3.2 Agri.Q dynamic modelling

The previously discussed kinematic model of an articulated vehicle composed of multi-axle skid-steering modules hardly suits the real behaviour of this kind of robot due to a large number of contact points and the non-negligible slippage to which the wheels are prone. Therefore, previous research focused on developing dynamic models of increasing complexity with the goal of understanding the actual behaviour of robots with such an architecture. [246] proposed a planar dynamic model of an articulated wheeled mobile robot with wheels slippage. The system dynamic equations were derived using the Newton-Euler technique, and a very basic ground-wheel contact force model was built to reflect wheel dynamics. The model parameters guiding the system longitudinal and lateral dynamics were estimated through an experimental identification done on a small articulated robot. The same dynamic model has been compared in [244] with a dynamic model of Agri.Q made with the multibody software ADAMS, where the contact forces were modelled with Pacejka's Magic Formula. In [247] a more sophisticated dynamic 3D model was developed with the intent of better characterising the contact forces. Also, the paper reported an experimental campaign to identify Agri.Q parameters required to model it.

The latter model is presented here and adapted to Agri.Q. The kinematic structure of an eight-wheeled robot is depicted in Figure 3.10 in a simplified planar version. There are a pair of drive units in each of the two modules. Two wheels on each drive unit are in contact with the ground. The two modules are linked together by a universal joint in **O** that is the combination of the two revolute joint J_δ and J_{α_B}, respectively the relative yaw and the relative roll joints. The front and rear positions of the two modules are defined by the corresponding reference frames, namely $\{F\}$ and $\{B\}$, respectively. The origins of the reference frames are both at the junction of the longitudinal axis and the axis of rotation of the driving units carriers. The reference frames are orientated so that the x axis is parallel to the module longitudinal axis and the z axis is parallel to the ascending vertical direction (perpendicular to the plane of motion). As a result, the y axis is parallel to the transversal direction and

points to the left driving units. A collection of six parameters determines the poses of $\{F\}$ and $\{B\}$, three for position and three for orientation. The coordinates of the reference frames are denoted by two vectors $\mathbf{p}_{\sim}$, which are

$$\mathbf{p}_{\sim} = \begin{bmatrix} x_{\sim} & y_{\sim} & z_{\sim} \end{bmatrix}^T \tag{3.31}$$

where $\sim$ stands for F and B for the front and back module respectively.

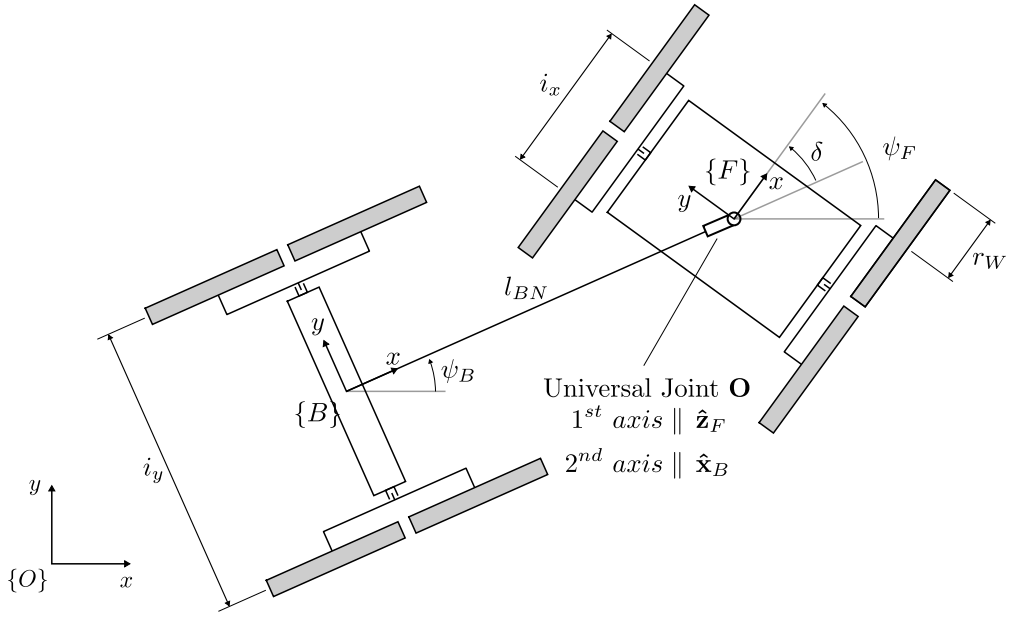

Fig. 3.10 Agri.Q kinematic diagram and geometric parameters

The attitude of the two modules must be carefully studied. During movements on flat surfaces, the construction of articulated robots prevents rotations along the longitudinal and transversal axes (x and y directions of $\{F\}$ and $\{B\}$). However, because such rotations cause non-symmetric wheel load distributions on the right and left sides of the rover, the kinematics model cannot ignore their impact. A x-y-z rotation around the axes of the global reference frame is used to define the orientation for this purpose:

$$\mathbf{R}_{\sim} = \mathbf{R}_{z,\psi_{\sim}} \mathbf{R}_{y,\gamma_{\sim}} \mathbf{R}_{x,\alpha_{\sim}} \tag{3.32}$$

where $\alpha_{\sim}$, $\gamma_{\sim}$ and $\psi_{\sim}$ are the roll, pitch and yaw angles respectively of the $\sim$ module. The resulting rotation matrix is simplified later by assuming small rotations of $\alpha_{\sim}$ and $\gamma_{\sim}$.

The kinematics of the wheels were also modified in order to develop a trustworthy and significantly simplified model. They were thought to be constantly in touch with the ground, with the movements of the rockers being ignored. The inertial contribution of both wheels and carriers has been taken into account, but their movement has been limited to the appropriate module, as illustrated later.

A Lagrangian approach was used to study the dynamics of Agri.Q. To make the kinematics formulation as simple as possible, the model was built using Lagrangian multipliers and a universal joint to constrain the front and rear modules. However, due to the non-negligible wheels slip, the soil-tyre contact was solely calculated using the exerted forces. In other words, the model that has been implemented is

$$\frac{d}{dt}\left(\frac{\partial \mathscr{L}}{\partial \dot{\mathbf{q}}}\right) - \frac{\partial \mathscr{L}}{\partial \mathbf{q}} + \mathbf{J}_{\mathbf{q}}\boldsymbol{\lambda} = \sum \mathbf{Q}_{\star} \tag{3.33}$$

where

- $\mathscr{L}$ is the system Lagrangian function, which is computed as the difference between kinetic and potential energy;
- $\mathbf{q}$ is the generalized coordinates vector defining the space of the configurations of the mechanical system whose definition is given later;
- $\mathbf{J}_{\mathbf{q}}$ is the Jacobian of the homogeneous constrain equations deriving from the kinematic joints in the mechanical system;
- $\boldsymbol{\lambda}$ is the Lagrangian multipliers vector
- $\mathbf{Q}_{\star}$ is the vector of the generalized forces exchanged by the $\star$ wheel on each coordinate; the meaning and the values of $\mathbf{Q}_{\star}$ are discussed later, as the wheel contact model is introduced.

Kinetic and potential energies

As aforementioned, the Lagrangian function $\mathscr{L}$ is defined as

$$\mathscr{L} = \sum_{\sim=F,B} T_{\sim} - V \tag{3.34}$$

where $T_\sim$ is the kinetic energy of the $\sim$ module (front and back), and V is gravity potential forces exerted on the bodies of the system.

The kinetic energy $T_\sim$ of the front and back modules are obtained as

$$T_\sim = \frac{1}{2}\dot{\mathbf{p}}_\sim^T m_\sim \dot{\mathbf{p}}_\sim + \frac{1}{2}\boldsymbol{\omega}_\sim^T \mathbf{I}_\sim \boldsymbol{\omega}_\sim \tag{3.35}$$

where $m_\sim$ is mass of the $\sim$ module and $\mathbf{I}_\sim$ is its inertia matrix with respect to the fixed reference frame, namely $\mathbf{I}_\sim = \mathbf{R}_\sim {}^{\{\sim\}}\mathbf{J}_\sim \mathbf{R}_\sim^T$ with ${}^{\{\sim\}}\mathbf{I}_\sim$ being the diagonal principal inertia matrix of the module. To simplify the model, the small angle hypothesis is done for rotations $\alpha_\sim$ and $\gamma_\sim$, therefore, the inertia matrix can be written by using only the yaw rotation $\psi_\sim$, thus

$$\mathbf{I}_\sim = \mathbf{R}_{z,\psi_\sim} \mathrm{diag}\left(\mathrm{I_{x,\sim}}, \mathrm{I_{y,\sim}}, \mathrm{I_{z,\sim}}\right) \mathbf{R}_{z,\psi_\sim}^T \tag{3.36}$$

Also, the modules centres of mass are also assumed to be positioned at the origin of the relevant reference frame $\{\sim\}$ for the sake of simplicity. Hence, the two velocity vectors $\dot{\mathbf{p}}_\sim$ and $\dot{\boldsymbol{\omega}}_\sim$ can be easily obtained as

$$\dot{\mathbf{p}}_\sim = \begin{bmatrix} \dot{x}_\sim \\ \dot{y}_\sim \\ \dot{z}_\sim \end{bmatrix} \tag{3.37}$$

and

$$\boldsymbol{\omega}_\sim = \begin{bmatrix} \dot{\alpha}_\sim \cos\gamma_\sim \cos\psi_\sim - \dot{\beta}_\sim \sin\psi_\sim \\ \dot{\alpha}_\sim \cos\gamma_\sim \sin\psi_\sim + \dot{\beta}_\sim \cos\psi_\sim \\ \dot{\psi}_\sim - \dot{\alpha}_\sim \sin\gamma_\sim \end{bmatrix} \tag{3.38}$$

Considering small pitch and roll rotations, the angular velocity $\boldsymbol{\omega}_\sim$ simplifies as

$$\boldsymbol{\omega}_\sim = \begin{bmatrix} \dot{\alpha}_\sim \cos\psi_\sim - \dot{\gamma}_\sim \sin\psi_\sim \\ \dot{\alpha}_\sim \sin\psi_\sim + \dot{\gamma}_\sim \cos\psi_\sim \\ \dot{\psi}_\sim \end{bmatrix} \tag{3.39}$$

The contributions of the wheels attached to the module to the kinetic energy is significant. If the rocker motion is neglected, part of their contribution is related to the kinematics of the module itself since they share the same velocity. Thus, it is possible to modify the inertial parameters of the front and back chassis to integrate

such a consideration. That is

$$\begin{aligned} m^*_{\sim} &= m_{\sim} + 4m_w \\ I^*_{x,\sim} &= I_{x,\sim} + 4I_{w,x} + 2m_w i_y^2 \\ I^*_{z,\sim} &= I_{z,\sim} + 4I_{w,z} + 2m_w \left(i_x^2 + i_y^2\right) \end{aligned} \tag{3.40}$$

where m_w is the mass of a wheel, $I_{w,x}$ and $I_{w,z}$ are the inertia matrix components computed with respect to a reference frame centered at the wheel centre of mass and oriented as $\{\sim\}$. All wheels have been considered identical. At last, the geometry parameters i_x and i_y respectively represent the module wheelbase and its transversal track, as depicted in Figure 3.10. Table 3.1 lists all relevant inertial parameters. The masses were measured whereas the inertia components were estimated by the CAD software.

Table 3.1 Agri.Q relevant inertial parameters

Parameter	**Value**	**Parameter**	**Value**
m^*_F	$66.1\,\mathrm{kg}$	m^*_B	$45.9\,\mathrm{kg}$
$I_{F,x}$	$5.729\,\mathrm{kg\,m^2}$	$I_{B,x}$	$2.604\,\mathrm{kg\,m^2}$
$I_{F,y}$	$5.729\,\mathrm{kg\,m^2}$	$I_{B,y}$	$2.604\,\mathrm{kg\,m^2}$
$I_{F,z}$	$9.167\,\mathrm{kg\,m^2}$	$I_{B,x}$	$4.167\,\mathrm{kg\,m^2}$
$I_{w,x} = I_{w,y}$	$0.155\,\mathrm{kg\,m^2}$	$I_{w,y}$	$0.038\,\mathrm{kg\,m^2}$

It is worth noting that the model ignores the likelihood that the wheels connected to their rocker move differently due to the simplified kinematics assumed for the rocker. From the standpoint of kinetic energy, this is a reasonable assumption, yet it may be important in terms of the vertical force produced by each wheel on the ground. This is now being investigated, even though the findings that will be presented later show that such simplification does not preclude the model from accurately following the experimental data.

The rotation of the wheels around their own axes would be investigated later since it is relevant for the developed transmission model. Also, the soil-tyre contact model is critical regarding the exchanged forces. These forces have an impact on the actual actuation workload as well as the robot overall behaviour, in particular along curved paths. As a result, it is important to estimate the motor-to-wheels power flow as accurately as possible with the aim of investigating wheels sliding and their contribution to robot dynamics.

The vector of the generalized coordinates is defined as

$$\mathbf{q} = \begin{bmatrix} \mathbf{q}_F \\ \mathbf{q}_B \end{bmatrix} \tag{3.41}$$

where

$$\mathbf{q}_{\sim} = \begin{bmatrix} x_{\sim} & y_{\sim} & z_{\sim} & \alpha_{\sim} & \gamma_{\sim} & \psi_{\sim} & \vartheta_{M\sim R} & \vartheta_{M\sim L} \end{bmatrix}^T \tag{3.42}$$

where $(x_{\sim},\ y_{\sim},\ z_{\sim})$ and $(\alpha_{\sim},\ \gamma_{\sim},\ \psi_{\sim})$ are respectively the coordinate and the attitude of $\{\sim\}$ in the global reference frame, whereas $\vartheta_{M\sim R}$ and $\vartheta_{M\sim L}$ are the rotation angles of the right and left motors respectively, whose derivatives are the motor angular velocities $\omega_{M\sim R}$ and $\omega_{M\sim L}$. The influence of such coordinates on the robot dynamics is described later as the transmission model is defined.

The potential energy V in Eq.(3.34) only considers the gravitational potential. Although it should be part of the potential energy, the energy component related to the vertical stiffness of the wheels is instead considered within the contact force model with the ground. Therefore, by considering as a reference the origin of the global reference frame, it is:

$$V = \sum_{\sim=F,B} m^*_{\sim} \mathbf{g}^T \mathbf{p}_{\sim} \tag{3.43}$$

where $\mathbf{g} = \begin{bmatrix} g_x & g_y & g_z \end{bmatrix}^T$ is the gravity acceleration vector and, thus, $\|\mathbf{g}\| = 9.81\,\mathrm{m\,s^{-2}}$. By appropriately varying the components of $\mathbf{g}$ it is also possible to replicate various sloping surfaces.

Kinematic constraints

As stated before, the articulated robot Agri.Q is made up of distinct front and rear modules linked by a universal joint. This kind of kinematic pair is made up of two revolute joints with perpendicular axes that cross at the connecting point **O**. The first revolute is parallel to $\hat{\mathbf{z}}_F$ and corresponds to the joint J_delta, whereas the second one is parallel to $\hat{\mathbf{x}}_B$ and correspond to the joint J_{α_B}. Hence, the resulting constraint equations are

$$\mathbf{\Phi} = \begin{bmatrix} \mathbf{p}_F + \mathbf{R}_F{}^{\{F\}}\mathbf{O} - \mathbf{p}_B - \mathbf{R}_B{}^{\{B\}}\mathbf{O} \\ \begin{bmatrix} 0 & 0 & 1 \end{bmatrix} \mathbf{R}_F^T \mathbf{R}_B \begin{bmatrix} 1 & 0 & 0 \end{bmatrix}^T \end{bmatrix} \tag{3.44}$$

where the first three rows ensure that the point **O** is part of both modules, while the fourth constrains the two axes of the universal joint to remain perpendicular (i.e., z axis of $\{F\}$ and x axis of $\{B\}$). This is equivalent to constraining the last row of $\mathbf{R}_F^T$, which is the last column of $\mathbf{R}_F$, to be perpendicular to the first column of $\mathbf{R}_B$. Consequently, the Jacobian matrix $\mathbf{J_q}$ is computed by differentiation of Eq.(3.44), that is

$$\mathbf{J_q} = \begin{bmatrix} \dfrac{\partial \mathbf{\Phi}_1}{\partial q_1} & \cdots & \dfrac{\partial \mathbf{\Phi}_1}{\partial q_{16}} \\ \vdots & \ddots & \vdots \\ \dfrac{\partial \mathbf{\Phi}_4}{\partial q_1} & \cdots & \dfrac{\partial \mathbf{\Phi}_4}{\partial q_{16}} \end{bmatrix} \tag{3.45}$$

which results in a 4×16 matrix.

3.2.1 Tyre contact forces

In modelling the dynamics of wheeled vehicles, the contact forces caused by the wheel-ground interaction are crucial. In most studies on wheel slip and skid, the Pacejka's Magic Formula [248] is employed to represent such forces. The Magic Formula tyre model is an experimental model whose parameters are identified experimentally. The Pacejka Magic Formula appears as follows in its most generic formulation

$$\frac{Y(X)}{F_z} = D \sin\left(C \arctan\left(BX - E\left(BX \ \arctan\left(BX\right)\right)\right)\right) \tag{3.46}$$

where F_z is the tyre normal force, Y can be either the tyre longitudinal force, the lateral force, or even an aligning torque, while X represents the longitudinal slip ratio, the slip angle, or the wheel camber angle. B, C, D, and E are the experimental coefficient. In particular, D is the peak value of $\frac{Y(X)}{F_z}$, whereas the product BCD is the stiffness related to X. The first iterations of the Magic Formula consider each component (longitudinal, lateral, and aligning torque) independent from the other, however, more recent versions of Pacejka's Magic Formula correctly combine their effects.

Unfortunately, identifying the experimental coefficients may be challenging both due to the nature of the actual tests required to obtain them and their number. Although in the automotive field there are some datasets available for some generic

tyres, data about bicycle tyres, like the ones mounted on Agri.Q, are scarce. Moreover, among the few experimental studies on the characterisation of bicycle tyres, the tyre longitudinal behaviour is completely neglected, and the assumption made by Maier et al. in [249] of using the dataset of a 120/70 ZR17 motorbike tyre to represent the longitudinal behaviour is shared among most of the studies. Dressel and Rahman [250] and Doria et al. [251] are the two works where most tyres were characterised on asphalt regarding the side slip and the camber angle effects. Both studies found quite similar side-slip coefficients, while the camber angle ones differ a bit. Bulsink et al. [252] developed a bicycle model based on the data in [251] and have also provided the data required to define the same tyre on ADAMS. As said before, for the longitudinal characteristics, the hypothesis of using motorbike tyre data is adopted, like in other works. More recently, Dressel and Sadauckas [253] conducted a characterization of four modern mountain bike tyres studying the effect of side-slip, camber, void ratio of tyre knobs, and tyre pressure.

Agri.Q mounts 16" $\times$ 1.95" mountain bike tyre, thus, initially a simpler model based on wheel normal, longitudinal, and lateral stiffness was developed and used. Such model was already validated in [244] for another smaller articulated robot with a similar architecture. Later, a Pacejka's Magic Formula model based on the data provided by [252] was implemented in ADAMS too.

In the following, the custom contact model is described. In the next chapter, the related experimental identification of the coefficients is reported. Regardless of its simplicity compared to Pacejka's Magic Formula, the proposed tyre-ground contact model takes into account the following phenomena:

- the longitudinal force imposed on the ground by the tyre as a result of wheel rotation. In particular, this force component is proportional to the tyre-ground relative velocity at the contact area centre;
- the tyre lateral force proportional to its lateral velocity; this phenomenon is particularly significant for Agri.Q and other articulated robots with similar architecture;
- the vertical elastic force proportional to the tyre vertical deformation;
- A torque opposed to the rotation sense is produced by a rolling resistance described as a non-symmetric distribution of pressure inside the contact region;

this phenomenon is formalized as a displacement in the longitudinal direction of the forces application point.

Referring to Figure 3.11, the considered force components are computed as

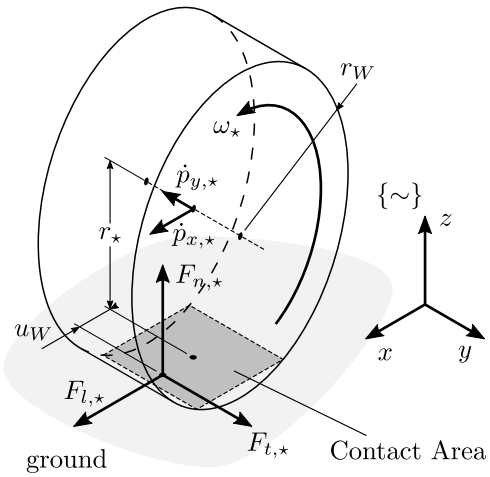

Fig. 3.11 Tyre-ground contact model

$$ {}^{\{\sim\}}\mathbf{F}_\star = \begin{bmatrix} F_{l,\star} \\ F_{t,\star} \\ F_{n,\star} \end{bmatrix} = \begin{bmatrix} k_l \left(r_W \omega_\star - \dot{p}_{x,\star} \right) \\ -k_t \dot{p}_{y,\star} \\ k_n \left(r_W - r_\star \right) \end{bmatrix} \tag{3.47} $$

where

- the subscript $\star$ identifies each wheel of the articulated robot equivalently to the previously introduced subscript $W \sim\sim\sim$, specifying which module of the robot (front and back, F and B), which side of the module (right and left, R and L), and which wheel within the rocker (front and back, F and B);
- k_n, k_t and k_l are the vertical, transversal and longitudinal tyre stiffness respectively; such parameters must be identified and strictly depend on the contact condition;
- $r_\star$ is the actual wheel radius, depending on the load applied on the $\star$ wheel;
- $\dot{p}_{x,\star}$ and $\dot{p}_{y,\star}$ are the longitudinal and transversal velocity components; Despite the fact that their values are dependent on wheel attitude, they were assumed

to be identical to those of the wheel connection point to the rocker (i.e., the wheel hub), which is a reasonable assumption for small roll angles $\alpha_{\sim}$;

- $\omega_{\star}$ is the wheel angular rate; such value is directly related to the respective motor velocity $\omega_{M\sim\sim}$ and, later on, it is described as a function of the locomotion unit transmission.

The vertical dynamics of the wheels have been ignored due to the robots low speeds and the lack of an elastic suspension system. Nevertheless, given the importance of tyre-ground contact in motion dynamics, the model was given a force saturation effect analogous to the Coulomb classic friction model. In particular, considering the force component of each wheel lying on the ground plane $F_{h,\star} = \sqrt{F_{l,\star} + F_{t,\star}}$, The forces exerted on the wheel-ground contact were changed as follows

$$F_{h,\star} > \mu_s F_{n,\star} \quad \Rightarrow \quad \begin{cases} F^*_{l,\star} = \mu_d F_{n,\star} \frac{F_{l,\star}}{F_{h,\star}} \\ F^*_{t,\star} = \mu_d F_{n,\star} \frac{F_{t,\star}}{F_{h,\star}} \end{cases} \tag{3.48}$$

The eight forces computed by Eq.(3.47) act on the corresponding $\mathbf{Q}_{\star}$ vector, which is computed using the virtual works concept as follows

$$\delta \mathbf{q}^T \mathbf{Q}_{\star} = \delta \mathbf{p}_{\star}^T \mathbf{F}_{\star} \Rightarrow \mathbf{Q}_{\star} = \sum_i \frac{\partial \mathbf{p}_{\star}^T}{\partial q_i} \mathbf{F}_{\star} \tag{3.49}$$

where the vectors $\mathbf{p}_{\star}$ and $\mathbf{F}_{\star}$ must be represented in the same reference frame, thus the actual orientation of each wheel has to be considered. For the sake of simplicity, the pitch and roll rotations of the modules have been ignored, since they only have a minor impact on the force components. Thus

$$\mathbf{Q}_{\star} = \sum_i \frac{\partial \mathbf{p}_{\star}^T}{\partial q_i} \mathbf{R}_{z,\psi_{\sim}}{}^{\{\sim\}} \mathbf{F}_{\star} \tag{3.50}$$

Also, the tyre-ground forces application point is defined as

$$\mathbf{p}_{\star} = \mathbf{p}_{\sim} + \mathbf{R}_{z,\psi_{\sim}} \mathbf{R}_{x,\alpha_{\sim}}{}^{\{\sim\}} \mathbf{p}_{\star} \tag{3.51}$$

It worth mentioning that the pitch angle $\gamma_{\sim}$ is ignored for wheel orientation since the rockers are not affected by this rotation because they are attached to the chassis

through a passive revolute joint parallel to the y axis of the relevant reference frame $\{\sim\}$. In addition, the assumption of small rotations $\alpha_s im$ simplifies the equation even further.

The eight constant vectors ${}^{\{\sim\}}\mathbf{p}_{\star}$ defining the position of the wheel-ground forces application point with respect to the corresponding module reference frame are

$$ {}^{\{\sim\}}\mathbf{p}_{\sim RF} = \begin{bmatrix} \frac{i_x}{2} + u_W & -\frac{i_y}{2} & 0 \end{bmatrix}^T \tag{3.52} $$

$$ {}^{\{\sim\}}\mathbf{p}_{\sim RB} = \begin{bmatrix} -\frac{i_x}{2} + u_W & -\frac{i_y}{2} & 0 \end{bmatrix}^T \tag{3.53} $$

$$ {}^{\{\sim\}}\mathbf{p}_{\sim LF} = \begin{bmatrix} \frac{i_x}{2} + u_W & \frac{i_y}{2} & 0 \end{bmatrix}^T \tag{3.54} $$

$$ {}^{\{\sim\}}\mathbf{p}_{\sim LB} = \begin{bmatrix} -\frac{i_x}{2} + u_W & \frac{i_y}{2} & 0 \end{bmatrix}^T \tag{3.55} $$

For simplicity's sake, the wheels centre and the origin of the corresponding referece frame $\{\sim\}$ were considered coplanar, thus ${}^{\{\sim\}}p_{z,\star} = 0$. Also, the displacement of the force application point in relation to the wheel rolling resistance is represented by the u_W parameter. As is well known, the length of such a contact is a function of the contact characteristics, particularly the wheel radius r_W and rolling resistance coefficient. Therefore,

3.2.2 Transmission model

As previously stated, the transmission power flow is critical for the modelling of mobile robots with a large number of wheels since the number of sliding tyre-soil contacts has a significant impact on their dynamic behaviour. The power flow model is graphically shown in Figure 3.12 and was used to achieve this goal.

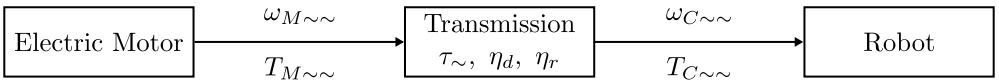

Direct Power Flow: $T_{M\sim\sim}\omega_{M\sim\sim} \geq 0 \ \Rightarrow \ \eta_d T_{M\sim\sim}\omega_{M\sim\sim} = T_{C\sim\sim}\omega_{C\sim\sim}$

Reverse Power Flow: $T_{M\sim\sim}\omega_{M\sim\sim} < 0 \ \Rightarrow \ T_{M\sim\sim}\omega_{M\sim\sim} = \eta_r T_{C\sim\sim}\omega_{C\sim\sim}$

Fig. 3.12 Transmission power flow diagram

$$T_{M\sim\sim} - T_{C\sim\sim}\frac{1}{\tau_\sim \eta} = \left(J_M + J_W \frac{1}{\tau_\sim^2 \eta}\right)\dot{\omega}_{M\sim\sim} \tag{3.56}$$

where

- $T_{M\sim\sim}$ is the torque exerted by the motor of the module $\sim$ at the side $\sim$;
- T_C $\sim\sim$ is the torque corresponding to the contact forces of both wheels of the same locomotion unit; for the four motors it is:

$$T_{CFR} = r_W\left(F_{l,FRF} + F_{l,FRB}\right) + u_W\left(F_{n,FRF} + F_{n,FRB}\right) \tag{3.57}$$
$$T_{CFL} = r_W\left(F_{l,FLF} + F_{l,FLB}\right) + u_W\left(F_{n,FLF} + F_{n,FLB}\right) \tag{3.58}$$
$$T_{CBR} = r_W\left(F_{l,BRF} + F_{l,BRB}\right) + u_W\left(F_{n,BRF} + F_{n,BRB}\right) \tag{3.59}$$
$$T_{CBL} = r_W\left(F_{l,BLF} + F_{l,BLB}\right) + u_W\left(F_{n,BLF} + F_{n,BLB}\right) \tag{3.60}$$

- $\tau_\sim$ is the reduction ratio of the transmission of the module considering the gearbox and the drive chain. Particularly, $\tau_F = 47.64$ and $\tau_F = 28.93$;
- J_M and J_W respectively are the inertial parameters of the motor rotor and of the attached wheels;
- η is the efficiency (< 1) of the transmission; such parameter assumes different meanings for direct and reverse power flows:

$$\begin{aligned} T_{M\sim\sim}\omega_{M\sim\sim} \geq 0 \Rightarrow \eta = \eta_d \\ T_{M\sim\sim}\omega_{M\sim\sim} < 0 \Rightarrow \eta = \frac{1}{\eta_r} \end{aligned} \tag{3.61}$$

  with η_d efficiency of the transmission when the power flows from the motor to the wheels, and η_r efficiency when the motor acts as a brake; such distinction is important because the difference among the values of η_d and η_r might be significant when the transmission ratio $\tau_\sim \ll 1$. In particular, the efficiency parameters have been assumed $\eta_d = 0.6$ and $\eta_r = 0.35$ based on the implemented locomotion unit transmission.

- $\dot{\omega}_{M\sim\sim} = \ddot{\vartheta}_{M\sim\sim}$ is the motor angular acceleration.

Four equations, one for each motor, are obtained using Eq.(3.56) to be added to the sixteen non trivial equations from Eq.(3.34).

In the next chapter, it is reported how the model parameters were identified together with some analysis of the identified model of Agri.Q

3.2.3 ADAMS multibody dynamic modelling

To address the limitation of the latter dynamic model, for example, among the others, the simplification of the small roll and pitch rotations, the rotation of the rockers about their passive pivot, two multibody models of Agri.Q have been created employing ADAMS by MSC, a modelling and simulation software for multibody systems.

The models are based on the available CAD of Agri.Q, where all joints and constraints have been defined accordingly. By doing so, the simulation software can easily handle the phenomena previously neglected. Another improvement from the previous analytic model is the modelling of realistic locomotion units, in particular how the motor drivers handle current saturation. This allows for more realistic simulations since Agri.Q motors tend to saturate during tight turns, as it is shown later.

The main difference between the two models is how the contact forces were defined. One model use the simplified contact model described before, while the second model uses the Pacejka's Magic Formula with the parameters provided by [252].

3.3 Robotic arm kinematic modelling

Agri.Q mounts a commercial redundant 7 DOF robotic arm at the end of its central chassis. As discussed in the previous chapter, such a configuration allows adapting the robotic arm workspace to the required task exploiting the mobile base mobility, in particular, the pitch motion of the central chassis. Although the synchronised motions of the mobile base and the robotic arm could lead to interesting applications, the precision of the mobile base motions and the relatively low speed of the pitching motion make separate control of both elements more suitable. Thus, this section focuses on the robotic arm alone, whereas the integration of the whole mobile

manipulator concept is briefly introduced but most of the topic will be treated in future.

The manipulator can be modelled as a kinematic chain consisting of eight members (whose lengths are collected in Table 2.4), which are connected by seven revolute joints (Figure 3.13a). The first member, member 0, is the base of the manipulator and is fixed to the central frame of Agri.Q. Member 7, on the other hand, is the manipulator end-effector. For the study of direct kinematics, the Denavit-Hartenberg convention was used, in analogy with the Kinova manual (Figure 3.13b), as reported in Table 3.2, where $\boldsymbol{\theta} = \left[\theta_1, \ldots, \theta_7\right]^T$ are the rotation angles of each revolute joint.

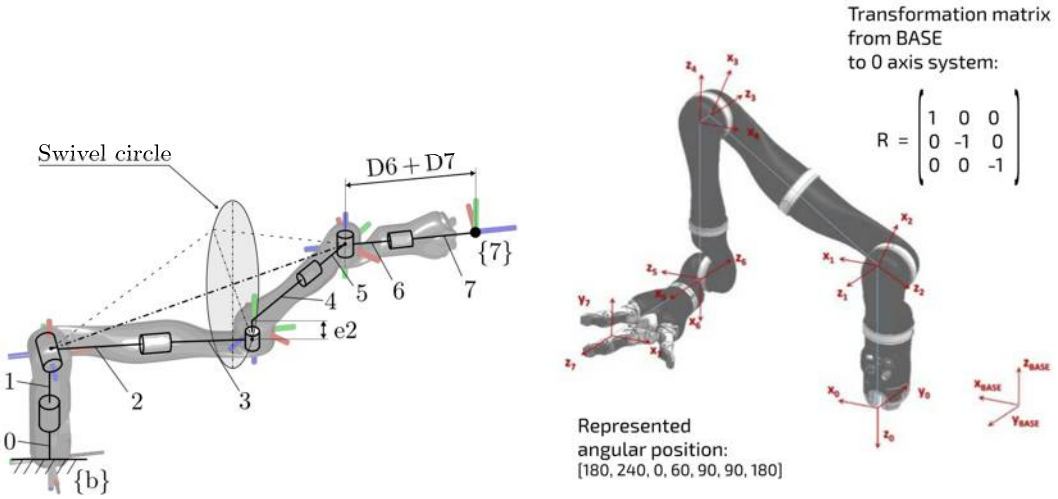

(a) (b)

Fig. 3.13 (a) Kinova Jaco2 kinematic diagram. (b) Kinova Jaco2 reference frames as defined in [1]

Table 3.2 *Kinova Jaco2 Denavit-Hartenberg parameters*

Link i	a_i	α_i	d_i	θ_i
1	0	$-\pi/2$	-D1	θ_1
2	0	$-\pi/2$	0	θ_2
3	0	$-\pi/2$	-(D2+D3)	θ_3
4	0	$-\pi/2$	-e2	θ_4
5	0	$-\pi/2$	-(D4+D5)	θ_5
6	0	$-\pi/2$	0	θ_6
7	0	π	-(D6+D7)	θ_7

Therefore, the following homogeneous transformation can be defined

$$
{}^{b}\mathbf{T}_1 = \begin{bmatrix} c_1 & 0 & -s_1 & 0 \\ s_1 & 0 & c_1 & 0 \\ 0 & -1 & 0 & -D1 \\ 0 & 0 & 0 & 1 \end{bmatrix} \tag{3.62}
$$

$$
{}^{1}\mathbf{T}_2 = \begin{bmatrix} c_2 & 0 & -s_2 & 0 \\ s_2 & 0 & c_2 & 0 \\ 0 & -1 & 0 & 0 \\ 0 & 0 & 0 & 1 \end{bmatrix} \tag{3.63}
$$

$$
{}^{2}\mathbf{T}_3 = \begin{bmatrix} c_3 & 0 & -s_3 & 0 \\ s_3 & 0 & c_3 & 0 \\ 0 & -1 & 0 & -(D2+D3) \\ 0 & 0 & 0 & 1 \end{bmatrix} \tag{3.64}
$$

$$
{}^{3}\mathbf{T}_4 = \begin{bmatrix} c_4 & 0 & -s_4 & 0 \\ s_4 & 0 & c_4 & 0 \\ 0 & -1 & 0 & -e2 \\ 0 & 0 & 0 & 1 \end{bmatrix} \tag{3.65}
$$

$$
{}^{4}\mathbf{T}_5 = \begin{bmatrix} c_5 & 0 & -s_5 & 0 \\ s_5 & 0 & c_5 & 0 \\ 0 & -1 & 0 & -(D4+D5) \\ 0 & 0 & 0 & 1 \end{bmatrix} \tag{3.66}
$$

$$
{}^{5}\mathbf{T}_6 = \begin{bmatrix} c_6 & 0 & -s_6 & 0 \\ s_6 & 0 & c_6 & 0 \\ 0 & -1 & 0 & 0 \\ 0 & 0 & 0 & 1 \end{bmatrix} \tag{3.67}
$$

$$
{}^{6}\mathbf{T}_7 = \begin{bmatrix} c_7 & s_7 & 0 & 0 \\ s_7 & -c_7 & 0 & 0 \\ 0 & 0 & -1 & -(D6+D7) \\ 0 & 0 & 0 & 1 \end{bmatrix} \tag{3.68}
$$

with $s_n = \sin\theta_n$ and $c_n = \cos\theta_n$, where $n = 1,\ldots,7$. By properly combining them, it is possible to obtain the transformation between any reference frames of the manipulator.

For the next section is useful to define the following transformations

$$
\begin{aligned}
{}^{b}\mathbf{T}_3 &= {}^{b}\mathbf{T}_1\,{}^{1}\mathbf{T}_2\,{}^{2}\mathbf{T}_3 = \\
&= \begin{bmatrix}
s_1 s_3 + c_1 c_2 c_3 & c_1 s_2 & c_3 s_1 - c_1 c_2 s_3 & c_1 s_2 \,(D2+D3) \\
c_2 c_3 s_1 - c_1 s_3 & s_1 s_2 & -c_1 c_3 - c_2 s_1 s_3 & s_1 s_2 \,(D2+D3) \\
-c_3 s_2 & c_2 & s_2 s_3 & c_2 \,(D2+D3) - D1 \\
0 & 0 & 0 & 1
\end{bmatrix}
\end{aligned}
\tag{3.69}
$$

and

$$
\begin{aligned}
{}^{4}\mathbf{T}_7 &= {}^{4}\mathbf{T}_5\,{}^{5}\mathbf{T}_6\,{}^{6}\mathbf{T}_7 = \\
&= \begin{bmatrix}
s_5 s_7 + c_5 c_6 c_7 & c_5 c_6 s_7 - c_7 s_5 & c_5 s_6 & c_5 s_6 \,(D6+D7) \\
c_6 c_7 s_5 - c_5 s_7 & c_5 c_7 + c_6 s_5 s_7 & s_5 s_6 & s_5 s_6 \,(D6+D7) \\
-c_7 s_6 & -s_6 s_7 & c_6 & c_6 \,(D6+D7) - D5 - D4 \\
0 & 0 & 0 & 1
\end{bmatrix}
\end{aligned}
\tag{3.70}
$$

Inverse kinematics

The following part is devoted to solving the inverse kinematics of the robotic manipulator, i.e. calculating the joint sizes required to obtain the desired end-effector pose. Since the robotic arm is redundant because the number of DOFs is larger than the dimensions (6) of the operational space, the inverse kinematics problem has ∞^1 solutions that can be computed by employing both analytical and numerical approaches. Here a closed-form solution based on the concept of swivel angle Φ [254, 255].

Figure 3.14 shows the manipulator with an alternative representation as it is composed of

- a spherical joint S at the intersection of first 3 revolute joints axes (rotations $\theta_1,\ \theta_2$, and θ_3);
- the elbow revolute joint E that define the rotation θ_4;
- a second spherical joint W at the intersectoin of the last 3 revolute joints axes (rotations $\theta_5,\ \theta_6$, and θ_7).

Consequently, by employing the kinematic decoupling, it is possible to solve for $\theta_1,\ \theta_2,\ \theta_3$ and θ_4 defining the end-effector position and for $\theta_5,\ \theta_6$, and θ_7 using

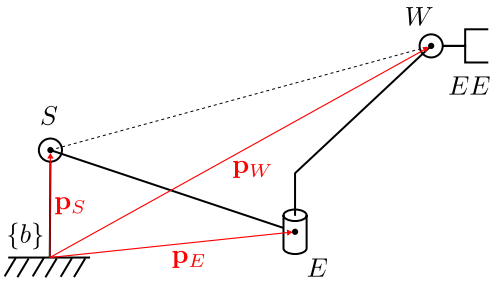

Fig. 3.14 Alternative kinematic representation of the manipulator

the end-effector orientation. In particular, by knowing the desired pose of the end effector $\mathbf{p}_{EE}$ it is possible to define the position $\mathbf{p}_W$ of the second spherical joint W

$$\mathbf{p}_W = \mathbf{p}_{EE} - (D6 + D7)\hat{\mathbf{z}}_7 \tag{3.71}$$

where $\hat{\mathbf{z}}_7$ is the z axis of the reference frame $\{7\}$ of the manipulator end-effector. Consequently, it is possible to project W onto the plane S_1 that contains the points S and E an perpendicular to the elbow joint axis (or equivalently to the offset length $e2$). The resulting point is W'. In such plane, the robotic arm is equivalent to a dyad composed of two links, namely $U = D2 + D3$ and $L = D4 + D5$, connected by the elbow revolute joint, as represented in Figure 3.15.

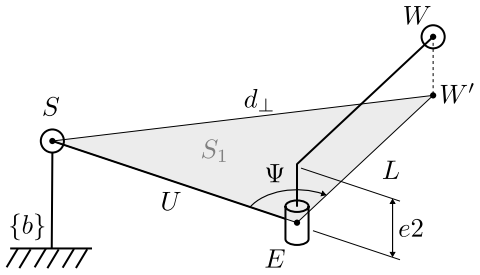

Fig. 3.15 Plane S_1 of the manipulator

Taking Figure 3.15 as reference, it is possible to define the distance $d_\perp$ as

$$d_\perp = \sqrt{|\mathbf{p}_W - \mathbf{p}_S|^2 + e2^2} \tag{3.72}$$

and the angle Ψ as

$$\Psi = \pm \arccos\left(\frac{L^2 + U^2 - d_\perp}{2UL}\right) \tag{3.73}$$

It is also possible to identify a plane S_2 as the one containing the points S, E, and W that is perpendicular to the swivel circle (Figure 3.16a). The swivel circle is the locus of all feasible elbow positions given $\mathbf{p}_W$ whose centre C lies along the segment joining points S and W and defines a reference frame whose axes are oriented as follow

$$\hat{\mathbf{n}} = \frac{\mathbf{p}_W - \mathbf{p}_S}{|\mathbf{p}_W - \mathbf{p}_S|}, \tag{3.74}$$

$$\hat{\mathbf{u}} = \frac{\hat{\mathbf{a}} - (\hat{\mathbf{a}} \cdot \hat{\mathbf{n}})\hat{\mathbf{n}}}{|\hat{\mathbf{a}} - (\hat{\mathbf{a}} \cdot \hat{\mathbf{n}})\hat{\mathbf{n}}|}, \tag{3.75}$$

$$\hat{\mathbf{v}} = \hat{\mathbf{n}} \times \hat{\mathbf{u}} \tag{3.76}$$

where $\hat{\mathbf{n}}$ is by definition the axis of the swivel circle, $\hat{\mathbf{a}}$ is an aribitrary unit vector, of which the component parallel to $\hat{\mathbf{n}}$ is eliminated in order to obtain the unit vector $\hat{\mathbf{u}}$ in the plane of the swivel circle. The unit vector $\hat{\mathbf{v}}$ is orthogonal to both.

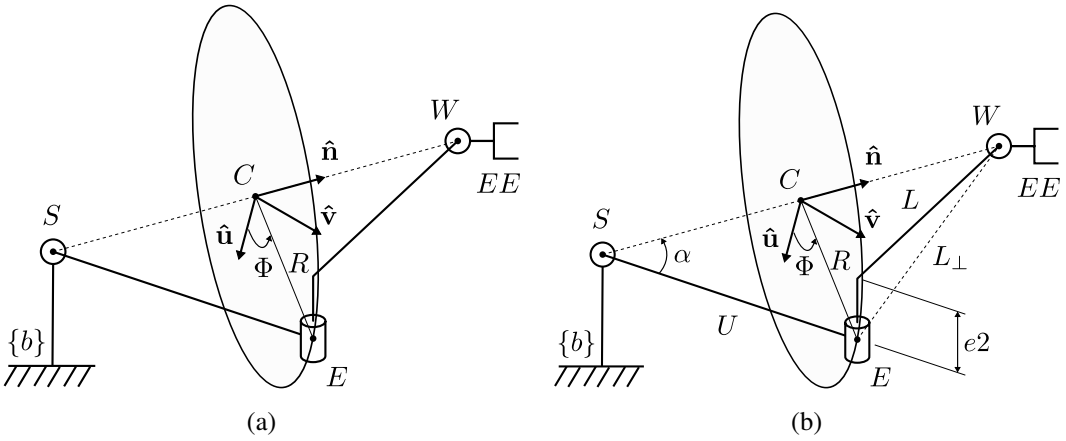

Fig. 3.16 (a) Manipulator swivel circle and its reference frame. (b) Relevant geometric quantities

From Figure 3.16b it is possible to define the following quantities

$$L_\perp = \sqrt{L^2 + e2^2}, \tag{3.77}$$

$$\alpha = \pm \arccos\left(\frac{U^2 + |\mathbf{p}_W - \mathbf{p}_S|^2 - L_\perp}{2|\mathbf{p}_W - \mathbf{p}_S|U}\right), \tag{3.78}$$

$$\mathbf{p}_C = \mathbf{p}_S + U\cos(\alpha)\hat{\mathbf{n}}, \tag{3.79}$$

$$R = U\sin\alpha \tag{3.80}$$

where $L_\perp$ is the projection of L into S_2. Such quantities together with the swivel angle Φ define the location of E as follows

$$\mathbf{p}_E = \mathbf{p}_C + R\left(\cos\left(\Phi\right)\hat{\mathbf{u}} + \sin\left(\Phi\right)\hat{\mathbf{v}}\right) \tag{3.81}$$

Finally, given $\mathbf{p}_W$, $\mathbf{p}_E$, and the end-effector orientation, it is possible to solve the manipulator inverse kinematics by computing $\boldsymbol{\theta} = \left[\theta_1, \ldots, \theta_7\right]^T$. Regarding θ_1 and θ_2, by considering that the translation vector in ${}^b\mathbf{T}_3$ is $\mathbf{p}_E$ Eq.(3.69), it turns

$$\theta_1 = -\arctan\left(\frac{y_{p_E}}{x_{p_E}}\right), \tag{3.82}$$

$$\theta_2 = \arctan\left(\frac{\sqrt{x_{p_E}^2 + y_{p_E}^2}}{D1 - z_{p_E}}\right) \tag{3.83}$$

Concerning θ_3, it is sufficient to note that

$$\mathbf{p}_W + L\hat{\mathbf{z}}_4 = \mathbf{p}_E + e2\hat{\mathbf{z}}_3 \tag{3.84}$$

where

$$\hat{\mathbf{z}}_3 = \left[-c_1c_2s_3 + s_1c_3,\ s_1c_2s_3 + c_1c_3,\ -s_2s_3\right]^T, \tag{3.85}$$

$$\hat{\mathbf{z}}_4 = \left[-s_4(c_1c_2c_3 + s_1s_3) + c_1s_2c_4,\ -s_4(s_1c_2c_3 + c_1s_3) - s_1s_2c_4 - s_2c_3s_4 - c_2c_4\right]^T \tag{3.86}$$

By solving Eq.(3.85) and Eq.(3.86) for s_3 and c_3, it is possible to compute θ_3 as

$$\theta_3 = \arctan\left(\frac{s_3}{c_3}\right) \tag{3.87}$$

The joint angle θ_4, instead, is by definition

$$\theta_4 = \Psi = \pm\arccos\left(\frac{L^2 + U^2 - d_\perp}{2UL}\right) \tag{3.88}$$

These joint values allow to define the transformation matrix ${}^{b}\mathbf{T}_4$, and thus its inverse ${}^{4}\mathbf{T}_b$. This homogeneous transformation matrix together with the one about the end-effector pose, ${}^{b}\mathbf{T}_7$, is useful to define

$$ {}^{4}\mathbf{T}_7 = {}^{4}\,\mathbf{T}_b\,{}^{b}\mathbf{T}_7 \tag{3.89} $$

From this last matrix, equivalent to Eq.(3.70), it is possible to compute the remaining joint angle as

$$ \theta_5 = \arctan\left(\frac{{}^{4}\mathbf{T}_7(2,3)}{{}^{4}\mathbf{T}_7(1,3)}\right), \tag{3.90} $$

$$ \theta_6 = \arctan\left(\frac{-{}^{4}\mathbf{T}_7(3,2)/\sin\theta_7}{{}^{4}\mathbf{T}_7(3,3)}\right), \tag{3.91} $$

$$ \theta_7 = \arctan\left(\frac{-{}^{4}\mathbf{T}_7(3,2)}{-{}^{4}\mathbf{T}_7(3,1)}\right) \tag{3.92} $$

where ${}^{4}\mathbf{T}_7(i,j)$ is the element of ${}^{4}\mathbf{T}_7$ at the row i and the column j.

Chapter 4

Results, Tests, and Integration

4.1 Agri.Q dynamic behaviour discussion

This part is dedicated to discussing the dynamic behaviour of Agri.Q. First, the experimental identification of some system parameters is described. Then, the results of the identification tests and of the dynamic model are compared and discussed.

4.1.1 Experimental system identification

Given Agri.Q primary mission of monitoring vineyards and crops in general, the rover might be subjected to a range of application scenarios. External elements such as soil unevenness and slopes, ground moisture, and grass prevalence are only a few examples of external factors that might influence robot behaviour. It is difficult to foresee an always valid collection of parameters. Nonetheless, once the model has been proven on a substantial application case, it may be used to build actuation schemes. Thus, as aforementioned, an experimental campaign was performed in order to identify the main system parameters, especially the one related to the tyre-ground contact model. The following is a summary of what has already been presented in [247] about the experimental identification.

For this piece of study, the tests concentrated on identifying the Agri.Q parameters in a rather basic setting, i.e., the tests were conducted on a flat grassy field with little unevenness. The rover was programmed to follow a trajectory made of four phases (Figure 4.1), namely

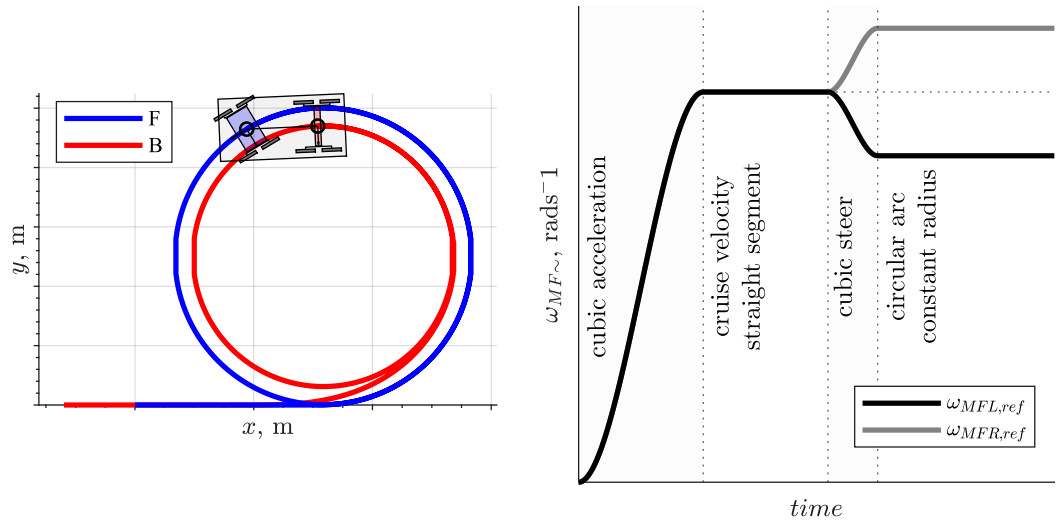

(a) (b)

Fig. 4.1 (a) Example reference kinematic trajectory. Agri.Q is commanded to do several revolutions during the circular path phase (b) Corresponding front traction motor reference velocities

- A transient acceleration phase from standing start to the cruise velocity $v_F = v_{F,cruise}$, where the velocity profile is a cubic function with $\dot{v}_F = 0.5\,\mathrm{m\,s^{-2}}$;
- a short straight segment at cruise speed;
- a quick cubic transient to steer the front module to achieve the cruise yaw rate; $\dot{\psi}_{F,cruise}$
- a circular path with constant radius and constant cruise velocity $v_{F,cruise}$.

The corresponding traction motors velocities were defined accordingly to the kinematic model reported in Section 3.1. Because of the model assumptions, the kinematic model uses a virtual axle with just two wheels per module (one on each side), rather than the real number of wheels, hence any wheel slippage is ignored. Figure 4.1 shows an example test trajectory and the corresponding traction motor velocities.

The robot was operated with varied values of the distribution ratio k_{TA} in a series of experiments with varying velocities and curve radius. In terms of soil evenness, the testing was conducted on a flat grassy field, which was comparable to the envisioned rover operating environment. The ground was virtually quite wet

due to the weather and humidity, providing a broad variety of operating circumstances, from slick patches with wet grass to muddy areas with less thick grass. The predetermined reference trajectory was provided to the front actuation units as mentioned earlier, while the rear motors contributions were determined using k_{TA}, as described in Section 2.6.2. The obtained data set was then utilized to identify the contact parameters for the tyres: the modelled articulated robot was driven by imposing reference quantities that were equal to those recorded on the rover during the experiments.

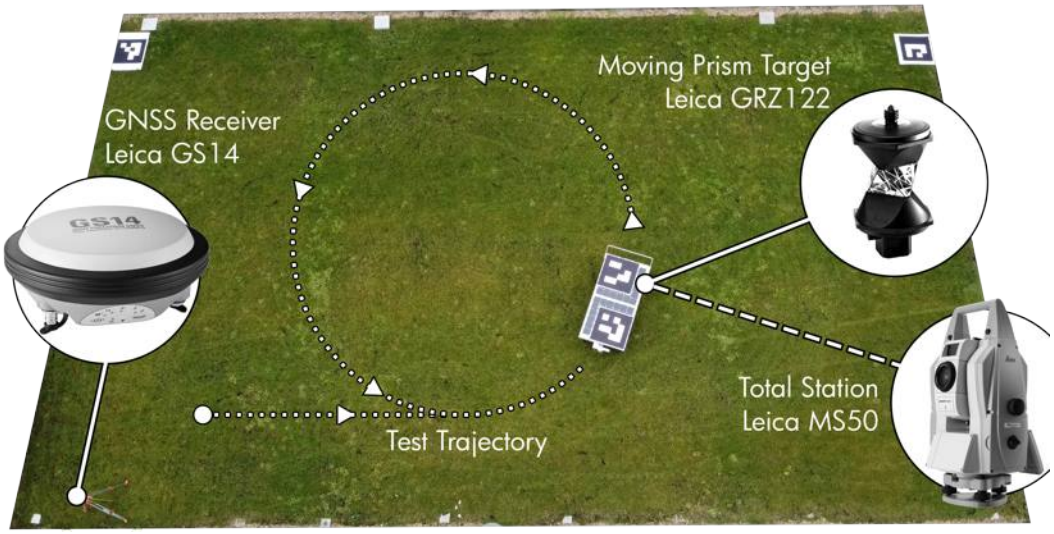

Fig. 4.2 Aerial view of the experimental identification setup

A properly measured reference trajectory is required to perform validation in terms of positioning accuracy. A total station (the Leica MS50 by Leica Geosystems) located on the vertices of a small geo-referenced topographic network tracing a moving 360° prism target (Leica GRZ122) mounted on the edge of the PV panels structure of the rover captured its trajectories, which were used as ground truth. The components of the prism location are in the same reference frame since the network is geo-referenced. The network was geo-referenced by placing two dual-frequency multi-constellation geodetic GNSS receivers (Leica GS14) on the materialised vertices in static acquisition for around an hour. Following that, the observations were post-processed using a differential technique and network corrected, to obtain coordinates tracking with centimetre-level accuracy projected in a cartographic system (WGS84 reference system with the UTM32N projection). An aerial view of the test setup is shown in Figure 4.2. The markers shown in the picture were not utilised

in this study. In fact, the same experimental tests were used to calibrate a visual positioning system based on the usage of a UAV by employing the methods discussed in [256, 257] and tested in [243, 246] with a static camera providing an aerial view of a small robot.

Finally, the estimated contact parameters are listed in Table 4.1 under the assumption that all eight wheels are identical.

Table 4.1 Relevant wheels contact parameters of Agri.Q

Parameter	**Symbol**	**Value**
Tyre longitudinal stiffness	k_l	$2939.81\ \mathrm{N\,s\,m^{-1}}$
Tyre lateral stiffness	k_t	$2039.05\ \mathrm{N\,s\,m^{-1}}$
Tyre vertical stiffness	k_n	$15 \times 10^3\ \mathrm{N\,m^{-1}}$
Rolling friction parameter	u_w	8.32×10^{-3} m
Static friction coefficient	μ_s	0.63
Dynamic friction coefficient	μ_d	0.30

4.1.2 Dynamic behaviour results and discussion

This section collects all relevant insights about the dynamic behaviour of Agri.Q and of articulated robot with a similar architecture presented in previous works. In particular, [243, 244, 246] discussed articulated robot more generally, whereas [247] reported actual experimental data about Agri.Q and its behaviour.

Experimental results

Figure 4.3 shows some comparison data for two trajectories that were not employed in the identification procedure in terms of planned, experimental and simulated trajectories, motor angular velocities, and torques. The experiments (hence referred to as Test 1 and Test 2) were conducted at various cruise velocities ($0.5\,\mathrm{m\,s^{-1}}$ and $1.0\,\mathrm{m\,s^{-1}}$) and intended curve radiuses (2 m and 3 m respectively). As can be seen, the model fits the real trajectories and torques with reasonable precision, and it may be considered verified for the application case under investigation, particularly for low range velocities. Despite this, there is a significant difference between the planned motion and the actual robot trajectory. This is due to at least two obvious

phenomena: on the one hand, the lateral contact forces acting on the tyres shift the robot away from a strictly holonomic behaviour; on the other hand, the driving motors appear to be unable to follow the reference velocity given by the motion planner with accuracy. This is visible in both the ω_{MFL} and ω_{MFR} curves in Figure 4.3, and it is supported by the torque graphs, which indicate that the motor on the outer side of the curve approaches its maximum thrust limit and then saturates to a lower torque, preventing the external wheels from achieving the desired motion in both cases. Also, this issue also affects the odometric trajectory. In fact, since the robot can not achieve the required motor velocities, the odometric trajectory derived from encoder readings does not match the planned kinematic path.

The deviation from the ideal position was determined using the error accumulated by the front module heading angle ψ_F while completing the motion in order to provide a dimensionless parameter to compare the modelled and experimental behaviours. It was utilised in particular e_ψ, which is defined as

$$e_{\psi_F} = \frac{\int_0^{t_f} \left(\psi_F - \psi_{F,ref}\right)\, dt}{\int_0^{t_f} \psi_{F,ref}\, dt} \tag{4.1}$$

where $\psi_{F,ref}$ is the reference front module heading angle, and t_f is the final instant of the simulated test. In order to evaluate the performance considering the Cartesina position of the robot front module, a second parameter, $e_{\mathbf{p}_F}$, was defined as

$$e_{\mathbf{p}_F} = \frac{\|\mathbf{p}_F - \mathbf{p}_{F,ref}\|}{\sigma} \tag{4.2}$$

where $\mathbf{p}_{F,ref}$ is the planned position of the front module at the end of the trajectory, and σ is the length of such planned path. For experimental, simulated, and odometric findings, the computed values of such parameters are recorded in Table 4.2.

As previously stated, the outer tyres are unable to achieve the necessary speed, resulting in an odometric estimate of the path that is considerably different from the one intended. The values of e_{ψ_F} and $e_{\mathbf{p}_F}$ in Table 4.2 substantially confirm this behaviour, as can be seen by values of e_{ψ_F} and $e_{\mathbf{p}_F}$. Instead, the disparity between odometric estimation and experimental trajectories reveals the impact of the wheels lateral forces on the trajectory: the robot is forced to execute increasingly greater curves with positioning and orienting errors that grow with cruise velocity and curve

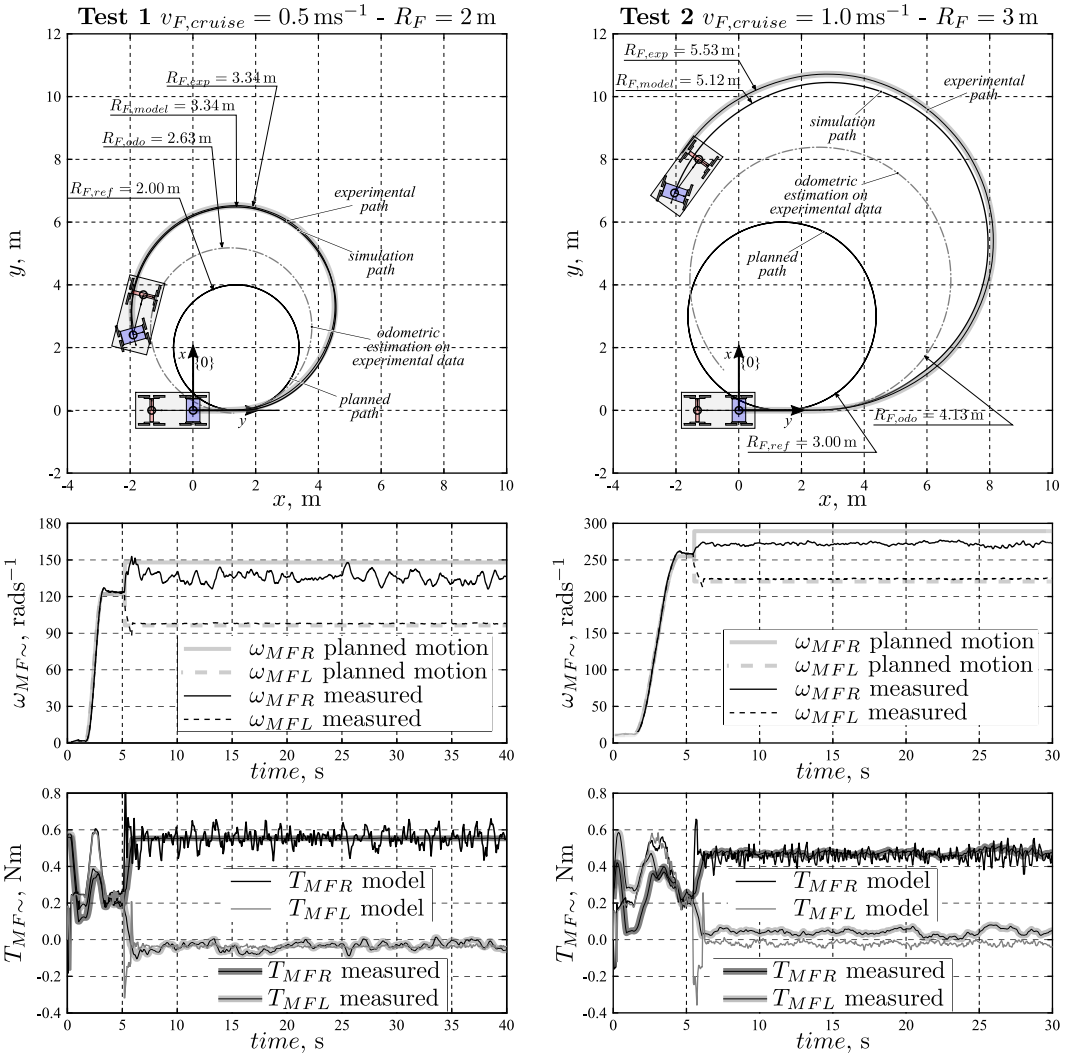

Fig. 4.3 Comparison among simulated and experimental variables for two trajectories with different radius and cruise velocity

Table 4.2 Positioning error parameters in terms of heading angle and Cartesian position of the front module for experimental and simulated trajectories

Parameter	**Test 1**	**Test 2**
e_{ψ_F}, experimental	-42.20%	-48.69%
e_{ψ_F}, simulation	-40.39%	-43.77%
e_{ψ_F}, odometric	-24.76%	-30.81%
$e_{\mathbf{p}_F}$, experimental	24.02%	16.45%
$e_{\mathbf{p}_F}$, simulation	24.30%	14.33%
$e_{\mathbf{p}_F}$, odometric	3.53%	5.05%

radius. Nonetheless, experimental and simulated data reveal a promising overlapping, indicating a low mutual deviation.

The radius of the robot circular trajectories might be a better approach to understanding its behaviour. The two reference radius were $R_{F,ref} = 2\,\mathrm{m}$ and $R_{F,ref} = 3\,\mathrm{m}$, as demonstrated in the two experiments in Figure 4.3. Because the external wheels were unable to achieve the requisite angular velocities, the resultant odometric path estimates deviate significantly from $R_{F,ref}$, as evidenced by the mean values $R_{F,odo} = 2.63\,\mathrm{m}$ and $R_{F,odo} = 4.13\,\mathrm{m}$. Due to the contact transversal forces of the wheels on the ground, the measured trajectories are still different from the reference one: experimental mean values of $R_{F,exp} = 3.34\,\mathrm{m}$ and $R_{F,exp} = 5.53\,\mathrm{m}$ were recorded. The dynamic model was identify to mimic this phenomenon and to match the real dynamics of Agri.Q as closely as possible. Following the parameter identification, the model returns $R_{F,model} = 3.34\,\mathrm{m}$ and $R_{F,model} = 5.12\,\mathrm{m}$ for the $0.5\,\mathrm{m\,s^{-1}}$ and $1.0\,\mathrm{m\,s^{-1}}$ trajectories, respectively. In conclusion, the model tends to underestimate the real curvature of the rover trajectory by almost 7.4% at relatively high velocity (Agri.Q top longitudinal speed is roughly $1.3\,\mathrm{m\,s^{-1}}$). Nonetheless, the accuracy of the proposed dynamics model at slower speeds makes it a valuable tool, in fact, it is used in the following to investigate the influence of the back drive units on overall machine manoeuvrability.

Simulated results

The dynamics model of articulated mobile robots developed and identified previously is utilised in this section to evaluate the influence of back actuation on the robot manoeuvrability. To do so, the model was simulated using the parameters stated before while performing the following trajectory:

- a transient acceleration phase with a cubic velocity profile from standing start to cruise velocity characterized by a maximum acceleration $\dot{v}_{F,max}$ along a straight path;
- a straight section of length s at constant cruise velocity $v_{F,cruise}$;
- a circular path with constant radius R_F and velocity $v_{F,cruise}$ covering an angular distance of $\frac{3}{2}\pi$ in counterclockwise direction;

- a circular path with constant radius R_F and velocity $v_{F,cruise}$ path for an angular distance of $\frac{3}{2}\pi$ in clockwise direction;
- a straight section of length s at constant cruise velocity v_c;
- a transient deceleration phase with a cubic velocity profile from cruise velocity $v_{F,cruise}$ to full stop characterized by a maximum deceleration $-\dot{v}_{F,max}$ in straight direction.

Table 4.3 details the complete trajectory parameters, while the resulting simulations are depicted in Figure 4.4. The reference motor velocities are passed to the driving units, just as they are with the actual prototype, with no indication of the robot actual stance. The simulations were repeated for several k_{TA} values, including $k_{TA} = 1$ (back motors turned off), $k_{TA} = 0.8$ (80% of the traction effort at tyres level is performed by the front module), and $k_{TA} = 0.6$ (60% of the traction effort at tyres level is performed by the front module). The cruising velocity chosen for the robot indicates the prototype maximum performance. Because the inertial effects on the robot behaviour grow as this value is increased, this decision enables the analysis of the worst potential operating state.

Table 4.3 Parameters of the simulated trajectory

Parameter	**Value**
R_F	2.00 m
s	2.00 m
$v_{F,cruise}$	1.00 m s^{-1}
$\dot{v}_{F,max}$	0.50 m s^{-2}

Due to the lack of external input correcting the influence of the lateral forces exerted on the wheels, Agri.Q is not able to follow the specified trajectory with accuracy. It is indeed worth noting that the front module wheels exactly follow the designed velocity profile if torque constraints are not simulated. To offer a quantitative comparison among the trajectories, the two performance parameters already introduced in Eq.(4.1) and Eq.(4.2) are employed again. Table 4.4 collects the results computed among the planned and completed trajectories with varying k_{TA}. The actuation of the rear module improves the ability of Agri.Q to follow curved trajectories, as evidenced by the results in Table 4.4 and the representations of Figure 4.4.

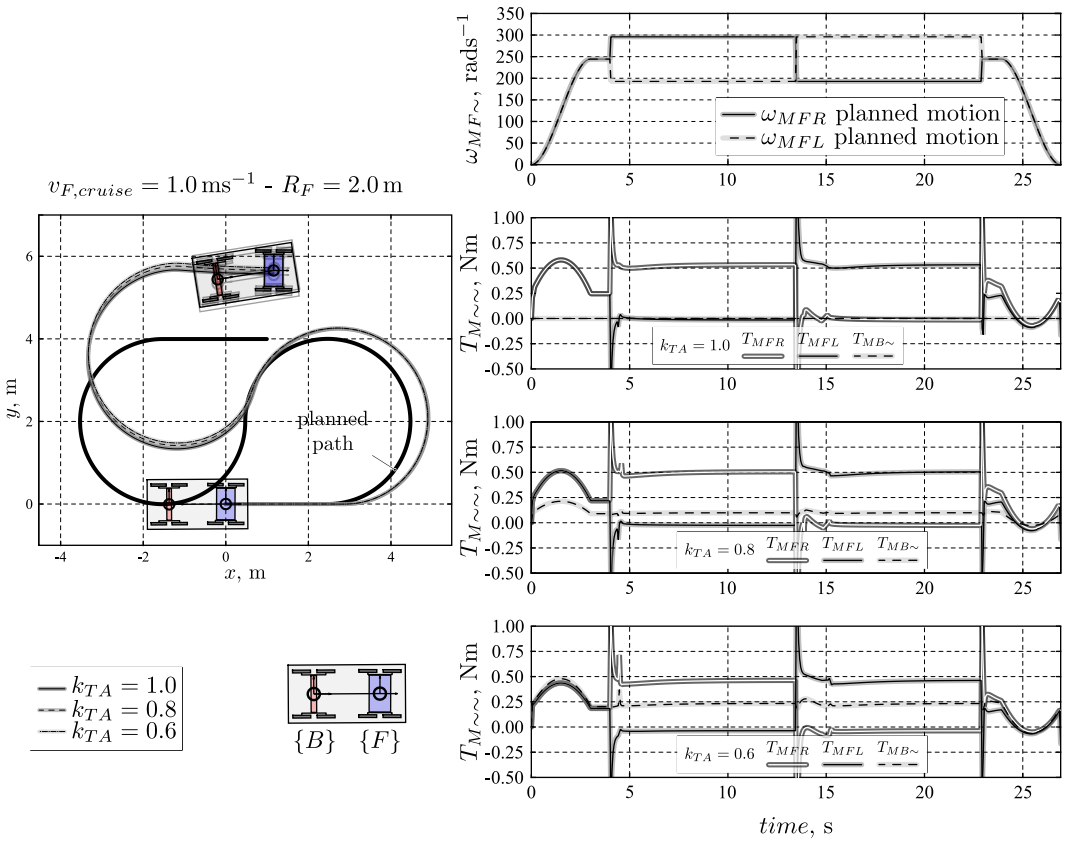

Fig. 4.4 Simulation performed on Agri.Q model to evaluate back driving units contribution

In terms of traction effort, the most significant improvement is made. In fact, it's evident how the actuation on the back drive units relieves some of the load on the front motors. This is especially crucial for Agri.Q, which has shown a critical behaviour when approaching tight curves due to the physical limitations of its motors in the test. As a result, using the rear locomotion units can improve manoeuvrability indirectly since the whole traction effort, or at least a portion of it, is distributed to the back motors, while the torque applied by the front motion units can be solely dedicated to steering the front module.

4.2 Traction allocation control integration and tests

In order to evaluate the effects of the proposed traction allocation strategy, an interesting evaluation method is the use of g-g diagrams, which is an extensively employed diagram in automotive sports as an indication of vehicle performance in

Table 4.4 Positioning error parameters in terms of yaw angle and Cartesian position of the front module

Parameter	Value
$e_{\psi_F}\ (k_{TA} = 0.6)$	4.36%
$e_{\psi_F}\ (k_{TA} = 0.8)$	4.52%
$e_{\psi_F}\ (k_{TA} = 1.0)$	5.10%
$e_{\mathbf{p}_F}\ (k_{TA} = 0.6)$	5.63%
$e_{\mathbf{p}_F}\ (k_{TA} = 0.8)$	6.83%
$e_{\mathbf{p}_F}\ (k_{TA} = 1.0)$	6.45%

terms of longitudinal and lateral acceleration [258]. A detailed discussion of this diagram, as well as its typical uses, is offered in [259].

To obtain the acceleration data, Agri.Q was manually driven along a paved test track, which is represented in Figure 4.5, while an accelerometer was measuring the longitudinal and lateral acceleration of the front module. The test consisted of three runs, each one with a different value of k_{TA}, namely 1.00, 0.70, and 0.62, where Agri.Q performed a single lap for each run. The robot started from a standstill and completed the lap by stopping again.

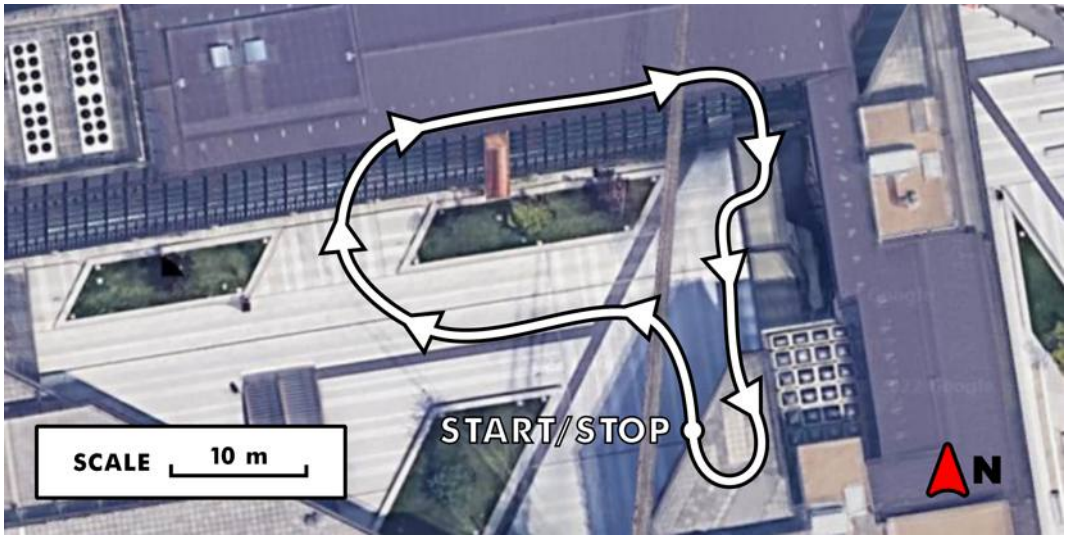

Fig. 4.5 Traction allocation control experimental track

The 9-axis IMU mounted inside the front module proved to be faulty. Thus, the tests were done by mounting a smartphone on the front module, as close as possible to the axis of the yaw joint J_δ, to employ the embedded IMU. In particular, the

mounted sensor was a BMI160 by Bosch, i.e., a low power low noise 16-bit 6 axis IMU designed for mobile applications. The sampling rate was limited to 10 Hz by the app used to collect the data from the sensor.

Figure 4.6 reports the test results in the form of g-g diagrams for each run and then one where the areas defined by the largest accelerations of all runs are compared. The vertical axis represents the longitudinal acceleration of the front, thus, the top half of the diagram represents Agri.Q accelerating while the bottom part is for the braking. Similarly, the horizontal axis represents the robot lateral acceleration during left and right turns. All points that do not lie along the two axes were recorded during manoeuvres where Agri.Q was both accelerating and turning. In theory, the maximum acceleration value (in module) is limited by the vehicle friction circle, or, in other words, by the maximum force that the tyres can sustain before sliding and losing traction. For Agri.Q, considering a very rough contact model and equal weight distribution, the maximum value should be equal to the static friction coefficient μ_S, which has been estimated equal to 0.63 on a grassy field. More realistically, in particular for the longitudinal acceleration, is limited by the traction motors characteristics. On the contrary, brakes can easily make the wheel skid if used improperly, therefore the deceleration limit is the friction circle, as for the lateral acceleration. Therefore, the maximum acceleration value is bounded by a saturated version of the friction circle at a defined value of acceleration.

Analysing the measured data, it can be observed that most of the points are located in the centre within a circle of radius of approximately $0.15\,g = 1.47\,\mathrm{m\,s^{-2}}$ for the three tests. This can be easily explained considering the very slow dynamics of Agri.Q whose maximum longitudinal speed is about $1.3\,\mathrm{m\,s^{-1}}$ and its maximum yaw rate was restricted to $1.08\,\mathrm{rad\,s^{-1}}$. The latter is probably also the cause of the invariance of the lateral acceleration between the various tests. The longitudinal acceleration is also limited by the controller defined in Section 2.6.1, since the longitudinal speed is reduced to guarantee the desired yaw rate.

Nevertheless, Figure 4.6d proves that Agri.Q can produce a larger longitudinal acceleration when the contribution of the rear traction unit increases. Yet, since Agri.Q can quickly reach its maximum speed, only short acceleration bursts are observed.

Repeating similar tests on an incline should prove even more the benefit of the traction allocation strategy, because the more the front motors are under strain, the

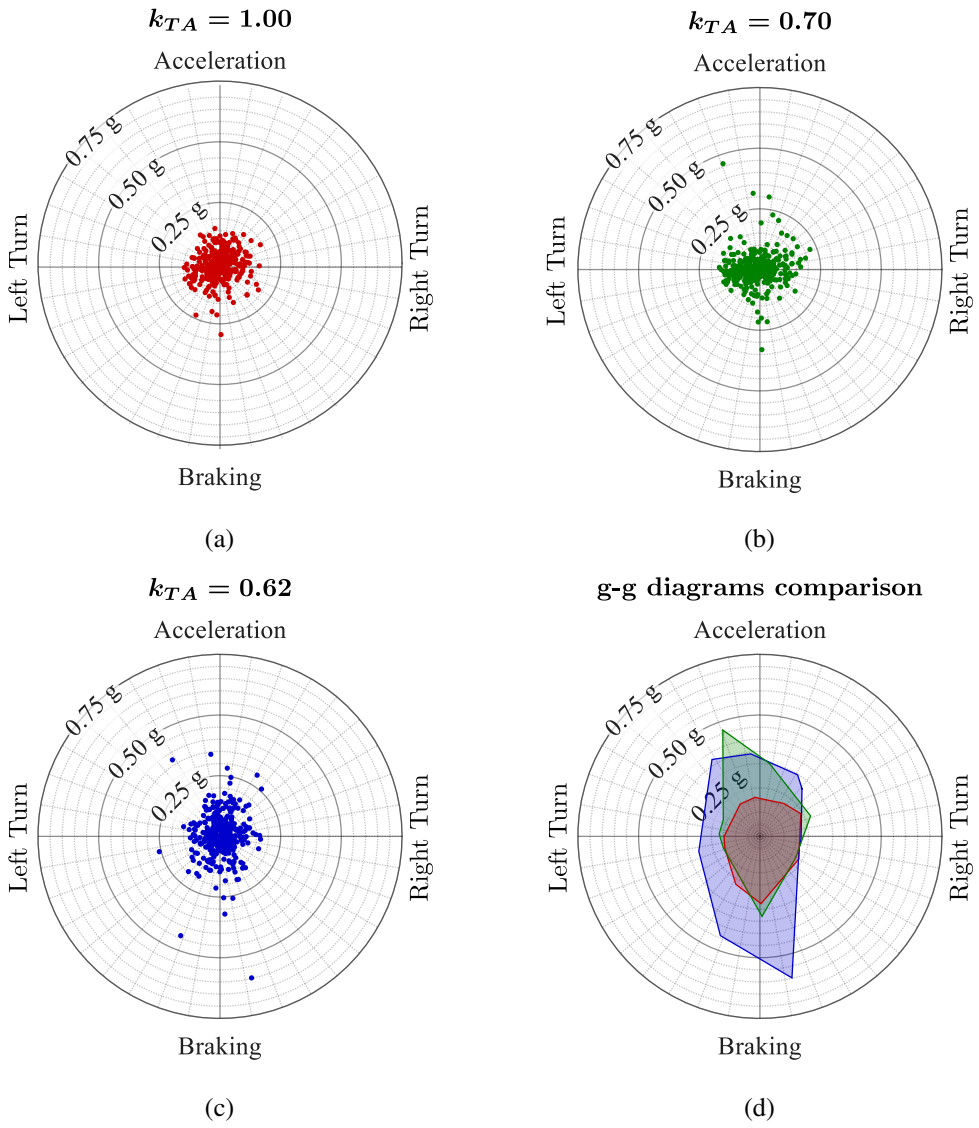

Fig. 4.6 Agri.Q traction tests g-g diagrams at various distribution ratios. (a) $k_{TA} = 1.00$, (a) $k_{TA} = 0.70$, (c) $k_{TA} = 1.62$, (d) Tests comparison

greater the contribution of the rear motors becomes. Alternatively, g-g diagrams could be helpful in developing different traction control methods that take advantage of the entire friction circle by managing wheel slip to maximize the tractive effort.

4.3 Agri.Q energy balance tests

Due to its nature, it is of particular interest to evaluate the energy expenditure of Agri.Q required to perform its activities and how well the PV panels can contribute to enhance its autonomy. Therefore, this section summarises and comments the experimental results collected in [220, 260] about Agri.Q power flows and energy balance.

Recalling Section 2.5.1, Agri.Q mounts two custom power sensors that monitor power flows from the PV panels to the battery and from the battery to the rest of the robot. Moreover, the traction motor drivers provide a measure of the current adsorbed by each traction motor, thus, by computing the corresponding torque and measuring the angular speed, it is possible to compute also the power required by the traction sub-system.

To assess Agri.Q power balance in various scenarios, a total of 8 tests were done. In the first test, the robot was left idle in an open field for around 5 minutes with its PV panels parallel to the ground, recharging itself. The PV panels were angled in the second test scenario to maximize solar energy gathering when the system was still idle. The sky was clear and no shadow was created on the solar panel for both of these experiments demonstrating two alternative approaches to the robot recharging technique. In the remaining tests, Agri.Q was in motion with its PV panels held parallel to the ground and sun exposition was not optimised. In the first two tests, it travelled along a straight path on a paved road for approximately 300m using only its front locomotion units (run 1) or all its traction motors (run 2). The robot then drove down a short straight section on a grassy field, first activating only its front motors (run 3) and then in AWD mode (run 4). To complete the tests, Agri.Q was programmed to perform circular trajectories in AWD mode on a paved surface (run 5) and on grass (run 6). All runs in AWD mode were done with a distribution ratio of $k_{TA} = 0.62$.

All tests were performed on May 12^{th} 2021 in Torino, Italy. Figure 4.7 shows the data provided by Solcast [261] in terms of reference solar power incident on the PV panels during the whole day and the two time frames when the tests were performed, where "Idle Tests" indicates the two done when Agri.Q is stationary, while the "Navigation Tests" are the runs from 1 to 6.

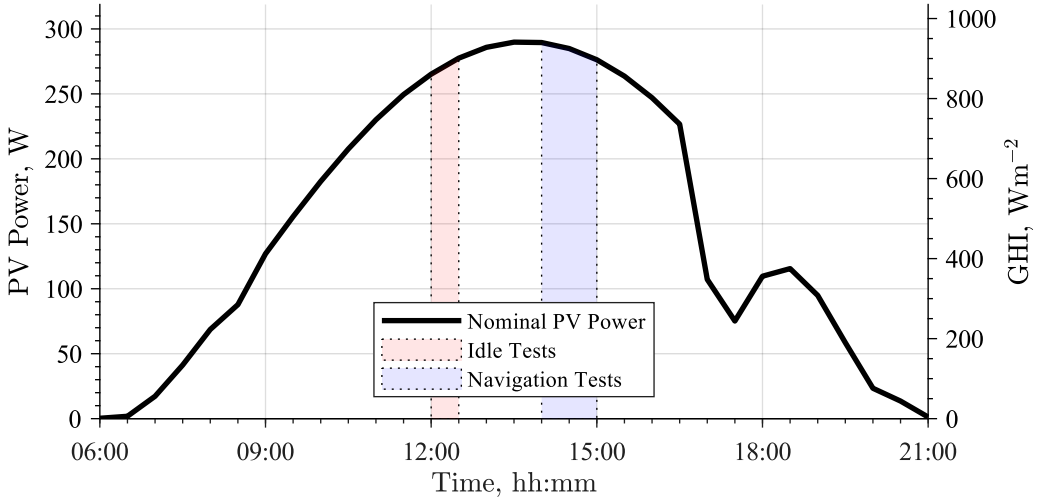

Fig. 4.7 Daily nominal solar power incident on the panels surface on May 12^{th} 2021 in Torino, Italy, and test time frames

The detail of the two idle tests while Agri.Q was static and recharging its battery is depicted in Figure 4.8. First, Agri.Q was positioned idle in a flat area with good solar exposure and no shadows casting on it. Its PV panels were kept parallel to the ground while recharging for about 5 minutes. After that, the PV panels were manually orientated perpendicular to the sun (Zenith = 29°, Azimuth = 151°) manually and left idle for 5 minutes. As expected, in a head-to-head comparison, Agri.Q generates roughly 9.8% more power from the sun exposure when the panels are angled to optimize incident solar irradiance than when the panels are kept horizontal. Furthermore, the generated power is lower in both situations than the projected nominal trend, but the differences are relatively small: the horizontal panels produce 19% less power than the estimated power, while the oriented panels generate 13% less power. Part of this small variation is because Solcast data are satellite collected and, therefore, they do not exactly represent the conditions at the test spot. Also, PV panels attitude was manually set, thus it is possible that the actual PV panels inclination was slightly off from the optimal orientation. In addition, sensor

noise and transient variations in lighting conditions are to blame for the occasional peaks in the collected data.

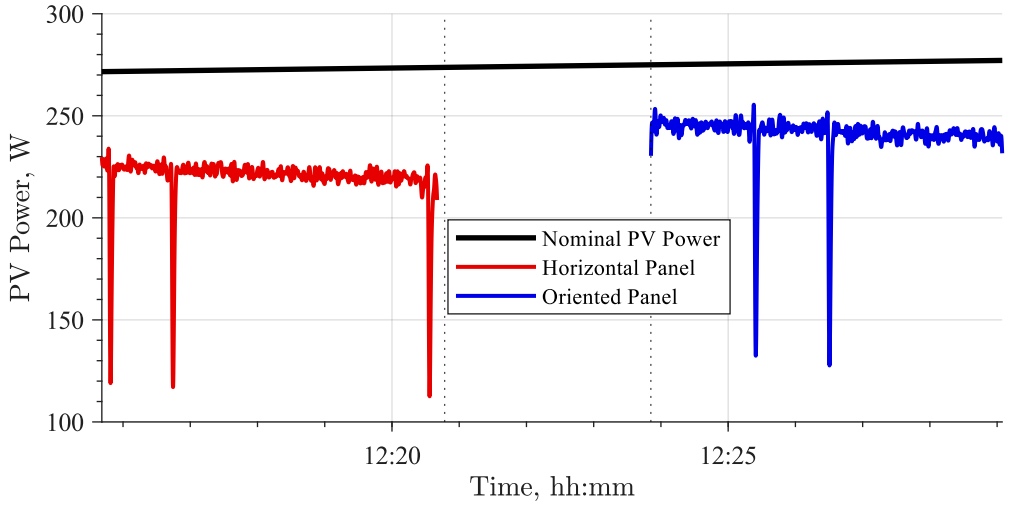

Fig. 4.8 Collected PV power while idle in different configurations

Likewise, Figure 4.9 represents how the panels behave whenever the robot is moving but not actively attempting to recharge. Consequently, in all subsequent test runs, the PV panels were held parallel to the ground and Agri.Q was driven independently of the sun exposure, trying to replicate plausible manoeuvres. Because the first two runs were done in partial or complete shade, the resultant collected power is noticeably lower than in the two prior scenarios with full sun exposure. Instead, Runs 3 and 4 took place in an open grass field with direct sun exposure; thus, the gathered power is similar to that of the horizontal panel when idling. As the latter two tests were conducted in regions overshadowed by nearby structures, the amount of solar energy captured was nearly zero.

To better assess the autonomy of the Agri.Q robot, the power required by the robot to complete its tasks was compared with the solar power gathered by its PV panels. This comparison is depicted in Figure 4.10 for the two tests done with the stationary robot. Agri.Q used roughly 74 W of power to run its electronics when it was idle, with the SBC, microcontroller, and motor drivers being the most energy-intensive components. With both horizontal and angled panels, the collected PV power is substantially higher than the idle one. The average collected power with the PV panels parallel to the ground was about three times greater than the idle power, whereas the oriented PV panels generated on average 3.3 times more power than

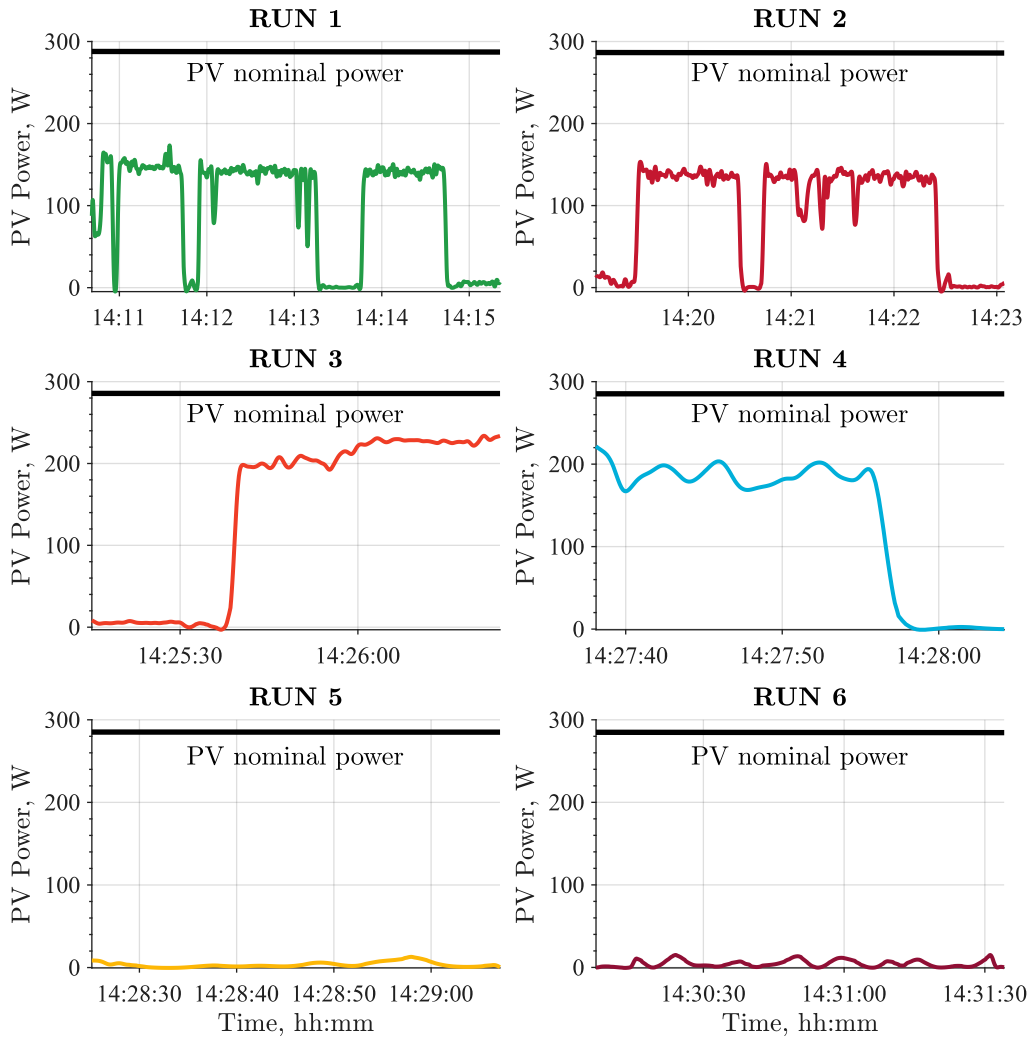

Fig. 4.9 Collected PV power during the navigation tests

required. Consequently, it is clear that the robot can effectively recharge its battery with decent sun exposure while idling.

solar exposure is not optimal when the robot is moving (runs 1-6); therefore, solar power was never enough to recharge the robot, but it can significantly minimise battery drain, as illustrated in Figure 4.11. For example, the power required to drive down a straight path on a paved road with only the front motors (run 1 in Figure 4.11) was nearly identical to the power generated by the panels during the same test run, even if they were partially or totally in shadow in some occasion (i.e., when the PV power is zero). The findings of run 2 simply indicate that increasing the necessary power by activating all locomotion units increases the required power. However, the

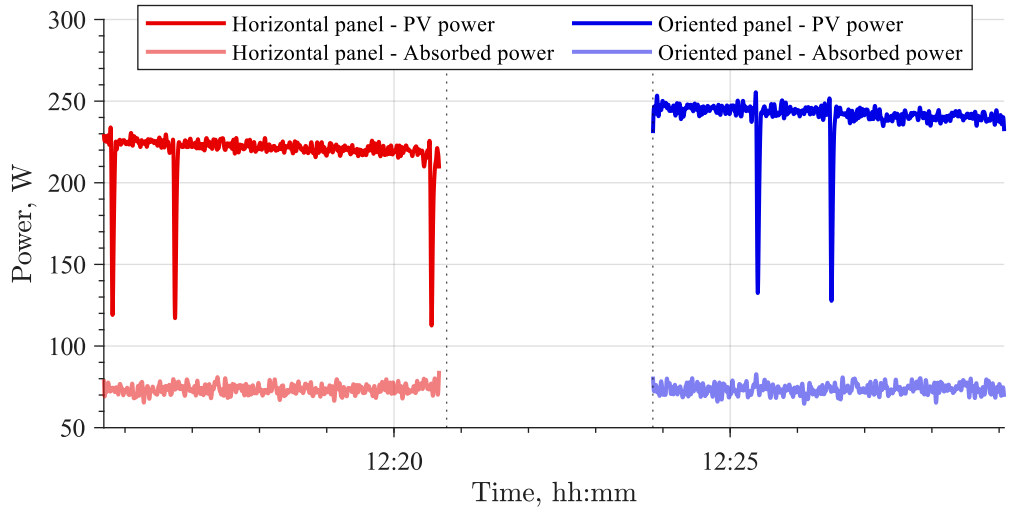

Fig. 4.10 Idling Agri.Q power balance

proposed strategy, whereby rear-wheel-drive power is a function of front-wheel drive power, results in a minimal increase in adsorbed power since little effort is required to negotiate a straight paved path. Although Runs 3 and 4 had better solar exposure, the power required to negotiate the grass field was also higher. Because the panels were shadowed for the final two tests (runs 5 and 6), the data concerning the power balance comparison are meaningless. However, the power necessary to guide the robot on a paved surface is roughly comparable to driving on a straight path on grass, and the power required to follow a circular course on grass is considerably more. In general, a well-known behaviour of this type of robot architecture is seen, which is vulnerable to severe lateral wheel slippage when following curved paths.

Although the previously reported tests lasted a relatively short time, it is possible to roughly estimate how long Agri.Q could work before draining its battery. On average, on flat ground, Agri.Q requires about 300 W, thus, considering its 56 A h battery with its nominal voltage of 25.2 V, it can be estimated that Agri.Q could last approximately 4.7 hours without using PV panels to reduce battery drain. Considering instead the case when the PV panels are active is less straightforward since the PV collected power is very variable throughout the day; however, it can be estimated that PV panels could almost double the robot autonomy, reaching about 9 hours of activities.

The data obtained show that on a sunny day with a clear sky, Agri.Q can sustain itself with a well-planned schedule of operations. The panels can replenish the

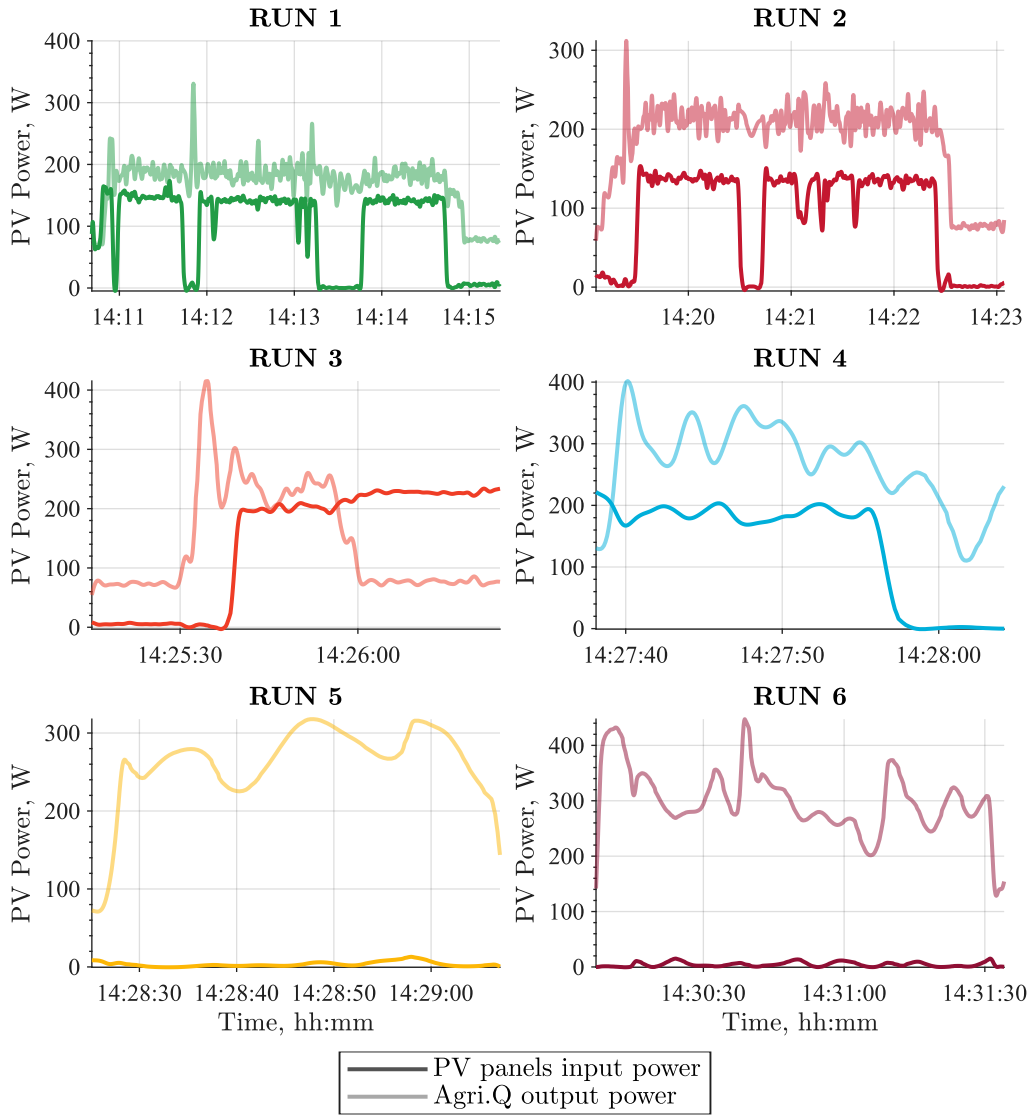

Fig. 4.11 Navigation tests power balance

battery if the robot is left inactive with adequate sun exposure. The recharging rate is improved even further by optimizing the solar panels orientation to enhance the gathering of direct solar irradiation. Although the PV panels are insufficient to completely balance the needed power while the robot moves, they contribute significantly to reducing battery drain, even if the sun is not actively tracked. As a result, by carefully planning Agri.Q tasks in a day, the robot endurance may be greatly increased. The panels orientation, for example, might be continually changed to maximize solar energy gathering in line with its activity. Furthermore, the time

near the solar irradiance peak might be used to undertake an optimal recharging phase while Agri.Q is idle. Further gains might be made by reducing the power usage of the robot and partially redesigning its electrical architecture. Some components may be replaced with low-power equivalents, components could be put into power-saving mode when idle, or the power distribution system might be modified to minimise inefficiency and heat losses, for example.

Chapter 5

Conclusions

In this thesis work, a novel prototype of rover for precision agriculture named Agri.Q is presented. Agri.Q is a rover capable of being both a mobile drone station and a strong answer to the needs of precision agriculture in vineyards, or more generally in fields with relevant inclination. The robot is designed to navigate autonomously between rows of vines and over rough terrain, monitoring the condition of the crops through a vision system and performing sampling or vineyard operations using a highly dexterous arm. In addition to making the robot energy independent, its photovoltaic panels can be used as a landing platform for drones. Thus, one or more drones can then collaborate with the rover to monitor the vineyard even more effectively by combining proximal and remote sensing.

The design requirements that guided the development of the project are mainly derived from the needs of viticulture, but also allow the rover to be used in other types of fruit growing and agriculture. The robot has a small footprint (about $1 \times 2\,\mathrm{m}$) and a mass of only 112 kg to reduce energy consumption and soil compaction. The 8-wheel locomotion system provides similar efficiency to wheeled vehicles and mobility on rough terrain comparable with tracked vehicles. There are four locomotion units, two in the front module and two in the rear module. Each unit has two wheels, a rocker mechanism and an electric gear motor to transmit motion to the wheels. The presence of rocker arms on the locomotion units and a passive rear roll joint allow a correct distribution of the normal load on the wheels in the presence of longitudinal and transversal irregularities. The upper surface, made using photovoltaic panels, has a dual function: landing platform for the drones, which cooperate with the rover

in monitoring activities, and surface for capturing solar radiation. In order to perform these tasks properly, the panel can be oriented thanks to two degrees of freedom that can be operated. Finally, the robot is equipped with a highly dexterous collaborative robotic arm (7 degrees of freedom) dedicated to sampling and picking operations, whose workspace is expandable thanks to the reconfiguration of Agri.Q

Part of this work is also dedicated to modelling, simulating, and testing the robot with a strong focus on its kinematic and dynamic behaviour as a vehicle. A short section is also dedicated to the robotic manipulator to define the initial foundations of a proper mobile manipulator.

The natural evolution of this project is the implementation of some levels of autonomous navigation and the integration of a set of sensors to perform some monitoring activities. In parallel, it is of great interest to keep developing the topic of traction allocation control, hereby introduced and tested with an initial proposal.

References

[1] Kinova. Kinova robotics homepage, 2021. URL https://assistive.kinovarobotics.com/product/jaco-robotic-arm.

[2] G. Sylvester. *E-agriculture in action: Drones for agriculture*. FAO, Bangkok, Thailand, 2018. ISBN 978-92-5-130246-0. URL https://www.fao.org/documents/card/en/c/I8494EN/.

[3] Eileen Crist, Camilo Mora, and Robert Engelman. The interaction of human population, food production, and biodiversity protection. *Science*, 356(6335):260–264, April 2017. doi: 10.1126/science.aal2011. URL https://www.science.org/doi/full/10.1126/science.aal2011. Publisher: American Association for the Advancement of Science.

[4] Navin Ramankutty, Zia Mehrabi, Katharina Waha, Larissa Jarvis, Claire Kremen, Mario Herrero, and Loren H. Rieseberg. Trends in Global Agricultural Land Use: Implications for Environmental Health and Food Security. *Annual Review of Plant Biology*, 69(1):789–815, 2018. doi: 10.1146/annurev-arplant-042817-040256. URL https://doi.org/10.1146/annurev-arplant-042817-040256.

[5] Ancha Srinivasan. *Handbook of precision agriculture: principles and applications*. CRC press, Boca Raton, 2006. ISBN 978-0-429-18030-9. doi: 10.1201/9781482277968. URL https://doi.org/10.1201/9781482277968.

[6] Martina Corti, Pietro Marino Gallina, Daniele Cavalli, Bianca Ortuani, Giovanni Cabassi, Gabriele Cola, Antonio Vigoni, Luigi Degano, and Simone Bregaglio. Evaluation of In-Season Management Zones from High-Resolution Soil and Plant Sensors. *Agronomy*, 10(8):1124, 2020. URL https://doi.org/10.3390/agronomy10081124. Publisher: Multidisciplinary Digital Publishing Institute.

[7] Terry W. Griffin and Elizabeth A. Yeager. Adoption of precision agriculture technology: A duration analysis. In *In Proceedings of 14th International Conference on Precision Agriculture. Monticello, IL: International Society of Precision Agriculture*, 2018.

[8] Antonio Barrientos, Julian Colorado, Jaime del Cerro, Alexander Martinez, Claudio Rossi, David Sanz, and João Valente. Aerial remote sensing in

agriculture: A practical approach to area coverage and path planning for fleets of mini aerial robots. *Journal of Field Robotics*, 28(5):667–689, 2011. ISSN 1556-4967. doi: 10.1002/rob.20403. URL https://onlinelibrary.wiley.com/doi/abs/10.1002/rob.20403.

[9] Ivan Beloev, Diyana Kinaneva, Georgi Georgiev, Georgi Hristov, and Plamen Zahariev. Artificial Intelligence-Driven Autonomous Robot for Precision Agriculture. *Acta Technologica Agriculturae*, 24(1):48–54, 2021.

[10] Francis J. Pierce and Peter Nowak. Aspects of Precision Agriculture. In *Advances in Agronomy*, volume 67, pages 1–85. Academic Press, January 1999. doi: 10.1016/S0065-2113(08)60513-1. URL https://www.sciencedirect.com/science/article/pii/S0065211308605131.

[11] Naiqian Zhang, Maohua Wang, and Ning Wang. Precision agriculture—a worldwide overview. *Computers and Electronics in Agriculture*, 36(2):113–132, November 2002. ISSN 0168-1699. doi: 10.1016/S0168-1699(02)00096-0. URL https://www.sciencedirect.com/science/article/pii/S0168169902000960.

[12] Mohammadreza Davoodi, Javad Mohammadpour Velni, and Changying Li. Coverage control with multiple ground robots for precision agriculture. *Mechanical Engineering*, 140(06):S4–S8, June 2018. ISSN 0025-6501. doi: 10.1115/1.2018-JUN-4. URL https://doi.org/10.1115/1.2018-JUN-4. Publisher: American Society of Mechanical Engineers.

[13] Pratap Tokekar, Joshua Vander Hook, David Mulla, and Volkan Isler. Sensor Planning for a Symbiotic UAV and UGV System for Precision Agriculture. *IEEE Transactions on Robotics*, 32(6):1498–1511, December 2016. ISSN 1941-0468. doi: 10.1109/TRO.2016.2603528. Conference Name: IEEE Transactions on Robotics.

[14] James Lowenberg-DeBoer, Iona Yuelu Huang, Vasileios Grigoriadis, and Simon Blackmore. Economics of robots and automation in field crop production. *Precision Agriculture*, 21(2):278–299, 2020.

[15] Yari Vecchio, Giulio Paolo Agnusdei, Pier Paolo Miglietta, and Fabian Capitanio. Adoption of precision farming tools: the case of italian farmers. *International journal of environmental research and public health*, 17(3):869, 2020.

[16] Marvin T Batte and Michael W Arnholt. Precision farming adoption and use in Ohio: case studies of six leading-edge adopters. *Computers and Electronics in Agriculture*, 38(2):125–139, February 2003. ISSN 0168-1699. doi: 10.1016/S0168-1699(02)00143-6. URL https://www.sciencedirect.com/science/article/pii/S0168169902001436.

[17] F. J. Pierce and T. V. Elliott. Regional and on-farm wireless sensor networks for agricultural systems in Eastern Washington. *Computers and Electronics*

in Agriculture, 61(1):32–43, April 2008. ISSN 0168-1699. doi: 10.1016/j.compag.2007.05.007. URL https://www.sciencedirect.com/science/article/pii/S0168169907001664.

[18] S. M. Swinton and J. Lowenberg-DeBoer. Evaluating the Profitability of Site-Specific Farming. *Journal of Production Agriculture*, 11(4):439–446, 1998. ISSN 2689-4114. doi: 10.2134/jpa1998.0439. URL https://onlinelibrary.wiley.com/doi/abs/10.2134/jpa1998.0439.

[19] S. Fountas, S. Blackmore, D. Ess, S. Hawkins, G. Blumhoff, J. Lowenberg-Deboer, and C. G. Sorensen. Farmer Experience with Precision Agriculture in Denmark and the US Eastern Corn Belt. *Precision Agriculture*, 6(2):121–141, April 2005. ISSN 1573-1618. doi: 10.1007/s11119-004-1030-z. URL https://doi.org/10.1007/s11119-004-1030-z.

[20] Katie Ellis, Tara Auxt Baugher, and Karen Lewis. Results from Survey Instruments Used to Assess Technology Adoption for Tree Fruit Production. *HortTechnology*, 20(6):1043–1048, December 2010. ISSN 1943-7714, 1063-0198. doi: 10.21273/HORTSCI.20.6.1043. URL https://journals.ashs.org/horttech/view/journals/horttech/20/6/article-p1043.xml. Publisher: American Society for Horticultural Science Section: HortTechnology.

[21] David W. Lamb, Paul Frazier, and Peter Adams. Improving pathways to adoption: Putting the right P's in precision agriculture. *Computers and Electronics in Agriculture*, 61(1):4–9, April 2008. ISSN 0168-1699. doi: 10.1016/j.compag.2007.04.009. URL https://www.sciencedirect.com/science/article/pii/S0168169907001652.

[22] United Nations. United nations sustainable development goals, 2016. URL https://www.un.org/sustainabledevelopment/.

[23] Juliana Dias Bernardes Gil, Pytrik Reidsma, Ken Giller, Lindsay Todman, Andrew Whitmore, and Martin van Ittersum. Sustainable development goal 2: Improved targets and indicators for agriculture and food security. *Ambio*, 48 (7):685–698, 2019.

[24] Yari Vecchio, Marcello De Rosa, Felice Adinolfi, Luca Bartoli, and Margherita Masi. Adoption of precision farming tools: A context-related analysis. *Land Use Policy*, 94:104481, 2020.

[25] United Nations. Sdg 2: Zero hunger, 2016. URL https://www.un.org/sustainabledevelopment/hunger/.

[26] United Nations. Sdg 6: Clean water and sanitation, 2016. URL https://www.un.org/sustainabledevelopment/water-and-sanitation/.

[27] United Nations. Sdg 12: Responsible consumption and production, 2016. URL https://www.un.org/sustainabledevelopment/sustainable-consumption-production/.

[28] United Nations. Sdg 13: Climate action, 2016. URL https://www.un.org/sustainabledevelopment/climate-change/.

[29] United Nations. Sdg 15: Life on land, 2016. URL https://www.un.org/sustainabledevelopment/biodiversity/.

[30] D. S. Long, G. R. Carlson, and S. D. DeGloria. Quality of Field Management Maps. In *Site-Specific Management for Agricultural Systems*, pages 251–271. John Wiley & Sons, Ltd, 1995. ISBN 978-0-89118-260-3. doi: 10.2134/1995.site-specificmanagement.c18. URL https://onlinelibrary.wiley.com/doi/abs/10.2134/1995.site-specificmanagement.c18.

[31] Said Nawar, Ronald Corstanje, Graham Halcro, David Mulla, and Abdul M. Mouazen. Chapter Four - Delineation of Soil Management Zones for Variable-Rate Fertilization: A Review. In *Advances in Agronomy*, volume 143, pages 175–245. Academic Press, January 2017. doi: 10.1016/bs.agron.2017.01.003. URL https://www.sciencedirect.com/science/article/pii/S0065211317300032.

[32] Fernando Alfredo Auat Cheein and Ricardo Carelli. Agricultural Robotics: Unmanned Robotic Service Units in Agricultural Tasks. *IEEE Industrial Electronics Magazine*, 7(3):48–58, September 2013. ISSN 1941-0115. doi: 10.1109/MIE.2013.2252957. Conference Name: IEEE Industrial Electronics Magazine.

[33] Wouter H. Maes and Kathy Steppe. Perspectives for Remote Sensing with Unmanned Aerial Vehicles in Precision Agriculture. *Trends in Plant Science*, 24(2):152–164, February 2019. ISSN 1360-1385. doi: 10.1016/j.tplants.2018.11.007. URL https://www.sciencedirect.com/science/article/pii/S1360138518302693.

[34] Panagiotis Radoglou-Grammatikis, Panagiotis Sarigiannidis, Thomas Lagkas, and Ioannis Moscholios. A compilation of UAV applications for precision agriculture. *Computer Networks*, 172:107148, May 2020. ISSN 1389-1286. doi: 10.1016/j.comnet.2020.107148. URL https://www.sciencedirect.com/science/article/pii/S138912862030116X.

[35] J. R. Rosell and R. Sanz. A review of methods and applications of the geometric characterization of tree crops in agricultural activities. *Computers and Electronics in Agriculture*, 81:124–141, February 2012. ISSN 0168-1699. doi: 10.1016/j.compag.2011.09.007. URL https://www.sciencedirect.com/science/article/pii/S0168169911002109.

[36] C. Wouter Bac, Eldert J. van Henten, Jochen Hemming, and Yael Edan. Harvesting Robots for High-value Crops: State-of-the-art Review and Challenges Ahead. *Journal of Field Robotics*, 31(6):888–911, 2014. ISSN 1556-4967. doi: 10.1002/rob.21525. URL https://onlinelibrary.wiley.com/doi/abs/10.1002/rob.21525.

[37] A. Gongal, S. Amatya, M. Karkee, Q. Zhang, and K. Lewis. Sensors and systems for fruit detection and localization: A review. *Computers and Electronics in Agriculture*, 116:8–19, August 2015. ISSN 0168-1699. doi: 10.1016/j.compag.2015.05.021. URL https://www.sciencedirect.com/science/article/pii/S0168169915001581.

[38] Manuel Vázquez-Arellano, Hans W. Griepentrog, David Reiser, and Dimitris S. Paraforos. 3-D Imaging Systems for Agricultural Applications—A Review. *Sensors*, 16(5):618, May 2016. ISSN 1424-8220. doi: 10.3390/s16050618. URL https://www.mdpi.com/1424-8220/16/5/618. Number: 5 Publisher: Multidisciplinary Digital Publishing Institute.

[39] Francisco Yandun Narvaez, Giulio Reina, Miguel Torres-Torriti, George Kantor, and Fernando Auat Cheein. A Survey of Ranging and Imaging Techniques for Precision Agriculture Phenotyping. *IEEE/ASME Transactions on Mechatronics*, 22(6):2428–2439, December 2017. ISSN 1941-014X. doi: 10.1109/TMECH.2017.2760866. Conference Name: IEEE/ASME Transactions on Mechatronics.

[40] Dimosthenis C. Tsouros, Stamatia Bibi, and Panagiotis G. Sarigiannidis. A review on UAV-based applications for precision agriculture. *Information*, 10(11):349, 2019. doi: 10.3390/info10110349. URL https://www.mdpi.com/2078-2489/10/11/349. Publisher: Multidisciplinary Digital Publishing Institute.

[41] Y. Chen, H. Zhu, and H. Ozkan E. Development of variable-rate sprayer with laser scanning sensor to synchronize spray outputs to tree structures. *Transactions of the ASABE*, 55(3):773–781, 2012. ISSN 2151-0032. URL https://handle.nal.usda.gov/10113/56263. PubAg AGID: 56263.

[42] A. Escolà, J. R. Rosell-Polo, S. Planas, E. Gil, J. Pomar, F. Camp, J. Llorens, and F. Solanelles. Variable rate sprayer. Part 1 – Orchard prototype: Design, implementation and validation. *Computers and Electronics in Agriculture*, 95:122–135, July 2013. ISSN 0168-1699. doi: 10.1016/j.compag.2013.02.004. URL https://www.sciencedirect.com/science/article/pii/S0168169913000331.

[43] Marco Mora, Felipe Avila, Marcos Carrasco-Benavides, Gonzalo Maldonado, Jeissy Olguín-Cáceres, and Sigfredo Fuentes. Automated computation of leaf area index from fruit trees using improved image processing algorithms applied to canopy cover digital photograpies. *Computers and Electronics in Agriculture*, 123:195–202, April 2016. ISSN 0168-1699. doi: 10.1016/j.compag.2016.02.011. URL https://www.sciencedirect.com/science/article/pii/S0168169916300485.

[44] Jan U. H. Eitel, Troy S. Magney, Lee A. Vierling, Tabitha T. Brown, and David R. Huggins. LiDAR based biomass and crop nitrogen estimates for rapid, non-destructive assessment of wheat nitrogen status. *Field Crops Research*, 159:21–32, March 2014. ISSN 0378-4290. doi: 10.1016/

j.fcr.2014.01.008. URL https://www.sciencedirect.com/science/article/pii/S0378429014000161.

[45] Wang Li, Zheng Niu, Hanyue Chen, Dong Li, Mingquan Wu, and Wei Zhao. Remote estimation of canopy height and aboveground biomass of maize using high-resolution stereo images from a low-cost unmanned aerial vehicle system. *Ecological Indicators*, 67:637–648, August 2016. ISSN 1470-160X. doi: 10.1016/j.ecolind.2016.03.036. URL https://www.sciencedirect.com/science/article/pii/S1470160X16301406.

[46] Ville Kankare, Markus Holopainen, Mikko Vastaranta, Eetu Puttonen, Xiaowei Yu, Juha Hyyppä, Matti Vaaja, Hannu Hyyppä, and Petteri Alho. Individual tree biomass estimation using terrestrial laser scanning. *ISPRS Journal of Photogrammetry and Remote Sensing*, 75:64–75, January 2013. ISSN 0924-2716. doi: 10.1016/j.isprsjprs.2012.10.003. URL https://www.sciencedirect.com/science/article/pii/S0924271612001876.

[47] Wei Ji, Dean Zhao, Fengyi Cheng, Bo Xu, Ying Zhang, and Jinjing Wang. Automatic recognition vision system guided for apple harvesting robot. *Computers & Electrical Engineering*, 38(5):1186–1195, September 2012. ISSN 0045-7906. doi: 10.1016/j.compeleceng.2011.11.005. URL https://www.sciencedirect.com/science/article/pii/S0045790611001819.

[48] A. Gongal, A. Silwal, S. Amatya, M. Karkee, Q. Zhang, and K. Lewis. Apple crop-load estimation with over-the-row machine vision system. *Computers and Electronics in Agriculture*, 120:26–35, January 2016. ISSN 0168-1699. doi: 10.1016/j.compag.2015.10.022. URL https://www.sciencedirect.com/science/article/pii/S016816991500335X.

[49] Mario M. Foglia and Giulio Reina. Agricultural robot for radicchio harvesting. *Journal of Field Robotics*, 23(6-7):363–377, 2006. ISSN 1556-4967. doi: 10.1002/rob.20131. URL https://onlinelibrary.wiley.com/doi/abs/10.1002/rob.20131.

[50] Manoj Karkee, Bikram Adhikari, Suraj Amatya, and Qin Zhang. Identification of pruning branches in tall spindle apple trees for automated pruning. *Computers and Electronics in Agriculture*, 103:127–135, April 2014. ISSN 0168-1699. doi: 10.1016/j.compag.2014.02.013. URL https://www.sciencedirect.com/science/article/pii/S016816991400060X.

[51] Hamlyn G. Jones, Rachid Serraj, Brian R. Loveys, Lizhong Xiong, Ashley Wheaton, Adam H. Price, Hamlyn G. Jones, Rachid Serraj, Brian R. Loveys, Lizhong Xiong, Ashley Wheaton, and Adam H. Price. Thermal infrared imaging of crop canopies for the remote diagnosis and quantification of plant responses to water stress in the field. *Functional Plant Biology*, 36(11):978–989, November 2009. ISSN 1445-4416, 1445-4416. doi: 10.1071/FP09123. URL https://www.publish.csiro.au/fp/FP09123. Publisher: CSIRO PUBLISHING.

[52] Lin Du, Wei Gong, Shuo Shi, Jian Yang, Jia Sun, Bo Zhu, and Shalei Song. Estimation of rice leaf nitrogen contents based on hyperspectral LIDAR. *International Journal of Applied Earth Observation and Geoinformation*, 44: 136–143, February 2016. ISSN 0303-2434. doi: 10.1016/j.jag.2015.08.008. URL https://www.sciencedirect.com/science/article/pii/S0303243415300209.

[53] W. A. P. Weerakkody and L. D. B. Suriyagoda. Estimation of leaf and canopy photosynthesis of pot chrysanthemum and its implication on intensive canopy management. *Scientia Horticulturae*, 192:237–243, August 2015. ISSN 0304-4238. doi: 10.1016/j.scienta.2015.05.028. URL https://www.sciencedirect.com/science/article/pii/S0304423815300170.

[54] Chuanyuan Zhao, Won Suk Lee, and Dongjian He. Immature green citrus detection based on colour feature and sum of absolute transformed difference (SATD) using colour images in the citrus grove. *Computers and Electronics in Agriculture*, 124:243–253, June 2016. ISSN 0168-1699. doi: 10.1016/j.compag.2016.04.009. URL https://www.sciencedirect.com/science/article/pii/S0168169916301272.

[55] Stephen Nuske, Kyle Wilshusen, Supreeth Achar, Luke Yoder, Srinivasa Narasimhan, and Sanjiv Singh. Automated Visual Yield Estimation in Vineyards. *Journal of Field Robotics*, 31(5):837–860, 2014. ISSN 1556-4967. doi: 10.1002/rob.21541. URL https://onlinelibrary.wiley.com/doi/abs/10.1002/rob.21541.

[56] Jayme Garcia Arnal Barbedo, Luciano Vieira Koenigkan, and Thiago Teixeira Santos. Identifying multiple plant diseases using digital image processing. *Biosystems Engineering*, 147:104–116, July 2016. ISSN 1537-5110. doi: 10.1016/j.biosystemseng.2016.03.012. URL https://www.sciencedirect.com/science/article/pii/S153751101530266X.

[57] Chandra Sekhar Nandi, Bipan Tudu, and Chiranjib Koley. A Machine Vision-Based Maturity Prediction System for Sorting of Harvested Mangoes. *IEEE Transactions on Instrumentation and Measurement*, 63(7):1722–1730, July 2014. ISSN 1557-9662. doi: 10.1109/TIM.2014.2299527. Conference Name: IEEE Transactions on Instrumentation and Measurement.

[58] Qi Wang, Stephen Nuske, Marcel Bergerman, and Sanjiv Singh. Automated Crop Yield Estimation for Apple Orchards. In *Experimental Robotics: The 13th International Symposium on Experimental Robotics*, Springer Tracts in Advanced Robotics, pages 745–758. Springer International Publishing, Heidelberg, 2013. ISBN 978-3-319-00065-7. doi: 10.1007/978-3-319-00065-7_50. URL https://doi.org/10.1007/978-3-319-00065-7_50.

[59] Javier Baluja, Maria P. Diago, Pedro Balda, Roberto Zorer, Franco Meggio, Fermin Morales, and Javier Tardaguila. Assessment of vineyard water status variability by thermal and multispectral imagery using an unmanned aerial vehicle (UAV). *Irrigation Science*, 30(6):511–522, November 2012. ISSN

1432-1319. doi: 10.1007/s00271-012-0382-9. URL https://doi.org/10.1007/s00271-012-0382-9.

[60] J. P. Wachs, H. I. Stern, T. Burks, and V. Alchanatis. Low and high-level visual feature-based apple detection from multi-modal images. *Precision Agriculture*, 11(6):717–735, December 2010. ISSN 1573-1618. doi: 10.1007/s11119-010-9198-x. URL https://doi.org/10.1007/s11119-010-9198-x.

[61] Giulio Reina, Annalisa Milella, Raphaël Rouveure, Michael Nielsen, Rainer Worst, and Morten R. Blas. Ambient awareness for agricultural robotic vehicles. *Biosystems Engineering*, 146:114–132, June 2016. ISSN 1537-5110. doi: 10.1016/j.biosystemseng.2015.12.010. URL https://www.sciencedirect.com/science/article/pii/S1537511015001889.

[62] Dawei Li, Lihong Xu, Chengxiang Tan, Erik D. Goodman, Daichang Fu, and Longjiao Xin. Digitization and Visualization of Greenhouse Tomato Plants in Indoor Environments. *Sensors*, 15(2):4019–4051, February 2015. ISSN 1424-8220. doi: 10.3390/s150204019. URL https://www.mdpi.com/1424-8220/15/2/4019. Number: 2 Publisher: Multidisciplinary Digital Publishing Institute.

[63] Yann Chéné, David Rousseau, Philippe Lucidarme, Jessica Bertheloot, Valérie Caffier, Philippe Morel, Étienne Belin, and François Chapeau-Blondeau. On the use of depth camera for 3D phenotyping of entire plants. *Computers and Electronics in Agriculture*, 82:122–127, March 2012. ISSN 0168-1699. doi: 10.1016/j.compag.2011.12.007. URL https://www.sciencedirect.com/science/article/pii/S016816991100319X.

[64] Weilin Wang and Changying Li. Size estimation of sweet onions using consumer-grade RGB-depth sensor. *Journal of Food Engineering*, 142:153–162, December 2014. ISSN 0260-8774. doi: 10.1016/j.jfoodeng.2014.06.019. URL https://www.sciencedirect.com/science/article/pii/S026087741400260X.

[65] Dionisio Andújar, Angela Ribeiro, César Fernández-Quintanilla, and José Dorado. Using depth cameras to extract structural parameters to assess the growth state and yield of cauliflower crops. *Computers and Electronics in Agriculture*, 122:67–73, March 2016. ISSN 0168-1699. doi: 10.1016/j.compag.2016.01.018. URL https://www.sciencedirect.com/science/article/pii/S0168169916000235.

[66] David J. Mulla. Twenty five years of remote sensing in precision agriculture: Key advances and remaining knowledge gaps. *Biosystems Engineering*, 114(4):358–371, April 2013. ISSN 1537-5110. doi: 10.1016/j.biosystemseng.2012.08.009. URL https://www.sciencedirect.com/science/article/pii/S1537511012001419.

[67] C. Hillnhütter, A. K. Mahlein, R. A. Sikora, and E. C. Oerke. Remote sensing to detect plant stress induced by Heterodera schachtii and Rhizoctonia solani in sugar beet fields. *Field Crops Research*, 122(1):70–77, April 2011. ISSN 0378-4290. doi: 10.1016/j.fcr.2011.02.007. URL https://www.sciencedirect.com/science/article/pii/S0378429011000566.

[68] P. J. Zarco-Tejada, V. González-Dugo, and J. A. J. Berni. Fluorescence, temperature and narrow-band indices acquired from a UAV platform for water stress detection using a micro-hyperspectral imager and a thermal camera. *Remote Sensing of Environment*, 117:322–337, February 2012. ISSN 0034-4257. doi: 10.1016/j.rse.2011.10.007. URL https://www.sciencedirect.com/science/article/pii/S0034425711003555.

[69] Jorge Torres-Sánchez, Francisca López-Granados, Ana Isabel De Castro, and José Manuel Peña-Barragán. Configuration and Specifications of an Unmanned Aerial Vehicle (UAV) for Early Site Specific Weed Management. *PLOS ONE*, 8(3):e58210, March 2013. ISSN 1932-6203. doi: 10.1371/journal.pone.0058210. URL https://journals.plos.org/plosone/article?id=10.1371/journal.pone.0058210. Publisher: Public Library of Science.

[70] M. Zaman-Allah, O. Vergara, J. L. Araus, A. Tarekegne, C. Magorokosho, P. J. Zarco-Tejada, A. Hornero, A. Hernández Albà, B. Das, P. Craufurd, M. Olsen, B. M. Prasanna, and J. Cairns. Unmanned aerial platform-based multi-spectral imaging for field phenotyping of maize. *Plant Methods*, 11(1):35, June 2015. ISSN 1746-4811. doi: 10.1186/s13007-015-0078-2. URL https://doi.org/10.1186/s13007-015-0078-2.

[71] A. AghaKouchak, A. Farahmand, F. S. Melton, J. Teixeira, M. C. Anderson, B. D. Wardlow, and C. R. Hain. Remote sensing of drought: Progress, challenges and opportunities. *Reviews of Geophysics*, 53(2):452–480, 2015. ISSN 1944-9208. doi: 10.1002/2014RG000456. URL https://onlinelibrary.wiley.com/doi/abs/10.1002/2014RG000456.

[72] Tomas Palleja and Andrew J. Landers. Real time canopy density estimation using ultrasonic envelope signals in the orchard and vineyard. *Computers and Electronics in Agriculture*, 115:108–117, July 2015. ISSN 0168-1699. doi: 10.1016/j.compag.2015.05.014. URL https://www.sciencedirect.com/science/article/pii/S0168169915001507.

[73] Alexandre Escolà, Santiago Planas, Joan Ramon Rosell, Jesús Pomar, Ferran Camp, Francesc Solanelles, Felip Gracia, Jordi Llorens, and Emilio Gil. Performance of an Ultrasonic Ranging Sensor in Apple Tree Canopies. *Sensors*, 11(3):2459–2477, March 2011. ISSN 1424-8220. doi: 10.3390/s110302459. URL https://www.mdpi.com/1424-8220/11/3/2459. Number: 3 Publisher: Molecular Diversity Preservation International.

[74] G. Alenyà, B. Dellen, and C. Torras. 3D modelling of leaves from color and ToF data for robotized plant measuring. In *2011 IEEE International Conference on Robotics and Automation*, pages 3408–3414, May 2011. doi: 10.1109/ICRA.2011.5980092. ISSN: 1050-4729.

[75] Supawadee Chaivivatrakul, Lie Tang, Matthew N. Dailey, and Akash D. Nakarmi. Automatic morphological trait characterization for corn plants via 3D holographic reconstruction. *Computers and Electronics in Agriculture*, 109:109–123, November 2014. ISSN 0168-1699. doi: 10.1016/

j.compag.2014.09.005. URL https://www.sciencedirect.com/science/article/pii/S0168169914002191.

[76] Wajahat Kazmi, Sergi Foix, and Guillem Alenyà. Plant leaf imaging using time of flight camera under sunlight, shadow and room conditions. In *2012 IEEE International Symposium on Robotic and Sensors Environments Proceedings*, pages 192–197, November 2012. doi: 10.1109/ROSE.2012.6402615.

[77] Efi Vitzrabin and Yael Edan. Adaptive thresholding with fusion using a RGBD sensor for red sweet-pepper detection. *Biosystems Engineering*, 146:45–56, June 2016. ISSN 1537-5110. doi: 10.1016/j.biosystemseng.2015.12.002. URL https://www.sciencedirect.com/science/article/pii/S1537511015001828.

[78] Noha M. Elfiky, Shayan A. Akbar, Jianxin Sun, Johnny Park, and Avinash Kak. Automation of Dormant Pruning in Specialty Crop Production: An Adaptive Framework for Automatic Reconstruction and Modeling of Apple Trees. In *Proceedings of the IEEE Conference on Computer Vision and Pattern Recognition Workshops*, pages 65–73, 2015. URL https://www.cv-foundation.org/openaccess/content_cvpr_workshops_2015/W05/html/Elfiky_Automation_of_Dormant_2015_CVPR_paper.html.

[79] Ricardo Sanz-Cortiella, Jordi Llorens-Calveras, Alexandre Escolà, Jaume Arnó-Satorra, Manel Ribes-Dasi, Joan Masip-Vilalta, Ferran Camp, Felip Gràcia-Aguilá, Francesc Solanelles-Batlle, Santiago Planas-DeMartí, Tomàs Pallejà-Cabré, Jordi Palacin-Roca, Eduard Gregorio-Lopez, Ignacio Del-Moral-Martínez, and Joan R. Rosell-Polo. Innovative LIDAR 3D Dynamic Measurement System to Estimate Fruit-Tree Leaf Area. *Sensors*, 11(6): 5769–5791, June 2011. ISSN 1424-8220. doi: 10.3390/s110605769. URL https://www.mdpi.com/1424-8220/11/6/5769. Number: 6 Publisher: Molecular Diversity Preservation International.

[80] Pyare Pueschel, Glenn Newnham, and Joachim Hill. Retrieval of Gap Fraction and Effective Plant Area Index from Phase-Shift Terrestrial Laser Scans. *Remote Sensing*, 6(3):2601–2627, March 2014. ISSN 2072-4292. doi: 10.3390/rs6032601. URL https://www.mdpi.com/2072-4292/6/3/2601. Number: 3 Publisher: Multidisciplinary Digital Publishing Institute.

[81] Kristina Koenig, Bernhard Höfle, Martin Hämmerle, Thomas Jarmer, Bastian Siegmann, and Holger Lilienthal. Comparative classification analysis of post-harvest growth detection from terrestrial LiDAR point clouds in precision agriculture. *ISPRS Journal of Photogrammetry and Remote Sensing*, 104: 112–125, June 2015. ISSN 0924-2716. doi: 10.1016/j.isprsjprs.2015.03.003. URL https://www.sciencedirect.com/science/article/pii/S0924271615000623.

[82] Karolina D. Fieber, Ian J. Davenport, James M. Ferryman, Robert J. Gurney, Jeffrey P. Walker, and Jorg M. Hacker. Analysis of full-waveform LiDAR data for classification of an orange orchard scene. *ISPRS Journal of Photogrammetry and Remote Sensing*, 82:63–82, August 2013. ISSN 0924-2716.

doi: 10.1016/j.isprsjprs.2013.05.002. URL https://www.sciencedirect.com/science/article/pii/S0924271613001238.

[83] Tristan Allouis, Sylvie Durrieu, Cédric Véga, and Pierre Couteron. Stem Volume and Above-Ground Biomass Estimation of Individual Pine Trees From LiDAR Data: Contribution of Full-Waveform Signals. *IEEE Journal of Selected Topics in Applied Earth Observations and Remote Sensing*, 6 (2):924–934, April 2013. ISSN 2151-1535. doi: 10.1109/JSTARS.2012.2211863. Conference Name: IEEE Journal of Selected Topics in Applied Earth Observations and Remote Sensing.

[84] Fernando A. Auat Cheein, José Guivant, Ricardo Sanz, Alexandre Escolà, Francisco Yandún, Miguel Torres-Torriti, and Joan R. Rosell-Polo. Real-time approaches for characterization of fully and partially scanned canopies in groves. *Computers and Electronics in Agriculture*, 118:361–371, October 2015. ISSN 0168-1699. doi: 10.1016/j.compag.2015.09.017. URL https://www.sciencedirect.com/science/article/pii/S0168169915002926.

[85] Yi Lin. LiDAR: An important tool for next-generation phenotyping technology of high potential for plant phenomics? *Computers and Electronics in Agriculture*, 119:61–73, November 2015. ISSN 0168-1699. doi: 10.1016/j.compag.2015.10.011. URL https://www.sciencedirect.com/science/article/pii/S0168169915003245.

[86] Yotam Livny, Feilong Yan, Matt Olson, Baoquan Chen, Hao Zhang, and Jihad El-Sana. Automatic reconstruction of tree skeletal structures from point clouds. In *ACM SIGGRAPH Asia 2010 papers*, SIGGRAPH ASIA '10, pages 1–8, New York, NY, USA, December 2010. Association for Computing Machinery. ISBN 978-1-4503-0439-9. doi: 10.1145/1866158.1866177. URL https://doi.org/10.1145/1866158.1866177.

[87] RA Viscarra Rossel, VI Adamchuk, KA Sudduth, NJ McKenzie, and Craig Lobsey. Proximal soil sensing: An effective approach for soil measurements in space and time. *Advances in agronomy*, 113:243–291, 2011.

[88] Barry Allred, Jeffrey J Daniels, and Mohammad Reza Ehsani. *Handbook of agricultural geophysics*. CRC Press, 2008.

[89] Katerina Zajícová and Tomas Chuman. Application of ground penetrating radar methods in soil studies: A review. *Geoderma*, 343:116–129, 2019.

[90] Anja Klotzsche, François Jonard, Majken Caroline Looms, Jan van der Kruk, and Johan A Huisman. Measuring soil water content with ground penetrating radar: A decade of progress. *Vadose Zone Journal*, 17(1):1–9, 2018.

[91] James A Doolittle and Eric C Brevik. The use of electromagnetic induction techniques in soils studies. *Geoderma*, 223:33–45, 2014.

[92] Anatja Samouëlian, Isabelle Cousin, Alain Tabbagh, Ary Bruand, and Guy Richard. Electrical resistivity survey in soil science: a review. *Soil and Tillage research*, 83(2):173–193, 2005.

[93] VI Adamchuk, B Allred, J Doolittle, K Grote, R Rossel, C Ditzler, and L West. Tools for proximal soil sensing. *Soil Survey Staff, C. Ditzler, and L. West, eds. Soil survey manual. United States Department of Agriculture Handbook*, 1 (18), 2015.

[94] Shimon Y. Nof. *Springer Handbook of automation*. Springer, Berlin, Heidelberg, 2009. ISBN 978-3-642-04089-4. URL https://link.springer.com/book/10.1007/978-3-540-78831-7.

[95] Q. Zhang. Opportunity of robotics in specialty crop production. In *IFAC Proceedings Volumes*, volume 46 of *5th IFAC Conference on Bio-Robotics*, pages 38–39, January 2013. ISBN 978-3-902823-30-4. doi: 10.3182/20130327-3-jp-3017.00011. URL https://www.sciencedirect.com/science/article/pii/S1474667016335029. ISSN: 1474-6670 Issue: PART 1.

[96] J. K. Schueller. CIGR handbook of agricultural engineering. *Information Technology*, VI, 2006. URL https://cigr.org/node/640.

[97] Yoshisada Nagasaka, Naonobu Umeda, Yutaka Kanetai, Ken Taniwaki, and Yasuhiro Sasaki. Autonomous guidance for rice transplanting using global positioning and gyroscopes. *Computers and Electronics in Agriculture*, 43(3): 223–234, June 2004. ISSN 0168-1699. doi: 10.1016/j.compag.2004.01.005. URL https://www.sciencedirect.com/science/article/pii/S0168169904000304.

[98] Chunlei Xia, Longtan Wang, Bu-Keun Chung, and Jang-Myung Lee. In Situ 3D Segmentation of Individual Plant Leaves Using a RGB-D Camera for Agricultural Automation. *Sensors*, 15(8):20463–20479, August 2015. ISSN 1424-8220. doi: 10.3390/s150820463. URL https://www.mdpi.com/1424-8220/15/8/20463. Number: 8 Publisher: Multidisciplinary Digital Publishing Institute.

[99] Simon Blackmore. Towards robotic agriculture. In *Autonomous Air and Ground Sensing Systems for Agricultural Optimization and Phenotyping*, volume 9866, pages 8–15. SPIE, June 2016. doi: 10.1117/12.2234051. URL https://www.spiedigitallibrary.org/conference-proceedings-of-spie/9866/986603/Towards-robotic-agriculture/10.1117/12.2234051.full.

[100] Christophe Cariou, Roland Lenain, Benoit Thuilot, and Michel Berducat. Automatic guidance of a four-wheel-steering mobile robot for accurate field operations. *Journal of Field Robotics*, 26(6-7):504–518, 2009. ISSN 1556-4967. doi: 10.1002/rob.20282. URL https://onlinelibrary.wiley.com/doi/abs/10.1002/rob.20282.

[101] Marcel Bergerman, John Billingsley, John Reid, and Eldert van Henten. Robotics in Agriculture and Forestry. In *Springer Handbook of Robotics*,

Springer Handbooks, pages 1463–1492. Springer International Publishing, Cham, 2016. ISBN 978-3-319-32552-1. doi: 10.1007/978-3-319-32552-1_56. URL https://doi.org/10.1007/978-3-319-32552-1_56.

[102] Nicolas Tremblay, Edith Fallon, and Noura Ziadi. Sensing of Crop Nitrogen Status: Opportunities, Tools, Limitations, and Supporting Information Requirements. *HortTechnology*, 21(3):274–281, June 2011. ISSN 1943-7714, 1063-0198. doi: 10.21273/HORTTECH.21.3.274. URL https://journals.ashs.org/horttech/view/journals/horttech/21/3/article-p274.xml. Publisher: American Society for Horticultural Science Section: HortTechnology.

[103] Nicolas Tremblay, Yacine M. Bouroubi, Carl Bélec, Robert William Mullen, Newell R. Kitchen, Wade E. Thomason, Steve Ebelhar, David B. Mengel, William R. Raun, Dennis D. Francis, Earl D. Vories, and Ivan Ortiz-Monasterio. Corn Response to Nitrogen is Influenced by Soil Texture and Weather. *Agronomy Journal*, 104(6):1658–1671, 2012. ISSN 1435-0645. doi: 10.2134/agronj2012.0184. URL https://onlinelibrary.wiley.com/doi/abs/10.2134/agronj2012.0184.

[104] Mariano Gonzalez-de Soto, Luis Emmi, Isaias Garcia, and Pablo Gonzalez-de Santos. Reducing fuel consumption in weed and pest control using robotic tractors. *Computers and Electronics in Agriculture*, 114:96–113, June 2015. ISSN 0168-1699. doi: 10.1016/j.compag.2015.04.003. URL https://www.sciencedirect.com/science/article/pii/S0168169915001106.

[105] Mariano Gonzalez-de Soto, Luis Emmi, Carmen Benavides, Isaias Garcia, and Pablo Gonzalez-de Santos. Reducing air pollution with hybrid-powered robotic tractors for precision agriculture. *Biosystems Engineering*, 143:79–94, March 2016. ISSN 1537-5110. doi: 10.1016/j.biosystemseng.2016.01.008. URL https://www.sciencedirect.com/science/article/pii/S153751101530177X.

[106] J. N Wilson. Guidance of agricultural vehicles — a historical perspective. *Computers and Electronics in Agriculture*, 25(1):3–9, January 2000. ISSN 0168-1699. doi: 10.1016/S0168-1699(99)00052-6. URL https://www.sciencedirect.com/science/article/pii/S0168169999000526.

[107] Keun Ha Choi, Sang Kwon Han, Sang Hoon Han, Kwang-Ho Park, Kyung-Soo Kim, and Soohyun Kim. Morphology-based guidance line extraction for an autonomous weeding robot in paddy fields. *Computers and Electronics in Agriculture*, 113:266–274, April 2015. ISSN 0168-1699. doi: 10.1016/j.compag.2015.02.014. URL https://www.sciencedirect.com/science/article/pii/S0168169915000563.

[108] Jesús Conesa-Muñoz, Mariano Gonzalez-de Soto, Pablo Gonzalez-de Santos, and Angela Ribeiro. Distributed Multi-Level Supervision to Effectively Monitor the Operations of a Fleet of Autonomous Vehicles in Agricultural Tasks. *Sensors*, 15(3):5402–5428, March 2015. ISSN 1424-8220. doi: 10.3390/s150305402. URL https://www.mdpi.com/1424-8220/15/3/5402. Number: 3 Publisher: Multidisciplinary Digital Publishing Institute.

[109] T. Burks, F. Villegas, M. Hannan, S. Flood, B. Sivaraman, V. Subramanian, and J. Sikes. Engineering and Horticultural Aspects of Robotic Fruit Harvesting: Opportunities and Constraints. *HortTechnology*, 15(1):79–87, January 2005. ISSN 1943-7714, 1063-0198. doi: 10.21273/HORTTECH.15.1.0079. URL https://journals.ashs.org/horttech/view/journals/horttech/15/1/article-p79.xml. Publisher: American Society for Horticultural Science Section: HortTechnology.

[110] Rong Xiang, Huanyu Jiang, and Yibin Ying. Recognition of clustered tomatoes based on binocular stereo vision. *Computers and Electronics in Agriculture*, 106:75–90, August 2014. ISSN 0168-1699. doi: 10.1016/j.compag.2014.05.006. URL https://www.sciencedirect.com/science/article/pii/S016816991400129X.

[111] John Billingsley, Arto Visala, and Mark Dunn. Robotics in Agriculture and Forestry. In *Springer Handbook of Robotics*, pages 1065–1077. Springer, Berlin, Heidelberg, 2008. ISBN 978-3-540-30301-5. doi: 10.1007/978-3-540-30301-5_47. URL https://doi.org/10.1007/978-3-540-30301-5_47.

[112] Avital Bechar and Clément Vigneault. Agricultural robots for field operations: Concepts and components. *Biosystems Engineering*, 149:94–111, September 2016. ISSN 1537-5110. doi: 10.1016/j.biosystemseng.2016.06.014. URL https://www.sciencedirect.com/science/article/pii/S1537511015301914.

[113] Avital Bechar and Clément Vigneault. Agricultural robots for field operations. Part 2: Operations and systems. *Biosystems Engineering*, 153:110–128, January 2017. ISSN 1537-5110. doi: 10.1016/j.biosystemseng.2016.11.004. URL https://www.sciencedirect.com/science/article/pii/S1537511015301926.

[114] Bianca Ortuani, Giovanna Sona, Giulia Ronchetti, Alice Mayer, and Arianna Facchi. Integrating geophysical and multispectral data to delineate homogeneous management zones within a vineyard in Northern Italy. *Sensors*, 19 (18):3974, 2019. Publisher: Multidisciplinary Digital Publishing Institute.

[115] Elena Belcore, Stefano Angeli, Elisabetta Colucci, Maria Angela Musci, and Irene Aicardi. Precision Agriculture Workflow, from Data Collection to Data Management Using FOSS Tools: An Application in Northern Italy Vineyard. *ISPRS International Journal of Geo-Information*, 10(4):236, 2021. Publisher: Multidisciplinary Digital Publishing Institute.

[116] Noa Schor, Avital Bechar, Timea Ignat, Aviv Dombrovsky, Yigal Elad, and Sigal Berman. Robotic Disease Detection in Greenhouses: Combined Detection of Powdery Mildew and Tomato Spotted Wilt Virus. *IEEE Robotics and Automation Letters*, 1(1):354–360, January 2016. ISSN 2377-3766. doi: 10.1109/LRA.2016.2518214. Conference Name: IEEE Robotics and Automation Letters.

[117] R. Ceres, J.L. Pons, A.R. Jiménez, J.M. Martín, and L. Calderón. Design and implementation of an aided fruit-harvesting robot (Agribot). *Industrial Robot: An International Journal*, 25(5):337–346, January 1998. ISSN 0143-991X. doi: 10.1108/01439919810232440. URL https://doi.org/10.1108/01439919810232440. Publisher: MCB UP Ltd.

[118] Tien Thanh Nguyen, Erdal Kayacan, Josse De Baedemaeker, and Wouter Saeys. Task and Motion Planning for Apple Harvesting Robot*. *IFAC Proceedings Volumes*, 46(18):247–252, August 2013. ISSN 1474-6670. doi: 10.3182/20130828-2-SF-3019.00063. URL https://www.sciencedirect.com/science/article/pii/S1474667015349922.

[119] Thomas Hellström and Ola Ringdahl. A software framework for agricultural and forestry robots. *Industrial Robot: An International Journal*, 40(1):20–26, January 2013. ISSN 0143-991X. doi: 10.1108/01439911311294228. URL https://doi.org/10.1108/01439911311294228. Publisher: Emerald Group Publishing Limited.

[120] Roberto Tazzari, Dario Mengoli, and Lorenzo Marconi. Design Concept and Modelling of a Tracked UGV for Orchard Precision Agriculture. In *2020 IEEE International Workshop on Metrology for Agriculture and Forestry (MetroAgriFor)*, pages 207–212, November 2020. ISBN 978-1-72818-783-9. doi: 10.1109/MetroAgriFor50201.2020.9277577.

[121] F. Cuesta, F. Gomez-Bravo, and A. Ollero. Parking maneuvers of industrial-like electrical vehicles with and without trailer. *IEEE Transactions on Industrial Electronics*, 51(2):257–269, April 2004. ISSN 1557-9948. doi: 10.1109/TIE.2004.824855. Conference Name: IEEE Transactions on Industrial Electronics.

[122] Chang Boon Low and Danwei Wang. GPS-Based Path Following Control for a Car-Like Wheeled Mobile Robot With Skidding and Slipping. *IEEE Transactions on Control Systems Technology*, 16(2):340–347, March 2008. ISSN 1558-0865. doi: 10.1109/TCST.2007.903100. Conference Name: IEEE Transactions on Control Systems Technology.

[123] S. Cubero, E. Marco-noales, N. Aleixos, S. Barbé, and J. Blasco. Robhortic: A field robot to detect pests and diseases in horticultural crops by proximal sensing. *Agriculture (Switzerland)*, 10(7):1–13, 2020. ISSN 2077-0472. doi: 10.3390/agriculture10070276.

[124] EarthSense. Terra Sentia by EarthSense, 2019. URL https://www.earthsense.co.

[125] Small Robot Company. Tom robot, 2021. URL https://www.smallrobotcompany.com.

[126] J.P. Underwood, C. Hung, B. Whelan, and S. Sukkarieh. Mapping almond orchard canopy volume, flowers, fruit and yield using lidar and vision sensors.

Computers and Electronics in Agriculture, 130:83–96, 2016. ISSN 0168-1699. doi: 10.1016/j.compag.2016.09.014.

[127] Tim Mueller-Sim, Merritt Jenkins, Justin Abel, and George Kantor. The Robotanist: A ground-based agricultural robot for high-throughput crop phenotyping. In *2017 IEEE International Conference on Robotics and Automation (ICRA)*, pages 3634–3639, May 2017. ISBN 978-1-5090-4633-1. doi: 10.1109/ICRA.2017.7989418.

[128] N. Virlet, K. Sabermanesh, P. Sadeghi-Tehran, and M.J. Hawkesford. Field Scanalyzer: An automated robotic field phenotyping platform for detailed crop monitoring. *Functional Plant Biology*, 44(1):143–153, 2017. ISSN 1445-4408. doi: 10.1071/FP16163.

[129] B. Rey, N. Aleixos, S. Cubero, and J. Blasco. XF-ROVIM. A field robot to detect olive trees infected by Xylella fastidiosa using proximal sensing. *Remote Sensing*, 11(3), 2019. ISSN 2072-4292. doi: 10.3390/rs11030221.

[130] William S. Barbosa, Adalberto I. S. Oliveira, Gustavo B. P. Barbosa, Antonio C. Leite, Karla T. Figueiredo, Marley M. B. R. Vellasco, and Wouter Caarls. Design and Development of an Autonomous Mobile Robot for Inspection of Soy and Cotton Crops. In *2019 12th International Conference on Developments in eSystems Engineering (DeSE)*, pages 557–562, October 2019. ISBN 978-1-72813-021-7. doi: 10.1109/DeSE.2019.00107. ISSN: 2161-1351.

[131] P. Menendez-Aponte, X. Kong, and Y. Xu. An approximated, control affine model for a strawberry field scouting robot considering wheel-terrain interaction. *Robotica*, 37(9):1545–1561, 2019. ISSN 0263-5747. doi: 10.1017/S0263574719000134.

[132] Marco Bietresato, Giovanni Carabin, Renato Vidoni, Alessandro Gasparetto, and Fabrizio Mazzetto. Evaluation of a LiDAR-based 3D-stereoscopic vision system for crop-monitoring applications. *Computers and Electronics in Agriculture*, 124:1–13, June 2016. ISSN 0168-1699. doi: 10.1016/j.compag.2016.03.017. URL https://www.sciencedirect.com/science/article/pii/S0168169916300862.

[133] M Bietresato, G Carabin, D D'Auria, R Gallo, G Ristorto, F Mazzetto, R Vidoni, A Gasparetto, and L Scalera. A tracked mobile robotic lab for monitoring the plants volume and health. In *2016 12th IEEE/ASME International Conference on Mechatronic and Embedded Systems and Applications (MESA)*, pages 1–6, August 2016. doi: 10.1109/MESA.2016.7587134.

[134] G. Ristorto, R. Gallo, A. Gasparetto, L. Scalera, R. Vidoni, and F. Mazzetto. A Mobile Laboratory for Orchard Health Status Monitoring in Precision Farming. *Chemical Engineering Transactions*, 58:661–666, June 2017. ISSN 2283-9216. doi: 10.3303/CET1758111. URL https://www.cetjournal.it/index.php/cet/article/view/CET1758111.

[135] Renato Vidoni, Raimondo Gallo, Gianluca Ristorto, Giovanni Carabin, Fabrizio Mazzetto, Lorenzo Scalera, and Alessandro Gasparetto. ByeLab: An agricultural mobile robot prototype for proximal sensing and precision farming. In *ASME International Mechanical Engineering Congress and Exposition*, volume 58370, page V04AT05A057. American Society of Mechanical Engineers, 2017.

[136] T. Bakker, K. Asselt, J. Bontsema, J. Müller, and G. Straten. Systematic design of an autonomous platform for robotic weeding. *Journal of Terramechanics*, 47(2):63–73, 2010. ISSN 0022-4898. doi: 10.1016/j.jterra.2009.06.002.

[137] O. Bawden, J. Kulk, R. Russell, C. McCool, A. English, F. Dayoub, C. Lehnert, and T. Perez. Robot for weed species plant-specific management. *Journal of Field Robotics*, 34(6):1179–1199, 2017. ISSN 1556-4959. doi: 10.1002/rob.21727.

[138] T. Utstumo, F. Urdal, A. Brevik, J. Dørum, J. Netland, Ø. Overskeid, T.W. Berge, and J.T. Gravdahl. Robotic in-row weed control in vegetables. *Computers and Electronics in Agriculture*, 154:36–45, 2018. ISSN 0168-1699. doi: 10.1016/j.compag.2018.08.043.

[139] Naïo Technologies. Autonomous Oz weeding robot, 2016. URL https://www.naio-technologies.com/en/oz/.

[140] Naïo Technologies. DINO vegetable weeding robot for large-scale vegetable farms, 2016. URL https://www.naio-technologies.com/en/dino/.

[141] Naïo Technologies. TED, the vineyard weeding robot, 2016. URL https://www.naio-technologies.com/en/ted/.

[142] CARRÉ. ANATIS by CARRÉ, July 2019. URL https://www.carre.fr/entretien-des-cultures-et-prairies/anatis/?lang=en.

[143] Ecorobotix. AVO The autonomous robot weeder from Ecorobotix, 2020. URL https://www.ecorobotix.com/en/avo-autonomous-robot-weeder/.

[144] L. Haibo, D. Shuliang, L. Zunmin, and Y. Chuijie. Study and Experiment on a Wheat Precision Seeding Robot. *Journal of Robotics*, 2015, 2015. ISSN 1687-9600. doi: 10.1155/2015/696301.

[145] P. Ruangurai, M. Ekpanyapong, C. Pruetong, and T. Watewai. Automated three-wheel rice seeding robot operating in dry paddy fields. *Maejo International Journal of Science and Technology*, 9(3):403–412, 2015. ISSN 1905-7873.

[146] Masood Ul Hassan, Mukhtar Ullah, and Jamshed Iqbal. Towards autonomy in agriculture: Design and prototyping of a robotic vehicle with seed selector. In *2016 2nd International Conference on Robotics and Artificial Intelligence (ICRAI)*, pages 37–44, November 2016. doi: 10.1109/ICRAI.2016.7791225.

[147] Nandagopal Srinivasan, Prithviraj Prabhu, S Sanjana Smruthi, N Vivek Sivaraman, S Joseph Gladwin, R Rajavel, and Abeshek Ram Natarajan. Design of an autonomous seed planting robot. In *2016 IEEE Region 10 Humanitarian Technology Conference (R10-HTC)*, pages 1–4, December 2016. doi: 10.1109/R10-HTC.2016.7906789.

[148] P V S Jayakrishna, M Suryavamsi Reddy, N Jaswanth Sai, N Susheel, and K P Peeyush. Autonomous Seed Sowing Agricultural Robot. In *2018 International Conference on Advances in Computing, Communications and Informatics (ICACCI)*, pages 2332–2336, September 2018. doi: 10.1109/ICACCI.2018.8554622.

[149] Amir Asghar Ali, Muhammad Zohaib, and Syed Atif Mehdi. An Autonomous Seeder for Maize Crop. In *Proceedings of the 2019 5th International Conference on Robotics and Artificial Intelligence*, ICRAI '19, pages 42–47, New York, NY, USA, November 2019. Association for Computing Machinery. ISBN 978-1-4503-7235-0. doi: 10.1145/3373724.3373737. URL https://doi.org/10.1145/3373724.3373737.

[150] Avinash S. Pramod and T. V. Jithinmon. Development of mobile dual PR arm agricultural robot. *Journal of Physics: Conference Series*, 1240(1): 012034, July 2019. ISSN 1742-6596. doi: 10.1088/1742-6596/1240/1/012034. URL https://doi.org/10.1088/1742-6596/1240/1/012034. Publisher: IOP Publishing.

[151] Cino Mathew Jose, A. P. Sudheer, and M. D. Narayanan. Modelling and Analysis of Seeding Robot for Row Crops. In *Innovative Product Design and Intelligent Manufacturing Systems*, Lecture Notes in Mechanical Engineering, pages 1003–1014, Singapore, 2020. Springer. ISBN 9789811526961. doi: 10.1007/978-981-15-2696-1_97.

[152] Hussain Nor Azmi, Sami Salama Hussen Hajjaj, Kisheen Rao Gsangaya, Mohamed Thariq Hameed Sultan, Mohd Fazly Mail, and Lee Seng Hua. Design and fabrication of an agricultural robot for crop seeding. *Materials Today: Proceedings*, April 2021. ISSN 2214-7853. doi: 10.1016/j.matpr.2021.03.191. URL https://www.sciencedirect.com/science/article/pii/S2214785321022100.

[153] Pankaj Kumar and G. Ashok. Design and fabrication of smart seed sowing robot. *Materials Today: Proceedings*, 39:354–358, January 2021. ISSN 2214-7853. doi: 10.1016/j.matpr.2020.07.432. URL https://www.sciencedirect.com/science/article/pii/S2214785320355425.

[154] Ismail Ibrahim Mohammed and Abdul Razzaq Abdul Latif Jassim. Design and Testing of an Agricultural Robot to Operate a Combined Seeding Machine. *Annals of the Romanian Society for Cell Biology*, 25(7):92–106, July 2021. URL https://www.annalsofrscb.ro/index.php/journal/article/view/9180. Number: 7.

[155] Suibing Li, Shuai Li, and Long Jin. The Design and Physical Implementation of Seeding Robots in Deserts. In *2020 39th Chinese Control Conference (CCC)*, pages 3892–3897, July 2020. doi: 10.23919/CCC50068.2020.9189220. ISSN: 1934-1768.

[156] Md Zafar Iqbal, Md Nafiul Islam, Mohammod Ali, Md Shaha Nur Kabir, Tusan Park, Tae-Gyoung Kang, Kyu-Sik Park, and Sun-Ok Chung. Kinematic analysis of a hopper-type dibbling mechanism for a 2.6 kW two-row pepper transplanter. *Journal of Mechanical Science and Technology*, 35(6):2605–2614, June 2021. ISSN 1976-3824. doi: 10.1007/s12206-021-0531-2. URL https://doi.org/10.1007/s12206-021-0531-2.

[157] Z. Liu, X. Wang, W. Zheng, Z. Lv, and W. Zhang. Design of a sweet potato transplanter based on a robot arm. *Applied Sciences (Switzerland)*, 11(19), 2021. ISSN 2076-3417. doi: 10.3390/app11199349.

[158] Rowbot. Rowbot, 2020. URL https://www.rowbot.com.

[159] Hiroaki Yaguchi, Kotaro Nagahama, Takaomi Hasegawa, and Masayuki Inaba. Development of an autonomous tomato harvesting robot with rotational plucking gripper. In *2016 IEEE/RSJ International Conference on Intelligent Robots and Systems (IROS)*, pages 652–657, October 2016. ISBN 978-1-5090-3762-9. doi: 10.1109/IROS.2016.7759122. ISSN: 2153-0866.

[160] Q. Feng, W. Zou, P. Fan, C. Zhang, and X. Wang. Design and test of robotic harvesting system for cherry tomato. *International Journal of Agricultural and Biological Engineering*, 11(1):96–100, 2018. ISSN 1934-6344. doi: 10.25165/j.ijabe.20181101.2853.

[161] Agrobot: Agricultural Robots. Robotic Harvesters | Agrobot, 2018. URL https://www.agrobot.com/e-series.

[162] Yuanyue Ge, Ya Xiong, Gabriel Lins Tenorio, and Pål Johan From. Fruit Localization and Environment Perception for Strawberry Harvesting Robots. *IEEE Access*, 7:147642–147652, 2019. ISSN 2169-3536. doi: 10.1109/ACCESS.2019.2946369. Conference Name: IEEE Access.

[163] Ya Xiong, Yuanyue Ge, Lars Grimstad, and Pål J. From. An autonomous strawberry-harvesting robot: Design, development, integration, and field evaluation. *Journal of Field Robotics*, 37(2), 2020. ISSN 1556-4967. doi: 10.1002/rob.21889. URL https://onlinelibrary.wiley.com/doi/abs/10.1002/rob.21889.

[164] C.W. Bac, J. Hemming, B.A.J. van Tuijl, R. Barth, E. Wais, and E.J. van Henten. Performance Evaluation of a Harvesting Robot for Sweet Pepper. *Journal of Field Robotics*, 34(6):1123–1139, 2017. ISSN 1556-4959. doi: 10.1002/rob.21709.

[165] B. Arad, J. Balendonck, R. Barth, O. Ben-Shahar, Y. Edan, T. Hellström, J. Hemming, P. Kurtser, O. Ringdahl, T. Tielen, and B. van Tuijl. Development of a sweet pepper harvesting robot. *Journal of Field Robotics*, 37(6):1027–1039, 2020. ISSN 1556-4959. doi: 10.1002/rob.21937.

[166] Chris Lehnert, Chris McCool, Inkyu Sa, and Tristan Perez. Performance improvements of a sweet pepper harvesting robot in protected cropping environments. *Journal of Field Robotics*, 37(7), 2020. ISSN 1556-4967. doi: 10.1002/rob.21973. URL https://onlinelibrary.wiley.com/doi/abs/10.1002/rob.21973.

[167] V. Raja, B. Bhaskaran, K.K.G. Nagaraj, J.G. Sampathkumar, and S.R. Senthilkumar. Agricultural harvesting using integrated robot system. *Indonesian Journal of Electrical Engineering and Computer Science*, 25(1):152–158, 2022. ISSN 2502-4752. doi: 10.11591/ijeecs.v25.i1.pp152-158.

[168] Simon Birrell, Josie Hughes, Julia Y. Cai, and Fumiya Iida. A field-tested robotic harvesting system for iceberg lettuce. *Journal of Field Robotics*, 37(2):225–245, 2020. ISSN 1556-4967. doi: 10.1002/rob.21888. URL https://onlinelibrary.wiley.com/doi/abs/10.1002/rob.21888.

[169] Adrian Leu, Mohammad Razavi, Lasse Langstädtler, Danijela Ristić-Durrant, Holger Raffel, Christian Schenck, Axel Gräser, and Bernd Kuhfuss. Robotic Green Asparagus Selective Harvesting. *IEEE/ASME Transactions on Mechatronics*, 22(6):2401–2410, December 2017. ISSN 1941-014X. doi: 10.1109/TMECH.2017.2735861. Conference Name: IEEE/ASME Transactions on Mechatronics.

[170] Hanwen Kang, Hongyu Zhou, and Chao Chen. Visual Perception and Modeling for Autonomous Apple Harvesting. *IEEE Access*, 8:62151–62163, 2020. ISSN 2169-3536. doi: 10.1109/ACCESS.2020.2984556. Conference Name: IEEE Access.

[171] Robert Bogue. Fruit picking robots: has their time come? *Industrial Robot: the international journal of robotics research and application*, 47(2):141–145, January 2020. ISSN 0143-991X. doi: 10.1108/IR-11-2019-0243. URL https://doi.org/10.1108/IR-11-2019-0243. Publisher: Emerald Publishing Limited.

[172] Luciano Cantelli, Filippo Bonaccorso, Domenico Longo, Carmelo Donato Melita, Giampaolo Schillaci, and Giovanni Muscato. A Small Versatile Electrical Robot for Autonomous Spraying in Agriculture. *AgriEngineering*, 1(3):391–402, September 2019. ISSN 2624-7402. doi: 10.3390/agriengineering1030029. URL https://www.mdpi.com/2624-7402/1/3/29. Number: 3 Publisher: Multidisciplinary Digital Publishing Institute.

[173] Adrien Danton, Jean-Christophe Roux, Benoit Dance, Christophe Cariou, and Roland Lenain. Development of a spraying robot for precision agriculture: An edge following approach. In *2020 IEEE Conference on Control Technology*

and Applications (CCTA), pages 267–272. IEEE, August 2020. doi: 10.1109/CCTA41146.2020.9206304.

[174] F.P. Terra, G.H. Nascimento, G.A. Duarte, and P.L.J. Drews-Jr. Autonomous Agricultural Sprayer using Machine Vision and Nozzle Control. *Journal of Intelligent and Robotic Systems: Theory and Applications*, 102(2), 2021. ISSN 0921-0296. doi: 10.1007/s10846-021-01361-x.

[175] Sneha A. Amrita, E. Abirami, A. Ankita, R. Praveena, and R. Srimeena. Agricultural Robot for automatic ploughing and seeding. In *2015 IEEE Technological Innovation in ICT for Agriculture and Rural Development (TIAR)*, pages 17–23, July 2015. ISBN 978-1-4799-7758-1. doi: 10.1109/TIAR.2015.7358525.

[176] Lars Grimstad and Pål Johan From. The Thorvald II Agricultural Robotic System. *Robotics*, 6(4):24, December 2017. ISSN 2218-6581. doi: 10.3390/robotics6040024. URL https://www.mdpi.com/2218-6581/6/4/24. Number: 4 Publisher: Multidisciplinary Digital Publishing Institute.

[177] Case IH. Case IH Autonomous Concept Vehicle, 2017. URL https://www.caseih.com/northamerica/en-us/Pages/campaigns/autonomous-concept-vehicle.aspx.

[178] Sitia. TREKTOR, 2020. URL https://www.sitia.fr/en/innovation-2/trektor/.

[179] John Deere. John Deere CES® 2022, 2022. URL https://ces2022.deere.com/.

[180] Agrobot: Agricultural Robots. Bug Vacuum, 2020. URL https://www.agrobot.com/bugvac.

[181] Henry Williams, Mahla Nejati, Salome Hussein, Nicky Penhall, Jong Yoon Lim, Mark Hedley Jones, Jamie Bell, Ho Seok Ahn, Stuart Bradley, Peter Schaare, Paul Martinsen, Mohammad Alomar, Purak Patel, Matthew Seabright, Mike Duke, Alistair Scarfe, and Bruce MacDonald. Autonomous pollination of individual kiwifruit flowers: Toward a robotic kiwifruit pollinator. *Journal of Field Robotics*, 37(2):246–262, 2020. ISSN 1556-4967. doi: 10.1002/rob.21861. URL https://onlinelibrary.wiley.com/doi/abs/10.1002/rob.21861.

[182] Rocco Galati, Giacomo Mantriota, and Giulio Reina. Design and Development of a Tracked Robot to Increase Bulk Density of Flax Fibers. *Journal of Mechanisms and Robotics*, 13(5), May 2021. ISSN 1942-4302. doi: 10.1115/1.4051017. URL https://doi.org/10.1115/1.4051017.

[183] D. Loukatos, E. Petrongonas, K. Manes, I.-V. Kyrtopoulos, V. Dimou, and K.G. Arvanitis. A synergy of innovative technologies towards implementing an autonomous diy electric vehicle for harvester-assisting purposes. *Machines*, 9(4), 2021. ISSN 2075-1702. doi: 10.3390/machines9040082.

[184] R. Oberti, M. Marchi, P. Tirelli, A. Calcante, M. Iriti, E. Tona, M. Hočevar, J. Baur, J. Pfaff, C. Schütz, and H. Ulbrich. Selective spraying of grapevines for disease control using a modular agricultural robot. *Biosystems Engineering*, 146:203–215, 2016. ISSN 1537-5110. doi: 10.1016/j.biosystemseng.2015.12.004.

[185] G. Adamides, C. Katsanos, I. Constantinou, G. Christou, M. Xenos, T. Hadzilacos, and Y. Edan. Design and development of a semi-autonomous agricultural vineyard sprayer: Human–robot interaction aspects. *Journal of Field Robotics*, 34(8):1407–1426, 2017. ISSN 1556-4959. doi: 10.1002/rob.21721.

[186] Rovitis 4.0. Rovitis 4.0, 2020. URL https://www.rovitisveneto.it/.

[187] A. Shafiekhani, S. Kadam, F.B. Fritschi, and G.N. Desouza. Vinobot and vinoculer: Two robotic platforms for high-throughput field phenotyping. *Sensors (Switzerland)*, 17(1), 2017. ISSN 1424-8220. doi: 10.3390/s17010214.

[188] D. Reiser, E.-S. Sehsah, O. Bumann, J. Morhard, and H.W. Griepentrog. Development of an autonomous electric robot implement for intra-row weeding in vineyards. *Agriculture (Switzerland)*, 9(1), 2019. ISSN 2077-0472. doi: 10.3390/agriculture9010018.

[189] T. Botterill, S. Paulin, R. Green, S. Williams, J. Lin, V. Saxton, S. Mills, X. Chen, and S. Corbett-Davies. A Robot System for Pruning Grape Vines. *Journal of Field Robotics*, 34(6):1100–1122, 2017. ISSN 1556-4959. doi: 10.1002/rob.21680.

[190] Yaqoob Majeed, Manoj Karkee, Qin Zhang, Longsheng Fu, and Matthew D. Whiting. Development and performance evaluation of a machine vision system and an integrated prototype for automated green shoot thinning in vineyards. *Journal of Field Robotics*, 38(6):898–916, 2021. ISSN 1556-4967. doi: 10.1002/rob.22013. URL https://onlinelibrary.wiley.com/doi/abs/10.1002/rob.22013.

[191] Vitibot. Bakus S, 2018. URL https://vitibot.fr/vineyards-robots-bakus/vineyard-robot-bakus-s/?lang=en.

[192] B. Thuilot, C. Cariou, P. Martinet, and M. Berducat. Automatic Guidance of a Farm Tractor Relying on a Single CP-DGPS. *Autonomous Robots*, 13(1):53–71, July 2002. ISSN 1573-7527. doi: 10.1023/A:1015678121948. URL https://doi.org/10.1023/A:1015678121948.

[193] Spyros Fountas, Nikos Mylonas, Ioannis Malounas, Efthymios Rodias, Christoph Hellmann Santos, and Erik Pekkeriet. Agricultural Robotics for Field Operations. *Sensors*, 20(9):2672, January 2020. ISSN 1424-8220. doi: 10.3390/s20092672. URL https://www.mdpi.com/1424-8220/20/9/2672. Number: 9 Publisher: Multidisciplinary Digital Publishing Institute.

[194] James Lowenberg-DeBoer, Iona Yuelu Huang, Vasileios Grigoriadis, and Simon Blackmore. Economics of robots and automation in field crop production. *Precision Agriculture*, 21(2):278–299, April 2020. ISSN 1573-1618. doi: 10.1007/s11119-019-09667-5. URL https://doi.org/10.1007/s11119-019-09667-5.

[195] Kadeghe G. Fue, Wesley M. Porter, Edward M. Barnes, and Glen C. Rains. An Extensive Review of Mobile Agricultural Robotics for Field Operations: Focus on Cotton Harvesting. *AgriEngineering*, 2(1):150–174, March 2020. ISSN 2624-7402. doi: 10.3390/agriengineering2010010. URL https://www.mdpi.com/2624-7402/2/1/10. Number: 1 Publisher: Multidisciplinary Digital Publishing Institute.

[196] Luiz F. P. Oliveira, António P. Moreira, and Manuel F. Silva. Advances in Agriculture Robotics: A State-of-the-Art Review and Challenges Ahead. *Robotics*, 10(2):52, June 2021. ISSN 2218-6581. doi: 10.3390/robotics10020052. URL https://www.mdpi.com/2218-6581/10/2/52. Number: 2 Publisher: Multidisciplinary Digital Publishing Institute.

[197] Renato Vidoni, Marco Bietresato, Alessandro Gasparetto, and Fabrizio Mazzetto. Evaluation and stability comparison of different vehicle configurations for robotic agricultural operations on side-slopes. *Biosystems Engineering*, 129:197–211, January 2015. ISSN 1537-5110. doi: 10.1016/j.biosystemseng.2014.10.003. URL https://www.sciencedirect.com/science/article/pii/S1537511014001780.

[198] M. V. Braunack. Changes in physical properties of two dry soils during tracked vehicle passage. *Journal of Terramechanics*, 23(3):141–151, 1986. ISSN 0022-4898. doi: 10.1016/0022-4898(86)90003-0. URL https://www.sciencedirect.com/science/article/pii/0022489886900030.

[199] M. V. Braunack. The residual effects of tracked vehicles on soil surface properties. *Journal of Terramechanics*, 23(1):37–50, 1986. ISSN 0022-4898. doi: 10.1016/0022-4898(86)90030-3. URL https://www.sciencedirect.com/science/article/pii/0022489886900303.

[200] M. V. Braunack and B. G. Williams. The effect of initial soil water content and vegetative cover on surface soil disturbance by tracked vehicles. *Journal of Terramechanics*, 30(4), 1993. ISSN 0022-4898. doi: 10.1016/0022-4898(93)90017-R. URL https://www.sciencedirect.com/science/article/pii/002248989390017R.

[201] P. D. Ayers. Environmental damage from tracked vehicle operation. *Journal of Terramechanics*, 31(3):173–183, 1994. ISSN 0022-4898. doi: 10.1016/0022-4898(94)90014-0. URL https://www.sciencedirect.com/science/article/pii/0022489894900140.

[202] Chad W. Prosser, Kevin K. Sedivec, and William T. Barker. Tracked vehicle effects on vegetation and soil characteristics. *Journal of Range Management*,

53(6):666–670, 2000. ISSN 0022-409X. doi: 10.2307/4003164. URL https://www.jstor.org/stable/4003164. Publisher: [Allen Press, Society for Range Management].

[203] Q. Li, P. D. Ayers, and A. B. Anderson. Modeling of terrain impact caused by tracked vehicles. *Journal of Terramechanics*, 44(6):395–410, 2007. ISSN 0022-4898. doi: 10.1016/j.jterra.2007.09.001. URL https://www.sciencedirect.com/science/article/pii/S0022489807000535.

[204] G. Molari, L. Bellentani, A. Guarnieri, M. Walker, and E. Sedoni. Performance of an agricultural tractor fitted with rubber tracks. *Biosystems Engineering*, 111 (1):57–63, 2012. ISSN 1537-5110. doi: 10.1016/j.biosystemseng.2011.10.008. URL https://www.sciencedirect.com/science/article/pii/S1537511011001838.

[205] Quyen Vu, Mirko Raković, Vlado Delic, and Andrey Ronzhin. Trends in Development of UAV-UGV Cooperation Approaches in Precision Agriculture. In *Interactive Collaborative Robotics*, Lecture Notes in Computer Science, pages 213–221, Cham, 2018. Springer International Publishing. ISBN 978-3-319-99582-3. doi: 10.1007/978-3-319-99582-3_22.

[206] Jurgen Zoto, Maria Angela Musci, Aleem Khaliq, Marcello Chiaberge, and Irene Aicardi. Automatic path planning for unmanned ground vehicle using uav imagery. In *International Conference on Robotics in Alpe-Adria Danube Region*, pages 223–230. Springer, 2019.

[207] Paolo Cinat, Salvatore Filippo Di Gennaro, Andrea Berton, and Alessandro Matese. Comparison of unsupervised algorithms for Vineyard Canopy segmentation from UAV multispectral images. *Remote Sensing*, 11(9):1023, 2019. Publisher: Multidisciplinary Digital Publishing Institute.

[208] Angela Ribeiro and Jesus Conesa-Muñoz. Multi-robot Systems for Precision Agriculture. In *Innovation in Agricultural Robotics for Precision Agriculture: A Roadmap for Integrating Robots in Precision Agriculture*, Progress in Precision Agriculture, pages 151–175. Springer International Publishing, Cham, 2021. ISBN 978-3-030-77036-5. doi: 10.1007/978-3-030-77036-5_7. URL https://doi.org/10.1007/978-3-030-77036-5_7.

[209] Enric Galceran and Marc Carreras. A survey on coverage path planning for robotics. *Robotics and Autonomous Systems*, 61(12):1258–1276, December 2013. ISSN 0921-8890. doi: 10.1016/j.robot.2013.09.004. URL https://www.sciencedirect.com/science/article/pii/S092188901300167X.

[210] ETH Zurich. Aerial Data Collection and Analysis, and Automated Ground Intervention for Precision Farming | Flourish Project | Fact Sheet | H2020 | CORDIS | European Commission, 2018. URL https://cordis.europa.eu/project/id/644227. Florish project.

[211] Subodh Bhandari, Amar Raheja, Robert L. Green, and Dat Do. Towards collaboration between unmanned aerial and ground vehicles for precision

agriculture. In *Autonomous Air and Ground Sensing Systems for Agricultural Optimization and Phenotyping II*, volume 10218, pages 26–39. SPIE, May 2017. doi: 10.1117/12.2262049. URL https://doi.org/10.1117/12.2262049.

[212] Pablo Gonzalez-de Santos, Angela Ribeiro, Cesar Fernandez-Quintanilla, Francisca Lopez-Granados, Michael Brandstoetter, Slobodanka Tomic, Stefania Pedrazzi, Andrea Peruzzi, Gonzalo Pajares, George Kaplanis, Manuel Perez-Ruiz, Constantino Valero, Jaime del Cerro, Marco Vieri, Gilles Rabatel, and Benoit Debilde. Fleets of robots for environmentally-safe pest control in agriculture. *Precision Agriculture*, 18(4):574–614, August 2017. ISSN 1573-1618. doi: 10.1007/s11119-016-9476-3. URL https://doi.org/10.1007/s11119-016-9476-3.

[213] Juan Jesús Roldán, Pablo Garcia-Aunon, Mario Garzón, Jorge De León, Jaime Del Cerro, and Antonio Barrientos. Heterogeneous Multi-Robot System for Mapping Environmental Variables of Greenhouses. *Sensors*, 16(7):1018, July 2016. doi: 10.3390/s16071018. URL https://www.mdpi.com/1424-8220/16/7/1018. Number: 7 Publisher: Multidisciplinary Digital Publishing Institute.

[214] Giuliano Vitali, Concetta Cardillo, Sergio Albertazzi, Marco Della Chiara, Guido Baldoni, Claudio Signorotti, Antonella Trisorio, and Maurizio Canavari. Classification of Italian Farms in the FADN Database Combining Climate and Structural Information. *Cartographica: The International Journal for Geographic Information and Geovisualization*, 47(4):228–236, December 2012. ISSN 0317-7173. doi: 10.3138/carto.47.4.1478. URL https://utpjournals.press/doi/10.3138/carto.47.4.1478. Publisher: University of Toronto Press.

[215] H Kaufmann and MM Blanke. Chilling requirements of mediterranean fruit crops in a changing climate. In *III International Symposium on Horticulture in Europe-SHE2016 1242*, pages 275–280, 2016.

[216] Domenico Pessina and Davide Facchinetti. A survey on fatal accidents for overturning of agricultural tractors in italy. *Chemical Engineering Transactions*, 58:79–84, 2017.

[217] G. Quaglia, P. Cavallone, and C. Visconte. Agri_q: Agriculture UGV for Monitoring and Drone Landing. In *Mechanism Design for Robotics*, Mechanisms and Machine Science, pages 413–423, Cham, 2019. Springer International Publishing. ISBN 978-3-030-00365-4. doi: 10.1007/978-3-030-00365-4_49.

[218] Giuseppe Quaglia, Carmen Visconte, Leonardo Sabatino Scimmi, Matteo Melchiorre, Paride Cavallone, and Stefano Pastorelli. Design of the positioning mechanism of an unmanned ground vehicle for precision agriculture. In *Advances in Mechanism and Machine Science*, Mechanisms and Machine Science, pages 3531–3540, Cham, 2019. Springer International Publishing. ISBN 978-3-030-20131-9. doi: 10.1007/978-3-030-20131-9_348.

[219] Giuseppe Quaglia, Carmen Visconte, Leonardo Sabatino Scimmi, Matteo Melchiorre, Paride Cavallone, and Stefano Pastorelli. Robot arm and control architecture integration on a UGV for precision agriculture. In *Advances in Mechanism and Machine Science*, Mechanisms and Machine Science, pages 2339–2348, Cham, 2019. Springer International Publishing. ISBN 978-3-030-20131-9. doi: 10.1007/978-3-030-20131-9_231.

[220] Giuseppe Quaglia, Carmen Visconte, Luca Carbonari, Andrea Botta, and Paride Cavallone. Agri. q: A Sustainable Rover for Precision Agriculture. In *Solar Energy Conversion in Communities*, pages 81–91. Springer, 2020.

[221] Paride Cavallone, Carmen Visconte, Luca Carbonari, Andrea Botta, and Giuseppe Quaglia. Design of the Mobile Robot Agri. q. In *Symposium on Robot Design, Dynamics and Control*, pages 288–296. Springer, 2020.

[222] Carmen Visconte, Paride Cavallone, Luca Carbonari, Andrea Botta, and Giuseppe Quaglia. Mechanism for the Locomotion Layout Reconfiguration of the Agri_q Mobile Robot. In *Advances in Service and Industrial Robotics*, pages 390–399, Cham, 2020. Springer International Publishing. ISBN 978-3-030-48989-2.

[223] Carmen Visconte, Paride Cavallone, Luca Carbonari, Andrea Botta, and Giuseppe Quaglia. Design of a Mechanism with Embedded Suspension to Reconfigure the Agri_q Locomotion Layout. *Robotics*, 10(1):15, 2021. Publisher: Multidisciplinary Digital Publishing Institute.

[224] Gian Luigi Corinto and Anna Maria Pioletti. Viticulture and Landscape in the Italian Northwestern Alpine Region. *Geography Notebooks*, 2, December 2019. doi: 10.7358/gn-2019-002-copi.

[225] Gilbert M. Masters. The solar resource. In *Renewable and Efficient Electric Power Systems*, pages 385–443. John Wiley & Sons, Ltd, 2004. ISBN 978-0-471-66882-4. doi: 10.1002/0471668826.ch7. URL https://onlinelibrary.wiley.com/doi/abs/10.1002/0471668826.ch7.

[226] Cecilia Scoccia, Giacomo Palmieri, Matteo Claudio Palpacelli, and Massimo Callegari. Real-time strategy for obstacle avoidance in redundant manipulators. In *The International Conference of IFToMM ITALY*, pages 278–285. Springer, 2020.

[227] Cecilia Scoccia, Giacomo Palmieri, Matteo Claudio Palpacelli, and Massimo Callegari. A collision avoidance strategy for redundant manipulators in dynamically variable environments: On-line perturbations of off-line generated trajectories. *Machines*, 9(2):30, 2021.

[228] Giorgia Chiriatti, Giacomo Palmieri, Cecilia Scoccia, Matteo Claudio Palpacelli, and Massimo Callegari. Adaptive obstacle avoidance for a class of collaborative robots. *Machines*, 9(6):113, 2021.

[229] Shuuji Torii, Eiichi Yaguchi, Kiyotaka Ozaki, Tomio Jindoh, Masatsugu Owada, and Gempei Naitoh. Electronically Controlled Torque Split System, for 4WD Vehicles. SAE Technical Paper 861349, SAE International, Warrendale, PA, 1986. URL https://www.sae.org/publications/technical-papers/content/861349/. ISSN: 0148-7191, 2688-3627.

[230] Genpei Naito, Eiichi Yaguchi, Toshiro Matuda, Masashi Asahi, Toru Nakata, and Iwane Inokuchi. New Electonically Controlled Torque Split 4WD System for Improving Cornering Performance. *SAE transactions*, pages 748–757, 1990. Publisher: JSTOR.

[231] A.J. Tremlett, M. Massaro, D.J. Purdy, E. Velenis, F. Assadian, A.P. Moore, and M. Halley. Optimal control of motorsport differentials. *Vehicle System Dynamics*, 53(12):1772–1794, December 2015. ISSN 0042-3114. doi: 10.1080/00423114.2015.1093150. URL https://doi.org/10.1080/00423114.2015.1093150.

[232] Eunhyek Joa, Kwanwoo Park, Youngil Koh, Kyongsu Yi, and Kilsoo Kim. A tyre slip-based integrated chassis control of front/rear traction distribution and four-wheel independent brake from moderate driving to limit handling. *Vehicle System Dynamics*, 56(4):579–603, April 2018. ISSN 0042-3114. doi: 10.1080/00423114.2017.1397276. URL https://doi.org/10.1080/00423114.2017.1397276.

[233] Jianbo Feng, Sizhong Chen, and Zhiquan Qi. Coordinated Chassis Control of 4WD Vehicles Utilizing Differential Braking, Traction Distribution and Active Front Steering. *IEEE Access*, 8:81055–81068, 2020. ISSN 2169-3536. doi: 10.1109/ACCESS.2020.2990729. Conference Name: IEEE Access.

[234] Francesco Pretagostini, Laura Ferranti, Giovanni Berardo, Valentin Ivanov, and Barys Shyrokau. Survey on Wheel Slip Control Design Strategies, Evaluation and Application to Antilock Braking Systems. *IEEE Access*, 8:10951–10970, 2020. ISSN 2169-3536. doi: 10.1109/ACCESS.2020.2965644. Conference Name: IEEE Access.

[235] Hojin Jung, Beomjoon Pyun, and Seibum Choi. Model Predictive Control of an All-Wheel Drive Vehicle Considering Input and State Constraints. *International Journal of Automotive Technology*, 21(2):493–502, April 2020. ISSN 1976-3832. doi: 10.1007/s12239-020-0046-3. URL https://doi.org/10.1007/s12239-020-0046-3.

[236] Irfan Khan, Stefano Feraco, Angelo Bonfitto, and Nicola Amati. A Model Predictive Control Strategy for Lateral and Longitudinal Dynamics in Autonomous Driving. In *Volume 4: 22nd International Conference on Advanced Vehicle Technologies (AVT)*, page V004T04A004, Virtual, Online, August 2020. American Society of Mechanical Engineers. ISBN 978-0-7918-8393-8. doi: 10.1115/DETC2020-22287. URL https://asmedigitalcollection.asme.org/IDETC-CIE/proceedings/IDETC-CIE2020/83938/Virtual,%20Online/1089871.

[237] Kanghyun Nam, Yoichi Hori, and Choonyoung Lee. Wheel Slip Control for Improving Traction-Ability and Energy Efficiency of a Personal Electric Vehicle. *Energies*, 8(7):6820–6840, July 2015. ISSN 1996-1073. doi: 10.3390/en8076820. URL https://www.mdpi.com/1996-1073/8/7/6820. Number: 7 Publisher: Multidisciplinary Digital Publishing Institute.

[238] Valentin Ivanov, Dzmitry Savitski, and Barys Shyrokau. A Survey of Traction Control and Antilock Braking Systems of Full Electric Vehicles With Individually Controlled Electric Motors. *IEEE Transactions on Vehicular Technology*, 64(9):3878–3896, September 2015. ISSN 1939-9359. doi: 10.1109/TVT.2014.2361860. Conference Name: IEEE Transactions on Vehicular Technology.

[239] Giovanni De Filippis, Basilio Lenzo, Aldo Sorniotti, Patrick Gruber, and Wouter De Nijs. Energy-Efficient Torque-Vectoring Control of Electric Vehicles With Multiple Drivetrains. *IEEE Transactions on Vehicular Technology*, 67(6):4702–4715, June 2018. ISSN 1939-9359. doi: 10.1109/TVT.2018.2808186. Conference Name: IEEE Transactions on Vehicular Technology.

[240] Xiaogang Wu, Dianyu Zheng, Tianze Wang, and Jiuyu Du. Torque Optimal Allocation Strategy of All-Wheel Drive Electric Vehicle Based on Difference of Efficiency Characteristics between Axis Motors. *Energies*, 12(6):1122, January 2019. doi: 10.3390/en12061122. URL https://www.mdpi.com/1996-1073/12/6/1122. Number: 6 Publisher: Multidisciplinary Digital Publishing Institute.

[241] Jeongmin Cho and Kunsoo Huh. Torque vectoring system design for hybrid electric–all wheel drive vehicle. *Proceedings of the Institution of Mechanical Engineers, Part D: Journal of Automobile Engineering*, 234(10-11):2680–2692, September 2020. ISSN 0954-4070. doi: 10.1177/0954407020906626. URL https://doi.org/10.1177/0954407020906626. Publisher: IMECHE.

[242] Andrea Sforza, Basilio Lenzo, and F Timpone. A state-of-the-art review on torque distribution strategies aimed at enhancing energy efficiency for fully electric vehicles with independently actuated drivetrains. *International Journal of Mechanics and Control*, 20(2):3–15, 2019.

[243] Andrea Botta, Paride Cavallone, Luigi Tagliavini, Luca Carbonari, Carmen Visconte, and Giuseppe Quaglia. An Estimator for the Kinematic Behaviour of a Mobile Robot Subject to Large Lateral Slip. *Applied Sciences*, 11(4):1594, 2021. Publisher: Multidisciplinary Digital Publishing Institute.

[244] Andrea Botta, Paride Cavallone, Luigi Tagliavini, Giovanni Colucci, Luca Carbonari, and Giuseppe Quaglia. Modelling and simulation of articulated mobile robots. *International Journal of Mechanics and Control*, 22(2):15–25, 2021. ISSN 1590-8844.

[245] Stefan Forrest Campbell. *Steering control of an autonomous ground vehicle with application to the DARPA urban challenge*. PhD thesis, Massachusetts Institute of Technology, 2007.

[246] Andrea Botta, Paride Cavallone, Luca Carbonari, Luigi Tagliavini, and Giuseppe Quaglia. Modelling and Experimental Validation of Articulated Mobile Robots with Hybrid Locomotion System. In *Advances in Italian Mechanism Science*, Mechanisms and Machine Science, pages 758–767, Cham, 2021. Springer International Publishing. ISBN 978-3-030-55807-9. doi: 10.1007/978-3-030-55807-9_84.

[247] Luca Carbonari, Andrea Botta, Paride Cavallone, Luigi Tagliavini, and Giuseppe Quaglia. Data-Driven Analysis of Locomotion for a Class of Articulated Mobile Robots. *Journal of Mechanisms and Robotics*, 13(5):050905, 2021. Publisher: American Society of Mechanical Engineers.

[248] Hans Pacejka. *Tire and Vehicle Dynamics*. Elsevier, April 2012. ISBN 978-0-08-097016-5. doi: 10.1016/C2010-0-68548-8.

[249] Oliver Maier, Benedikt Györfi, Jürgen Wrede, and Roland Kasper. Design and validation of a multi-body model of a front suspension bicycle and a passive rider for braking dynamics investigations. *Multibody System Dynamics*, 42(1): 19–45, January 2018. ISSN 1573-272X. doi: 10.1007/s11044-017-9576-5. URL https://doi.org/10.1007/s11044-017-9576-5.

[250] Andrew Dressel and Adeeb Rahman. Measuring sideslip and camber characteristics of bicycle tyres. *Vehicle System Dynamics*, 50(8):1365–1378, August 2012. ISSN 0042-3114. doi: 10.1080/00423114.2011.615408. URL https://doi.org/10.1080/00423114.2011.615408.

[251] Alberto Doria, Mauro Tognazzo, Gianmaria Cusimano, Vera Bulsink, Adrian Cooke, and Bart Koopman. Identification of the mechanical properties of bicycle tyres for modelling of bicycle dynamics. *Vehicle System Dynamics*, 51(3):405–420, March 2013. ISSN 0042-3114. doi: 10.1080/00423114.2012.754048. URL https://doi.org/10.1080/00423114.2012.754048.

[252] Vera E Bulsink, Alberto Doria, Dorien van de Belt, and Bart Koopman. The effect of tyre and rider properties on the stability of a bicycle. *Advances in Mechanical Engineering*, 7(12):1687814015622596, December 2015. ISSN 1687-8132. doi: 10.1177/1687814015622596. URL https://doi.org/10.1177/1687814015622596. Publisher: SAGE Publications.

[253] Andrew Dressel and James Sadauckas. Characterization and Modelling of Various Sized Mountain Bike Tires and the Effects of Tire Tread Knobs and Inflation Pressure. *Applied Sciences*, 10(9):3156, January 2020. ISSN 2076-3417. doi: 10.3390/app10093156. URL https://www.mdpi.com/2076-3417/10/9/3156. Number: 9 Publisher: Multidisciplinary Digital Publishing Institute.

[254] P. Artemiadis. Closed-form inverse kinematic solution for anthropomorphic motion in redundant robot arms. In *ICRA 2013*, 2013. doi: 10.4172/2168-9695.1000110.

[255] Carlos Faria, Flora Ferreira, Wolfram Erlhagen, Sérgio Monteiro, and Estela Bicho. Position-based kinematics for 7-DoF serial manipulators with global configuration control, joint limit and singularity avoidance. *Mechanism and Machine Theory*, 121:317–334, 2018. doi: 10.1016/j.mechmachtheory.2017.10.025.

[256] Andrea Botta and Giuseppe Quaglia. Low-Cost Localization For Mobile Robot With Fiducial Markers. In *Proceedings of the 25th Jc-IFToMM Symposium (2019) 2nd International Jc-IFToMM Symposium 26th October 2019, Kanagawa*, Kanagawa, October 2019.

[257] Andrea Botta and Giuseppe Quaglia. Performance Analysis of Low-Cost Tracking System for Mobile Robots. *Machines*, 8(2):29, June 2020. doi: 10.3390/machines8020029. URL https://www.mdpi.com/2075-1702/8/2/29. Number: 2 Publisher: Multidisciplinary Digital Publishing Institute.

[258] William F. Milliken and Douglas L. Milliken. *Race Car Vehicle Dynamics*. SAE, 1994. ISBN 978–1-56091-526-3.

[259] R. S. Rice. MEASURING CAR-DRIVER INTERACTION WITH THE g-g DIAGRAM. SAE Technical Paper 730018, SAE International, Warrendale, PA, February 1973. URL https://www.sae.org/publications/technical-papers/content/730018/. ISSN: 0148-7191, 2688-3627.

[260] Andrea Botta and Paride Cavallone. Robotics Applied to Precision Agriculture: The Sustainable Agri.q Rover Case Study. In *Proceedings of I4SDG Workshop 2021*, Mechanisms and Machine Science, pages 41–50, Cham, 2022. Springer International Publishing. ISBN 978-3-030-87383-7. doi: 10.1007/978-3-030-87383-7_5.

[261] Solcast. Global solar irradiance data and PV system power output data, 2021. URL https://solcast.com/.